PhD program in Science and Technology (Universidad Internacional Menéndez Pelayo)

PhD program in Chemistry (Università degli Studi di Milano)

EFFECT OF MICROTUBULE-TARGETING AGENTS ON STRUCTURAL SIGNALING AND CHEMICAL TRANSPORT IN CELLS

Francesca Bonato

2023

Main supervisors (Centro de Investigaciones Biológicas Margarita Salas, CSIC)

Dr. José Fernando Díaz Pereira

Dr. María Ángela Oliva Blanco

Co-primary supervisor (Università degli Studi di Milano)

Prof. Daniele Passarella


The research presented in this PhD thesis was performed under the Marie Skłodowska – Curie Actions, at Centro de Investigaciones Biológicas Margarita Salas (CSIC), Madrid, Spain and at Università degli studi di Milano, Italy, under a co-tutelle agreement between Universidad Internacional Menéndez Pelayo and Università degli Studi di Milano. It was financially supported by the European Union's Framework Programme for Research and Innovation Horizon H2020-MSCA-ITN-European Joint Doctorate "Tuning Tubulin Dynamics and Interactions to Face Neurotoxicity: a Multidisciplinary Approach for Training and Research", named with the acronym TubInTrain, Grant agreement n°: 860070.

www.tubintrain.eu

Occorre diffidare del quasi-uguale (…), del praticamente identico, del pressapoco, dell'oppure, di tutti i surrogati e di tutti i rappezzi. Le differenze possono essere piccole, ma portare a conseguenze radicalmente diverse, come gli aghi degli scambi; il mestiere del chimico consiste in buona parte nel guardarsi da queste differenze, nel conoscerle da vicino, nel prevederne gli effetti.

Primo Levi, *Il sistema periodico*

Acknowledgments

At the outset of this thesis, I wish to extend my gratitude to all the people that have helped and supported me to reach the successful completion of my doctoral research.

I am profoundly thankful to my thesis supervisors, Dr. José Fernando Díaz Pereira, Dr. María Ángela Oliva Blanco and Prof. Daniele Passarella for granting me the invaluable opportunity to work with them in high-level scientific research groups, allowing me to expand my knowledge and nurturing my growth as a scientist. I extend my heartfelt appreciation for their guidance and encouragement throughout my doctoral journey, and for providing me with the essential tools and insights to navigate the intricate intersection between chemistry and biology, bridging these two realms in pursuit of new research horizons.

My gratitude extends to the entire TubInTrain consortium, where a multi-disciplinary framework has provided a space to exchange and compare ideas, foster collaboration, and share our collective passion for discovery. It has been a privilege to be part of this intellectually stimulating and supportive community.

Thank you, from the deep of my heart, to all the members of the research groups in Madrid and Milano. Collaborating and working alongside each of you has been both an honor and a privilege. The collective knowledge, collaborative spirit, and camaraderie we cultivated form the very foundation of this thesis. Research, as I have come to realize, is never a solitary journey but rather a team expedition into uncharted territory.

I am thankful to my friends, both near and far, for keeping me grounded and reminding me of the broader perspective beyond academia. Their attentive ears and comforting words have been a constant source of support.

To my sister, Valentina, you have been my confidant and cheerleader. Your unwavering belief in my abilities and your countless words of encouragement have sustained me through the peaks and valleys of this journey.

Thanks to my mother and father for supporting me, emotionally and practically. Thank you for your attentive listening, for your wise advice and for your unconditional affection: you have always been by my side. I am proud of you; now I hope to make you equally proud of me.

Lastly, I want to give special thanks to Simone for standing by my side with patience and love at every juncture of this remarkable journey – be it the moments of self-doubt, the trials of challenges, and the small and big accomplishments.

Table of contents

List of abbreviations

Å	Angström
A.U.	Arbitrary units
Abs	Absorbance
AC	Alternate current
AcOEt	Ethyl acetate
ADC	Antibody-drug conjugate
ADP	Adenosine diphosphate
amu	Atomic mass unit
ATP	Adenosine triphosphate
BBB	Blood-brain barrier
BSA	Bovine serum albumin
Cbz	Benzyloxy carbonyl group
CIPN	Chemotherapy-induced peripheral neurotoxicity
CM	Constrained motion
Da	Dalton
DAPI	4',6-Diamidino-2-phenylindole
DBP	Dynein-binding peptide
DCC	*N, N*'-Dicyclohexylcarbodiimide
DEAE	Diethyl-aminoethyl group
DIC	Differential interference contrast
DMAP	4-Dimethylaminopyridine
DMEM	Dulbecco's modified eagle medium
DMF	*N, N*-Dimethylformamide
DMSO	Dimethyl sulfoxide
DMSO-d_6	Deuterated dimethyl sulfoxide
DNA	Deoxyribonucleic acid
DTT	Dithiothreitol

ECM	Extracellular matrix
EDC·HCl	1-Ethyl-3-(3-dimethylaminopropyl)carbodiimide hydrochloride
EDTA	Ethylenediaminetetraacetic acid
EGTA	Ethylene glycol-bis(2-aminoethylether)-N,N,N’,N’-tetraacetic acid
EM	Electron microscopy
ESI	Electrospray ionization
EtOH	Ethanol
eV	Elettronvolt
FDA	Food and Drug Administation
Fmoc	Fluorenylmethyloxycarbonyl protecting group
FTX2	Flutax-2
GDP	Guanosine diphosphate
GMPCPP	Guanosine-5’-[(α,β)-methyleno]triphosphate
GTP	Guanosine triphosphate
HPLC	High-performance liquid chromatography
HXFTX	Hexaflutax
Hz	Hertz
IC_{50}	Half maximal inhibitory concentration
KBP	Kinesin-binding peptide
KHC	Kinesin heavy chain
KLC	Kinesin light chain
MACF	Microtubule – actin crosslinking factor
MAP	Microtubule-associated protein
MC	Methylcellulose
MD	Molecular dynamics
MDA	Microtubule-destabilizing agent
MDR	Multi-drug resistant
MeOH	Methanol
MHz	Megahertz
min	Minute
MIP	Microtubule-internal protein

MS	Mass spectrometry
MSA	Microtubule-stabilizing agent
MSD	Mean square displacement
MT	Microtubule
MTA	Microtubule-targeting agent
MTOC	Microtubule-organizing center
MTT	3-(4,5-Dimethylthiazol-2-yl)-2,5-diphenyltetrazolium bromide
MW	Molecular weight
MWCO	Molecular weight cut-off
NADH	Nicotinamide adenine dinucleotide (reduced form)
NADPH	Nicotinamide adenine dinucleotide phosphate (reduced form)
NMR	Nuclear magnetic resonance
Nt	Nucleotide
PAGE	Polyacrylamide gel electrophoresis
PBS	Phosphate buffer solution
PDB	Protein data bank
Pd/C	Palladium on carbon
P-gp	P-glycoprotein
ppm	Part per million
PTM	Post – translational modifications
PTX	Paclitaxel
Py	Pyridine
RNA	Ribonucleic acid
SAR	Structure-activity relationship
SAXS	Small-angle X-ray scattering
SD	Standard deviation
SDS	Sodium dodecyl sulfate
sec	Second
SEM	Standard error of the mean
SPPS	Solid phase peptide synthesis
T_2	Dimeric tubulin

TBAF	Tetrabutylammonium fluoride
THF	Tetrahydrofuran
TIPN	Taxane-induced peripheral neurotoxicity
TLC	Thin layer chromatography
TM	Transported motion
TMSE	2-(Trimethylsilyl)ethanol
Tris	Tris(hydroxymethyl)aminomethane
Triton X-100	*tert*-Octylphenoxypolyethoxyethanol
TSE	2-(Trimethylsilyl)ethyl protecting group
ULF	Unit-length filament
UV-Vis	Ultraviolet-visible
γ-TuRC	γ-Tubulin ring complex

Abstract

Microtubules, along with actin and intermediate filaments, are key components of the cellular cytoskeleton and play pivotal roles in several biological functions, including intracellular trafficking, positioning of cellular components in interphase, mitotic spindle formation during cell division, maintaining of cell morphology and cell motility. Structurally, microtubules are formed by αβ-tubulin heterodimers that polymerize in a head-to-tail fashion to create protofilaments, which subsequently assemble into hollow cylindrical polar filaments. Microtubules' behavior and function depend on their polymerization dynamics, with the first layer of regulation being the GTPase cycle of tubulin and its addition to the growing microtubule end. This process causes tubulin to transition from a curved conformation in solution to a straight conformation in the microtubule lattice. In cells, secondary layers of regulation (associated proteins, post-translational modifications, and tubulin isotypes levels) allow for a more precise modulation and differentiation of microtubule activities.

Due to their involvement in key cellular activities, compounds that interfere with the microtubule cytoskeleton have been developed as cytotoxic agents, demonstrating remarkable efficacy against a wide spectrum of cancer types. Paclitaxel, a natural product extracted from yew tree bark, was the first microtubule-targeting agent (MTA) to be approved for clinical use in 1992, followed by two synthetic derivatives, docetaxel and cabazitaxel. These molecules bind to the taxane binding site in the microtubule, inducing its structural stabilization and preventing depolymerization events. Although the ability of taxanes to disrupt microtubule dynamics is closely linked to their chemotherapeutic effects, the exact cellular mechanism behind their anticancer activity remains under debate. At present, taxanes remain among the first-line treatments for several solid tumors, including breast cancer, ovarian carcinoma, pancreatic adenocarcinoma, non-small lung cancer, and prostate cancer. However, the clinical use of these molecules is limited by taxane-induced peripheral neurotoxicity, which severely affects up to 30% of patients and frequently leads to therapy discontinuation.

To protect neurons from damage during taxane chemotherapy, it is essential to gain an improved mechanistic understanding of these drugs' pathological effects on neurons. Due to their complex and elongated structures, neurons rely on intracellular active transport for cargo movement along the axon, making them especially susceptible to deficits in this process caused by taxane treatment. A recent hypothesis links axonal transport impairment to lattice expansion, a structural alteration induced by taxanes that appears to be unrelated to the stabilization effect. Locally expanded dimers may act as lattice point defects and cause premature detachment or stalling of the microtubule-associated motor proteins. Moreover, since current models of the microtubule structure describe the expanded lattice as a distinct structural feature localized near the tip, the spread of this structural signal along the whole lattice could impact the recognition patterns of motor proteins. Interestingly, unpublished results from our laboratory show that flutax-2, a C7-modified fluorescent taxane, does not induce microtubule lattice expansion.

The present work, titled “Effects of microtubule-targeting agents on structural signaling and chemical transport in cells” focuses on two primary objectives. First, it aims to investigate the influence of C7-modifications of the taxane core on the cellular, biochemical, and structural properties of microtubules, in particular on lattice axial expansion. Second, it seeks to describe the relationship between the microtubule structural modifications induced by taxanes and the impairment of intracellular transport. These objectives were pursued through a multidisciplinary approach that included the *in-silico* design and chemical synthesis of new C7-decorated taxanes engineered to emulate the binding mode of flutax-2. Subsequently, the *in vitro* biochemical and structural characterization of these compounds was carried out, and their effect on cellular systems was extensively investigated.

The findings presented in this thesis highlight the potential of C7-modification for generating taxanes able to override common cellular resistance mechanisms and/or to exert reduced impact on microtubule structure, thereby mitigating their interference over intracellular transport. Furthermore, the results obtained suggest that microtubule lattice expansion alone cannot account for the altered transport within taxanes-treated cells.

1 Introduction

1.1 The cell cytoskeleton: a brief history

The discovery of the cell and its components is deeply intertwined with the evolution of imaging technology. The advent of optical microscopes in the late 16th century enabled scientists to observe living cells, laying the foundation for the field of cellular biology. Technological constraints in cellular imaging reinforced the notion of the cell as a uniform and static entity, until the early 19th century when the first observations of subcellular structures were reported. Throughout the rest of the century, scientists accumulated observations of the cell's intricate internal organization and dynamic events, while a growing scientific curiosity emerged around how the cell coordinates its spatial and mechanical functions. The first hints came from observations of remarkable physical resilience: the postulation of some sort of intracellular network was supported by the experiments of Edward Conklin (1917)[1] and Paul Wintrebert (1931)[2], who observed the fast internal reorganization of oocytes subjected to strong mechanical stimuli. In his work, Wintrebert coined the term *cytoskeleton* (*cytosquelette* in French) to refer to this elastic network capable of redistributing the displaced intracellular contents. Further studies, strongly dependent on the development of electron microscopy techniques (EM), revealed the cytoskeleton to be a dynamic network of protein filaments whose interplay with crosslinkers and associated proteins provides the framework for nearly all cellular processes[3–8]. While statically providing mechanical resistance to deformation and arranging the organelles' positions, the cytoskeleton also enables the cell's dynamic events, including motility, intracellular transport, endocytosis, and mitosis. Figure 1-1 outlines the significant historical discoveries that have contributed to our current scientific understanding of the cytoskeleton [9,10].

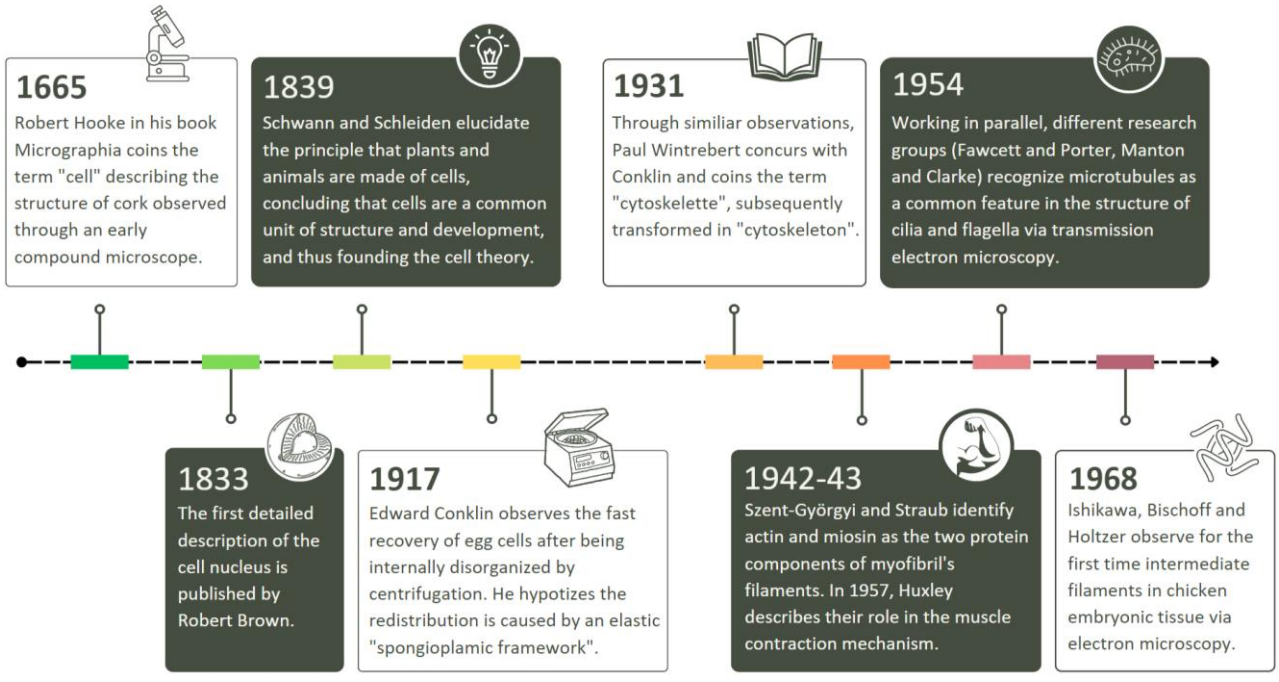

Figure 1-1. The timeline shows in chronological order some of the milestones that led to the discovery and description of the cellular cytoskeleton.

In eukaryotic organisms, the cytoskeleton is composed of three types of polymers - actin filaments, intermediate filaments, and microtubules – with distinct mechanical properties, dynamics, and biological roles. Through the regulation of the dynamic behavior and assembly pf these three filament systems, eukaryotic cells can build an enormous range of higher-order structures. The fibroblast in panel A of Figure 1-2 displays the typical distribution of the various cytoskeletal networks within the cell [11].

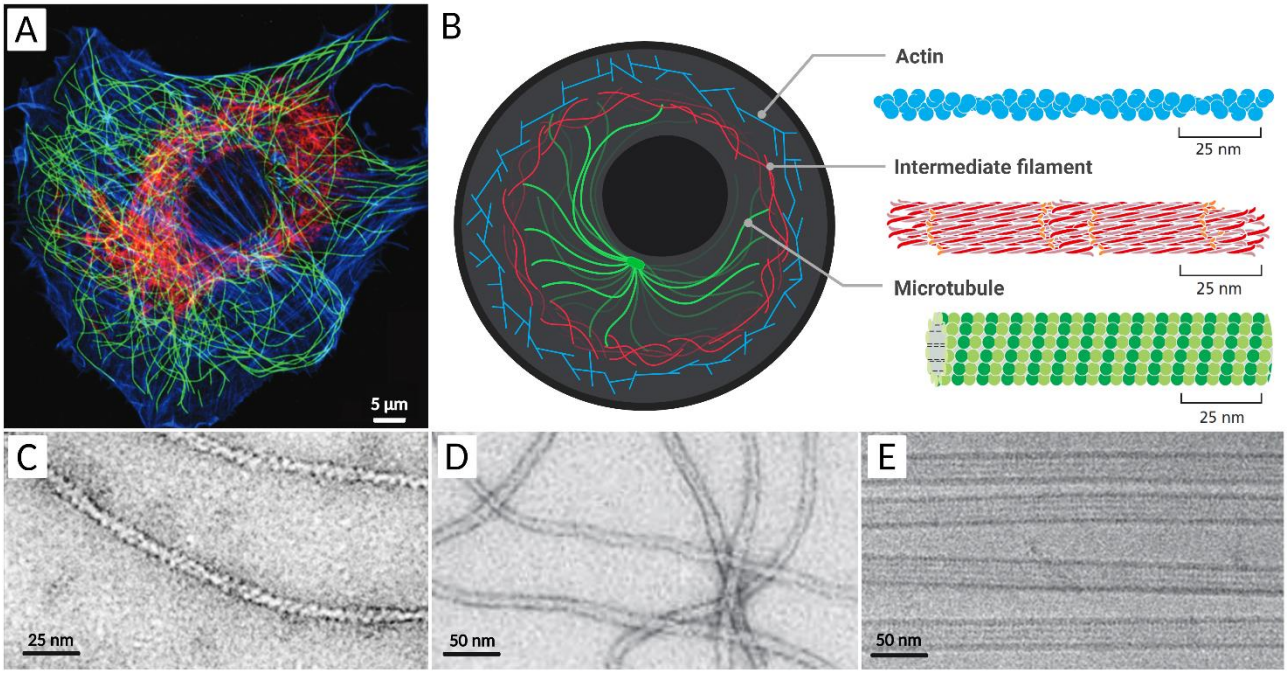

Figure 1-2. Cytoskeletal polymers in eukaryotic cells. Panel **A**: Fibroblast with fluorescently labeled cytoskeleton components: microtubules in green, intermediate filaments in red, and actin filaments in blue. Image adapted from [11]. Panel **B**: Schematic representation of the cytoskeleton components (right) and their localization within the cell (left). Panel **C**: Negative stain electron microscopy image of F-actin. Image adapted from [12]. (**D**) Electron micrograph of intermediate filaments. Image adapted from [13]. Panel **E**: Electron micrograph of microtubules. Image adapted from [14].

The actin cytoskeleton, which is prominently localized in the cell *cortex* beneath the plasma membrane, continuously assembles and disassembles under physiological conditions. Actin filament elongation is driven by the addition of ATP-bound monomers (G-actin) to the growing end, resulting in a twisted, filamentous two-stranded structure with a diameter of 8-9 nm (F-actin). Upon the formation of stable filaments, the bound ATP is hydrolyzed and the γ-phosphate is released, which promotes filament depolymerization inducing a dynamic behavior. Actin filaments provide mechanical support to the cell *cortex* and are integral to maintaining cellular morphology. They function in tandem with myosin motor proteins to generate contractile forces that drive muscle contraction and cytokinesis. In addition to these mechanical functions, the specific interaction between actin filaments and myosin motors also plays a crucial role in endocytosis and exocytosis, enabling vesicular transport between the plasma membrane and the cytoplasm[11,13].

Intermediate filaments form a complex network concentrated in the perinuclear region. From there, filaments radiate toward the cell surface where they are anchored to intercellular junctions (desmosomes) and cell-extracellular-matrix junctions (hemidesmosomes). These robust filaments, which are 10-11 nm in

diameter, are composed of one or more members of a large family of homologous proteins with a conserved central α-helical domain. This domain allows the proteins to associate in pairs to form extended coiled-coil structures. A pair of parallel dimers subsequently associates in an antiparallel fashion to form a staggered tetramer. An average of eight tetramers pack together laterally to form unit-length filaments (ULFs), which then assemble end-to-end to constitute the intermediate filament. Unlike G-actin or tubulin, intermediate filament subunits do not contain a nucleotide binding site. Furthermore, mature intermediate filaments lack the polarity inherent in the structure of F-actin and microtubules due to the opposite orientation of dimers within the tetrameric subunits, which might explain why no motors are known to move along them. The strong lateral hydrophobic interactions typical of coiled-coil proteins give intermediate filaments a ropelike character, making them easy to bend but resistant to stretching. Due to these properties, intermediate filaments are involved in a variety of cellular functions, including the maintenance of cell shape and integrity, the formation of the nuclear lamina, and the anchorage of organelles. They also play a role in tissue-specific functions, such as the formation of hair and nails[11,13].

The microtubule network represents the third component of the eukaryotic cytoskeleton. It emanates from the juxtanuclear centrosome, the main microtubule-organizing center (MTOC) of the cell, and extends toward the cell periphery. However, this cytoplasmic array can quickly rearrange itself to form a bipolar mitotic spindle during cell division. Additionally, microtubules can form cilia, which function as motile whips or sensory devices on the surface of the cell, or serve as polar tracks for the transport of cellular cargo by kinesins and dyneins motors. Microtubules differ from the other cytoskeletal filaments due to their greater stiffness and larger diameter (24 nm), which allows their visualization by light microscopy. The following sections will present a more comprehensive overview of the architecture, functions, and characteristics of microtubules and their constituent protein subunits.

1.2 The microtubule subunit: the αβ-tubulin heterodimer

Microtubule filaments can reach from one end of the cell to the other, spanning tens or even hundreds of micrometers. Yet the individual protein molecules that form the filaments are only a few nanometers in size. The small protein bricks that constitute microtubules belong to the superfamily of *tubulins*, which comprises seven known families – α, β, γ, δ, ε, ζ, and η-tubulins. Among these, the first three families described in scientific literature[15,16] – α, β, and γ-tubulins – stand out as the only members ubiquitously present in eukaryotic cells: α and β-tubulins are the primary building blocks forming the microtubule lattice, conferring structural integrity and functionality, whereas γ-tubulin plays a regulatory role in microtubule nucleation at MTOCs. The identification of the remaining four tubulin families – δ, ε, ζ, and η-tubulins – is chronologically more recent[17–19]. While much remains unknown about these tubulin families' distribution and function in

eukaryotes, their physiological roles appear to be closely associated with the duplication and assembly of centrioles and basal bodies within the cell.

Among all members within the superfamily, α- and β-tubulins are the most crucial for microtubule function. These two globular proteins, present in the cytoplasm at a concentration of 4-24 μM[20,21], spontaneously associate to form an αβ-tubulin heterodimer that constitutes the fundamental subunit of the microtubule. Both proteins are GTPases of 445-450 amino acids that share approximately 40% of their primary sequence and possess a highly conserved tertiary structure, as confirmed by the atomic-level structural resolution of the αβ-tubulin heterodimer, obtained by Eva Nogales in 1998 via electron crystallography (PDB accession code: 1TUB)[22]. Three years later, Jan Löwe refined the structural model from 3.8 Å to 3.5 Å resolution through improved data processing (PDB accession code: 1JFF)[23]. According to these models, tubulin's structure can be divided into three functional domains: N-terminal, intermediate, and C-terminal domains. These domains are represented in Figure 1-3 in gray, blue and steel blue, respectively.

The N-terminal domain (residues 1-205) includes a Rossmann fold, consisting of six parallel β-sheets (S1-S6) alternated by six α-helices (H1-H6). The loops (T1-T6) connecting the α-helices and the β-sheets create a pocket that can accommodate a guanosine-based nucleotide, typically a GTP or GDP molecule under physiological conditions (depicted in multi-colored sphere representation in Figure 1-3). The GTP bound to α-tubulin is physically trapped at the intra-dimer interface and is never hydrolyzed or exchanged; therefore, it is considered an integral part of the tubulin heterodimer structure. The nucleotide on the β-tubulin, in contrast, may be in either the GTP or the GDP form and is exchangeable within the soluble (unpolymerized) tubulin dimer. The two nucleotide-binding sites on the heterodimer are therefore referred to as the N-site (non-exchangeable) and E-site (exchangeable) based on their distinct properties. When an α,β-heterodimer is incorporated into the microtubule, the E-site nucleotide remains located at the interdimer interface in direct contact with loop T7 (connecting helices H7 and H8) and helix H8 of the adjacent subunit along the protofilament. Both N- and E-sites of tubulin also fit a magnesium ion that is critical for microtubule assembly and GTPase activity [24].

Connected to the N-terminal domain by helix H7, the intermediate domain (residues 206-381) comprises four-stranded mixed β-sheets (S7-S10), flanked by two helices on one side and one on the other (H8-H10). This domain harbors several key structural features of the protein, including helix H7 itself (also referred to as central helix, depicted in red-orange in Figure 1-3) that plays an important role in β-tubulin's dynamics by acting as a hinge around which the conformational changes necessary for the polymerization process take place. As already mentioned, loop T7 and helix H8 lay at the longitudinal interface between monomers, in direct contact with the nucleotide of the neighboring subunit. In α-tubulin, the T7 loop is also known as the catalytic loop (in magenta in Figure 1-3), as the presence a glutamic acid in place of the 254-lysine of β-tubulin

enables the catalytic activation of a water molecule that is essential for GTP hydrolysis. Importantly, the location of the catalytic loop in a different subunit makes tubulin self-assembly an important prerequisite for the construction of the catalytic binding site. This is confirmed by the drastically lower hydrolysis rate of the unpolymerized dimer compared to its polymerized form (0.054 min^{-1} vs. 12.21 min^{-1}) [25]. Another noteworthy structural feature of the intermediate domain is the S7-H9 loop, also known as M-loop (depicted in green in Figure 1-3), which strongly contributes to the lateral interaction between protofilaments.

Lastly, the C-terminal domain (residues 382-440) is composed of the two antiparallel α-helices H11 and H12 and an unfolded tail. These two helices overlap the previous domains while sitting on the outside surface of the microtubule, where most microtubule-associated proteins (MAPs) bind. The last C-terminal residues of each monomer (approximately 10 residues in α-tubulin and 18 residues in β) form a hypervariable solvent-exposed acidic coil where most variations between isotypes and post-transcriptional modifications occur.

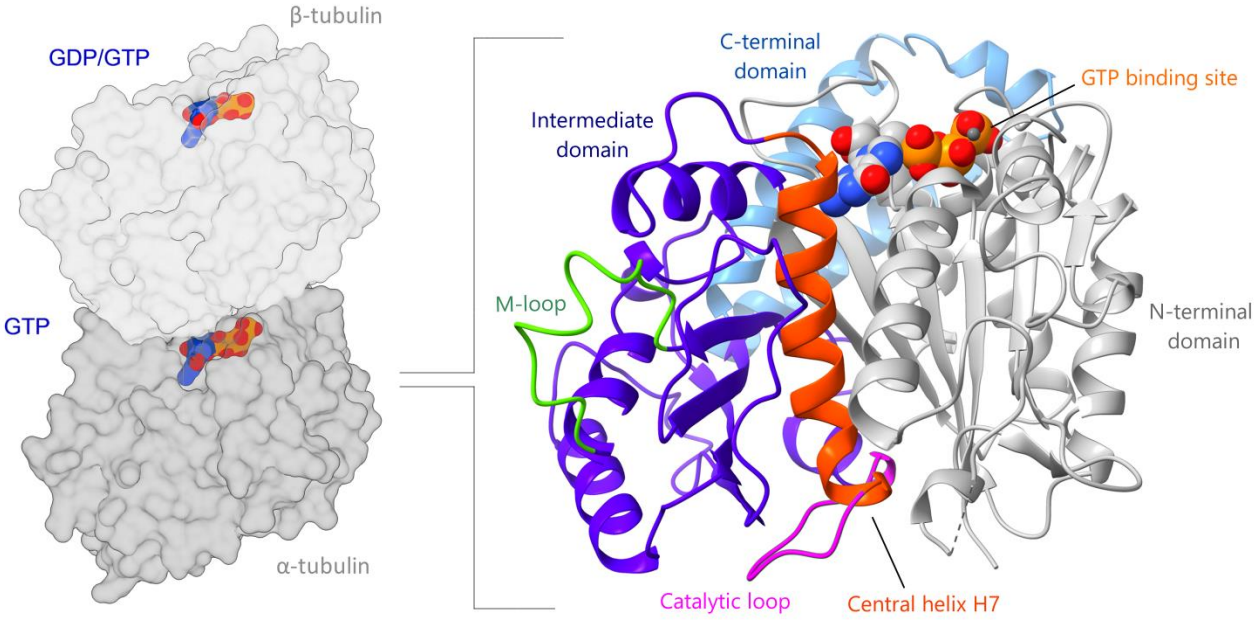

Figure 1-3. Microtubule's subunit structure. The illustration on the right displays a tubulin heterodimer in surface representation, which consists of a tightly linked pair of α- (grey) and β-tubulin (white) monomers. Under physiological conditions, the α-tubulin monomer can only bind a GTP molecule, which cannot be exchanged and constitutes an integral part of the protein, while the β-tubulin monomer can bind either a GDP or a GTP molecule. The nucleotides of both monomers are shown in sphere representation. On the left, the structure of α-tubulin is depicted n ribbon representation, with the GTP molecule in sphere representation. The side of the tubulin molecule facing the reader corresponds to a view from the inside of the microtubule. Key structural features are highlighted in different colors: the N-terminal domain in gray, the intermediate domain in blue, the C-terminal domain in steel blue, the central helix H7 in red-orange, the catalytic loop in magenta, the M-loop in green, and the nucleotide-binding site colored by heteroatom (PDB accession code: 6DPV).

The association of α- and β-tubulin is facilitated by several cofactors[26–28] within the cytoplasmatic environment, leading to the formation of a highly stable dimer of 110 kDa. However, assessing the stability of this αβ-tubulin heterodimer has proved to be a challenging task, as calculated thermodynamic and kinetic parameters have shown significant variability across different studies[29–33]. More specifically, the research on this topic yielded heterodimer dissociation constants ranging from 10^{-11} to 10^{-6} M, and dissociation rates from

10^{-5} to 10^{-2} s^{-1}. These discrepancies stem from a combination of experimental difficulties in measuring affinities in the sub micromolar range and biochemical differences between tubulins from different species. The recent application of mass photometry to this challenging problem[34] has enabled more precise measurements of the αβ-heterodimer dissociation constants, which were found to be 8.48 ± 1.22 nM and 3.69 ± 0.65 nM in the absence and presence of GTP, respectively, with a dissociation rate exceeding 10^{-2} s^{-1}.

1.3 From subunit to structure: the microtubule's dynamic architecture

1.3.1 Microtubule structure

In vivo, αβ-tubulin heterodimers tend to polymerize in a head-to-tail arrangement, leading to the formation of a protofilament. Commonly, thirteen protofilaments[35] associate in parallel and curl around to create a pipe-like structure with a diameter of approximately 24 nm (Figure 1-4). Since tubulin dimers assemble in a head-to-tail fashion, microtubules are polar structures with two distinct ends: the rapid-growing (+)-end with exposed β-subunits and the slow-growing (-)-end with exposed α-subunits.

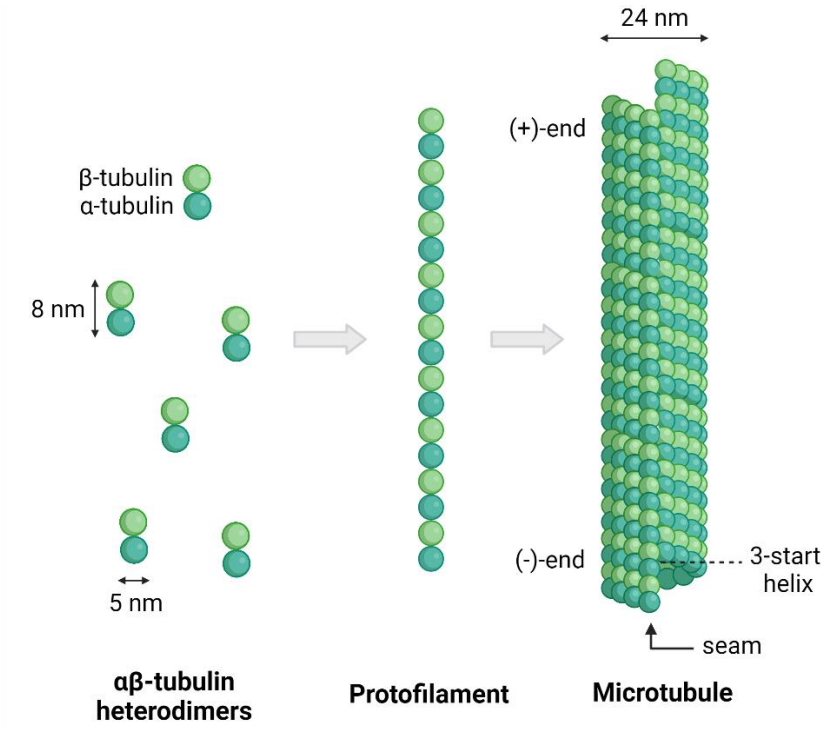

Figure 1-4. Schematic representation of microtubule structure and organization. In solution, αβ-tubulin heterodimers (left, α-tubulin in dark green and β-tubulin in light green) assemble head-to-tail into protofilaments (middle). The lateral interaction of several protofilaments leads to the formation of the microtubule's pseudo-helical and polar structure (right).

Although the microtubule's structural features are now well understood due to the availability of several high-resolution structural models[36–38] (the first dating back to 1999, by Eva Nogales[39]), low-resolution electron microscopy had already revealed important information about the microtubule lattice years before. In 1986, when it was already clear that adjacent protofilaments were axially offset and overall, the

microtubule lattice was characterized by a helical feature, Eva-Maria Mandelkow measured an approximate 0.9 nm subunit rise between adjacent protofilaments[40]. In a 13-protofilament microtubule, this resulted in a total axial rise of 12 nm per helical turn, approximately three times the length of a tubulin monomer (4 nm). This information allowed for the attribution of a 3-start helix identity to 13-protofilament microtubules (referred to as 13_3 microtubules from now on). It was also possible to establish that lateral contacts between protofilaments involved homologous contacts between monomers (α-α and β-β), interrupted by a discontinuity (called seam) of heterologous interactions (α-β). Due to the presence of the seam, the symmetry of the microtubule is actually pseudo-helical.

However, the 13_3 lattice is not an intrinsic property of αβ-tubulin polymers. Microtubules assembled from purified αβ-tubulin incorporate variable protofilament numbers (from 9 to 16, with 14-protofilament microtubules being the most prevalent *in vitro*[41]) and different tubulin subunit helical-start numbers[42]. Hence, the uniformity observed *in vivo* suggests that cells determine their protofilament count as 13 during the nucleation process. In most cases, the number of protofilaments is dictated by a nucleation template, such as the 13 γ-tubulins of the γ-tubulin ring complex (γ-TuRC), as well as nucleation factors such as MAPs and microtubule-internal proteins (MIPs)[43]. The conservation of the 13_3 lattice across all eukaryotic supergroups, with rare exceptions, has been explained with the so-called *straight-filament hypothesis*[44]. Due to the helical arrangement of subunits within the lattice, only the 13_3 geometry allows protofilaments to run straight relative to the microtubule's axis. In contrast, alternative geometries with a different number of protofilaments or helix start induce the protofilaments to supertwist around the microtubule[45] (as in the case of the 14-protofilament microtubule depicted in Figure 1-5).

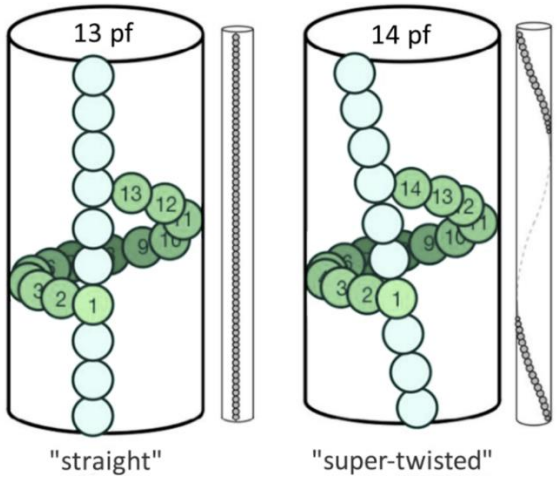

Figure 1-5. Twist on microtubule's protofilaments. Adjacent protofilaments have a longitudinal offset of 9.2 Å between tubulins such that 13-protofilament microtubules have straight protofilaments (left). Non-13-protofilament microtubules (14-protofilament lattice depicted, right) are forced to accommodate by introducing a supertwist in the protofilament arrangement. Image modified from [43].

A skew angle may also arise from variations in the longitudinal spacing between monomers in the protofilament, which can be caused by non-natural nucleotides[46] (e.g., GMPCPP) or by the action of

microtubule-targeting agents. The dependency of the skew angle θ_{the} on all these factors is described by the following equation[47]:

$$\theta_{the} = \tan^{-1}\left[\frac{1}{\delta x} - \left(\frac{S \cdot a}{N} - r\right)\right] \quad [1]$$

where δx is the lateral separation between protofilaments, S is the helix start, a is the longitudinal monomer spacing, N is the protofilament number, and r is the inter-protofilament rise.

According to the straight-protofilament theory, there must be an evolutionary pressure to maintain straight protofilaments in microtubules, possibly related to their mode of functioning. For example, straight protofilaments might offer a selective advantage in effective long-range transport or for ciliary beating[43]. More specifically, the straight protofilaments of a 13-protofilament A-tubule may be necessary for the B-tubule to attach without twisting around the B-tubule (see Figure 1-13 for the structure of cilia and flagella).

The multiple contacts among subunits make microtubules stiff and difficult to bend, with a persistence length (i.e., the average filament length at which random thermal fluctuations are likely to cause it to bend) of several millimeters[13]. Nonetheless, the static structural description of microtubules discussed thus far fails to convey a crucial aspect of their nature: their dynamic behavior. Indeed, the ability to rapidly change their length and shape is essential for microtubules' proper functioning *in vivo*. The fundamental aspects of this dynamic nature will be elaborated in the following section.

1.3.2 Microtubule dynamics

The study of microtubule dynamics *in vitro* started in 1972, when Richard Weisenberg reported the reversible self-assembly of tubulin at 37°C in buffers containing a calcium chelator (EGTA), magnesium ions, and GTP [48]. Measuring microtubule polymerization entails identifying changes in a physical property that differentiates a dimeric tubulin solution from a polymer solution. The most noticeable attribute is the size, as discerned by F. Gaskin, C. Cantor, and M. Shelanski in 1974 [49]. The formation of polymers increases the solution's light scattering, resulting in a higher optical density. This change can be easily measured using a spectrophotometer, with the resulting turbidity readings yielding quantitative measurements of assembly kinetics and steady-state polymer concentrations. The assembly curve obtained is characterized by three phases: a lag time during which nucleation occurs, a net growth period where microtubules elongate through the addition of new tubulin dimers to their ends, and a plateau corresponding to the steady state (Figure 1-6). In the steady state, microtubules alternate between lengthening and shortening phases, but the total mass of the polymer remains unchanged.

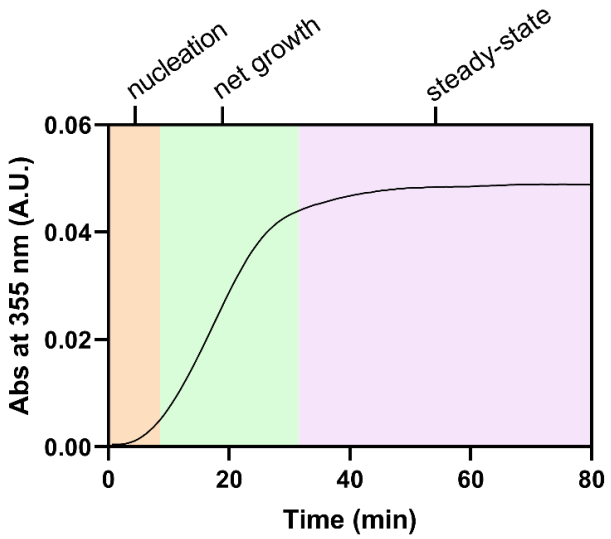

Figure 1-6. Representative curve of a tubulin polymerization turbidimetric assay in GAB buffer (see section 3.2.7 of Material and Methods). The assembly of tubulin at 37°C is followed by monitoring the increase in absorbance at λ = 355 nm in a plate reader. The polymerization curve is divided into three phases: an initial lag time corresponding to nucleation (orange), a period of exponential net growth due to microtubule elongation (green), and a plateau corresponding to the steady state (violet) which indicates the total mass of polymer formed.

In 1984, Tim Mitchison and Marc Kirschner first inferred a new mechanism, termed *dynamic instability*, from the analysis of length distributions of fixed microtubules[50]. This model postulates that while a population of microtubules maintains a bulk steady state, individual microtubules never reach a steady state length but undergo extended periods of polymerization and depolymerization, with infrequent transitions between these states. The existence of dynamic instability was then verified through direct visualization of single microtubules by dark field and differential interference contrast (DIC) video microscopy[51,52]. Numerous studies since 1984 have convincingly established the occurrence of microtubule dynamic instability both *in vitro* and *in vivo*, leading to its widespread recognition as the predominant mechanism controlling microtubule polymerization dynamics.

Dynamic instability (Figure 1-7) is a highly non-equilibrium behavior and therefore requires an energy source. The only possible source is GTP hydrolysis, which occurs in the β-tubulin subunit upon recruitment of the α-subunit's catalytic E254 residue of a new dimer incorporating in the lattice. More specifically, GDP-tubulin remains inactive in the cytoplasm until GTP exchange at the E-site occurs, activating the dimer and providing interactive surfaces prone to addition into protofilaments. The formation of lateral contacts between protofilaments at the microtubule tip induces the tubulin subunits to adopt a more rigid and "straight" conformation. This conformational change, known as *curved-to-straight transition*[53], is key to the formation of a hydrolysis-competent state. Microtubule elongation occurs by the addition of GTP-bound tubulin at both ends of the microtubule, but it is significantly faster at the (+) end. Due to the delay between assembly and hydrolysis, the tip of the microtubule contains GTP-bound dimers (referred to as the GTP-cap)[54], while the central body of the microtubule contains GDP-bound molecules. Since GDP-bound tubulin dimers are more prone to depolymerization, when hydrolysis catches up to the tip of a microtubule it causes its shrinkage in

an event known as catastrophe. However, GTP-bound tubulin polymerizes again to the not fully depolymerized filament, providing a new protective cap: this is referred to as rescue. The GDP-bound tubulin forming the body of the microtubule has a compact, straight, and regular lattice, whereas the lattice pattern of the GTP-cap is still debated. Since the early 90s, cryo-EM imaging has provided a range of partially-curved conformations, stabilized by early lateral contacts between protofilaments. In these images, the protofilaments assume different arrangements such as short blunt ends, tapered structures, and sheet-like protofilament aggregates[55]. However, a more recent model (2018) derived from cryo-EM studies in combination with tomography shows that the growing end of the microtubule might consist of flared curved protofilaments that resemble those of depolymerizing microtubules [56]. According to this model, the curvature of protofilaments at the tip is similar between growing and shrinking microtubules, and the later contacts formation occurs after protofilaments elongation.

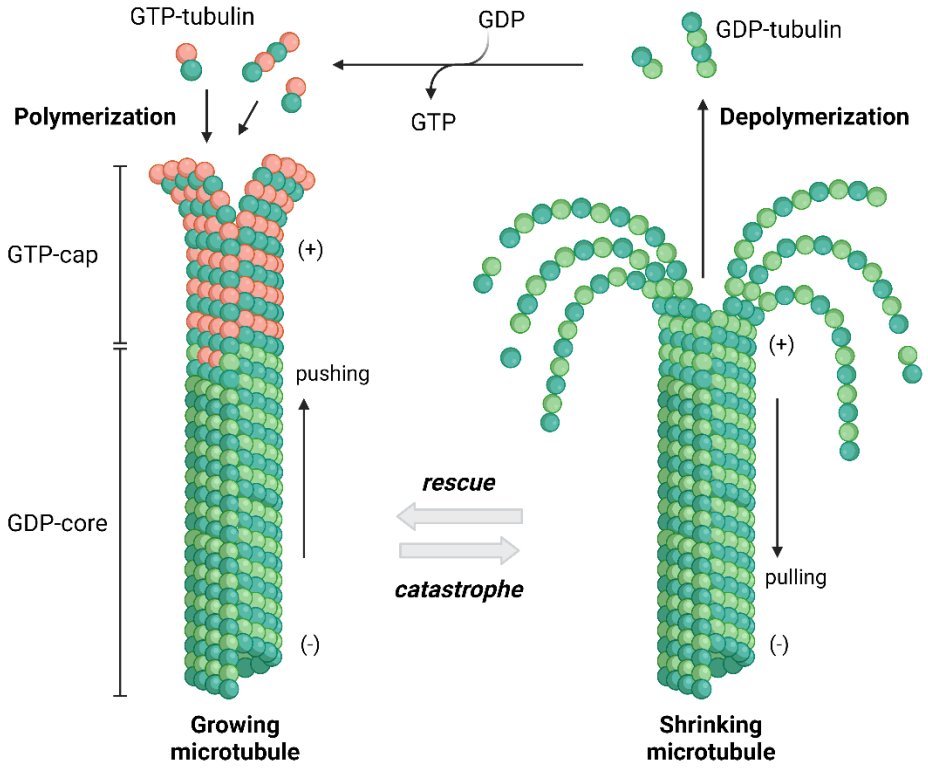

Figure 1-7. Schematic representation of microtubule dynamic instability. Active GTP-tubulin produces microtubule growth and the delay between the dimer addition and the GTP hydrolysis causes the formation of the microtubule cap. When hydrolysis reaches the microtubule tip and the cap disappears, the microtubule undergoes catastrophe unless the microtubule incorporates new GTP-tubulin subunits, producing the microtubule rescue. The scheme represents α-tubulin in dark green and β-tubulin in light green when bound to GDP or in red when bound to GTP. Growing and shrinking microtubules can exert pushing ang pulling forces, respectively.

1.4 Physiological functions of microtubules

As already mentioned in section **Error! Reference source not found.**, microtubules play a fundamental role in many essential cellular processes thanks to their mechanical properties and their ability to exert forces through dynamic instability. Besides their mechanical support function, microtubules are also known regulators of directional cell migration, vesicle and organelle trafficking, and mitosis.

1.4.1 Mechanical support, cell shape, and adhesion

Eukaryotic cells are exposed to various mechanical forces arising from factors such as gravity, fluid flow, and contraction generated by neighboring cells. These forces can significantly deform a cell, which needs a certain level of elasticity to preserve its original shape when subjected to such forces or after they are released. The cell's viscoelasticity is ensured by the three-dimensional (3D) network of protein filaments that make up the cytoskeleton, including microtubules. An interesting property of this network is that its stiffness increases the more it is deformed – a feature absent in flexible polymer gels such as polyacrylamide, and that might help cells limit their deformation[57]. The strain-stiffening properties of the network are activated not only due to external strains but also by internal stresses, such as those generated by the movement of motor proteins. Besides their role in maintaining cell shape, microtubules also contribute to the cell's adhesion processes to the extracellular matrix (ECM). Specifically, they appear to be implicated in the regulation of focal adhesions, large multi-protein assemblies through which mechanical forces and regulatory signals are transmitted between the ECM and the cell[58].

1.4.2 Intracellular transport

By providing tracks for molecular motors hauling cellular cargo, microtubules also ensure the efficient movement of molecules and organelles within the cytoplasm's complex environment. The intracellular transport system is responsible for distributing essential nutrients, proteins, lipids, and energy-carrying molecules like ATP to various cellular compartments while also removing waste products and damaged components. The transport of ATP is particularly important as it provides the energy required for numerous cellular processes, including active transport mechanisms, biosynthesis, and cellular signaling. By facilitating the delivery of newly synthesized proteins to their target locations, moving ATP to sites with the highest energy demands, and enabling the recycling or degradation of cellular constituents, intracellular transport helps maintain cellular homeostasis, support metabolic processes, and regulate cell signaling pathways. Moreover, it contributes to extracellular communication by facilitating the secretion of signaling molecules such as hormones or neurotransmitters and supporting the uptake of extracellular signals through receptors on the cell surface. This intercellular communication is essential for coordinating responses among groups of cells and maintaining the overall tissue and organ function.

Hence, the sophisticated network of intracellular transport mechanisms serves as the foundation for cellular function and organization, allowing cells to adapt, grow, and respond effectively to their ever-changing surroundings. Neurons, as specialized cells with unique morphologies and complex functions, are particularly dependent on efficient intracellular transport, often referred to as axonal transport in this specific context. Axons are the long, slender projections of neuronal cells, capable of transmitting electrical signals over

considerable distances. In the human body, their length can range from a few millimeters up to one meter (the longest axons being those of the sciatic nerve, which extend from the base of the spinal cord to the big toe of each foot). Owing to their dimensions, it becomes evident that axons cannot rely solely on diffusion processes to transport products of the nucleus and organelles from the cell body to the synaptic termini (anterograde transport) and *vice versa* (retrograde transport).

Traditionally, two main classes of axonal transport are distinguished depending on the rate at which the particles travel the axon length: a *slow* axonal transport, which moves mainly cytoskeleton components and cytosolic protein complexes at a rate of less than 10 mm per day (0.0002 – 0.1 µm/s), and a *fast* axonal transport, which transport carries membranous organelles, proteins and mRNA granules at a speed of 50/400 mm per day (0.6 – 5 µm/s)[59]. Both fast and slow axonal transport are mediated by the same molecular motors that move cargoes along microtubules: proteins of the *kinesins* superfamily, which are primarily responsible for anterograde transport, and proteins of the *dyneins* family, involved in retrograde transport (Figure 1-8). In both instances, the energy required for transport is supplied by ATP hydrolysis[60], while the differences in overall speed are caused by prolonged pauses between movement phases in slow axonal transport.

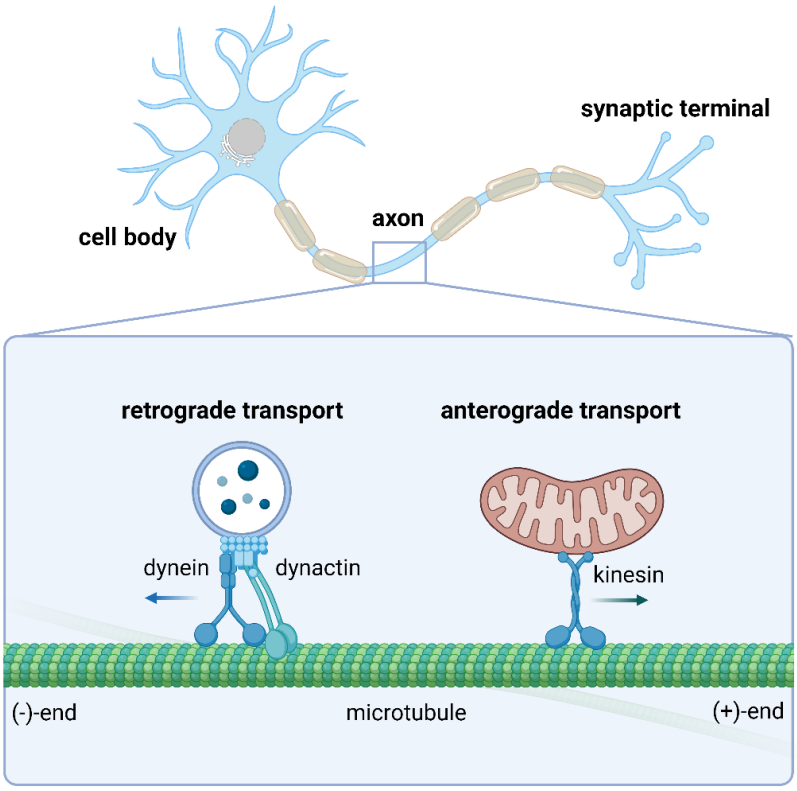

Figure 1-8. Schematic representation of axonal transport. Axonal microtubules are uniformly orientated with their plus end pointing away from the cell body. Hence, kinesins mediate anterograde transport away from the cell body toward the axon terminal, and cytoplasmic dynein drives retrograde transport from the distal axon toward the cell body. Cytoplasmic dynein works in tandem with dynactin, a multiprotein complex that acts as a co-factor for dynein activation.

1.4.2.1 Kinesin motor proteins

The superfamily of kinesins constitutes a broad class of proteins with more than 45 members in humans. Following phylogenetic analyses, these have been divided into 15 families, termed from kinesin-1 to kinesin-14B, that share a highly conserved globular catalytic domain (or *motor domain*) responsible for ATP hydrolysis, microtubule binding, and force production. However, outside the motor domain each kinesin is characterized by a unique sequence; for this reason, another widespread classification system groups them depending on the position of the motor domain in the molecule: *N-kinesins* have the motor domain in the amino-terminal region, *M-kinesins* in the middle, and *C-kinesins* in the carboxy-terminal region. The N-kinesins are the most numerous and are responsible for (+)-end-directed motility on microtubules, with kinesin-1 family members being the most studied representatives[61].

Kinesin-1 motors are $\alpha_2\beta_2$ heterotetramers composed of two heavy-chain domains (KHCs, ~120 kDa each) and two light-chain domains (KLCs, ~64 kDa each). As illustrated in Figure 1-9, each KHC domain possesses a *head–stalk–tail* structure, where the amino-terminal motor domain (*head*) is connected via a short and flexible linker (neck linker) to a central α-helical coiled-coil domain (*stalk*) which ends in the carboxy-terminal domain (*tail*). The stalk domain is responsible for KHC-KHC inter-subunit interactions, allowing the formation of the tetramer, while the C-terminal domain associates with one KLC. In most cases transported cargoes bind to the kinesin light chains, but in some cases they can bind the C-terminal tail of the KHC[62].

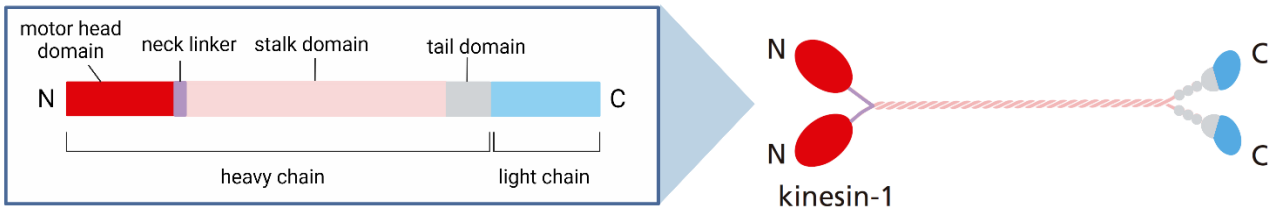

Figure 1-9. Schematic representation of kinesin-1 structure. On the left, a block representation shows the domains' organization: each monomer is composed by an N-terminal heavy chain and a C-terminal light chain (in light blue). In turn, the heavy chain domain is composed of a motor head domain (in red), a short neck linker region (in purple), a stalk domain responsible for dimerization (in pink), and a tail domain (in gray). On the right, a schematic 3D representation of kinesin-1 shows the entire dimer.

Kinesin-1 moves along microtubules in a *head-over-head* stepwise manner, using alternate microtubule-binding heads as holdfasts. The step size is 8 nm, corresponding to the axial distance between tubulin heterodimers, and each head specifically binds to β-tubulin[63]. The mechanochemical cycle of kinesin is tightly regulated by the turnover of ATP, as depicted in Figure 1-10. Kinesin in solution is usually in an ADP-binding state, but interaction with the microtubule induces ADP release, converting the motor domain to an empty (*apo*) state that strongly binds to β-tubulin. The subsequent binding of ATP to the apo-head triggers the closure of the two switch regions flanking the catalytic site. The ATP-bound state is still characterized by a strong interaction with the microtubule. The conformational change of the catalytic site (switch closure)

facilitates ATP hydrolysis, which is followed by the γ-phosphate release and the generation of a new ADP-bound state. This state has the lowest affinity to the microtubule, thus inducing the detachment of the motor domain. At this point, the motor head undergoes a mechanical step, often referred to as the "power stroke," which propels it forward. This mechanochemical cycle occurs for both motor domains (lagging and leading heads) in a coordinated fashion that allows kinesin to walk along the microtubule[64].

The directionality of the stepping mechanism is also regulated by the nucleotide-bound state: when a motor head interacting with the microtubule wall is also binding ATP in its catalytic site, a conformational change occurs in the neck linker region. This area of ~15 amino acids connecting the head and the stalk domains becomes immobilized and extended towards the microtubule (+)-end, forcing the forward direction of the step. When the γ-phosphate is released, after nucleotide hydrolysis, the neck linker reverts to a more mobile conformation[65].

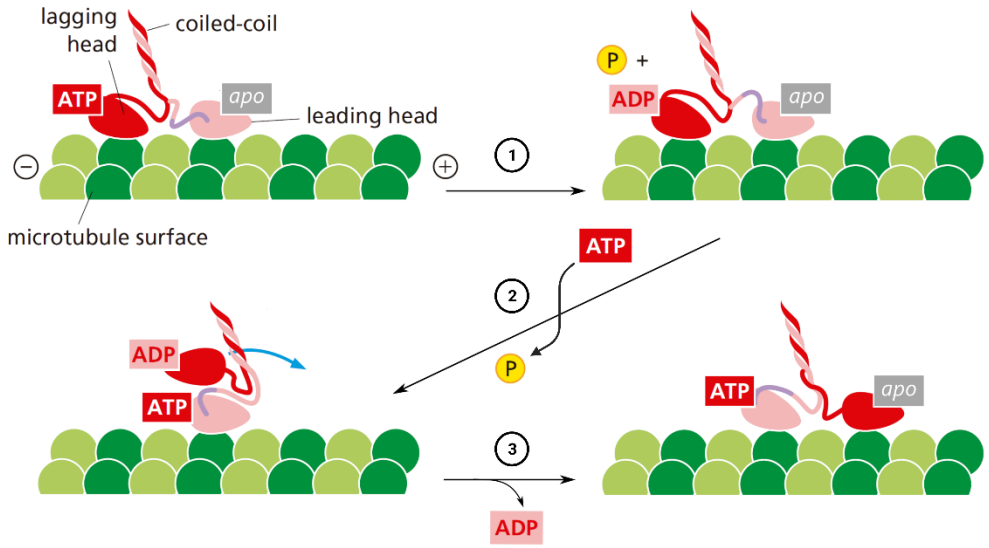

Figure 1-10. The mechanochemical cycle of kinesin-1. Kinesin-1 is a dimer of two ATP-binding motor domains (heads) that are connected through a long coiled-coil tail. The two kinesin motor domains work in a coordinated manner; during a kinesin "step," the rear head detaches from its tubulin binding site on the microtubule, passes the partner motor domain, and then rebinds to the next available binding site. At the start of each step, both kinesin motor domain heads are bound to the microtubule, with the rear or lagging head (dark red) binding ATP, and the front or leading head in an apo-state. Then, hydrolysis of ATP in the rear head occurs **[1]**. The γ-phosphate release causes the detachment of the rear head from the microtubule, while the concomitant binding of ATP in the leading head causes a small peptide called the neck linker to shift from a rearward-pointing to a forward-pointing conformation (the neck linker is drawn here as a purple connecting line between the leading motor domain and the intertwined coiled-coil) **[2]**. This shift pulls the rear head forward, and the interaction with the microtubule induces the ADP release **[3]**. The kinesin molecule is now poised for the next step, which proceeds by an exact repeat of the same process. Image modified from [13].

1.4.2.2 Dynein motor proteins

The second major group of cytoskeletal motor proteins is the dynein family, divided into cytoplasmic, axonemal, and intra-flagellar transport dyneins[66]. Axonemal and intra-flagellar dynein is only found in cilia and flagella, where the former is responsible for the beating movement (see following section), while the latter is specifically involved in cargo transport along the microtubules of the axoneme. On the other hand, cytoplasmic dynein is found across the entire microtubule network, where it is responsible for the retrograde transport of various cargoes towards the (-)-end of the microtubules. Unlike kinesin motors, there is only one

dynein-1 heavy chain gene which is responsible for all cytoplasmic intracellular transport. An additional difference compared to kinesin is the size of the motor protein: dynein constitutes a massive multi-subunit complex (1.4 MDa) composed of six different polypeptides, all of which are present in two copies. There are two dynein heavy chains (DHC, ~530 kDa), two intermediate chains (DIC, 74 kDa), two light intermediate chains (DLIC, ~54 kDa), and six light chains (DLC). Moreover, it has been proved that to perform its activities *in vivo* dynein associates with a wide number of activating adaptor proteins and another high-molecular weight complex, named dynactin (1.1 MDa)[67].

Similar to kinesin, dimerization of the DHCs is a necessary condition for the processive movement along microtubules. Each DHC is composed of an N-terminal tail domain, a motor domain, and a C-terminal domain. The tail domain consists of a dimerization region responsible for DHC-DHC interactions and a long linker region made of nine consecutive helical bundles that connect to the motor head. The motor domain itself contains six AAA+ domains (highly conserved ATPase folds) arranged in a ring shape, connected to a microtubule-binding region via a coiled-coil stalk (Figure 1-11).

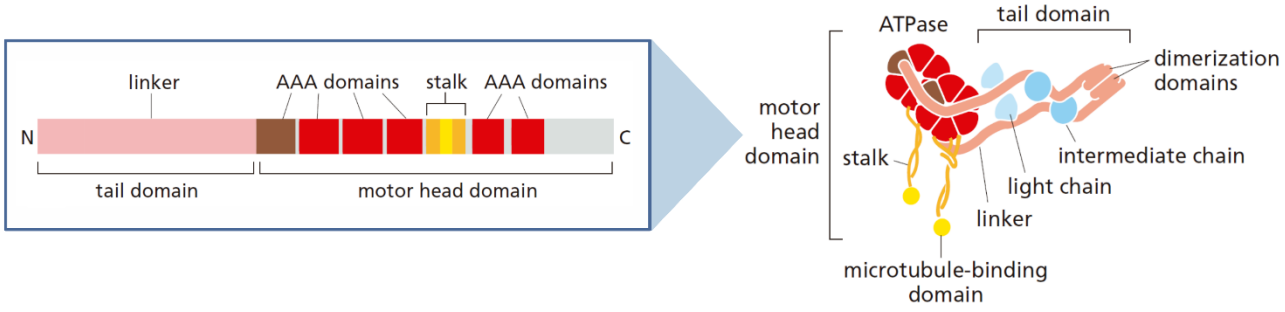

Figure 1-11. Schematic representation of the cytoplasmic dynein structure. On the left, a block representation shows the organization of domains in the dynein heavy chain: the N-terminal tail domain (in pink) is connected to the motor head domain, containing six AAA+ domains (in red and brown) and a microtubule-binding region (in yellow); a stalk region (in orange) connects the two. Of the six AAA+ domains, only four retain ATP-binding sequences but most of the ATPase activity is concentrated in the first one (brown). On the right, a schematic 3D representation of cytoplasmic dynein shows the two heavy chains that contain a motor head with domains for microtubule binding and ATP hydrolysis, connected by a long stalk. The tail domain consists of a linker that connects the motor heads to a dimerization domain. Bound to the linker domain are multiple intermediate chains and light chains (blue) that help to mediate many of dynein's functions. Image modified from [13].

The mechanochemical cycle of dynein is mainly driven by the nucleotide state (apo, ATP-bound, ADP-bound, ADP·Pi-bound) of the first AAA+ site, which controls a series of conformational changes in the linker and microtubule-binding regions, leading to the detachment of the monomer from the microtubule and the reorientation of its linker domain to produce a net step towards the microtubule end. However, the order of events between ATP binding and hydrolysis is still unclear. High-resolution tracking studies revealed that the stepping behavior differs substantially between kinesin and dynein motor proteins. While kinesin-1 takes uniform 8 nm steps on a single protofilament, with virtually no backward movement[68], dynein monomers are often located on adjacent protofilaments and can perform both forward and (infrequent) backward steps of different sizes, as well as sidestepping on neighboring protofilaments[69].

1.4.3 Cell division: mitotic spindle formation

In vitro, microtubule growth progresses through small early oligomeric intermediates for which disassembly is energetically favored over assembly, resulting in slow initial growth. To bypass this slow initial phase, cells have evolved specialized nucleation sites for microtubules. These sites are clusters of regulatory proteins and γ-tubulin ring complexes (γ-TuRC) that cap the microtubule (-)-end and act as fast polymerization primers inducing the formation of 13_3 microtubules in mammals[70]. MTOCs are specific intracellular locations particularly enriched in nucleation sites. In animal cells, the primary MTOC is the centrosome, a non-membranous organelle composed of two orthogonal centrioles surrounded by pericentriolar material. Its structure is depicted in panel A of Figure 1-12.

During interphase (phases G_1, S, and G_2 of the cell cycle) the centrosome is situated near the nucleus, projecting microtubules to the cell periphery. This organizing element is replicated during the S phase, along with the cell's genome. As the cell enters prophase, the first phase of mitosis (M), the replicated DNA begins to condense into chromosomes and the entire microtubule network loses stability, largely dissolving due to increased phosphorylation of its protein components. The general solubilization of interphase cytoskeletal polymers decreases cytoplasmic viscosity, allowing for the diffusive randomization of medium-sized cytoplasmic objects. Simultaneously, the two centrosomes migrate to the cell poles, where they initiate the formation of the bipolar mitotic spindle. This specialized cytoskeletal structure forms during cell division to separate sister chromatids between daughter cells. The microtubules composing the mitotic spindle are more phosphorylated and consequently more labile than their interphase counterparts, exhibiting a 10-fold increase in the rate of dynamic instability.

Subsequently, the cell enters prometaphase, during which the nuclear envelope breaks down and the chromosomes engage the mitotic spindle. More specifically, the so-called *kinetochore microtubules* are the main responsible for chromosome segregation. By probing the region in which chromosomes reside via increased dynamic instability and diffusive rotations ("search and capture" scenario), they attach sister-chromatid pairs at large protein structures called *kinetochores*, which are located at the *centromere* of each sister chromatid. Kinetochores are multi-protein complexes that include proteins able to bind to the microtubule wall and motors with both directionalities. This includes dynein and at least one type of kinesin for (+)-directed motion, as well as non-transport M-kinesins (such as members of the kinesin-13 family) that act as depolymerization enhancers. During metaphase, the third phase of mitosis, attached chromosomes are aligned at the spindle equator, between the two poles. At this point, each kinetochore binds numerous microtubules that are cross-linked to form thick microtubule bundles called *K-fibers*. These fibers move separated sister chromatids toward the poles during anaphase, the fourth stage of mitosis.

In addition to kinetochore microtubules, the mitotic spindle also contains relatively short and unstable *interpolar microtubules*. These are densely packed between the poles and cross-linked by various proteins to

form a dynamic and adaptable scaffolding network that provides structural stability to the spindle. Some of these microtubules are embedded in the spindle poles, but many are found away from the poles, sometimes with their (-)-ends attached to the sides of other microtubules. Lastly, in most animal cells, spindles also contain *astral microtubules* that radiate outward from the poles and contact the cell cortex, helping to position the spindle in the cell.

During the last phase of mitosis, telophase, the two sets of chromosomes arrive at the poles of the spindle and decondense. A new nuclear envelope reassembles around each set, completing the formation of two separated nuclei. Finally, during cytokinesis the cytoplasm division is carried out by a contractile ring of actin and myosin filaments, leading to the formation of two daughter cells. In conclusion, as cells in mitosis organize their many components for equal partitioning at cytokinesis, the microtubule cytoskeleton plays an essential role through its assembly into the mitotic spindle, allowing for the organization and segregation of both chromosomes and centrosomes (Figure 1-12, panel B)[13,71].

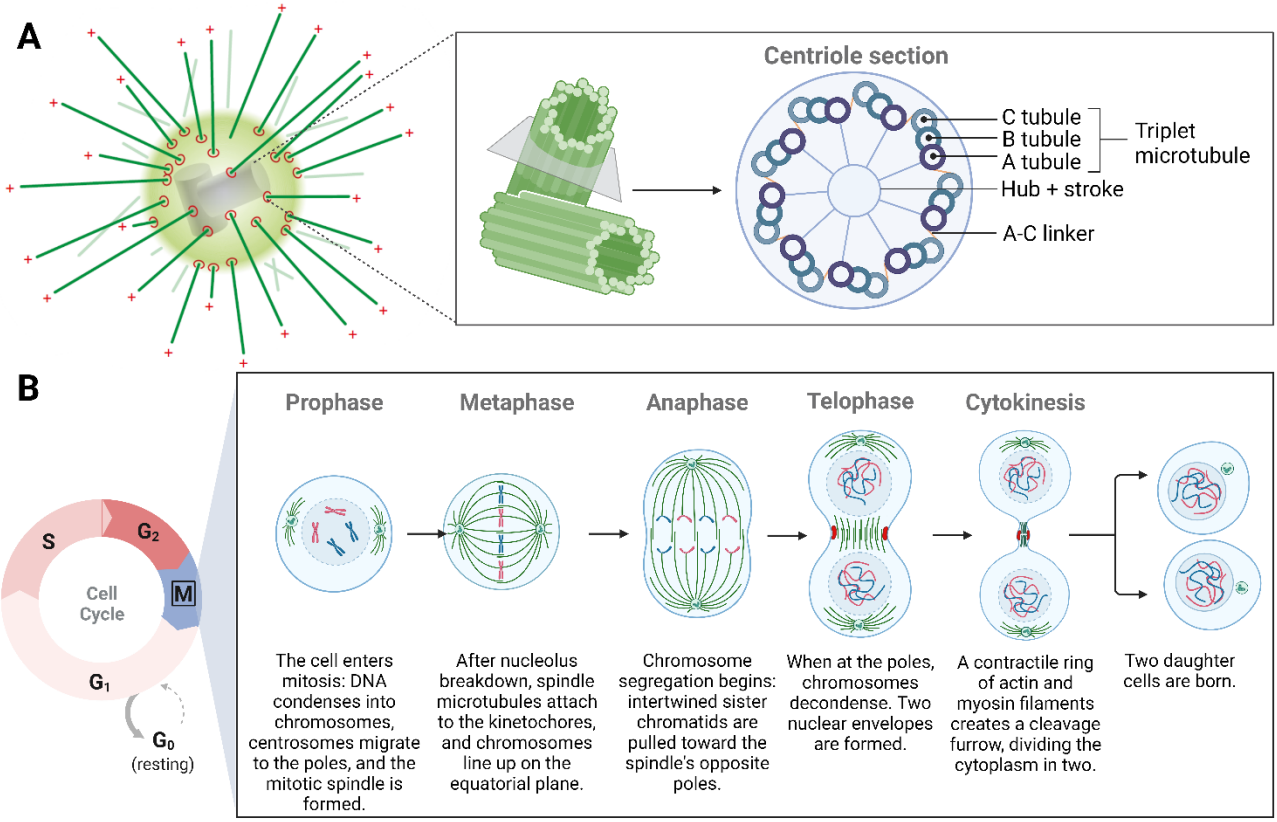

Figure 1-12. Microtubule cellular organization and mitotic spindle formation. Panel **A**: Schematic representation of the centrosome, the major MTOC in animal cells. It consists of a pair of centrioles surrounded by an amorphous matrix of fibrous proteins, the pericentriolar material, in which are embedded several γ-TuRCs (red rings) that nucleate microtubule growth. Microtubules (green lines) grow from γ-TuRCs with their (+)-ends pointing outward. Each centriole is a cylinder with a diameter of ~ 250 nm composed of 9 radially symmetric triplet microtubules. Each triplet is made of one complete tubule (A) and two incomplete tubules (B and C) that share a common microtubule wall. Other filamentous protein structures connect adjacent triplets (A-C linkers), while the A tubules of each triplet are connected by radial filaments forming a hub structure with 9 strokes. Panel **B**: Cell cycle scheme and overview of the events of eukaryotic cell division as seen under a microscope.

1.4.4 Cell migration and motility

The mechanisms behind cell migration, i.e., the active movement from one location to another, differ depending on whether the cell uses specific structures to propel itself in a liquid environment or crawls on a solid substrate. In both scenarios, the process is highly dependent on microtubule function.

In the case of motility in a liquid environment, cells rely on cilia and flagella[13,72]. These beating, hair-like organelles differ in length but share a common microtubule-based cytoskeletal structure known as *axoneme*. In eukaryotes, the axoneme has a 9 + 2 structure, which consists of nine outer doublet microtubules and a pair of singlet microtubules, collectively called the central pair (Figure 1-13). Each outer doublet is composed of one complete and one partial microtubule, known as *A-tubule* and *B-tubule* respectively, fused to share a common tubule wall. Axonemal dynein molecules are anchored to a microtubule doublet, and by attempting to walk along an adjacent one, they generate the force for bending. The movement of dynein motors would cause the microtubule doublets to slide relative to one another but, due to inter-doublet connections (nexin linkages), they generate a bending motion instead. Other protein complexes are thought to play mechanical roles in the motion of the axonemes, particularly in coordinating the movement of dynein motors so that they work in a synchronized fashion. This might be one of the crucial roles played by the radial spokes, T-shaped complexes that project from each set of outer doublets toward the central microtubules. In cells, cilia and flagella are generated at plasma membrane-associated structures called *basal bodies* that firmly root them at the cell surface. At the core of each basal body is a centriole, the same structure found embedded at the center of animal centrosomes, with nine groups of fused triplet microtubules arranged in a cartwheel.

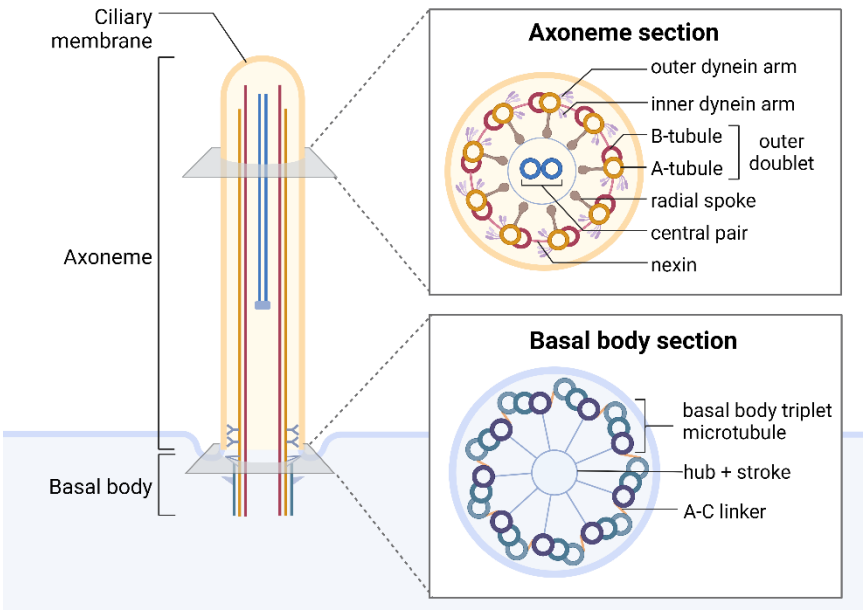

Figure 1-13. Structure of motile cilia and flagella, composed of the basal body and the axoneme central structure, delimited by the ciliary membrane. The cross section of the axoneme shows the typical 9+2 structure comprising nine outer doublets (A tubule + B tubule) and two singlet central microtubules (the central pair). The outer doublets are linked between each other by nexin bridges, and to the central pair through the radial spoke complexes. The outer and inner dynein arms anchored to each microtubule doublet generate the bending motion by walking along the immediately adjacent doublet. The basal body is a centriole, its structure is explained in panel A of Figure 1-12.

In the case of non-propelled cell migration, cells rely solely on their intracellular machinery to perform their movement[73]. Despite the wide variety of migration types, the general mechanism entails four steps in a strict chronological order: (1) protrusion, (2) adhesion, (3) contraction, and (4) retraction. External cues, such as chemical gradients or the substrate's physical properties, determine the directionality of the migration. To detect these factors, cells establish connections with the ECM and neighboring cells. Moreover, precise spatial regulation is essential to prevent protrusions from occurring around the entire cell periphery and to avoid random contractions that could stall cell motility. A migrating cell must therefore present a protruding front opposite to a retracting rear edge. The molecular pathways controlling protrusion and adhesion on one side, and retraction and detachment on the other, must be segregated, resulting in a front-rear polarized organization. In this context, microtubules together with actin filaments have been identified as essential regulators in all four steps of cell migration. The formation of lamellipodial protrusions at the front edge of the migrating cell requires pushing forces generated by the cytoskeleton underlying the plasma membrane. In relatively small cells, actin polymerization is the main responsible for membrane extension. Conversely, in large and branched cells (e.g., neurons) microtubules take a primary goal in protrusion formation. Between these extreme cases a variety of cell types, including fibroblasts, epithelial cells, and endothelial cells, rely on both types of cytoskeletal filaments. Regarding the adhesion and contraction steps, microtubules are involved in regulating the formation and disassembly of focal adhesion complexes, as mentioned in section 1.4.1. Moreover, the microtubule network also plays a role in the front-rear polarization required for the migration process. While the actin cytoskeleton forms local and independently functioning structures at the front and rear of the cell, microtubules create a single polarized network that spreads throughout the cytoplasm, allowing for intracellular polarized trafficking of molecules and membranes from the contracting to the protruding regions.

1.5 Microtubule dynamics regulation

Precise regulation of microtubules' dynamic behavior is key for the proper progression of the numerous diverse cellular functions described in the previous section. To achieve this, cells evolved a vast array of endogenous regulatory elements (post-translational modifications, different tubulin isotypes, associated proteins) that influence microtubule assembly and disassembly, as well as their interaction with cellular structures. On the other hand, that same involvement in essential biological functions makes microtubules an appealing pharmacological target in many diseases. As a result, exogenous regulators of microtubule dynamic instability have been a focus of drug discovery research since their initial identification in the first half of the XX century. This paragraph aims to offer an outline of the complex regulatory framework of microtubule dynamics in cells, as well as how this regulation can be disrupted by external, non-physiological disruptive agents.

1.5.1 Endogenous regulation

The dynamic instability of microtubules and their connections to cellular structures are spatially and temporally controlled by numerous regulatory factors. The first layer of regulation lies in the *tubulin code*, i.e., the molecular pattern generated by combinations of different tubulin isotypes and post-translational modifications (PTMs).

Both α- and β-subunits have numerous isotypic forms, originating from a superfamily of genes that diversified through duplications and mutations from a common ancestor. The human genome contains at least 10 genes for α-tubulin and 10 genes for β-tubulin (reported in Table 1-1), along with several pseudogenes. However, not much is known about the physiological relevance of different isotypes. Generic α- tubulin and β-tubulin isotypes are highly conserved between evolutionarily distant species, while rarer isotypes seem to have evolved alongside novel microtubule functions. For instance, β1-tubulin (encoded by TUBB1) co-evolved with platelets, small cell fragments essential for blood coagulation that are unique to mammals. This highly divergent isotype (25% sequence divergence with all other β-tubulin isotypes) does not have close homologs in philia that do not have platelets. Thus, β1-tubulin may have specifically evolved to support the high degree of microtubule bending required for the formation of the *marginal band*, a specialized microtubule array unique to platelets that gives them their round shape[74]. Isotypes also display common cell- or tissue-specific expression profiles. For example, the β3-tubulin isotype (encoded by TUBB3) is conserved across mammals in both sequence and neuronal-specific expression, suggesting its significance in microtubule functions associated with neuronal settings[75].

Table 1-1. Human genes expressing α- and β-tubulin isotypes (https://ncbi.nlm.nih.gov/, 10/09/2023).

Species	Phylum	α-tubulin isotypes	β-tubulin isotypes
Homo sapiens (human)	Chordata	*TUBAL3* *TUBA1A* *TUBA1B* *TUBA1C* *TUBA3C* *TUBA3D* *TUBA3E* *TUBA4A* *TUBA4B* *TUBA8*	*TUBB* *TUBB1* *TUBB2A* *TUBB2B* *TUBB3* *TUBB4A* *TUBB4B* *TUBB6* *TUBB8* *TUBB8B*

Furthermore, tubulin undergoes numerous PTMs, which also serve a regulatory function. These modifications mainly occur at the C-terminal tail of tubulin, primarily involving the incorporation and removal of tyrosine, glutamate, and glycine. Other regions of the protein also experience modifications, with polyamination, phosphorylation, and acetylation being the most common. The tubulin code's regulatory

function can be explained by two reasons. Firstly, different isotypes and post-translationally modified tubulins possess unique biochemical and mechanical properties that support specific microtubule functions. Emerging evidence suggests that tubulin isotypes and PTMs can influence the protofilament number of the microtubule formed, as well as mechanical properties such as flexibility and breakage tendency. Secondly, the tubulin code potentially alters microtubule dynamics regulation by enhancing or diminishing the association with specific microtubule-associated proteins (MAPs). This is supported by the observation that sequence variations between isotypes and PTMs are primarily concentrated within the C-terminal tail, which is also the region most involved in MAPs interaction[74]. Consequently, mutations in human tubulin isotypes and alterations in the physiological patterns of PTMs are linked to various pathological disorders, collectively called tubulinopathies. These disorders are associated with, among others, impaired cilia-related functions, coagulation disorders, congenital neurological disorders, and neurodegenerative processes[75].

As already mentioned, MAPs recognize the tubulin code's molecular signals and serve a secondary layer of microtubule regulation[76]. While some MAPs bind to the microtubule lattice, others can specifically recognize one of the two different polar ends of the microtubule: the (+)-end tracking proteins (+TIPS) and (-)-end tracking proteins (-TIPS). According to their regulatory functions, MAPs can be broadly classified as polymerases, depolymerases, and cross-linkers. Molecular motor proteins can also be considered regulatory MAPs, as their ability to exert pushing and pulling forces can direct microtubule growth and positioning at specific cellular locations. Microtubule polymerases, such as members of the CLASP and XMAP215 families of +TIPS, actively recruit tubulin dimers and increase the rate of tubulin addition to growing tips *in vivo* compared to the one *in vitro*. Other MAPs, like the protein Tau, stabilize the straight protofilament conformation, thus favoring microtubule formation and preventing the inside-out curled arrangement typical of peeling protofilaments during catastrophe. On the other hand, microtubule disassembly is promoted by depolymerases, such as some members of the kinesin superfamily. Kinesin-8, kinesin-13, and yeast kinesin-14 family members all exhibit microtubule-depolymerizing activity. Katanin, a microtubule-severing AAA protein, can also be classified as a depolymerase as it cuts microtubules, generating new ends lacking the protective GTP cap and thus quickly leading to catastrophe. The activity of other MAPs is more difficult to classify. For instance, EB proteins, a family of autonomous (+)-tip trackers, promote microtubule catastrophe *in vitro*, but in cells mostly promote rather than suppress microtubule elongation, possibly by counteracting the activity of more potent depolymerases. Another example is stathmin, a tubulin-sequestering protein that directly regulates the equilibrium between unassembled and polymerized forms by modulating the amount of free tubulin in solution. Moreover, several MAPs act as cytoskeletal crosslinkers by connecting microtubules to actin and/or intermediate filaments. Two major cytoskeletal crosslinkers are the microtubule–actin crosslinking factors 1 and 2 (MACF1 and MACF2). By guiding microtubules along actin bundles, these proteins can steer the direction of growth of the microtubule network and determine its architecture.

1.5.2 Exogenous regulation

Microtubule-targeting agents (MTAs) are a diverse group of chemical compounds with the ability to interact with tubulin, altering its structure and function. Depending on their effects, tubulin binders are broadly categorized into microtubule-stabilizing agents (MSAs) and microtubule-destabilizing agents (MDAs). MSAs promote microtubule polymerization by reinforcing lateral and/or longitudinal tubulin contacts within the microtubule lattice. Conversely, MDAs trigger microtubule depolymerization either by obstructing the formation of native tubulin contacts or by blocking the curved-to-straight conformational shift[77]. However, at low and clinically relevant concentrations both MSAs and MDAs primarily suppress microtubule dynamics without significantly affecting the microtubule-polymer mass[78].

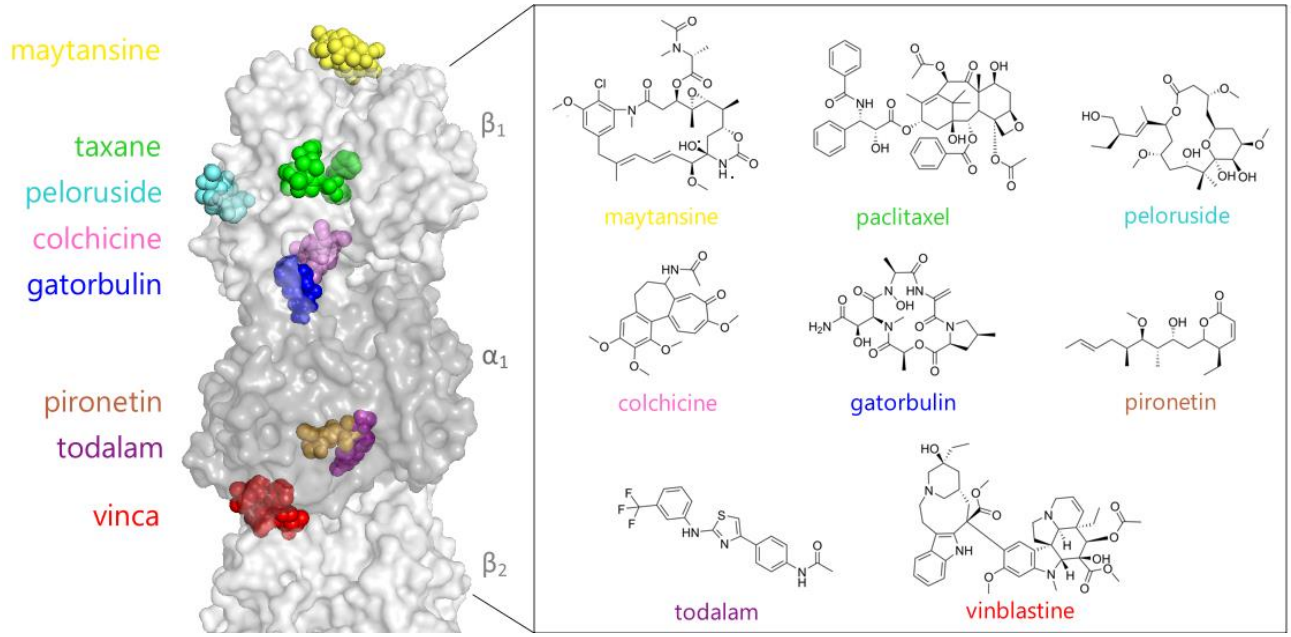

Figure 1-14. Pharmacological regulation sites described on tubulin. On the right, the eight different binding sites on tubulin are highlighted in different colors. On the left, the chemical structure of each site's representative MTA is depicted.

Numerous MTAs have been identified and characterized to date, binding to eight unique tubulin sites. These include maytansine, taxane, laulimalide-peloruside, and colchicine sites on β-tubulin; gatorbulin site at the intra-dimer interface; pironetin site on α-tubulin; and vinca and todalam sites at the inter-dimer interface (Figure 1-14). This remarkable collection is the result of decades of research, spanning from the discovery of the first tubulin binder, colchicine, in 1935[79] to the most recent one, todalam, described just last year[80]. The binding sites are named after their most prominent representative members, that primarily consist of natural products derived from plants, marine sponges, or bacteria and their synthetic derivatives. As illustrated in Figure 1-14, their chemical structures often feature macrocyclic rings and multiple stereocenters. Todalam constitutes the only exception, being a fully synthetic molecule rationally designed from small inactive fragments able to bind to tubulin[80]. Interestingly, pharmacological regulation by external molecules predominantly involves the β-subunit, with pironetin being the only known MTA interacting

exclusively with the α-subunit. While no widely accepted explanation for this phenomenon exists, one possible reason is that both the GTP hydrolysis cycle – which drives microtubule dynamic instability – and the main heterodimer conformational changes upon microtubule incorporation occur within the β-tubulin. Thus, ligands targeting this subunit could potentially interfere with these functionally critical processes.

The previously mentioned MTA binding sites are associated with fully active molecules that can induce polymerizing or destabilizing effects on tubulin. In 2021, Mühlethaler and co-workers discovered five additional tubulin binding sites occupied by small inactive fragments. Their research combined computational and crystallographic screening methods to identify fifty-six chemically diverse fragments binding to ten distinct tubulin sites (Figure 1-15), with six of them being novel. The following year, one of these six new sites was renamed the "todalam site", after the discovery of a molecule capable of modulating microtubule dynamics.

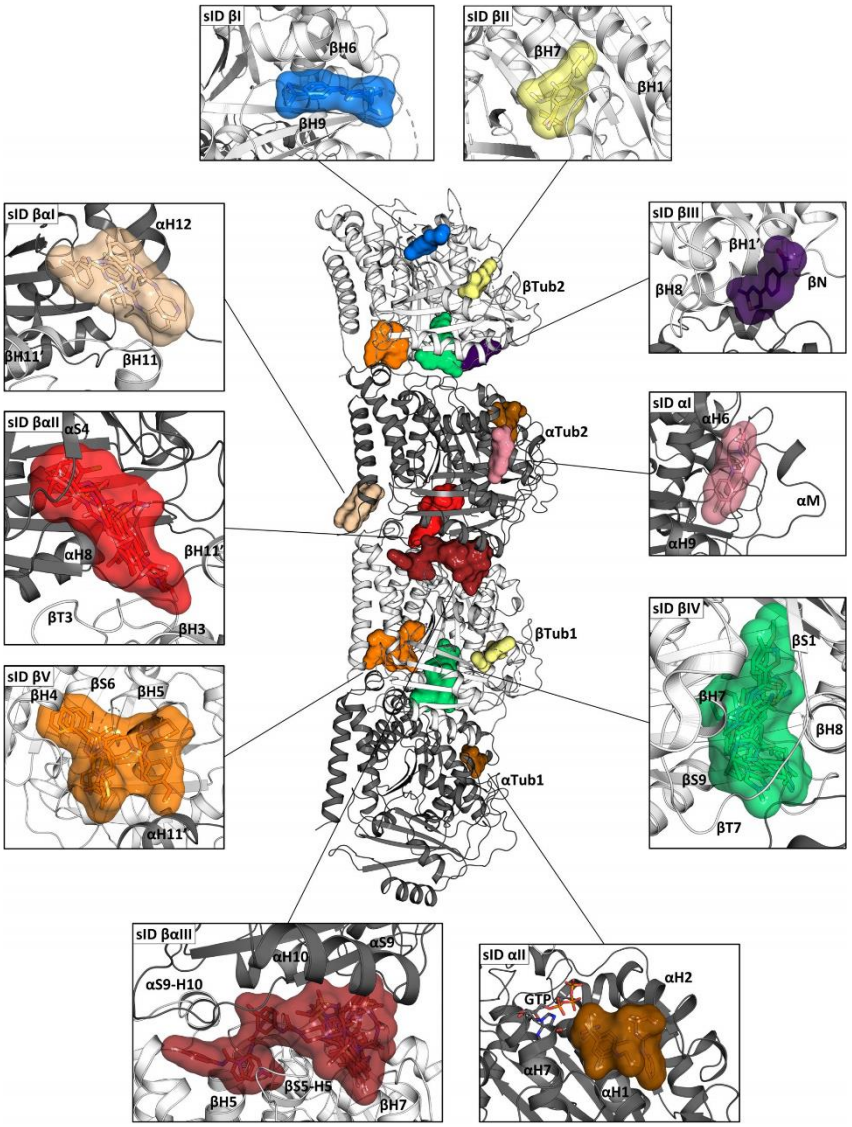

Figure 1-15. An extensive X-ray crystallography screening of 708 fragments led to the identification of 56 fragments capable of binding to 10 distinct sites. The figure showcases the structure of two tubulin heterodimers, αTub1-βTub1 and αTub2-βTub2, as observed in the T_2R-TTL tubulin crystallization complex, with the fragment binding-sites highlighted in different colors. Image adapted from [81].

1.6 The taxane binding site

Paclitaxel was the first taxane site binder described in scientific literature. Initially isolated from the bark of the Pacific yew tree (*Taxus brevifolia*) in 1971[82], this natural product alkaloid preferentially binds to the *straight* tubulin conformation, consequently promoting the polymerization of soluble tubulin dimers and stabilizing assembled microtubules. *In vivo*, this leads to impaired microtubule dynamic instability, ultimately disrupting cell cycle progression. Following its FDA approval for the treatment of ovarian cancer (1992), paclitaxel has been successfully used in clinics under the brand name Taxol®. Over time, its applications have expanded to include breast, non–small cell lung, esophageal, lung, cervical, and pancreatic cancers, as well as Kaposi's sarcoma[83]. A challenge that initially delayed paclitaxel's widespread use in clinical settings was its limited supply due to low extraction yields from yew trees. This issue was later resolved by the development of a semi-synthetic pathway from baccatin[84], a precursor obtained from *Taxus baccata*. Paclitaxel's total synthesis was also reported a few years later[85].

Paclitaxel's remarkable success in cancer chemotherapy led to the exploration of numerous synthetic and semi-synthetic analogs. The goal was to improve the molecule's pharmacokinetic properties and gain valuable insights into its structure-activity relationship (SAR)[86–88]. This research resulted in the development of two more potent semi-synthetic derivatives: docetaxel and cabazitaxel. Both drugs have found their application in clinics for the treatment of breast cancer (Taxotere®) and prostate cancer (Jevtana®), respectively. Nonetheless, the clinical use of taxanes still faces several challenges, such as low solubility, drug resistance and severe side effects like peripheral neurotoxicity (see section 1.8). To address these limitations, several taxane derivatives are currently being investigated, including oral taxanes tesetaxel and milataxel, both of which are undergoing Phase II clinical trials. Oral taxanes offer a range of advantages, such as increased patient convenience, the elimination of lipid carriers and associated allergic reactions, enhanced bioavailability, reduced toxicity profiles, improved efficacy, and activity in tumors expressing the multidrug-resistance (MDR) gene.

In addition to taxanes, new chemically-diverse taxane site binders that exhibit paclitaxel-like microtubule stabilizing activity were discovered. The structures of the most representative taxane site binders are reported in Figure 1-16. Epothilones, a group of macrocyclic lactones with better water solubility and brain permeability than taxanes, were first isolated in 1987 from the soil myxobacterium *Sporangium cellulosum*. Following their evaluation as chemotherapeutics in multiple clinical trials, ixabepilone (Ixempra®) was the first epothilone approved by the FDA for treating aggressive metastatic or locally advanced breast cancer. Other known taxane-site ligands include covalent binders such as zampanolide, cyclostreptin, or taccalonolides, and more non-covalent binders like dictyostatin and discodermolide. These compounds are gaining interest as most of them can overcome P-gp-mediated drug resistance mechanisms.

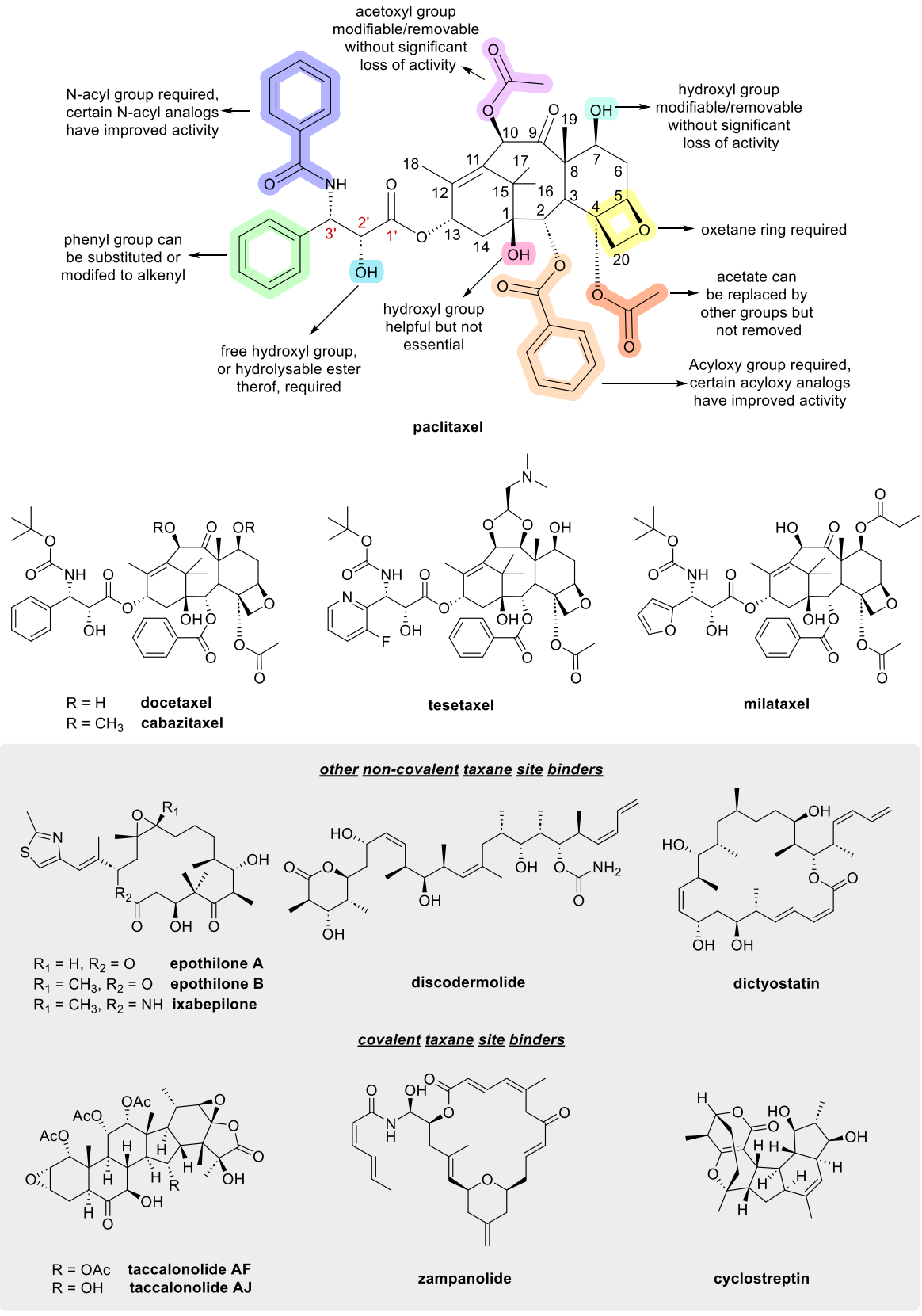

Figure 1-16. The chemical structure of paclitaxel is composed by a diterpenic taxane ring fused with a four-membered oxetane ring, a benzoyl side chain at the C2 position and an ester side chain at C13. The upper image highlights the primary activity-modulating modifications described by SAR studies. Below, the chemical structures of the most representative taxane site binders are reported.

In recent times, the availability of numerous high resolution X-ray crystallography and cryo-EM structures of tubulin and microtubules complexed with these ligands has allowed for a precise structural description of the taxane binding site. The site, located in the β-subunit between the N-terminal and intermediate domains, is formed by the hydrophobic residues of helix H7, strand S7, and loops H6–H7, S7–H9 (the M-loop), and S9–S10 of β-tubulin (Figure 1-17, panel A). All taxane-site ligands establish hydrophobic and polar contacts with those secondary structural elements, while zampanolide, cyclostreptin and taccalonolide AJ form an additional covalent interaction with His229 or Asp226[77]. However, a precise understanding of the mechanism of action of taxane-site binders remained elusive until recently. This includes the determination of the reasons behind their preferential binding to microtubules and the identification of the specific conformational changes involved in the stabilization mechanism.

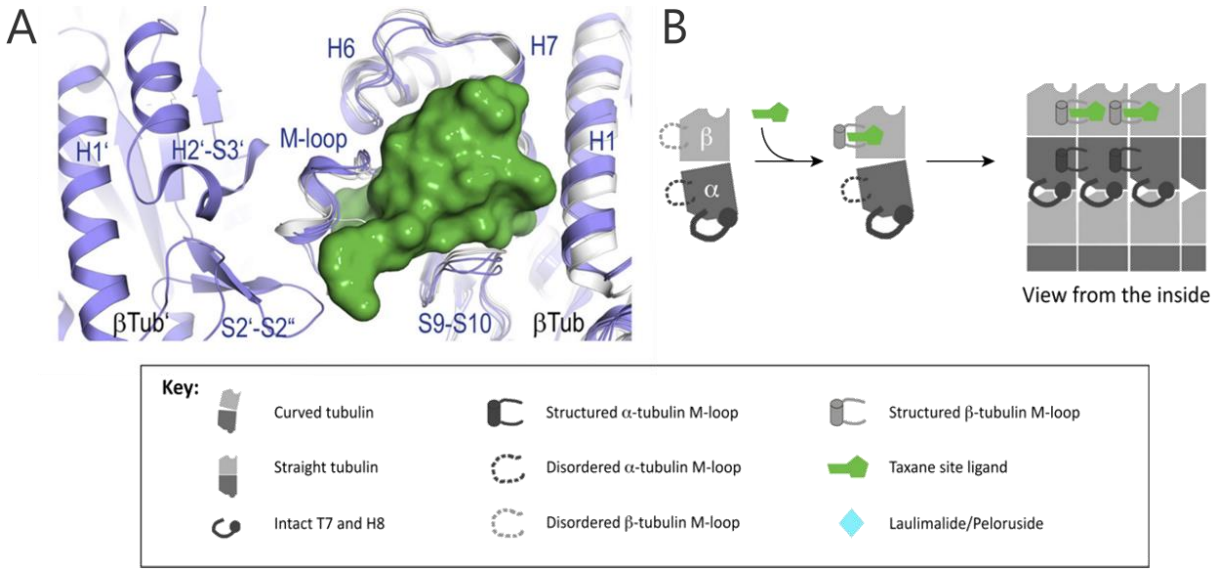

Figure 1-17. The taxane binding site. Panel **A**: A close-up view of the taxane site (green) within tubulin in curved (white) and straight (blue) conformational states. β-Tub and β-Tub' indicate β-tubulin subunits that belong to neighboring protofilaments. Panel **B**: Schematic illustration of the general mechanism of action of taxane site ligands. Upon ligand binding, the otherwise disordered M-loop of β-tubulin organizes into a short helix. The stabilized M-loop promotes tubulin assembly into a microtubule, where the α-tubulin M-loops also adopt a helical conformation. Image modified from [77].

A recent work conducted by Prota and colleagues[89] addressed these open questions using a combination of X-ray crystallography, X-ray fiber diffraction and molecular dynamics (MD) techniques on a subset of C13-modified taxanes and their precursor baccatin III. The study found that the selective recognition of microtubules by taxanes is determined by two factors. The first one is the presence of a bulky C13 side chain, as the 3'-N-benzamido phenyl ring of paclitaxel precludes its binding to curved tubulin. The second factor is the occupancy of the taxane site by the βM-loop in the absence of lateral contacts, which accounts for the significant loss in affinity when binding to unassembled tubulin vs. microtubules for all taxane-site ligands. Furthermore, the study provided evidence that taxanes promote microtubule stability by inducing partial stabilization of the βM-loop, a region responsible for inter-protofilament contacts. A similar mechanism has also been proposed for non-taxane site binders after the description of the X-ray crystallography structures of curved tubulin in complex with zampanolide and epothilone A[90]. In these structures, the otherwise

disordered M-loop organizes into a short helix capable of establishing new inter-protofilament contacts that compensate for those lost after GTP hydrolysis (Figure 1-17, panel B). Similarly, discodermolide and dictyostatin were also proposed to stabilize the M-loop conformation, although no helical structure was observed[91].

The binding of taxanes to tubulin is also known to produce another conformational change, the displacement of the βS9-βS10 loop, that induces the axial expansion of the microtubule lattice. Although this conformation change was previously considered to be involved in the microtubule stabilization process[36], new data show that it is a general feature associated to taxane binding, present even with the biologically inert baccatin III, and thus does not constitute an important factor contributing to stabilization[89]. Molecular modeling simulations successfully reproduced the expansion behavior, showing that the βS9-βS10 loop motion propagates toward the attached α-tubulin subunit so that the distance between the α_1- and β_2-tubulin subunits of two longitudinally aligned, consecutive tubulin dimers increases by roughly 2 Å as compared to the unbound filament[89].

Another important aspect to consider regarding the taxane binding site is its luminal position within the microtubule, which makes it not directly accessible from the outside. Initially, it was hypothesized that ligands could reach this binding site through diffusion via the microtubule tips. However, kinetic binding studies using flutax-2, a fluorescent paclitaxel analog, demonstrated that tip diffusion could not account for the probe's rapid and uniform binding. Instead, flutax-2 exhibited a two-step binding mechanism[92,93], suggesting a diffusion process through the microtubule wall mediated by fenestrations between the lattice tubulin dimers. In 2007, Buey and coworkers described the type I pore as an external taxane site that acts as a receptor[94,95]. After a taxane site ligand swiftly binds to the pore I site, a second rate-determining step involves its transition to the luminal taxane binding site. This transition is enabled by a molecular rearrangement of the pore, triggered by the compound's interaction with the H6-H7, which is common to both binding sites[96].

1.7 Microtubules as pharmacological targets

As described in section 1.5.2, nature has yielded numerous compounds that bind to tubulin/microtubules and disrupt microtubule function. These natural products and their semi-synthetic derivatives have found an early clinical application as chemotherapeutics, being up to date some of the most effective drugs used in the treatment of solid tumors and hematological malignancies. For decades, these drugs were thought to work solely through their ability to inhibit mitosis. However, accumulating evidence demonstrates that their actions are much more complex, in that they also have significant effects on microtubules in nondividing cells by modulating a diverse range of signaling pathways, including those involved in inflammatory response, neuronal function and viral infection.

1.7.1 MTAs as chemotherapeutics

The antitumor mechanism of paclitaxel, as well as other MTAs, continues to be a subject of ongoing discussion. The compound's effects on rapidly dividing cell cultures *in vitro* provide the foundation for the traditionally proposed anti-mitotic mechanism. According to this theory, impairment of dynamic instability prevents the mitotic spindle from properly attaching to the chromosomes' kinetochores on both sides during pro-metaphase (see section 1.4.3). The presence of a small number of unattached kinetochores prevents the silencing of the spindle assembly checkpoint, a control mechanism of cell division that delays the separation of the chromosomes until each pair has made stable attachments. Consequently, the cell enters mitotic arrest, which ultimately leads to apoptosis[97]. However, this model presents two weaknesses. First, unlike cultured cancer cells, tumor cells in living organisms typically exhibit slow rates of proliferation. This raises questions about how a few doses of paclitaxel can eradicate an entire, slowly growing tumor in a responsive patient if it primarily targets dividing cells. Second, it is also unclear how any cytotoxic drug can exert potent anticancer effects at the dose limit imposed by bone marrow and gut toxicity when relative proliferation rates serve as the sole basis for selectivity[98]. Hence, an antitumor mechanism focused on suppressing dividing cells may not be consistent[99]. In recent years, several alternative theories have been proposed[98], with one gaining significant attention. It proposes that paclitaxel's antitumor effects can be explained with an inflammatory micronucleation mechanism[100]. According to this model, at low drug concentrations cancer cells tend to resist the apoptotic effect of paclitaxel through an abnormal exit from mitosis. This phenomenon, known as *mitotic slippage*, is not associated with a delay in mitosis and entails the division of chromosomes on multipolar spindles. Consequently, chromosome missegregation occurs, ultimately leading to the formation of non-viable aneuploid micronucleated cells[101]. These abnormal cells can persist for days and accumulate in the tumor matrix until they activate pro-inflammatory signals that ultimately eliminate the entire solid tumor[102].

Although MTAs are often effective in treating various types of tumors, cancer cells tend to develop chemoresistance after prolonged therapy. Several mechanisms contribute to drug resistance, including: (1) overexpression of the ATP-binding cassette (ABC) superfamily of drug efflux proteins, especially the P-glycoprotein (P-gp) pump, which exports drugs out of the cells and affects the internal drug concentration; (2) upregulation of less-sensitive β-tubulin isotypes, such as β-III and β-IVa; (3) changes in cellular levels of anti- and pro-apoptotic proteins, like Bcl-2 family members, which directly correlate to chemosensitivity[102]. In line with this framework, patient studies have shown that increased drug efflux by ABC pump proteins, β-III tubulin and Bcl-2 overexpression serve as useful predictive factors for survival and sensitivity to MTAs in various cancers. The use of tubulin binders as chemotherapeutics is also limited by the occurrence of serious adverse effects, including peripheral neuropathy (see section 1.8) and neutropenia, as well as gut toxicity and alopecia. Additionally, many poorly soluble MTAs require vehicles for administration, which can

exacerbate adverse effects and lead to allergic reactions. For this reason, optimizing MTA drug delivery and distribution has become an important direction in anticancer therapy research. Some modern drug delivery systems include albumin nanoparticles (paclitaxel, Abraxane®), albumin bound nanoparticles (paclitaxel, Pazenir®), liposomes (vincristine, Marquibo®) and microspheres. Additionally, some MTAs are now employed in antibody-drug conjugates (ADCs) as cytotoxic payloads, as part of targeted therapies for cancer treatment. Their goal is to increase the therapeutic index of cytotoxic drugs by selectively delivering chemotherapy to tumors while sparing healthy tissues, thereby mitigating undesired side effects[103]. Examples are trastuzumab emtansine and lorvotuzumab mertansine, two maytansinoid-based ADCs approved for clinical use.

1.7.2 MTAs as antiparasitic and antifungal drugs

In addition to their anti-cancer applications, the antimitotic activity of tubulin binders offers a powerful way to halt parasite replication[104]. Although α- and β- tubulin are highly conserved proteins, subtle structural differences do exist in organisms belonging to distinct evolutionary groups. These variations can be exploited to selectively target parasite species while protecting the infected human or animal host. For instance, benzimidazolic colchicine site binders, such as mebendazole and albendazole, are clinically used as antiprotozoal and anthelminthic drugs. They effectively treat a range of parasitic infections, including ascariasis, giardia, pinworm and hookworm infections[105,106]. Another selective tubulin binder clinically used is griseofulvin which, due to its ability to differentially inhibit microtubule polymerization of fungal vs. mammalian tubulin, is widely employed as antifungal medication to treat several types of dermatophytoses[107]. All these drugs are inserted in the World Health Organization Essential Medicines List owing to their safety and efficacy. For this reason, the rational development of parasite-specific MTAs is gaining increasing interest in recent times. Parabulin, an anti-tubulin drug specifically targeting Apicomplexa parasites (causing malaria, toxoplasmosis, and cryptosporidiosis), was rationally designed in 2021 by Gaillard and colleagues [108]. Their study demonstrated the possibility of developing species-selective MTAs by employing a combined approach of X-ray crystallography and cryo-electron microscopy to identify significant differences between the drug-binding sites of evolutionary distant tubulins.

1.7.3 MTAs in neurodegeneration

Numerous neurodegenerative diseases are characterized by alterations in the structure and organization of microtubules and MAPs. Examples include the reduced microtubule mass observed in the brain of Parkinson's disease patients, changes in tubulin levels of PTMs – particularly acetylation – in Huntington's disease, or the aggregation of tau in neurofibrillary tangles typical of Alzheimer's disease[109]. In addition to its role in pathological conditions, microtubule dynamics dysfunction is also likely to contribute to age-related neuronal degeneration[110]. Hence, modulating microtubule dynamics and restoring impaired microtubule

stability may serve as an effective neuroprotective strategy to counteract the disruption of the microtubule system in disease and aging. In agreement with this hypothesis, several MSAs have demonstrated protective effects in different neurodegeneration models, and two of them – the BBB-permeable taxane TPI-287 and epothilone D – have been tested in Phase I clinical studies for the treatment of neurodegenerative disorders[110]. However, despite the promising data *in vitro* and in animal models, no clear beneficial effect was observed in patients. One major issue with this therapeutic approach is that MSAs generally act non-specifically on microtubules across several cell types and subcellular compartments. For instance, studies on the effect of epothilone D in neurons affected by tauopathies suggested that microtubule stabilization is beneficial in the axonal compartment but detrimental in the dendrites, as the reduced microtubule dynamicity led to impairment of the structural and functional plasticity[111]. Therefore, research in this field is shifting focus towards a more subtle regulation of neuronal microtubules, such as the development of MSAs with increased specificity for axonal microtubules[110]. This could be achieved by targeting specific features of the microtubules of the axon, e.g., their PTMs pattern or their characteristic high density and bundling.

1.7.4 MTAs as antivirals

The exploration of tubulin binders' activity against viral infections is a new emerging field that gained momentum following the outbreak of the COVID-19 (Coronavirus Disease 2019) pandemic. For successful replication, viruses must penetrate cells and navigate through the cytoplasm to reach their sub-cellular sites of replication. Once there, they create new viral progeny that must then return to the cell surface in order to be released and spread. Owing to a dense and viscous cytosolic environment that greatly impedes free diffusion of macromolecules, viruses have evolved an array of strategies to exploit their hosts' microtubule-based transport networks and associated regulatory factors for their own movement. Some viruses directly associate with the microtubule-dependent motors [112], while others are transported inside endosomes, exploiting the characteristic vesicular movement that targets either kinesins or dyneins upon endosomal maturation[113]. Furthermore, evidence supports the additional role of non-motile MAPs, including +TIPs, in viral trafficking within infected cells[114]. Consequently, pharmacological modulation of microtubules could potentially inhibit virus replication and spreading. In a recent study by Oliva and colleagues, an array of different tubulin binders was tested against DNA and RNA viruses, including SARS-CoV-2, demonstrating that MTA treatment can affect viral replication, although efficacy was highly variable among different virus[115]. In particular, MDAs proved more effective than MSAs, with benzimidolic colchicine site binders (mebendazole, albendazole) being among the most active compounds. These compounds exhibit lower antimitotic activity compared to most MDAs, making them attractive candidates for the development of site-directed antivirals in combinatorial drug therapy.

1.8 Taxane-induced peripheral neurotoxicity

Chemotherapy-induced peripheral neurotoxicity (CIPN) is a highly prevalent, severe, and dose-limiting toxicity that often leads to dose interruptions, subtherapeutic dosing, or discontinued therapy for many chemotherapeutic agents. Typical symptoms of CIPN include pain, tingling, numbness and weakness in the hands and feet. Many patients also experience allodynia, a condition in which normal stimuli, such as light touch, are experienced as severe pain. The onset of CIPN is influenced by numerous factors, including the physical and chemical properties of the anticancer drug and its dosage. Importantly, the peripheral nervous system lacks a protective structure akin to the central nervous system's blood-brain barrier (BBB), leaving peripheral neurons vulnerable to the direct toxic effects of antineoplastic drugs. Sensory neurons are preferentially affected, with symptoms typically manifesting first in distal extremities, which indicates an increased vulnerability of neurons with the longest axons. Besides direct effects, indirect toxicity also contributes to the development of CIPN, primarily through inflammatory reactions[116].

The use of MTAs in anticancer treatment is also limited by neurotoxicity, with the incidence of severe cases varying among different tubulin binders. For instance, vincristine and eribulin, both vinca site ligands, have the highest and lowest incidence of severe neuropathy, respectively[117]. In the specific context of taxane-induced peripheral neurotoxicity (TIPN), most previous studies have shown a higher incidence in patients treated with paclitaxel compared to docetaxel, with an overall incidence in the first case from 57% to 83% and severity in 2% - 33% of cases[118]. However, the cellular mechanisms by which MTAs cause neuropathy remain unknown. In the case of taxanes, it is unclear why mature neurons, which typically possess a larger population of highly stable microtubules, suffer from increased microtubule stabilization. This is especially true for axonal microtubules, whose stability is manifest in their resistance to depolymerization in the face of cold, elevated calcium, or nocodazole[119–121]. A widely cited hypothesis for how taxane-induced stabilization could lead to axonal degeneration is through the disruption of axonal transport. Indeed, it is noteworthy that TIPN is most apparent in the distal extremities, where sensory neurons are longer and where transport problems may manifest more quickly. The correlation between paclitaxel exposure and impaired axonal transport is proved by numerous studies conducted in cells[122–124], sciatic nerves[125] and squid axoplasms[117]. However, it is challenging to discern whether these effects on axonal transport are a cause or a consequence of axonal degeneration. To establish this potential cause-effect relationship, recent research has focused on exploring the possible molecular mechanisms through which taxanes could affect intracellular transport. Several mechanistic hypotheses have been proposed, but to date, there is insufficient evidence to conclusively favor any of them:

1. Taxanes might act by blocking the binding or movement of molecular motors. As the taxane site is located on the inner surface of the microtubule, a steric obstruction is highly improbable. However, the

conformational change of tubulin associated with taxanes' binding could lead to an allosteric alteration of the externally exposed residues.

2. More stable microtubules are known to undergo changes in PTMs patterns, with tubulin experiencing increased acetylation, polyglutamylation and de-tyrosination. Consistently, paclitaxel treatment of cultured neurons leads to these three changes[126]. As PTMs influence MAPs and motor proteins recognition (see section 1.5.1), these changes could potentially impact microtubule-based transport.

3. The impairment of motor protein movement could be generated by an increase in the microtubule lattice defects upon taxanes binding. Lattice defects, which have been well documented with electronic microscopy and atomic force microscope, can include vacancies (missing dimers), dislocations (points at which the number of protofilaments changes in the microtubule), transitions in periodicity of the lattice (a change in the pitch of the helix) or a combination of those[127]. It is possible that impairment of dynamic instability caused by taxanes prevents the physiological self-repair process of microtubules, resulting in the accumulation of damaged subunits and dislocations in the microtubule wall that cannot be edited out and that could serve as roadblocks to motors. Indeed, *in vitro* studies have established that lattice defects negatively impact kinesin-mediated transport[128].

4. Lastly, motor protein dysfunction could be related to a specific type of microtubule lattice alteration, axial expansion, which occurs upon taxanes binding to microtubules. There are two reasons why longitudinal elongation of the lattice can potentially be detrimental for intracellular transport. The first one is that kinesin moves along microtubules with a fixed stepping size of 8 nm, corresponding to the axial rise of one heterodimer (see section 1.4.2.1). Lattice expansion resulting by taxane treatment necessarily modifies the step size, potentially leading to the early detachment of the motors. The second reason is that lattice expansion is normally a structural signal localized in a specific area of the microtubule close to the tip, and its spreading along the whole fiber might once again affect motor proteins movement. The traditional model of microtubule's structure proposed an initial right-handed, expanded lattice for the GTP-bound tubulin of the cap, which would then shrink and change twist upon hydrolysis during the transition state[36]. However, in a work published in 2020 Estévez-Gallego and colleagues posit an alternative model, according to which tubulin GTP-, GDP·Pi- and GDP-bound states are all characterized by a compact lattice, with the expansion occurring as a transient state between the MT's cap (GDP·Pi) and core (GDP) regions to facilitate Pi release (Figure 1-18)[46]. In both cases, due to its strategic localization near the (+)-end, lattice expansion is a structural signal likely to be involved in the recognition by regulatory MAPs and motors of microtubule's polarity.

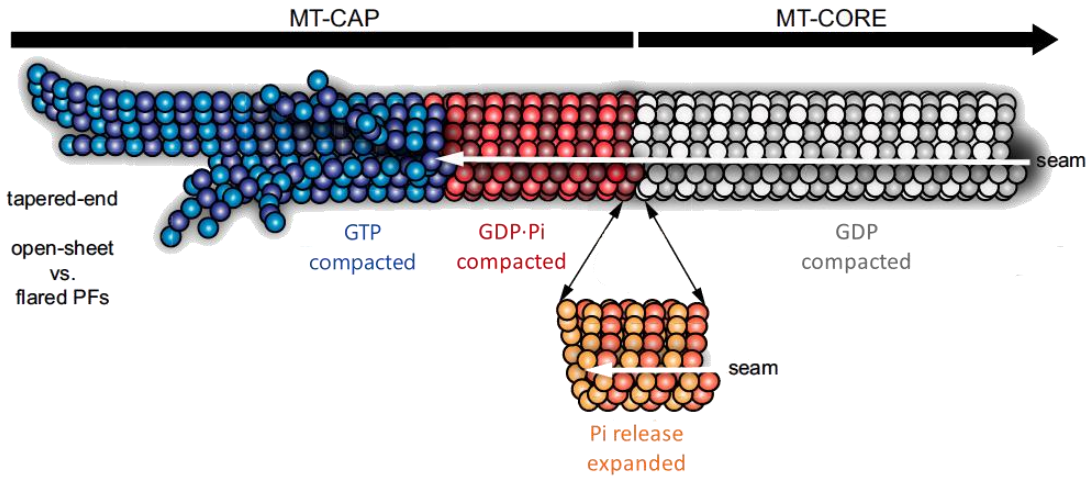

Figure 1-18. Microtubule model illustrating specific lattice features of the GTPase cycle. This mosaic structure shows that: (i) the GTP-bound tip (blue) contains curved PFs/sheets that come together into a straight lattice due to the formation of lateral contacts, (ii) the post-hydrolysis GDP·Pi lattice (red) retains overall MT structure, (iii) hypothetically, lattice undergoes an energy-consuming expansion phase (orange) that contributes to Pi release, and (iv) in the GDP state (gray) subtle changes on the PF skew distinguish the metastable compact lattice. Figure adapted from [46].

2 Aim of the thesis

In order to protect neurons from damage during paclitaxel chemotherapy, it is essential to gain an improved mechanistic understanding of the drug's pathological effects on neurons. If particular, if the neurotoxicity is not directly linked to microtubule stabilization, but rather connected to other downstream alterations in the microtubules, this knowledge could help design ameliorative treatments for aggressive cancers that require high chemotherapeutic doses and improve the quality of life for cancer patients and survivors who are affected by TIPN.

One such downstream structural alteration is taxane-induced lattice expansion. In fact, a recent study resulting from an extensive collaboration between our laboratory and several different research groups[89] has concluded that it does not represent a contributing factor to the stabilization mechanism. Yet, it remains a constant feature of microtubules assembled in the presence of paclitaxel, docetaxel, and even baccatin III – their inactive synthetic precursor lacking the C13 side chain.
For microtubules treated with sub-stoichiometric concentrations of paclitaxel, locally expanded dimers may act as point defects that motor proteins need to navigate around, potentially causing premature detachment and/or stalling. Moreover, since current models of the microtubule structure describe the expanded lattice as a distinct structural feature localized near the tip, the spread of this structural signal along the whole lattice could impact the recognition patterns of different MAPs, including kinesins and dyneins.

Strikingly, X-ray fiber diffraction measurements obtained by our research group[129] revealed that flutax-2 – a paclitaxel derivative originally developed as a fluorescent probe of the taxane binding site[92] – does not induce axial expansion of the lattice. Instead, it seems to induce the compaction of intrinsically expanded lattice models. This finding makes flutax-2 a compelling candidate for investigating the effect microtubule's structural signaling on kinesin- and dynein-mediated transport. The chemical structure of flutax-2 differs from paclitaxel only for the presence of a bulky di-fluoro-fluorescein moiety connected via an alanine linker to position C7 (Figure 2-1).

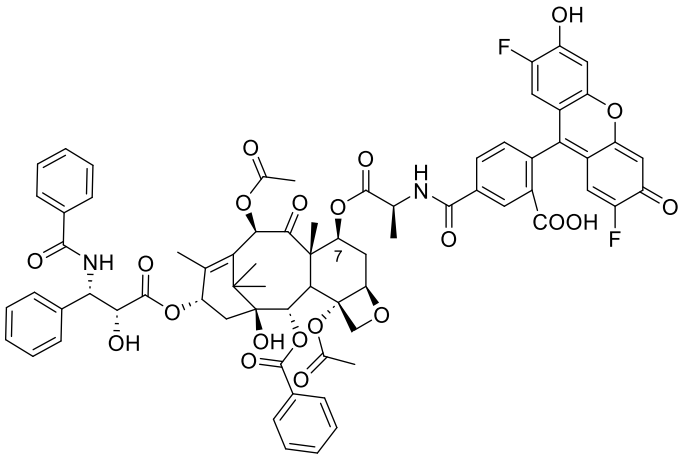

Figure 2-1. Chemical structure of flutax-2, a fluorescent paclitaxel derivative.

Although the molecular mechanism behind flutax-2's unique behavior in the microtubule lattice expansion process remains unclear, a possible hypothesis involves the C7-decoration interacting with the fenestration in the microtubule wall that allows the passage of taxanes from the pore I transient site to the luminal binding site, as mentioned in section 1.6. In this case, the effect of the C7-decoration might be attributed to its steric hindrance or to a specific pattern of interactions established with the protein. To investigate this intriguing structural effect, the design and synthesis of two new C7-decorated taxanes mimicking the binding mode of flutax-2 to tubulin was proposed.

This thesis work, performed within the EU-funded Innovative Training Network – European Joint Doctorate TubInTrain, via a cotutelle agreement between Universidad Internacional Menénedez Pelayo and Università degli Studi di Milano, seeks to achieve the following objectives:

1. Investigate the influence of C7-modifications of the taxane core on the biochemical and structural properties of microtubules. For this purpose, the concrete proposed objectives are:

    1.1. Design, synthetize and characterize new C7-modified paclitaxel derivatives capable of emulating the binding mode of flutax-2 to tubulin.
    1.2. Determine the biochemical and structural effects caused by the interaction of these compounds with tubulin and microtubules.
    1.3. Unravel whether microtubule lattice expansion induced by taxanes is related to the absence or presence of C7-bulky modifications of the taxane core.

2. Explore the potential interplay between the microtubule structural modifications induced by taxanes and the intracellular transport impairment, as an approach to gain insight into the molecular mechanism behind taxane-induced peripheral neurotoxicity. To this end, the targeted specific objectives are:

    2.1. Characterize the cellular effects of C7-modified taxanes compared to paclitaxel, in particular their effect on intracellular transport.
    2.2. Examine the correlation between taxane-induced microtubule alterations, especially axial expansion, and the impairment of kinesin- and dynein-mediated transport in cells.

3 Materials and Methods

3.1 Chemistry

3.1.1 General experimental procedures

Reagents were purchased from general suppliers (Merck, Fluorochem, TCI) and used without further purification. Paclitaxel was kindly supplied by Indena s.p.a. (Italy). All solvents were of reagent grade or HPLC grade. All reactions were carried out in oven-dried glassware and dry solvents, under nitrogen atmosphere, and were monitored by glasses or aluminum TLC on silica gel (Merck precoated 60F254 plates), with detection by UV light (254 nm), or by TLC stains as potassium permanganate, bromocresol green or p-anisaldehyde stain.

Purification of intermediates and final products was mostly carried out by flash column chromatography, using high purity grade silicagel (Merck Grade, pore size 60 Å, 230-400 mesh particle size, Sigma Aldrich) as stationary phase. Alternatively, purification was performed using Biotage Isolera® One system in direct phase using Biotage® Sfär Silica D cartridges (4/10/35 g).

^{1}H-NMR and ^{13}C-NMR spectra were recorded on a Bruker Avance Spectrometer 400 MHz using commercially available deuterated solvents (chloroform-d, dimethylsulfoxide-d_6) at room temperature. Chemical shifts (δ) are reported in parts per million (ppm) and are reported relative to tetramethylsilane, used as an internal standard. Data for ^{1}H-NMR are reported as follows: chemical shift (δ/ppm), multiplicity, and coupling constants (Hz). Multiplicities are reported as follows: s = singlet, d = doublet, t = triplet, m = multiplet, br s= broad singlet. Data for ^{13}C-NMR are reported in terms of chemical shift (δ/ppm).

Mass spectrometry (MS) analyses were performed by direct infusion of the samples into an LCQ Fleet ion trap mass spectrometer equipped with an electrospray ionization (ESI) source. This soft ionization technique relies on the formation of an electrostatically charged aerosol by the application of a high voltage to a solution of the sample. Typically, quasi-molecular ions are observed with little to no fragmentation. MS-SCAN conditions: 50-2000 amu, SCAN-time: 0.2 sec.

Specific optical rotation, or $[\alpha]_D$, was measured on a Jasco P-1030 polarimeter in chloroform. This intrinsic property of chiral compounds is defined by the formula $[\alpha]_\lambda = \alpha/\gamma l$, where α is the angle through which plane polarized light is rotated by a compound's solution of mass concentration γ and path length l (in this case l is equal to 10 cm, the length of the polarimeter cell). The superscript indicates the Celsius temperature at which the measurement is carried out, while the wavelength of the measurement is reported in the subscript. The letter D indicates that the wavelength used corresponds to the sodium D line (589 nm). The standard deviation is calculated over 10 measurements.

3.1.2 Synthesis of 2'-carboxybenzoylpaclitaxel (7)

Benzyl chloroformate (990 µL, 7.02 mmol) was added in 10 eq. aliquots (165 µL per aliquot) at 10 min intervals to a solution of paclitaxel (100 mg, 0.117 mmol) and dry pyridine (950 µL, 11.71 mmol) in dry CH_2Cl_2 (5 mL), at RT and under nitrogen atmosphere. The reaction was stirred for 25h, after which it was quenched with 2 mL of saturated aqueous NH_4Cl. After the addition of AcOEt (10 mL), the organic phase was washed with saturated aqueous NH_4Cl (3 x 5 mL) and brine (2 x 5 mL). The organic layer was then dried over Na_2SO_4, and the solvent was evaporated under reduced pressure. The crude product was purified by flash chromatography (silicagel, eluent mixture: 1:1 n-hexane/AcOEt) to obtain pure **7** (80.8 mg, 0.082 mmol, 70% yield).

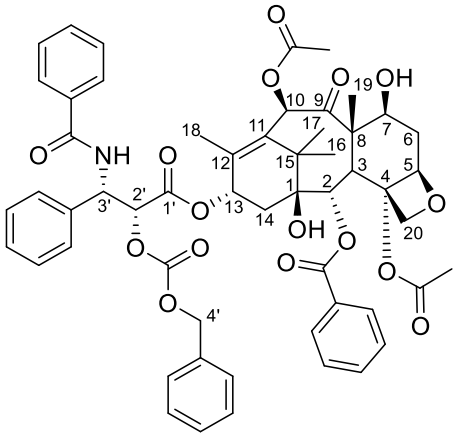

^{1}H NMR (400 MHz, $CDCl_3$) δ 8.17 (d, *J* = 7.4 Hz, 2H, ***o*-2-BzO**), 7.76 (d, *J* = 7.1 Hz, 2H, ***o*-3'-NHBz**), 7.68 – 7.59 (m, 1H, ***p*-2-BzO**), 7.56-7.50 (m, 3H, ***m*-2-BzO**, ***p*-3'-NHBz**), 7.49 – 7.34 (m, 12H, ***m*-3'-NHBz**, ***o,m,p*-2'-CbzO**, ***o,m,p*-3'-Ph**), 6.98 (d, *J* = 9.3 Hz, 1H, **3'-NH**), 6.37 – 6.28 (m, 2H, **10-H**, **13-H**), 6.02 (dd, *J* = 9.3, 2.7 Hz, 1H, **3'-H**), 5.72 (d, *J* = 7.1 Hz, 1H, **2-H**), 5.48 (d, *J* = 2.7 Hz, 1H, **2'-H**), 5.26 – 5.14 (m, 2H, **4'-H**), 5.01 (dd, *J* = 9.7, 2.3 Hz, 1H, **5-H**), 4.47 (dd, *J* = 10.9, 6.6 Hz, 1H, **7-H**), 4.35 (d, *J* = 8.5 Hz, 1H, , **20a-H**), 4.24 (d, *J* = 8.5 Hz, 1H, **20b-H**), 3.85 (d, *J* = 7.0 Hz, 1H, **3-H**), 2.59 (ddd, *J* = 14.7, 9.7, 6.5 Hz, 1H, **6a-H**), 2.49 (s, 3H, **4-OAc**), 2.47 – 2.41 (m, 1H, **14a-H**), 2.26 (s, 3H, **10-OAc**), 2.28 – 2.22 (m, 3H, **14a-H**), 1.96 (s, 3H, **18-H**), 1.98 – 1.86 (m, 1H, **6b-H**), 1.72 (s, 3H, **19-H**), 1.28 (s, 3H, **17-H**), 1.17 (s, 3H, **16-H**).

^{13}C NMR (101 MHz, $CDCl_3$) δ 203.97, 171.42, 170.01, 168.01, 167.23, 167.20, 142.89, 133.84, 132.97, 132.17, 130.39, 129.26, 129.06, 128.90, 128.85, 128.66, 128.56, 127.31, 126.74, 84.61, 81.24, 79.39, 77.02, 76.62, 75.76, 75.28, 72.31, 72.23, 70.93, 58.70, 52.91, 45.72, 35.76, 35.68, 27.00, 22.85, 22.32, 20.98, 14.96, 9.76 (detectable peaks).

3.1.3 Synthesis of hexanedioic acid *mono*(2-(trimethylsilyl)ethyl) ester (5a)

Hexanedioic acid (1 g, 6.84 mmol) was added to a mixture of dry CH_2Cl_2 and dry pyridine (25 and 2.5 mL respectively, 10:1 ratio) and stirred at RT, under nitrogen atmosphere, until complete dissolution. Then 2-(trimethylsilyl) ethanol (392 µL, 2.74 mmol), EDC·HCl (788 mg, 4.11 mmol) and DMAP (167 mg, 1.39 mmol) were added, and the solution was stirred for 24h. The reaction mixture was washed with phosphoric acid 10% (2 x 15 mL) and brine (20 mL). The organic phase was then dried over Na_2SO_4, and the solvent was evaporated under reduced pressure. The mono-protected product was isolated by flash chromatography (silicagel, eluent mixture: 8:2 n-hexane/AcOEt + 1% formic acid) to obtain pure **5a** (446 mg, 1.81 mmol, 66% yield).

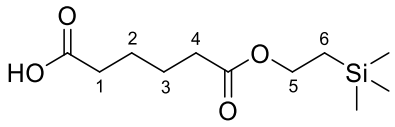

^{1}H NMR (400 MHz, $CDCl_3$) δ 10.94 (br s, 1H, **COOH**), 4.09 – 3.94 (m, 2H, **5-H**), 2.29 – 2.06 (m, 4H, **1-H, 4-H**), 1.54 (br s, 4H, **2-H**, **3-H**), 0. 91 – 0.76 (m, 2H, **6-H**), -0.12 (m, 9H, **$SiMe_3$**).

^{13}C NMR (101 MHz, $CDCl_3$) δ 178.87, 173.45, 62.43, 33.83, 33.42, 24.08, 23.89, 17.08, -1.82.

3.1.4 Synthesis of nonanedioic acid *mono*(2-(trimethylsilyl)ethyl) ester (5b)

Nonanedioic acid (1 g, 5.31 mmol) was added to a mixture of dry CH_2Cl_2 and dry pyridine (25 and 2.5 mL respectively, 10:1 ratio) and stirred at RT, under nitrogen atmosphere, until complete dissolution. Then 2-(trimethylsilyl) ethanol (304 µL, 2.12 mmol), EDC·HCl (612 mg, 3.19 mmol) and DMAP (130 mg, 1.06 mmol) were added, and the solution was stirred for 24h. The reaction mixture was washed with phosphoric acid 10% (2 x 15 mL) and brine (20 mL). The organic phase was then dried over Na_2SO_4, and the solvent was evaporated under reduced pressure. The mono-protected product was isolated by flash chromatography (silicagel, eluent mixture: 75:25 n-hexane/AcOEt + 1% formic acid) to obtain pure **5b** (430mg, 1.49 mmol, 70% yield).

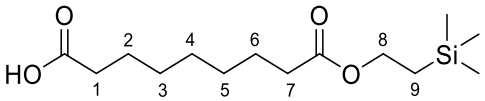

^{1}H NMR (400 MHz, $CDCl_3$) δ 10.98 (s, 1H, **COOH**), 4.15 – 4.05 (m, 2H, **8-H**), 2.33 – 2.16 (m, 4H, **1-H**, **7-H**), 1.63 – 1.49 (m, 4H, **2-H**, **6-H**), 1.32 – 1.21 (m, 6H, **3-H**, **4-H**, **5-H**), 0.97 – 0.86 (m, 2H, **9-H**), 0.01 (s, 9H, **SiMe3**).

^{13}C NMR (101 MHz, $CDCl_3$) δ 179.99, 174.13, 62.51, 34.52, 34.09, 28.97, 28.93, 28.91, 24.94, 24.66, 17.39, -1.43.

3.1.5 Synthesis of 2'-*O*-Cbz-7-*O*-(1''-*O*- (2'''-(trimethylsilyl)ethyl)hexanedioyl)-paclitaxel (4a)

A solution of acid **5a** (49 mg, 0.2 mmol) in CH_2Cl_2 (1 mL) was added to a stirred solution of 2'-*O*-Cbz-paclitaxel **7** (50 mg, 0.05 mmol) and DMAP (6 mg, 0.05 mmol) in CH_2Cl_2 (1 mL), at RT and under N_2 atmosphere. Then DCC (42 mg, 0.2 mmol) was added, and the reaction mixture was stirred at RT for 18h. The mixture was diluted with CH_2Cl_2 (5 mL) and it was filtered to remove the urea formed as a byproduct. The collected organic phase was washed with saturated aqueous NH_4Cl (2 x 5 mL) and brine (2 x 5 mL), then it was dried over Na_2SO_4, and the solvent was evaporated under reduced pressure. The resulting crude was purified by flash chromatography (silicagel, eluent mixture: 6.5:3.5 n-hexane/AcOEt) to obtain compound **4a** (55 mg, 0.045 mmol, 90% yield).

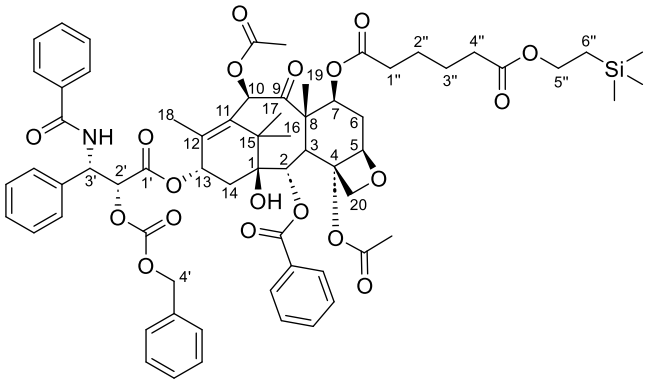

^{1}H NMR (400 MHz, $CDCl_3$) δ 8.p (d, 2H, ***o*-2-BzO**), 7.62 – 7.55 (m, 2H, ***o*-3'-NHBz**), 7.51 – 7.42 (m, 1H, ***p*-2-BzO**), 7.41 – 7.30 (m, 3H, ***m*-2-BzO**, ***p*-3'-NHBz**), 7.30 – 7.16 (m, 12H, ***m*-3'-NHBz**, ***o,m,p*-2'-CbzO**, ***o,m,p*-3'-Ph**), 6.78 (d, *J* = 9.3 Hz, 1H, **3'-NH**), 6.13 (s, 1H, **H-10**), 6.16 – 6.07 (m, 1H, **H-13**), 5.84 (dd, *J* = 9.3, 2.7 Hz, 1H, **3'-H**), 5.55 (d, *J* = 6.9 Hz, 1H, **2-H**), 5.45 (dd, *J* = 10.5, 7.0 Hz, 1H, **7-H**), 5.32 (d, *J* = 2.7 Hz, 1H, **2'-H**), 5.08 – 4.96 (m, 2H, **4'-H**), 4.82 (dd, *J* = 9.6, 1.9 Hz, 1H, **5-H**), 4.19 (d, *J* = 8.4 Hz, 1H, **20a-H**), 4.05 (d, *J* = 8.4 Hz, 1H, **20b-H**), 4.04 – 3.98 (m, 3H, **5''-H**), 3.81 (d, *J* = 6.9 Hz, 1H, **3-H**), 2.46 (ddd, *J* = 14.4, 9.6, 7.1 Hz, 1H, **6a-H**), 2.30 (s, 3H, **4-OAc**), 2.25 (m, 2H, **14a-H**), 2.19 – 2.10 (m, 4H, **1''-H, 4''-H**), 2.07 (m, **14b-H**), 2.01 (s, 3H, **10-OAc**), 1.85 (s, 3H, **18-H**), 1.67 (s, 3H, **19-H**), 1.73 – 1.67 (m, 1H, **6b-H**) 1.54 – 1.44 (m, 4H, **2''-H**, **3''-H),** 1.07 (s, 3H, **17-H**), 1.02 (s, 3H, **16-H**), 0.89 – 0.79 (m, 2H, **6''-H**), -0.11 (s, 9H, **SiMe$_3$**).

^{13}C NMR (101 MHz, $CDCl_3$) δ 201.87, 173.45, 172.17, 169.38, 168.60, 167.77, 167.08, 166.72, 153.82, 140.90, 136.50, 134.12, 133.50, 133.34, 132.36, 131.81, 130.01, 128.97, 128.90, 128.68, 128.54, 128.52, 128.49, 128.34, 128.29, 126.96, 126.40, 83.81, 80.69, 78.46, 76.55, 76.17, 75.02, 74.39, 71.83, 71.02, 70.61, 62.25, 55.85, 52.59, 46.68, 43.09, 35.21, 33.97, 33.45, 33.17, 26.25, 24.13, 23.72, 22.44, 21.09, 20.51, 17.11, 14.31, 10.69, -1.69.

3.1.6 Synthesis of 6-*O*-(2',3'-dihydroinden-1'-yl)-1-*O*-(2''-(trimethylsilyl)ethyl) hexanedioate (10a)

DMAP (26 mg, 0.21 mmol), EDC·HCl (119 mg, 0.62 mmol), and 1-indanol (87 mg, 0.62 mmol) were added sequentially to a solution of **5a** (101.5 mg, 0.41 mmol) in dry CH_2Cl_2 and pyridine (18 and 2 mL respectively, 10:1 ratio), at RT and under N_2 atmosphere. The reaction mixture was stirred for 6h. When TLC monitoring confirmed reaction completion, HCl 1M was added (40 mL). The aqueous phase was extracted with CH_2Cl_2 (4 x 15 mL), then the collected organic layer was dried over Na_2SO_4, and the solvent was evaporated under reduced pressure. The crude oil was purified by Biotage® direct phase flash chromatography (eluent mixture: n-hexane/AcOEt from 98:2 to 80:20) to afford pure compound **10a** (90.9 mg, 0.25 mmol, 61%).

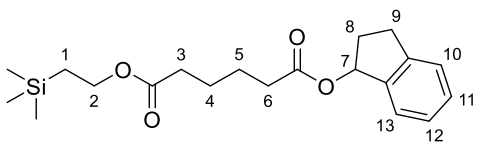

^{1}H NMR (400 MHz, $CDCl_3$) δ 7.39 (d, *J* = 7.4 Hz, 1H, **10-H**), 7.31 – 7.16 (m, 3H, **13-H**, **12-H**, **11-H**), 6.21 (dd, *J* = 6.9, 3.9 Hz, 1H, **7-H**), 4.20 – 4.11 (m, 2H, **H-2**), 3.16 – 3.04 (m, 1H, **9a-H**), 2.92 – 2.81 (m, 1H, **9b-H**), 2.56 – 2.43 (m, 1H, **8a-H**), 2.36 – 2.24 (m, 4H, **3-H**, **6-H**), 2.13 – 2.01 (m, 1H, **8b-H**), 1.71 – 1.61 (m, 4H, **4-H**, **5-H**), 1.02 – 0.93 (m, 2H, **1-H**), 0.04 (s, 9H, **-SiMe$_3$**).

^{13}C NMR (101 MHz, $CDCl_3$) δ 173.45, 173.35, 144.39, 141.19, 128.95, 126.76, 125.55, 124.85, 78.31, 62.53, 34.22, 34.14, 32.40, 30.26, 24.55, 24.47, 17.41, -1.42.

3.1.7 Synthesis of hexanedioic acid *mono*(2',3'-dihydroinden-1'-yl) ester (9a)

TBAF 1M in THF (1 mL, 1 mmol) was added dropwise to a stirred solution of **10a** (90 mg, 0.25 mmol) in dry THF (10 mL), at -5°C and under N_2 atmosphere. The reaction mixture was warmed up to RT and stirred for 4h. When TLC monitoring confirmed reaction completion, saturated aqueous NH_4Cl (15 mL) was added. The aqueous phase was extracted with AcOEt (4 x 15 mL), then the collected organic layer was dried over Na_2SO_4 and evaporated under reduced pressure. The crude oil was purified by flash chromatography (silicagel, eluent mixture: 8:2 n-hexane/AcOEt + 1% formic acid) to obtain pure **9a** (41.3 mg, 0.157 mmol, 63% yield).

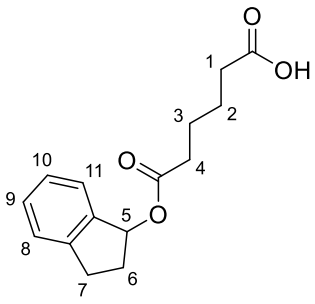

^{1}H NMR (400 MHz, $CDCl_3$) δ 7.38 (d, J = 7.4 Hz, 1H, **8-H**), 7.37 – 7.05 (m, 3H, **11-H**, **10-H**, **9-H**), 6.20 (dd, J = 6.9, 3.8 Hz, 1H, **5-H**), 3.15 – 3.03 (m, 1H, **7a-H**), 2.92 – 2.80 (m, 1H, **7b-H**), 2.55 – 2.43 (m, 1H, **6a-H**), 2.39 – 2.29 (m, 4H, **1-H**, **4-H**), 2.18 – 2.00 (m, 1H, **6b-H**), 1.79 – 1.54 (m, 4H, **2-H, 3-H**). **^{13}C NMR** (101 MHz, $CDCl_3$) δ 173.42, 144.50, 141.18, 129.05, 126.84, 125.62, 124.93, 78.46, 34.23, 33.52, 32.44, 30.32, 24.46, 24.19.

3.1.8 Synthesis of 2'-*O*-Cbz-7-*O*-(6''-*O*-(2''',3'''-dihydroinden-1'''-yl)hexanedioyl) paclitaxel (2a)

A solution of compound **9a** (28 mg, 0.107 mmol) in CH_2Cl_2 (2 mL) was added to a stirred solution of 2'-*O*-Cbz-paclitaxel **7** (70 mg, 0.071 mmol) and DMAP (8.7 mg, 0.071 mmol) in CH_2Cl_2 (3 mL), at RT and under N_2 atmosphere. Then, DCC (58 mg, 0.284 mmol) was added and the reaction mixture was stirred at RT for 29h. The mixture was diluted with CH_2Cl_2 (8 mL) and filtered on a plug of celite. The organic phase was washed with saturated aqueous NH_4Cl (2 x 10 mL) and brine (2 x 10 mL), then it was dried over Na_2SO_4, and the solvent was evaporated under reduced pressure. The resulting crude was purified by flash chromatography (silicagel, eluent mixture: 7:3 n-hexane/AcOEt) to obtain compound **2a** (61.1 mg, 0.050 mmol, 70% yield).

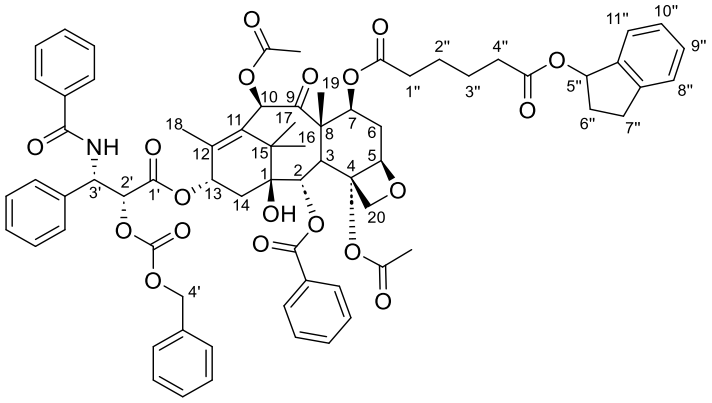

^{1}H NMR (400 MHz, $CDCl_3$) δ 8.12 (d, *J* = 7.3 Hz, 2H, ***o*-2-BzO**), 7.73 (d, *J* = 7.3 Hz, 2H, ***o*-3'-NHBz**), 7.64 – 7.56 (m, 1H ***p*-2-BzO**), 7.54 – 7.44 (m, 3H, ***m*-2-BzO**, ***p*-3'-NHBz**), 7.43 – 7.29 (m, 13H, ***m*-3'-NHBz**, ***o,m,p*-2'-CbzO**, ***o,m,p*-3'-Ph**, **8''-H**), 7.29 – 7.18 (m, 3H, **9''-H**, **10''-H**, **11''-H**), 6.95 (d, *J* = 9.3 Hz, 1H, **3'-NH**), 6.28 – 6.20 (m, 2H, **10-H**, **13-H**), 6.19 (dd, *J* = 7.0, 3.9 Hz, 1H, **5''-H**), 5.97 (dd, *J* = 9.3, 2.5 Hz, 1H, **3'-H**), 5.69 (d, *J* = 6.9 Hz, 1H, **2-H**), 5.58 (dd, *J* = 10.4, 7.1 Hz, 1H, **7-H**), 5.46 (d, *J* = 2.7 Hz, 1H, **2'-H**), 5.21 – 5.10 (m, 2H, **4'-H**), 4.95 (d, *J* = 8.9 Hz, 1H, **5-H**), 4.32 (d, *J* = 8.4 Hz, 1H, **20a-H**), 4.19 (d, *J* = 8.4 Hz, 1H, **20b-H**), 3.95 (d, *J* = 6.9 Hz, 1H, **3-H**), 3.15 – 3.03 (m, 1H, **7''a-H**), 2.86 (ddd, *J* = 16.0, 8.5, 5.1 Hz, 1H, **7''b-H**), 2.59 (ddd, *J* = 14.5, 9.4, 7.4 Hz, 1H, **6a-H**), 2.56 – 2.44 (m, 1H, **6''a-H**), 2.44 (s, 3H, **4-OAc**), 2.41 – 2.16 (m, 6H, **14-H**, **1''-H**, **4''-H**), 2.12 (s, 3H, **10-OAc**), 2.11 – 2.00 (m, 2H), 1.99 (s, 3H, **18-H**), 1.94 – 1.82 (m, 1H, **6b-H**), 1.80 (s, 3H, **19-H**), 1.71 – 1.57 (m, 4H, **2''-H**, **3''-H**), 1.20 (s, 3H, **17-H**), 1.16 (s, 3H, **16-H**).

^{13}C NMR (101 MHz, $CDCl_3$) δ 202.06, 172.34, 169.59, 168.79, 167.98, 166.99, 141.14, 136.78, 133.72, 133.60, 132.57, 132.00, 130.23, 129.11, 128.90, 128.86, 128.75, 128.71, 128.55, 128.50, 127.17, 126.72, 126.63, 125.53, 124.78, 84.03, 80.92, 78.75, 78.19, 76.81, 76.41, 75.24, 74.62, 72.04, 71.23, 70.82, 56.09, 52.84, 46.91, 43.31, 35.45, 34.23, 33.95, 33.65, 32.36, 30.21, 26.48, 24.39, 23.90, 22.66, 21.30, 20.70, 14.53, 10.90 (detectable peaks).

3.1.9 Synthesis of 7-*O*-(6''-*O*-(2''',3'''-dihydroinden-1'''-yl)hexanedioyl) paclitaxel (1a)

Pd/C (10% w/w, 3 mg) was added to a solution of **2a** (30 mg, 0.024 mmol) in dry MeOH (2 mL) under hydrogen atmosphere. The reaction mixture was stirred at RT, and it was monitored by TLC until completion (5h). The reaction mixture was then filtered on a celite pad, which was washed with MeOH (5 mL x2). The organic phase was dried with Na_2SO_4, and the solvent was evaporated under reduced pressure to afford pure compound **1a** in high yield (27.6 mg, 0.0238 mmol, 98% yield).

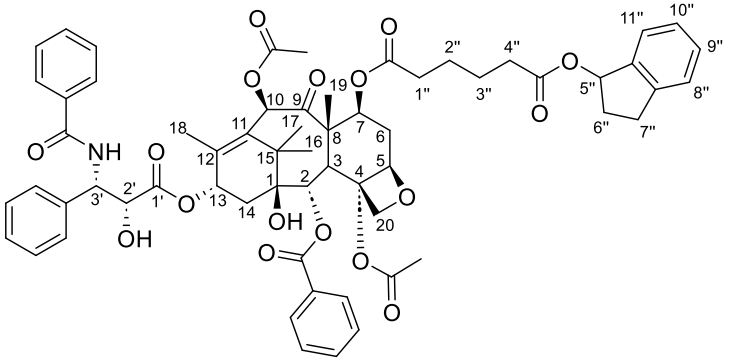

^{1}H NMR (400 MHz, $CDCl_3$) δ 8.13 (d, *J* = 7.3 Hz, 2H, ***o*-2-BzO**), 7.79 (d, *J* = 7.3 Hz, 2H, ***o*-3'-NHBz**), 7.68 – 7.59 (m, 1H, ***p*-2-BzO**), 7.57 – 7.33 (m, 11H, ***m*-2-BzO**, ***m*,*p*-3'-NHBz**, ***o*,*m*,*p*-3'-Ph**, **8''-H**), 7.33 – 7.19 (m, 4H, **3'-NH**, **9''-H**, **10''-H**, **11''-H**), 6.26 – 6.15 (m, 3H, **10-H**, **13-H**, **5''-H**), 5.87 – 5.80 (m, 1H, **3'-H**), 5.69 (d, *J* = 6.9 Hz, 1H, **2-H**), 5.57 (dd, *J* = 10.3, 7.3 Hz, 1H, **7-H**), 4.95 (d, *J* = 9.0 Hz, 1H, **5-H**), 4.82 (d, *J* = 2.4 Hz, 1H, **2'-H**), 4.33 (d, *J* = 8.4 Hz, 1H, **20a-H**), 4.21 (d, *J* = 8.4 Hz, 1H, **20b-H**), 3.93 (d, *J* = 6.7 Hz, 1H, **3-H**), 3.18 – 3.06 (m, 1H, **7''a-H**), 2.89 (ddd, *J* = 15.9, 8.5, 5.1 Hz, 1H, **7''b-H**), 2.65 – 2.45 (m, 2H, **6a-H**, **6''a-H**), 2.40 (s, 3H, **4-OAc**), 2.38 – 2.20 (m, 6H, **14-H**, **1''-H**, **4''-H**), 2.16 (s, 3H, **10-OAc**), 2.16 – 2.04 (m, 1H, **6''b-H**), 1.88 – 1.79 (m, 7H, **6b-H**, **18-H**, **19-H**), 1.75 – 1.57 (m, 4H, **2''-H**, **3''-H**), 1.21 (s, 3H, **17-H**), 1.18 (s, 3H, **16-H**).

^{13}C NMR (101 MHz, $CDCl_3$) δ 202.56, 174.14, 173.19, 173.13, 171.00, 169.57, 169.52, 167.69, 167.54, 157.68, 145.01, 141.80, 141.06, 138.81, 134.43, 133.61, 132.54, 130.84, 129.77, 129.59, 129.53, 129.39, 129.33, 128.89, 127.76, 127.37, 126.16, 125.45, 84.58, 81.72, 79.15, 78.86, 77.11, 75.92, 75.02, 74.04, 72.69, 71.88, 56.84, 55.63, 47.63, 43.90, 36.24, 34.86, 34.52, 34.31, 33.00, 30.86, 27.18, 25.03, 24.55, 23.22, 21.48, 21.38, 15.29, 11.48 (detectable peaks).

MS (ESI): m/z $[M + Na]^+$ calcd. for $C_{62}H_{67}NO_{17}Na$: 1120.43, found: 1120.75.

$[\alpha]_D^{25}$ ± SD: -290°± 6.

3.1.10 Synthesis of 2'-(trimethylsilyl)ethyl (*S*)-9-((7''-methoxy-1'',2'',3'',4''-tetrahydro naphthalen-2''-yl)amino)-9-oxononanoate (10b)

DMAP (29.6 mg, 0.243 mmol), EDC·HCl (99.8 mg, 0.52 mmol) and (*S*)-7-methoxy-2-aminotetralin (92.2 mg, 0.52 mmol) were added sequentially to a solution of **5b** (99.5 mg, 0.345 mmol) in dry CH_2Cl_2 and pyridine (15 and 1.5 mL respectively, 10:1 ratio), at RT and under nitrogen atmosphere. The reaction mixture was stirred for 4h. When TLC monitoring confirmed reaction completion, HCl 1M was added (35 mL). The aqueous phase was extracted with CH_2Cl_2 (3 x 15 mL), then the collected organic layer was dried over Na_2SO_4, and the solvent was evaporated under reduced pressure. The crude oil was purified by direct phase flash chromatography (silicagel, eluent mixture: 85:25 n-hexane/AcOEt + 1% formic acid) to afford pure compound **10b** in high yield (153.8 mg, 0.344 mmol, 98%).

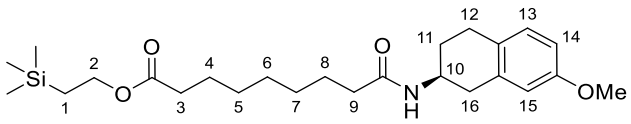

^{1}H NMR (400 MHz, $CDCl_3$) δ 6.96 (d, *J* = 8.4 Hz, 1H, **13-H**), 6.67 (dd, *J* = 8.4, 2.7 Hz, 1H, **14-H**), 6.54 (d, *J* = 2.7 Hz, 1H, **15-H**), 6.32 (d, *J* = 7.9 Hz, 1H, **10-NH**), 4.28 – 4.15 (m, 1H, **10-H**), 4.16 – 4.10 (m, 2H, **2-H**), 3.72 (s, 3H, **14-OMe**), 3.03 (dd, *J* = 16.4, 5.3 Hz, 1H, **16a-H**), 2.86 – 2.68 (m, 2H, **12-H**), 2.61 (dd, *J* = 16.4, 8.5 Hz, 1H, **16b-H**), 2.24 (t, *J* = 7.5 Hz, 2H, **3-H**), 2.20 – 2.12 (m, 2H, **9-H**), 2.03 – 1.93 (m, 1H, **11a-H**), 1.72 (dtd, *J* = 12.6, 9.1, 6.2 Hz, 1H, **11b-H**), 1.65 – 1.51 (m, 4H, **4-H**, **8-H**), 1.28 (br s, 6H, **5-H**, **6-H**, **5-H**), 1.01 – 0.92 (m, 2H, **1-H**), 0.03 (s, 9H, SiMe).

^{13}C NMR (101 MHz, $CDCl_3$) δ 174.59, 173.26, 135.89, 130.37, 128.22, 114.61, 113.20, 63.03, 55.89, 55.88, 45.54, 37.52, 36.63, 35.10, 29.69, 29.61, 29.55, 29.47, 26.83, 26.36, 25.53, 17.99, -1.43.

3.1.11 Synthesis of (*S*)-9-((7'-methoxy-1',2',3',4'-tetrahydronaphthalen-2'-yl)amino)-9-oxononanoic acid (9b)

TBAF 1M in THF (1.117 mL, 1.117 mmol) was added dropwise to a stirred solution of **10b** (125 mg, 0.279 mmol) in dry THF (11 mL), at -5°C and under nitrogen atmosphere. The reaction mixture was then warmed up to RT and stirred for 4h. When TLC monitoring confirmed reaction completion, saturated aqueous NH_4Cl (15 mL) was added. The aqueous phase was extracted with AcOEt (3 x 15 mL), then the collected organic layer was dried over Na_2SO_4, and the solvent was evaporated under reduced pressure. The crude oil was purified by Biotage® direct phase flash chromatography (eluent mixture: n-hexane/AcOEt + 1% formic acid from 90:10 to 20:80) to obtain pure **9b** (84.6 mg, 0.243 mmol, 87% yield).

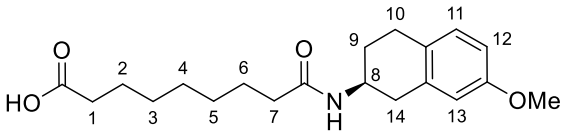

^{1}H NMR (400 MHz, $CDCl_3$) δ 7.01 (d, *J* = 8.4 Hz, 1H, **11-H**), 6.71 (dd, *J* = 8.4, 2.7 Hz, 1H, **12-H**), 6.59 (d, *J* = 2.7 Hz, 1H, **13-H**), 5.49 (d, *J* = 7.8 Hz, 1H, **8-NH**), 4.37 – 4.24 (m, 1H, **8-H**), 3.77 (s, 3H, **OMe**), 3.09 (dd, *J* = 16.4, 5.1 Hz, 1H, **14a-H**), 2.90 – 2.71 (m, 2H, **10-H**), 2.61 (dd, *J* = 16.4, 7.6 Hz, 1H, **14b-H**), 2.34 (t, *J* = 7.5 Hz, 2H, **1-H**), 2.20 – 2.11 (m, 2H, **7-H**), 2.07 – 1.95 (m, 1H, **9a-H**), 1.84 – 1.71 (m, 1H, **9b-H**), 1.68 – 1.56 (m, 4H, **2-H**, **6-H**), 1.32 (br s, 6H, **3-H**, **4-H**, **5-H**).

^{13}C NMR (101 MHz, $CDCl_3$) δ 179.37, 173.75, 158.41, 135.81, 130.40, 128.21, 114.63, 113.25, 55.92, 45.67, 37.48, 36.54, 34.67, 29.63, 29.55, 29.50, 29.39, 26.77, 26.37, 25.32.

3.1.12 Synthesis of 2'-*O*-Cbz-7-*O*-((*S*)-9''-(7'''-methoxy-1''',2''',3''',4'''-tetrahydronaphthalen-2'''-yl)amino)-9''-oxononanoyl) paclitaxel (2b)

A solution of compound **9b** (30.6 mg, 0.088 mmol) in CH_2Cl_2 (1.5 mL) was added to a stirred solution of 2'-*O*-Cbz-paclitaxel **7** (58 mg, 0.059 mmol) in CH_2Cl_2 (1.5 mL), at RT and under N_2 atmosphere. Subsequently, DCC (49 mg, 0.236 mmol) and DMAP (10 mg, 0.082 mmol) were added and the reaction mixture was stirred at RT for 26h. The mixture was diluted with CH_2Cl_2 (10 mL) and it was filtered on a plug of celite. The organic layer was washed with saturated aqueous NH_4Cl (2 x 10 mL) and brine (2 x 10 mL), then it was dried over Na_2SO_4, and the solvent was evaporated under reduced pressure. The resulting crude was purified by Biotage® direct phase flash chromatography (eluent mixture: n-hexane/AcOEt from 88:12 to 0:100) to obtain compound **2a** (67.5 mg, 0.051 mmol, 87% yield).

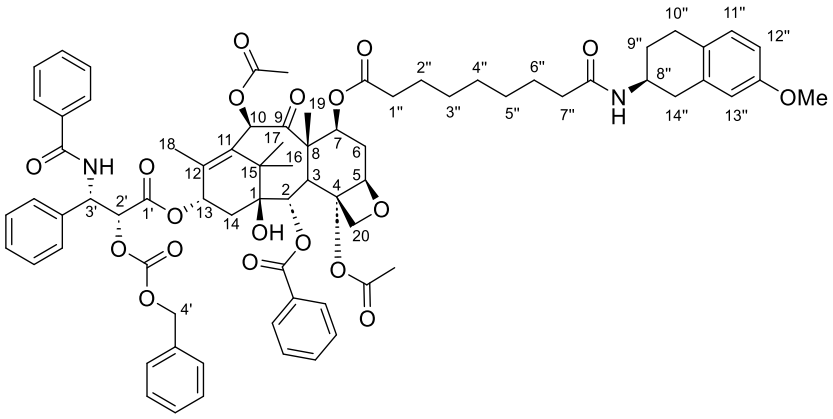

^{1}H NMR (400 MHz, $CDCl_3$) δ 8.12 (d, *J* = 7.2 Hz, 2H, ***o*-2-BzO**), 7.73 (d, *J* = 7.2 Hz, 2H, ***o*-3'-NHBz**), 7.64 – 7.56 (m, 1H, ***p*-2-BzO**), 7.54 – 7.44 (m, 3H, ***m*-2-BzO**, ***p*-3'-NHBz**), 7.42 – 7.28 (m, 12H, ***m*-3'-NHBz**, ***o,m,p*-2'-CbzO**, ***o,m,p*-3'-Ph**), 7.04 (d, *J* = 9.3 Hz, 1H, **3'-NH**), 6.99 (d, *J* = 8.6 Hz, 1H, **11''-H**), 6.70 (d, *J* = 8.5 Hz, 1H, **12''-H**), 6.58

(d, *J* = 2.9 Hz, 1H, **13''-H**), 6.31 – 6.20 (m, 2H, **10-H**, **13-H**), 5.97 (dd, *J* = 9.3, 2.9 Hz, 1H, **3'-H**), 5.68 (dd, *J* = 16.5, 7.5 Hz, 2H, **2-H**, **7-H**), 5.64 – 5.54 (m, 1H, **8''-NH**), 5.46 (d, *J* = 2.8 Hz, 1H, **2'-H**), 5.21 – 5.10 (m, 2H, **4'-H**), 4.95 (d, *J* = 9.3 Hz, 1H, **5-H**), 4.32 (d, *J* = 8.4 Hz, 1H, **20a-H**), 4.29 – 4.22 (m, 1H, **8'-H**), 4.19 (d, *J* = 8.4 Hz, 1H, **20b-H**), 3.95 (d, *J* = 6.9 Hz, 1H, **3-H**), 3.74 (s, 3H, **OMe**), 3.07 (dd, *J* = 16.4, 5.1 Hz, 1H, **14''a-H**), 2.86 – 2.72 (m, 2H, **10''-H**), 2.60 (dd, *J* = 16.6, 7.8 Hz, 2H, **14''b-H**, **6a-H**), 2.44 (s, 3H, **4-OAc**), 2.42 – 2.17 (m, 4H, **14a-H**, **1''-H**), 2.16 – 2.09 (m, 5H, **10-OAc**, **7''-H**), 2.00 (s, 3H, **18-H**), 1.95 – 1.84 (m, 2H, **6b-H, 9''a-H**), 1.81 (s, 3H, **19-H**), 1.77 – 1.64 (m, 1H, **9''b-H**), 1.63 – 1.52 (m, 4H, **2''-H**, **8''-H**), 1.34 – 1.23 (m, 6H, **3''-H**, **4''-H**, **5''-H**), 1.21 (s, 3H, **17-H**), 1.16 (s, 3H, **16-H**).

^{13}C NMR (101 MHz, DMSO-d_6) δ 201.59, 171.86, 171.58, 169.87, 169.12, 168.65, 166.33, 165.21, 157.21, 156.61, 153.87, 139.81, 137.01, 135.94, 134.92, 134.07, 133.60, 132.70, 131.57, 129.77, 129.59, 129.35, 128.80, 128.71, 128.55, 128.36, 128.29, 127.57, 127.41, 127.37, 113.50, 112.15, 82.81, 79.75, 77.15, 76.60, 74.50, 74.05, 71.01, 70.83, 69.81, 55.28, 54.91, 54.08, 47.51, 44.57, 42.91, 35.40, 35.33, 33.33, 31.69, 28.92, 28.49, 28.42, 26.61, 26.20, 25.31, 24.44, 22.51, 21.17, 20.47, 13.92, 10.59 (detectable peaks).

3.1.13 Synthesis of 7-*O*-((*S*)-9''-(7'''-methoxy-1''',2''',3''',4'''-tetrahydronaphthalen-2'''-yl)amino) -9''-oxononanoyl) paclitaxel (1b)

Pd/C (10% w/w, 4.6 mg) was added to a solution of **2b** (57 mg, 0.043 mmol) in dry MeOH (4.25 mL) under hydrogen atmosphere. The reaction mixture was stirred at RT, and it was monitored by TLC until completion (4h). The reaction mixture was then filtered on a celite pad, which was washed with MeOH (5 mL x2). The organic phase was dried with Na_2SO_4, and the solvent was evaporated under reduced pressure. The crude product was purified by Biotage® direct phase flash chromatography (eluent mixture: CH_2Cl_2/MeOH from 100:0 to 96:4) to afford pure compound **1b** (27.6 mg, 0.0238 mmol, 45% yield).

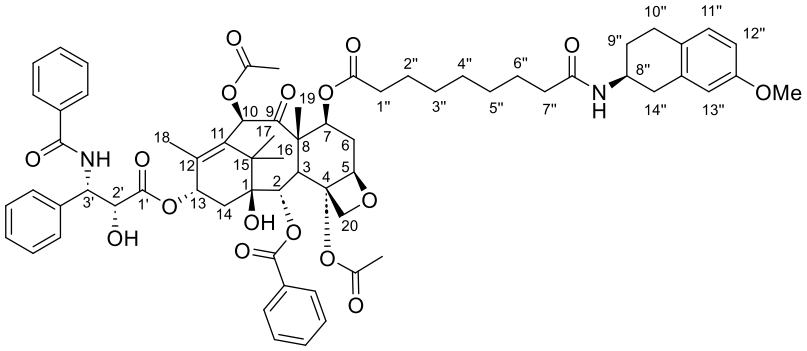

^{1}H NMR (400 MHz, $CDCl_3$) δ 8.12 (d, *J* = 7.1 Hz, 2H, ***o*-2-BzO**), 7.78 (d, *J* = 7.1 Hz, 2H, ***o*-3'-NHBz**), 7.66 – 7.58 (m, 1H, ***p*-2-BzO**), 7.55 – 7.31 (m, 10H, ***m*-2-BzO**, ***m,p*-3'-NHBz**, ***o,m,p*-3'-Ph**), 7.24 (d, *J* = 9.0 Hz, 1H, **3'-NH**), 7.01 (d, *J* = 8.4 Hz, 1H, **11''-H**), 6.71 (dd, *J* = 8.4, 2.9 Hz, 1H, **12''-H**), 6.60 (d, *J* = 2.8 Hz, 1H, **13''-H**), 6.24 (s, 1H,

10-H), 6.17 (t, *J* = 8.2 Hz, 1H, **13-H**), 5.81 (dd, *J* = 9.0, 2.7 Hz, 1H, **3'-H**), 5.67 (d, *J* = 6.9 Hz, 1H, **2-H**), 5.55 (dd, *J* = 10.6, 7.2 Hz, 2H, **7-H**, **8''-NH**), 4.94 (d, *J* = 7.6 Hz, 1H, **5-H**), 4.79 (d, *J* = 2.6 Hz, 1H, **2'-H**), 4.35 – 4.23 (m, 2H, **20a-H**, **8''-H**), 4.19 (d, *J* = 8.5 Hz, 1H, **20b-H**), 3.92 (d, *J* = 6.9 Hz, 1H, **3-H**), 3.77 (d, *J* = 2.6 Hz, 3H, **OMe**), 3.09 (dd, *J* = 16.5, 5.3 Hz, 1H, **14''a-H**), 2.89 – 2.73 (m, 2H, **10''-H**), 2.66 – 2.53 (m, 2H, **14''b-H**, **6a-H**), 2.38 (s, 3H, **4-OAc**), 2.36 – 2.29 (m, 3H, **14a-H**, **1''-H**), 2.29 – 2.17 (m, 1H, **14b-H**), 2.15 (d, *J* = 6.9 Hz, 5H, **10-OAc**, **7''-Hp**), 2.02 – 1.85 (m, 1H, **9''a-H**), 1.82 (d, *J* = 8.0 Hz, 7H, **18-H**, **19-H**, **6b-H**), 1.80 – 1.65 (m, 1H, **9''b-H**), 1.59 (d, *J* = 13.3 Hz, 4H, **2''-H**, **8''-H**), 1.34 – 1.22 (m, 6H, **3''-H**, **4''-H**, **5''-H**), 1.20 (s, 3H, **17-H**), 1.17 (s, 3H, **16-H**).

^{13}C NMR (101 MHz, $CDCl_3$) δ 202.08, 173.04, 172.78, 172.53, 170.43, 168.96, 167.09, 167.02, 157.85, 140.52, 138.28, 135.37, 133.90, 133.09, 132.01, 130.30, 129.87, 129.23, 129.06, 128.86, 128.80, 128.37, 127.72, 127.22, 114.07, 112.71, 84.06, 81.17, 78.62, 76.59, 75.40, 74.47, 73.47, 72.15, 71.25, 56.34, 55.39, 55.08, 47.11, 45.01, 43.37, 37.07, 36.10, 35.71, 34.17, 33.99, 33.61, 29.16, 29.01, 28.93, 26.66, 25.71, 25.03, 24.51, 22.67, 20.92, 20.88, 14.76, 10.96.

MS (ESI): m/z $[M + Na]^+$ calcd. for $C_{67}H_{78}N_2O_{17}Na$: 1205.52, found: 1205.44.

$[\alpha]_D^{25}$ ± SD: -235°± 5.

3.2 Biochemistry and structural biology

3.2.1 Buffers

- NaPi: 10 mM NaH_2PO_4, 10 mM Na_2HPO_4, pH 7.0.
- PMS: NaPi buffer, 0.5 mM $MgCl_2$, 0.24 M sucrose, pH 7.0.
- PMG: NaPi buffer, 0.5 mM $MgCl_2$, 0.1 mM GTP, pH 7.0.
- 0.4 M KCl PMG: PMG buffer, 0.4 M KCl.
- 0.8 M KCl PMG: PMG buffer, 0.8 M KCl.
- Cryo-PMG-trehalose: PMG buffer, 0.25 M trehalose.
- NaPi-SDS: NaPi buffer, 1% sodium dodecyl sulfate, pH 7.0.
- PEDTA: NaPi buffer, 1 mM EDTA, 0.1 mM GTP, pH 7.0.
- GAB: NaPi buffer, 3.4 M glycerol, 1 mM EGTA, 0.1 mM GTP, pH 6.7.
- 0.05-GAB: NaPi buffer, 3.4 M glycerol, 1 mM EGTA, 0.05 mM GTP, pH 6.7.
- FD: 80 mM PIPES-K, 1 mM EGTA, 0.2 M Tris, 1 mM DTT, 3 mM $MgCl_2$, pH 6.8.
- FD-MC: FD buffer, 2% methylcellulose.
- PBS: 8.1 mM Na_2HPO_4, 1.5 mM NaH_2PO_4, 137 mM NaCl, 2.7 mM KCl, pH 7.2.
- MTT solution: PBS buffer, 2.5 mg/mL MTT.
- MTT solubilizer: 45% DMF, 10% SDS, pH 5.5.
- PEM: 100 mM PIPES-K, 1 mM EGTA, 2 mM $MgCl_2$, pH 6.8.
- Fixation buffer: PEM buffer, 3.7% formaldehyde, 1% DMSO.
- PEMP: PEM buffer, 4% PEG8000.
- PEMT: PEM buffer, 0.5% Triton X-100.

3.2.2 Chemicals and Proteins

Chemicals were purchased from general suppliers (Merck, TAAB, Jena Bioscience Gmb) and used without further purification. Paclitaxel was purchased from Alfa Aesar (Thermo Scientific Chemicals), flutax-2 and hexaflutax were synthesized by Dr. Fang at the Institute of Materia Medica (Beijing, China). Ligands were diluted in 99.8% DMSO-d^6 (Merck) to a final concentration of 50 mM and stored at −80°C.

Purification of calf brain tubulin was performed using a previously described protocol[130] and the resulting protein was lyophilized for storage. The entire process was carried out in a cold room and all centrifugations were performed at 4°C to ensure protein stability and improve the yield of the purification process. Calf brains were kindly provided by Ganadería Fernando Díaz.

3.2.3 Calf brain tubulin purification

Six to eight freshly slaughtered calf brains were processed to remove meninges and blood clots before being chopped. After the addition of PMS buffer up to a volume of 2.7 L, the chopped brains were liquefied in an Osterizer® 869-16G electric blender (385W) using pulses of 45 sec interrupted by 1 min cool-off intervals until homogenization. The homogenate was centrifuged to separate the cellular membranes at 7500 rpm for 55 min in a Beckman Coulter™ JLA-8.1000 rotor. Then, a two-step salting out procedure was used to remove most of the non-target proteins from the clarified supernatant. First, ammonium sulfate was added under constant stirring up to 32% saturation, followed by centrifugation at 7500 rpm for 45 min using a Beckman Coulter™ JLA-8.1000 rotor. Then, the pellet was discarded and ammonium sulfate was added to the supernatant up to 43% saturation. The solution was centrifuged again at 7500 rpm for 45 min in a Beckman Coulter™ JLA-8.1000 rotor, but this time the supernatant was discarded. The tubulin-containing pellet was dissolved in PMG buffer and mixed with 15 g of DEAE-Sephadex A50 resin (General Electric Healthcare) to perform batch anion exchange chromatography. Before adding it to the dissolved pellet, the resin was pre-hydrated in 1.5 L of NaPi buffer and equilibrated in PMG buffer. A first elution step with 0.4 M KCl PMG was carried out to eliminate contaminating proteins, then 0.8 M KCl PMG was used for tubulin elution. The resulting tubulin solution was concentrated by precipitation with ammonium sulfate (43% saturation) and centrifugation at 13500 rpm for 60 min using a Thermo Scientific Fiberlite™ F14-6x250y rotor. The pelleted protein was dissolved in PMG buffer and desalted by size exclusion chromatography using a 400 mL Sephadex G25 column (General Electric Healthcare). Fractions of 3.5 mL were collected, and assembly-competent tubulin was selected by its ability to polymerize in the presence of 40 mM $MgCl_2$. These fractions were pooled and centrifuged at 12000 rpm for 5 min in a Thermo Scientific Fiberlite™ F21-8x50y rotor. The pellet was resuspended in Cryo-PMG-Trehalose and the excess of $MgCl_2$ was removed by a 16h dialysis in the same buffer within a Slyde-a-Lyzer® dialysis cassette (Thermo-Scientific) with a MWCO of 10 kDa. The solution was then centrifuged again to remove aggregates in a Thermo Scientific Fiberlite™ F21-8x50y rotor at 12000 rpm for 20 min. Finally, tubulin's concentration in the supernatant was determined by absorption spectrometry in an ultraviolet-visible spectrophotometer (see section 3.2.4), the protein was aliquoted and stored at -20°C after lyophilization. The degree of purity of the protein was verified post-lyophilization via polyacrylamide gel electrophoresis (PAGE).

3.2.4 Ultraviolet-visible spectroscopy

The absorbance measurements in the ultraviolet-visible (UV-Vis) spectrum were carried out at room temperature in a double-beam Evolution 201 spectrophotometer (Thermo Scientific) using black quartz cuvettes of 1 cm optical path. Tubulin concentration was determined through duplicate measurements of 1/200 dilutions in NaPi-SDS buffer. The concentration was determined as a function of the Beer-Lambert law,

employing a molar extinction coefficient (ε) of tubulin of 109000 M^{-1} cm^{-1} at λ = 276 nm[131]. In cases in which the absorbance contribution from the GTP/GDP in solution was non-negligible (nucleotide concentration > 0.1 mM) the total absorbance at 276 nm was corrected for the contribution of the nucleotide by applying the following system (T_2 = dimeric tubulin, Nt = nucleotide):

$$\begin{cases} \sum Abs_{276} = Abs_{276}(T_2) + 8100 \cdot Abs_{276}(Nt) \\ \sum Abs_{254} = 0.6 \cdot Abs_{276}(T_2) + 13100 \cdot Abs_{276}(Nt) \end{cases} \quad [2]$$

The absorbance spectra of chemical compounds were determined in the range 240 – 340 nm employing 20 µM solutions of the compounds in spectroscopy-grade ethanol. For the calculation of their extinction coefficient the absorption relative maxima at λ > 260 nm were considered, to minimize the error derived from the superposition of the signal of the ligands with that of the solvent in which they are dissolved (DMSO). This cutoff was chosen due to the minimal absorption of DMSO above 260 nm.

3.2.5 Solubility tests

To evaluate the solubility of compounds **1a** and **1b** in aqueous medium, these were dissolved at room temperature in NaPi buffer to the desired concentration (5-10-20-50 µM). The UV-Vis spectrum of the solutions between 240 nm and 340 nm was immediately recorded (see section 3.2.4). The solutions were then incubated for 20 min at 25°C and subsequently ultracentrifuged at 50000 rpm in a Beckman Coulter TLA-120.2 rotor, employing brand-new polycarbonate tubes. Then, the UV-Vis spectrum of the supernatants was collected in the same experimental conditions. The solubility at each concentration was evaluated by comparing the former with the latter spectrum and by measuring the decrease in the signal intensity.

3.2.6 Tubulin preparation for biochemical assays

Lyophilized calf brain tubulin was equilibrated on ice for approximately 5 min, after which it was dissolved in ice-cold working buffer to a final concentration of 15 mg/mL. The mixture was incubated for an additional 10 min on ice, with occasional pipetting to aid protein dissolution. Special care was taken to prevent air injection and bubble formation during pipetting. The solution was then ultracentrifuged at 50000 rpm in a Beckman Coulter TLA-120.2 rotor to remove any aggregates. The concentration of tubulin was quantified spectrophotometrically as described in section 1.2.2 and adjusted to the desired concentration. Then, the concentration of $MgCl_2$ and GTP were adjusted to 6 mM and 1 mM, respectively, and the resulting tubulin solution was kept on ice until used.

3.2.7 Turbidimetric polymerization assays

A 25 µM tubulin solution in PEDTA buffer was prepared as described in section 3.2.6 and dispended in a clear Falcon® 96-well microplate (polystyrene, flat bottom). Then, the control ligands (paclitaxel, flutax-2) and the problem ligands (**1a**, **1b**) were added to the wells to a final concentration of 27.5 µM (10% stoichiometric excess). Control reactions were performed employing tubulin with DMSO (vehicle), at the highest volume used in the other experiments. Assembly time courses at 37°C were recorded in an automated multiwell plate reader (Appliskan® ThermoFisher®) by measuring the absorbance at λ = 355 nm (filter bandwidth 40 nm) for at least 150 measurements with a kinetic interval of 30 sec. Duplicate experimental curves were obtained for each condition. Each curve was normalized by subtraction of its minimum absorbance value, then the two duplicate curves were averaged for representation.

3.2.8 Preparation of cross-linked microtubules

The preparation of stabilized cross-linked microtubules was performed by modifying a previously described protocol[92]. A 15 mg/mL tubulin solution in GAB buffer was prepared as described in section 3.2.6, without any further dilution. Microtubules were assembled by incubating tubulin at 37°C for 40 min, then, 0.2% glutaraldehyde was added (to a final concentration of approximately 20 mM), and the solution was incubated at 37°C for an additional 10 min. Glutaraldehyde behaves as a cross-linking agent reacting with the primary amine groups of lysine residues through a surprisingly large number of possible reactions[132]. Due to the rapid nature of the reaction, precise control of the incubation time is crucial to ensure the optimal degree of cross-linking within microtubules. The excess glutaraldehyde was then quenched by dropwise addition of 60 mM $NaBH_4$ on ice. The solution was left for 10 min on ice to allow dissipation of the foam generated, and it was subsequently degassed by bursts of light centrifugation on a bench centrifuge at RT. Finally, the microtubule solution was dialyzed overnight against GAB buffer, 0.05 mM GTP, 6 mM $MgCl_2$, and the resulting sample was drop-frozen and stored in liquid nitrogen at -195.8°C.

3.2.9 Determination of the concentration of pharmacologically active taxane binding sites

One or two drops of cross-linked microtubules were thawed, and the concentration of total protein was determined spectrophotometrically from the absorbance at 276 nm corrected for the contribution of the nucleotide, as reported in section 3.2.4. Then, the concentration of the solution was adjusted to 2 µM using the dialysis buffer. Three replicates of 200 µL were incubated with 5 µM flutax-2 both with and without 100 µM docetaxel. The samples were incubated for 20 min in dark and centrifuged for 20 min at 50000 rpm in a Beckman Coulter TLA-120.2 rotor. The pelleted microtubules were then dissolved in 200 µL of NaPi-SDS and

diluted 1:10 in the same buffer to perform fluorescence spectrometry of flutax-2 in an ISA FluoroMax-2 spectrofluorometer (Horiba – Yobin Yvon) at λ_{exc} = 492 nm and λ_{em} = 523 nm. These measurements allowed the determination of the amount of fluorescent probe bound to the cross-linked microtubules in each condition. The concentration of flutax-2 in the sample with docetaxel corresponds to the concentration of unspecific binding sites in the sample, while the concentration of fluorescent probe in the sample without docetaxel corresponds to the concentration of total binding sites. The difference between the two reveals the concentration of active binding sites in 2 µM microtubules. To calculate the concentration of active sites in the stock solution of cross-linked microtubules it is sufficient to apply the following formula:

$$c_{active\ sites}(stock) = c(stock) \cdot \frac{c_{total\ sites}(2\ \mu M) - c_{unspecific\ sites}(2\ \mu M)}{c_{total\ sites}(2\ \mu M)} \quad [3]$$

3.2.10 Equilibrium binding constant determination of taxanes

The equilibrium binding constants of taxanes **1a** and **1b** were determined by the displacement of flutax-2 from its binding site by each of these compounds, which was measured by monitoring its *anisotropy* or *fluorescence polarization* variation, as previously described[133]. In general, the anisotropy r of a fluorophore describes the extent of polarization of its emission, which can be defined as the ratio of the intensity of the polarized component ($I_z - I_x$) to the total intensity of light emitted ($I_z + I_x + I_y$). When the excitation is polarized along the z-axis, the emission from the fluorophore is symmetrical around the z-axis (Figure 3-1). Hence, statistically $I_x = I_y$. As $I_z = I_{\parallel}$ and $I_x = I_{\perp}$, we have:

$$r = \frac{I_z - I_y}{I_z + I_x + I_y} = \frac{I_{\parallel} - I_{\perp}}{I_{\parallel} + 2I_{\perp}} \quad [4]$$

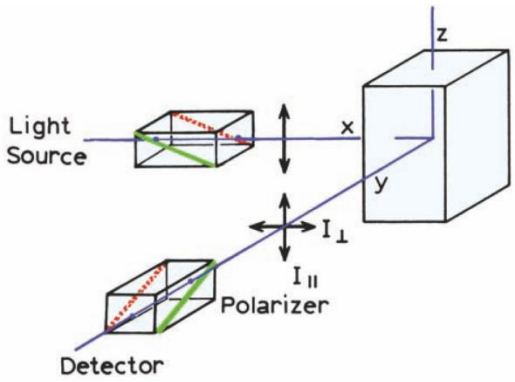

Figure 3-1. Schematic diagram for measurement of fluorescent anisotropy and polarization.

It is possible to understand why the polarized component of the emitted light is equivalent to the difference $I_{\parallel} - I_{\perp}$ by regarding it as the excess intensity on the plane parallel to the excitation. In other words, when the sample emits completely unpolarized light, it emits light on the parallel plane with an intensity equal to the one emitted on the perpendicular plane (this means $I_{\parallel} = I_{\perp}$ and therefore, $r = 0$ as expected). An excess of emission on the parallel plane must be caused by light specifically polarized on that plane.

An alternative physical quantity to anisotropy is the fluorescence polarization P of the system, which differs from it only by a factor of 2 and it's defined by the equation:

$$P = \frac{I_{\parallel} - I_{\perp}}{I_{\parallel} + I_{\perp}} \qquad [5]$$

Both r and P are dimensionless and independent from the total intensity of the sample. They contain the same information; hence they are used interchangeably in experimental settings.

An increase in the intensity of polarized light emitted by the fluorophore is usually observed upon binding to a macromolecule, due to the reduction of rotational freedom of the emitter (Figure 3-2). Consequently, an increase in r and P is also observed.

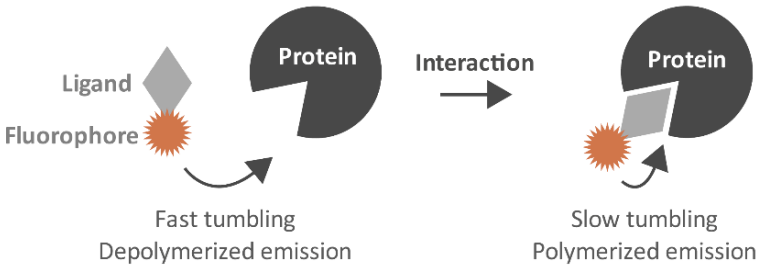

Figure 3-2. Schematic representation of the fluorescence anisotropy variation upon binding of a fluorophore to a macromolecule.

Nowadays, high-end fluorescence polarization plate readers are often preferred over traditional fluorometers, as they offer robust results with minimal variability and larger assay windows, while simplifying the experimental design and allowing for high-throughput screening. These instruments employ an L-format geometry for emission detection, meaning that the emitted light is observed in a single emission channel. However, the intensities measured by the instrument are not the desired parallel and perpendicular emitted intensities, but rather intensities that are proportional to the transmission efficiencies of the detector for each polarized component. These experimentally measured intensities are indicated with two subscripts (V = vertical, H = horizontal), which indicate the orientation of the excitation and emission polarizers, respectively. For example, I_{HV} corresponds to horizontally polarized excitation and vertically polarized emission. It's important to consider that the detection system's sensitivities usually differ for parallel and

perpendicular polarized light. To compensate for the difference in response of the optical components, a correction factor denoted with the letter "G" (for grating factor) must be introduced, defined as:

$$G = \frac{S_V}{S_H} = \frac{I_{HV}}{I_{HH}} \quad [6]$$

where S_V and S_H are the sensitivities of the emission channel for the vertically and horizontally polarized components. The demonstration of this relationship can be found in chapter 10.4.1 of Principles of Fluorescence Spectroscopy by J. R. Lakowicz[134]. Therefore, the experimental measurement of fluorescence polarization can be derived from equations [5] and [6], and it is equal to:

$$P_{\exp} = \frac{I_{VV} - GI_{VH}}{I_{VV} + GI_{VH}} \quad [7]$$

A Spark® Tecan plate reader in fluorescence polarization mode was used to perform the measurements. During the microplate assay, the G factor was calculated as a mean over several wells in different conditions (at least one well containing the fluorophore used in the assay as reference and at least one well for blanking containing the assay solution without the fluorophore). The plate reader reported the results in "milli-polarization" units ($mP = 1000 \cdot P$).

Glutaraldehyde-stabilized cross-linked microtubules prepared as described in section 3.2.8 were employed in the assay. First, samples containing 50 nM taxane active sites (from cross-linked microtubules), 50 nM flutax-2, and increasing concentrations of competitor ligands (from 12.5 nM to 25 µM) were prepared in 0.05-GAB buffer and dispensed in a black Falcon® 96-well microplate (polystyrene, flat bottom). The competitor ligands tested were taxanes **1a**, **1b,** and docetaxel (used as a control). Three samples containing 50 nM taxane binding sites were employed as blanks, and three samples containing 50 nM solution of flutax-2 in 0.05-GAB were employed as reference standards. The microplate was mixed in the plate reader for 10 min by shaking at 250 rpm, incubated at the desired temperature for an additional 20 min, and then the fluorescence polarization values were measured at λ_{em}= 535 nm (filter bandwidth = 25 nm), with readings of 40 µsec and λ_{ex}= 485 nm (filter bandwidth= 20 nm). The measurements were repeated at three different temperatures (26°C – 35°C – 42°C).

The first step to calculate the binding affinity of a competitor ligand to the taxane site requires the calculation of the molar saturation fraction X_b of the reference probe for each competitor concentration used, *i.e.* the ratio between the concentration of bound probe and the total probe concentration in solution. At increasing competitor ligand concentrations, X_b decreases and its value can be determined from the fluorescence

polarization values measured, P. In addition, the fluorescence polarization values of the reference probe when completely displaced (P_0) and in the absence of a competitor ligand (P_{sat}) are needed. Having these experimental measurements, the value of X_b can be determined using equation [8] as a fraction of the maximum X_{sat} (molar saturation fraction of the reference probe in the absence of competitor ligands).

$$X_b = \frac{P - P_0}{P_{sat} - P_0} \cdot X_{sat} \qquad [8]$$

In turn, X_{sat} can be calculated as demonstrated in Figure 3-3 from the known parameters of the system: the concentration of taxane binding sites (50 nM), the total concentration of reference probe (50 nM), and the binding constant of the reference probe at different temperatures (Table 3-1).

Table 3-1. Association constants and molar saturation fractions of flutax-2 binding to microtubules.

	26°C		**35°C**		**42°C**	
	$K_R\ [M^{-1}]$	X_{sat}	$K_R\ [M^{-1}]$	X_{sat}	$K_R\ [M^{-1}]$	X_{sat}
flutax-2	6.5 x10^7	0.578	3.0 x10^7	0.451	1.8 x10^7	0.364

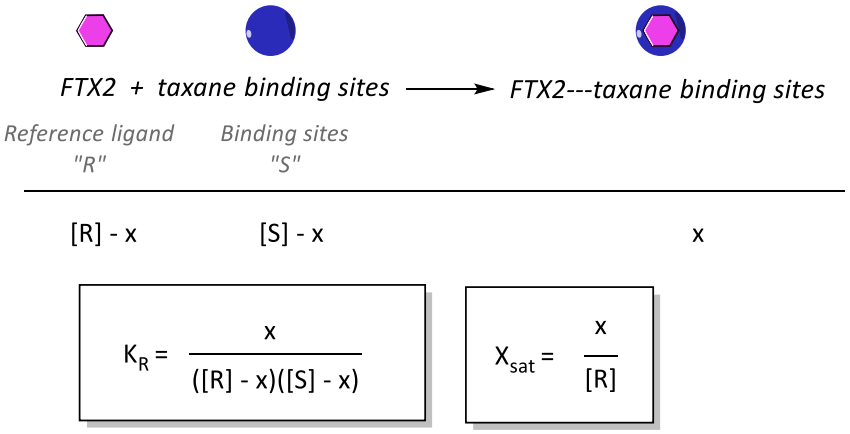

Figure 3-3. Determination of the molar saturation fraction of flutax-2 (FTX-2).

The saturation fractional values of flutax-2 at different competitor ligand concentrations were fitted by least-squares to the equilibrium binding constant K_C of the competitor ligand assuming unitary stoichiometry, using an *ad hoc* computer program created by Dr. Fernando Díaz (Equigra v5, unpublished). The program solves the following system of mass equations:

$$K_C = \frac{[C]_b}{[S]_f \cdot [C]_f} \quad [9]$$

$$K_R = \frac{[R]_b}{[S]_f \cdot [R]_f} \quad [10]$$

$$[R]_f = [R]_t - [R]_b \quad [11]$$

$$[C]_f = [C]_t - [C]_b \quad [12]$$

$$[S]_f = [S]_t - [R]_b - [C]_b \quad [13]$$

where C, R, S are the competitor ligand, the reference ligand (flutax-2), and the taxane binding sites, respectively. The subscripts f, b, t refer to the concentration of free form, of bound form or the total concentration.

The final equilibrium binding constants of the competitor ligands (renamed K_b) reported in this thesis are an average value over three independent experiments with duplicates in each one. Equilibrium dissociation constants (K_d) were calculated as the reciprocal of K_b values. From the binding constant value, it was also possible to calculate the apparent standard free energy of association at a given temperature as:

$$\Delta G^0_{app} = -RTlnK_b \quad [14]$$

where R is the ideal gas constant (8.314 J K^{-1} mol^{-1}) and T is the absolute temperature. Moreover, once the equilibrium binding constants were measured at different temperatures, it was possible to calculate the enthalpic and entropic contributions to the binding reaction using the GraphPad Prism® 8 software. The apparent standard enthalpy of the binding reaction was calculated from the representation of lnK_b vs. $1/T$ (Van't Hoff representation), where the slope of the linear regression multiplied by $-R$ was equal to ΔH^0_{app}. Finally, the apparent standard entropy of binding ΔS^0_{app} was calculated from the slope of the linear regression of ΔG^0_{app} vs. $-T$. Applying the theory of error propagation, the standard deviation of ΔG^0_{app} and ΔH^0_{app} were calculated as the square root of the sum of the squares of the product of the partial derivatives of each variable by the standard deviation of that variable:

$$\sigma_{\Delta G^0_{app}} = \left|\frac{\partial G}{\partial K_b} \cdot \sigma_{K_b}\right| = \frac{RT}{K_b} \cdot \sigma_{K_b} \quad [15]$$

$$\sigma_{\Delta H^0_{app}} = \left|-R \cdot \sigma_{slope}\right| \quad [16]$$

The standard deviation on ΔS^0_{app} was simply obtained from the standard error on the slope of the linear regression.

3.2.11 Sample preparation for X-ray fiber diffraction assays

Lyophilized calf brain tubulin was equilibrated on ice for approximately 5 min, after which it was dissolved in ice-cold FD buffer to achieve a concentration of 10 mg/mL (approximately 100 µM). The mixture was incubated for an additional 10 min on ice, with occasional pipetting to aid protein dissolution. Special care was taken to prevent air injection and bubble formation during pipetting. The tubulin solution was then centrifuged at 4°C for 10 min at 13500 rpm in an Eppendorf® 5416 R microcentrifuge through a Spin-X® 0.45 µM centrifuge filters in cellulose acetate (Costar®) to remove any aggregates. The mixture was supplemented with either 2 mM GTP or 0.5 mM GMPCPP and mixed carefully. Then, the tubulin solution was aliquoted in 70 µL volumes and the tested ligands were added to a final concentration of 200 µM. The samples were incubated for 20 – 30 min at 37°C to induce polymerization, then a 1:1 volume ratio of FD-MC buffer was added and carefully mixed. Due to the ½ dilution, the final concentrations in the samples were 50 µM tubulin, 1 mM GTP or 0.25 mM GMPCPP, 100 µM problem compounds, and 1% methylcellulose. Before their loading in the shear-flow machine, the samples were briefly spun down in a bench centrifuge to remove any bubbles that could contribute to the X-ray radiation scattering.

3.2.12 X-ray fiber diffraction image acquisition

X-ray fiber diffraction patterns were acquired at BL11-NCD-SWEET beamline (ALBA synchrotron, Cerdanyola del Vallès, Spain). The samples, prepared as described in section 3.2.11, were transferred to a custom-built sample holder designed to induce shear-flow alignment of the microtubules. The sample holder consisted of a copper cylinder equipped with a 0.2 mm-thick mica window on one base and a copper plate with a quartz window, placed face to face and spaced by one or more ring slips of varying thickness to adjust the chamber volume (Figure 3-4). A chamber gap of 0.72 mm was employed in these experiments. The entire system was rotated using a direct-drive AC motor (HM2225 F12H + MD501 driver, Technohands®), which was coupled to both the copper plate and the cylinder via neodymium magnets. Temperature control was achieved through an in-house system employing a temperature probe on the copper plate, connected to an E5EC-RX4DMB temperature controller (Omron®) looped to a thermocouple heater. The sample holder was aligned with the optical path of the synchrotron X-ray beam, allowing image acquisition during the rotation of the sample.

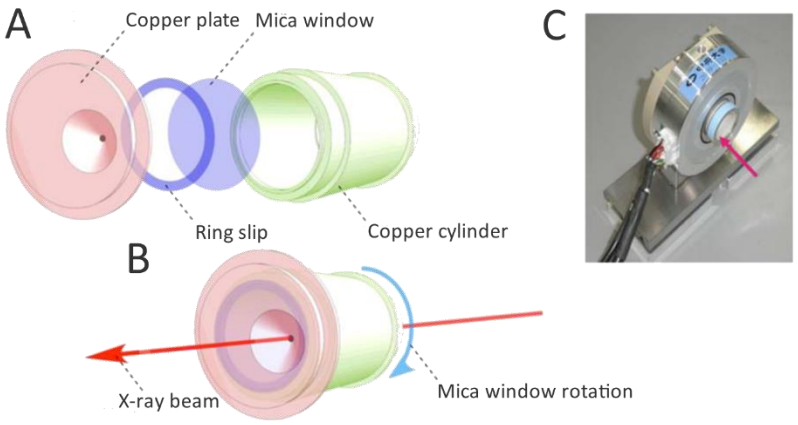

Figure 3-4. Schematic illustration of the shear-flow apparatus. The rotation chamber components (panel A), which generate shear flow upon assembly (panel B), enable the incident X-ray beam (depicted by red arrows) to pass through the copper plate's window. Panel C shows the shear flow device mounted on a stand and connected to the direct-drive AC motor. Image modified from [135].

A volume of sample equal to 110-120 µL was placed in the space between the mica window and the copper plate, then the entire system was rotated at 10 rps to achieve microtubule alignment. The temperature was left equilibrating at 37°C, after which 4 diffraction images per sample were collected (a single diffraction image was obtained per beam exposure, with an exposure time of 150s). The number of frames collected was fixed to 4 as higher numbers often resulted in sample radiation damage. For each tested condition, 8 – 12 diffraction images were acquired from 2 – 3 independent experiments. Background images were obtained in the same conditions, using FD buffer with 1% methylcellulose. The incident beam, delivered by an IVU21 in-vacuum undulator and collimated with several optics (including a channel cut Si (111) monochromator, beryllium focusing lenses, and several vertical and horizontal slits) was fixed to an energy of 15 keV. The diffracted X-rays were collected with the hybrid-pixel photon counting detector Pilatus3 S 1M (Dectris®, pixel size: 172 µm x 172 µm, detector active area (W x H): 168.7 mm x 179.4 mm, pixel array (W x H): 981 x 1043, readout time: 2.03 msec, maximum frame rate: 25 Hz, energy range: 5 – 36 keV).

3.2.13 X-ray fiber diffraction data analysis and interpretation

Prior to conducting image analysis, spatial calibration is essential to determine the relative positions of the three components of the system, namely the X-ray beam, the sample, and the detector. This ensures an accurate measurement of the sample-to-detector distance z, of the coordinates of the center of the beam, and of the detector's rotations, which are necessary to assign the reciprocal-space distance q to the acquired images. Calibration is performed using a calibrant of known lattice constant d and employing radiation of known wavelength λ. For the experiments reported in this thesis, silver behenate powder (d = 5.8376 nm) was used as the calibrant and an incident wavelength of 0.08265 nm was employed. Silver behenate's elastic scattering creates a ring-shaped diffraction pattern at regular positions p from the beam center[136]. The value of z can be calculated using the following equation:

$$z = \frac{p \cdot d}{l \cdot \lambda} \qquad [17]$$

where l is the diffraction order. By fitting the positions p to a straight line, z can be inferred by its slope. Moreover, the diffraction signals of silver behenate are used to perform the q-calibration, that is, to assign its corresponding scattering vector q to the distance p. The scattering vector associated with each layer line is always the same and depends on the value of d according to the simple relationship:

$$q = \frac{2\pi}{d} \qquad [18]$$

Images from a given experimental condition were batch averaged and background subtracted using FiDAT, an unpublished computer software for fiber diffraction image analysis developed by Óscar Fernández Blanco (Centr. de Investig. Biol. Margarita Salas, CSIC, Madrid, Spain) and Maxim Shevlev (UMR 7140 CNRS, Univ. de Strasbourg, Strasbourg, France). For representation purpose only, a logarithmic function was applied to the fiber diffraction images shown in this thesis work to enhance the visualization of the layer lines, using the Fiji® package software. The mathematical operation applied to each pixel p of the batch-averaged and background subtracted images is as follows:

$$f(p) = \frac{\ln(p) \cdot (max - min)}{\ln\,(max - min)} \qquad [19]$$

where max and min are the image maximum and minimum intensity values, respectively. FiDAT software was also used to calculate the standard deviation images for the determination of the standard errors of microtubule lateral metrics (detailed below). Employing the calibration spatial file, FiDAT program performed an azimuthal integration of the diffraction intensities of the acquired image over the scattering vector q and the radial angle θ. This operation resulted in a caked image with q values on the x-axis [nm^{-1}] and radial angle values on the y-axis [degrees]. Then, a secondary integration over q was performed either of the intensities that lay on the meridian (θ = 90°, red dotted line in Figure 3-5) or of the intensities that lay on the equator of the image (θ = 0°, blue dotted line in Figure 3-5). The resulting *meridional* and *equatorial* profiles were used, respectively, for the determination of the average axial monomer length and the average lateral microtubule metrics (radius, inter-protofilament distance, and protofilament number).

Microtubules were modeled as cylinders with a 3-start helical pattern and a protofilament number N, as previously described[45,137]. According to the helical selection rule[137], the microtubule's diffraction pattern comprises several layer line reflections (l) perpendicular to the meridional axis, which fall at fixed q values determined by the lattice constant d as determined by equation [18] (in this case d is the axial tubulin spacing). Indeed, the first-order layer line reflection (l = 1) at a q value of 1.57 nm^{-1}, arises from an approximate 4 nm axial repeat within the microtubule, corresponding to the longitudinal spacing between

tubulin monomers. Its harmonic reflections (l = 2, 3, 4…) fall at q values that are double, triple, four times, etc., the value of l = 1 (q = 3.14, 4.72, and 6.22 nm^{-1}, respectively), corresponding to an approximate real axial spacing of 2, 1.33, and 1 nm.

Each of these layer lines can be described by a group of Bessel functions of order n, as represented in Figure 3-5. The first-order layer line is defined by the *third* (J_3) plus N-*3* (J_{N-3}) order Bessel functions. Similarly, the second-, third- and fourth-order layer lines are derived from the *sixth* (J_6) plus N-*6* (J_{N-6}), the *ninth* (J_9) plus N-*9* (J_{N-9}), and the *twelfth* (J_{12}) plus N-*12* (J_{N-12}), order Bessel functions.

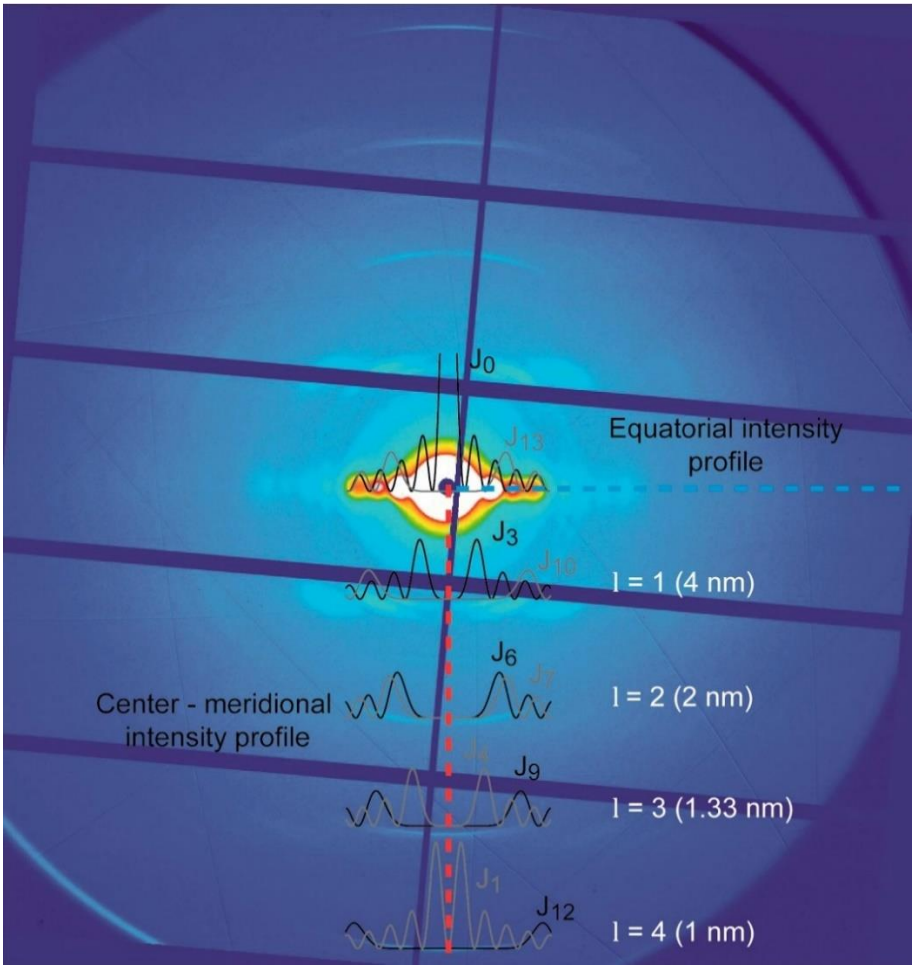

Figure 3-5. Example of a microtubule diffraction pattern, highlighting the equatorial and meridional axes (blue and red dotted lines, respectively). Diffraction layer lines (l = 0 – 4) and their respective Bessel functions (black and gray profiles) are represented, considering model microtubules with 13 protofilaments and a radius of 12 nm.

The exact value of the monomer axial repeat in the microtubule is inferred from the peak position of the fourth-order reflection in the meridional axis. In fact, the main contribution to the mixture of Bessel equations that describes the 1 nm layer line is given by the functions of order J_0 to J_2 (deriving from microtubules with protofilament number N = 10 – 14). The peaks of these functions are more centered than the J_3– J_9 functions that are prevalent in the description of the layer lines reflections from 4 to 1.33 nm, making the former less subject to errors due to signal shifting (which can be caused by protofilament skewing and non-perfect microtubule alignment)[135]. To determine the exact peak position of the 1 nm meridional

reflection, its intensity profile was fitted to a single-peaked Lorentzian function[46] using FiDAT software. The position of the intensity maximum was multiplied by 4 to obtain the average monomer length at the reciprocal space. The standard error was obtained from the standard deviation of the regression applied, which resulted in a maximum deviation of 0.025%. Nonetheless, the overestimation of the tubulin axial repeat value caused by the obliqueness of protofilaments is never above 0.38%, as the microtubule's maximum skew angle is 5°.[6]

Then, the intensity profile of equatorial reflections was used to determine the lateral metrics of the microtubule. In the zero-order layer line (l = 0), the diffraction intensity $I_{l,N}(q)$ is a function of the *zero* (J_0) and N (J_N) order Bessel function. The exact equation (demonstrated in [46,135]) is:

$$< I_{l,N}(q) > = \sum_N w_N \left[(f(q) \cdot J_0(q \cdot r_N))^2 + (f(q) \cdot J_N(q \cdot r_N))^2 \right] \quad [20]$$

where w_N is the fraction of microtubules with N protofilaments, r_N is the radius of a microtubule with N protofilaments and $f(q)$ is a function used to take into account the thickness of the microtubule wall. It is equal to:

$$f(q) = 4\pi r_t^3 \frac{\sin(q \cdot r_N) \cdot \cos(q \cdot r_N)}{(q \cdot r_N)^3} \quad [21]$$

where r_t is the radius of the tubulin monomer considered as a sphere, with a value of 2.48 nm. Equation [20] was used for iterative fitting by least squares of the experimental intensities using FiDAT software. The standard deviation σ of r_N is calculated as:

$$\sigma(r_N) = \left| r_N \cdot \frac{\sigma(I_{max})}{I_{max}} \right| \quad [22]$$

where I_{max} is the intensity maximum of the batch-averaged, background subtracted diffraction image, and $\sigma(I_{max})$ is the value of the average standard deviation image (computed by FiDAT software) in the same point. To calculate the inter-protofilament distance (d_N), the microtubule was considered as an N-apex polygon of apothem r_N, with a protofilament centered on each side (Figure 3-6, panel A). The linear distance between two adjacent protofilaments can be calculated as:

$$d_N(r_N) = 2r_N \sin\left(\frac{\pi}{N}\right) \quad [23]$$

the geometrical demonstration of which is detailed in Figure 3-6, panel B. Applying the theory of error propagation, the standard deviation of d_N was calculated as the square root of the sum of the squares of the product of the partial derivatives of each variable by the standard deviation of that variable. Therefore:

$$\sigma_{d_N} = \sqrt{\left(-\frac{2\pi r_N}{N^2}\cos\left(\frac{\pi}{N}\right)\sigma_N\right)^2 + \left(2\sin\left(\frac{\pi}{N}\right)\sigma_{r_N}\right)^2} \quad [24]$$

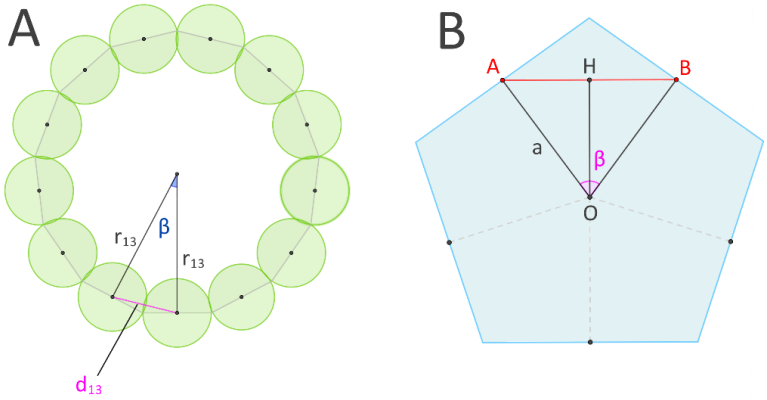

Figure 3-6. Panel A: a 13-protofilament microtubule is modeled as a 13-apex polygon of apothem r_{13} with a protofilament centered on each side, the inter-protofilament distance is indicated as d_{13}. Panel B: for any regular polygon (e.g. pentagon) with N sides and apothem a, it's possible to divide the central angle (2π) into N angles, each of measure 2π/N. It is possible to establish the relationship between the segment AB and the central angle β = 2π/N of the isosceles triangle AOB by drawing the median OH of AB, and observing that it is also the bisector of β. Then, AB = 2AH, where AH = AO sin(β/2) = a sin(π/N). Consequently, AB = 2a sin (π/N). The images were made with 2023 GeoGebra geometry suite (GeoGebra GmbH).

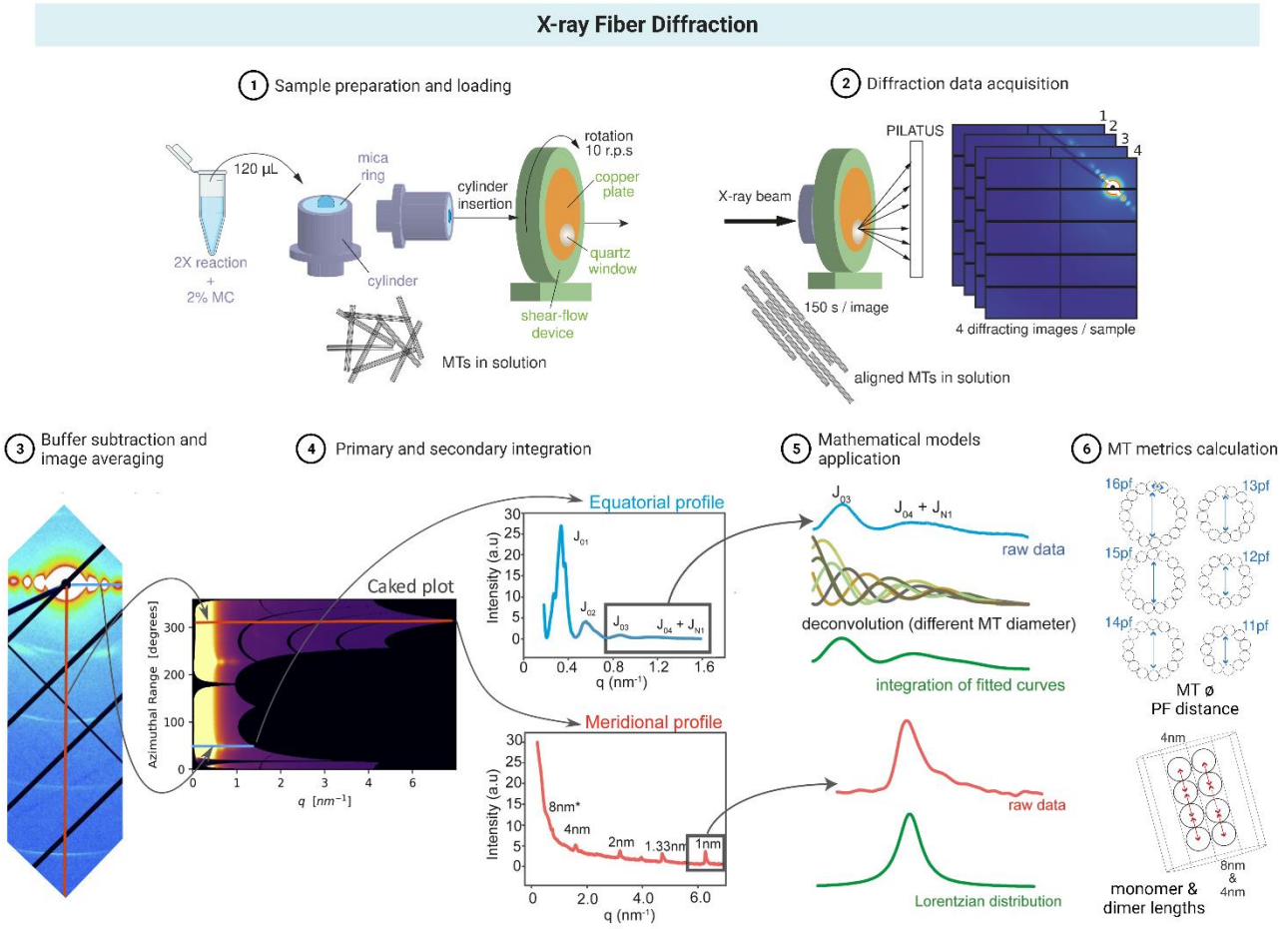

Figure 3-7. Schematic representation of the experimental set-up and data processing of shear-flow X-ray fiber diffraction applied to microtubules' investigation. (**1**) Preparation and insertion of the sample in the shear-flow device. (**2**) Acquisition of X-ray diffraction images. (**3**) Buffer images are subtracted from averaged experimental diffraction images. (**4**) A radial integration of the processed image from the beam center produces a caked plot. The equatorial (blue line) and meridional (red line) intensity profiles are integrated and analyzed. (**5**) J_{03} and J_{04} + J_{N1} are deconvolved from the equatorial intensity profile according to the populations of microtubules with different protofilament numbers. The fitted curves are summed and correlated with experimental data. The meridional profile analysis involves the fitting of the 1 nm layer line peak to a Lorentzian distribution to determine the exact position of the intensity maximum. (**6**) Microtubule's lateral and axial metrics are calculated from the fitted data. Image modified from [46].

3.3 Cellular biology

3.3.1 Cell lines and culture conditions

All cell culture work was performed in a sterile Logic Labconco® Purifier® Biological Safety Cabinet (Total Lab Systems Ltd, New Zealand). Several different human cell lines were used in this thesis project. A549 non-small-cell lung carcinoma cells, cervical adenocarcinomas HeLa, HeLaβIII (MDR overexpressing βIII tubulin isotype), Kb-3.1 (HeLa subclone), and Kb-V1 (MDR overexpressing P-gp) cells were cultured at 37°C in Dulbecco's modified Eagle medium (Gibco™ DMEM, Thermo Fischer Scientific) supplemented with 10% v/v fetal calf serum, 2 mM L-glutamine, 1 mM sodium pyruvate, 40 µg/mL gentamycin, 100 IU/mL penicillin and 100 µg/mL streptomycin in a 5% CO_2 air atmosphere. To passage cells, these were detached from the culture plate using trypsin-EDTA (Invitrogen®) and incubated for 5 min at 37°C and 5% CO_2. Then, trypsin-EDTA was removed, and the cells were resuspended in fresh culture medium. Human SHSY5Y neuroblastoma cells were cultured in the same conditions, but trypsin-EDTA was not used for dissociation from the culture plate; since SHSY5Y cells were very labile a gentle pipetting was sufficient to resuspend them. For long-term storage, all cell lines were placed in liquid nitrogen in 1.5 mL cryotubes at 10^6 cells/mL in DMEM supplemented with 10% DMSO.

3.3.2 MTT cellular viability assays

A549, HeLa, HeLaβIII, Kb-3.1, Kb-V1 cells were seeded into clear Falcon® 96-well microplates (polystyrene, flat bottom, tissue culture treated) at a concentration of either $6.5 \cdot 10^4$ cells/well (A549, HeLa, Kb-3.1) or 10^5 cells/well (HeLaβIII, Kb-V1) and incubated for 24h at 37°C and 5% CO_2. Cells were then treated with serial dilutions of drugs (10 µM – 0.5 nM **1a** or **1b**, 800 nM – 0.05 nM paclitaxel for A549, HeLa, and Kb-3.1; 80 µM – 10 nM **1a** or **1b**, 30 µM – 1.5 nM paclitaxel for HeLaβIII and Kb-V1) and incubated for 48h at 37°C and 5% CO_2. DMSO was used as vehicle for the tested drugs, where less than 0.5% v/v was employed in the assay. A 20 µL aliquot of MTT solution was added to each well, followed by incubation for 2h at 37°C, 5% CO_2. The purple formazan crystals were solubilized with 100 µL of MTT solubilizer solution overnight at 37°C, 5% CO_2, and the microplates were covered with aluminum foil to protect them from light until the end of the procedure. The effect of various drug concentrations on cell viability was quantified spectrophotometrically measuring the absorbance at 570/690 nm in an automated multi-well plate reader (Appliskan® ThermoFisher). Control wells containing medium without cells were used as blanks. The MTT response is expressed as a percentage of the control (untreated) cells:

$$\%\ of\ control = \frac{Abs_{570-690}(sample) - Abs_{570-690}(blank)}{Abs_{570-690}(avg\ control) - Abs_{570-690}(blank)} \cdot 100 \qquad [25]$$

where $Abs_{570-690}$ is the difference between the absorbance at 570 nm and 690 nm, which is used as reference wavelength to compensate for nonspecific background values. Using the SigmaPlot software package (version 14.5, Systat Software, Inc., SanJose, CA, USA), individual logarithmic dose-response scatter plots were built for each experimental condition. The data were then fitted following a variable slope model, using the following four-parameter logistic curve:

$$y = min + \frac{max - min}{1 + \left(\frac{x}{IC_{50}}\right)^{-hillslope}} \quad [26]$$

where IC_{50} is the inflection point of the curve, i.e. the concentration of drug that gives a response halfway between the maximum (max) and the minimum (min) value of the curve, and the hillslope is a parameter that describes the steepness of the curve. The final IC_{50} values reported in this thesis are the mean ± SEM values of three independent experiments with duplicates in each one.

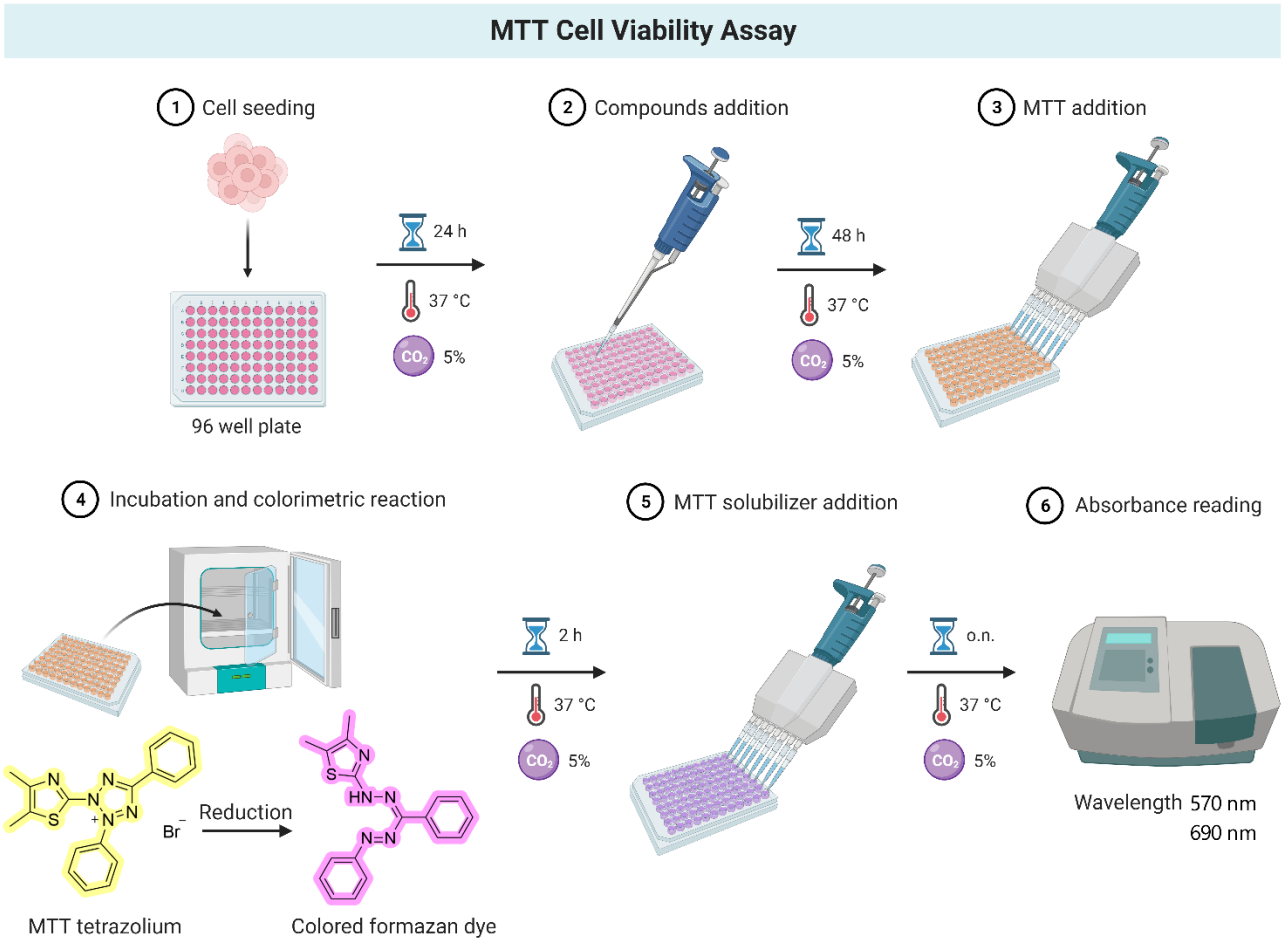

Figure 3-8. Schematic representation of an MTT colorimetric assay. Cells are seeded in a 96-well microplate and incubated for 24h at 37°C, 5% CO_2 [**1**]. Serial dilutions of the tested compounds are added to the plated cells, which are incubated for 48h at 37°C, 5% CO_2 [**2**]. MTT is added to the wells [**3**] and the microplate is incubated for 2h at 37°C, 5% CO_2. During this time, the reduction of the tetrazolium ring of MTT takes place, producing purple-colored formazan crystals [**4**]. The reaction is stopped by addition of the MTT solubilizer solution [**5**]. The absorbance at 570 nm is measured the following day in a plate reader, giving a quantitative measurement of the number of viable cells at each compound concentration [**6**].

3.3.3 Indirect immunofluorescence imaging

A549 cells were seeded at a density of $3.5 \cdot 10^4$ cells/well onto 18 mm round microscopy coverslips, previously laid at the bottom of a clear Falcon® 12-wells microplate (polystyrene, flat bottom, tissue culture treated). The cells were cultured overnight at 37°C and 5% CO_2, then DMSO (drug vehicle) or different amounts of the tested compounds were added. DMSO was added at the highest concentration employed in the other experiments, but it always maintained below 0.5% v/v. The concentration range for each tested compound (**1a**, **1b**, paclitaxel) was selected based on its IC_{50} in A549 cells, with concentrations ranging from half the IC_{50} to twelve times the IC_{50}. After 24h incubation at 37°C and 5% CO_2, A549 cells permeabilized and fixated by successive incubations in PEMP buffer (5 min), PEMT (2 min), and formaldehyde-containing fixation buffer (30 min) at RT. Subsequently, the cells were rinsed thrice with PBS and blocked with PBS supplemented with 3% bovine serum albumin (BSA) for 30 min at RT. Attached cells were incubated for 1h at 37°C with a 1:2000 dilution in PBS/BSA 3% of a primary mouse monoclonal antibody (DM1A, Sigma-Aldrich) reacting with α-tubulin. After that, samples were washed thrice with PBS and incubated for 1h at 37°C in dark with a 1:1000 dilution in PBS/BSA 3% of a secondary fluorescent goat anti-mouse antibody (IgG Alexa Fluor™ Plus 488 or AF488, Thermo Fisher Scientific). Cells were washed four times in PBS and incubated for 30 min at RT with a 1:100 dilution PBS/BSA 3% of DAPI to stain the DNA. After washing with PBS thrice, the coverslips were mounted on glass microscope slides with a drop of glycine, sealed with nail polish, and stored at -20°C in dark until visualization. The slides were examined with a Leica DM 6000 B epifluorescence microscope employing a 100× objective with a N.A. of 1.46 and images were acquired through LAS AF software using a Leica DFC360 FX CCD camera. Exposure times of approximately 500 msec and 50 msec were employed for cytoskeleton and nuclei image acquisition, respectively.

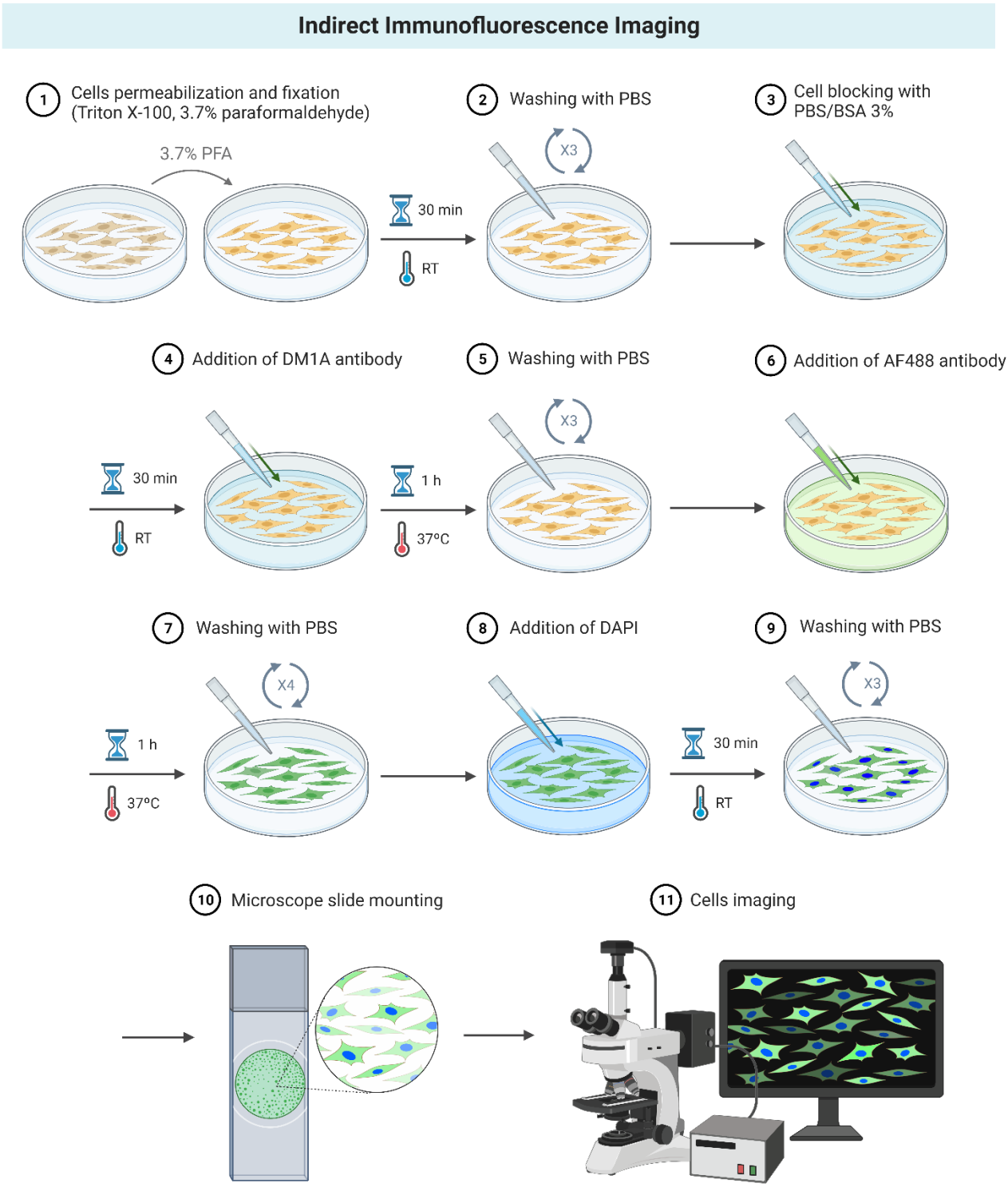

Figure 3-9. Schematic illustration of the workflow of indirect immunofluorescence with epithelial cells adherently growing on coverslips. After cultivation, cells are permeabilized with a detergent (Triton X-100) to enable the antibodies to cross the cellular membranes and fixed with a chemical crosslinker (paraformaldehyde) [**1**]. After rinsing with PBS to remove the excess chemicals [**2**], a blocking step with bovine serum albumin (BSA) is performed to reduce the unspecific binding of antibodies to non-target structures [**3**]. Next the incubation with the first antibody (DM1A) takes place, which specifically recognizes α-tubulin [**4**]. After rinsing with PBS to remove the excess primary antibody [**5**], the incubation of the fluorescence-coupled secondary antibody (AF488) is carried out, during which time it binds to the first antibody and therefore allows microtubules visualization [**6**]. Again, cells are rinsed with PBS [**7**], and nuclei staining is performed with DAPI, a DNA-intercalating agent [**8**]. A final washing step with PBS [**9**] precedes the mounting of the coverslip with glycine on a microscope slide [**10**]. Finally, the immunofluorescence preparation can be visualized in an epifluorescence microscope [**11**].

3.3.4 Cy5-KBP and Cy5-DBP tracking peptides

Cy5-KBP and Cy5-DBP tracking peptides were synthesized at Centro de Investigaciones Biológicas Margarita Sala (CIB-MS, CSIC) in collaboration with Dr. María del Valle Palomo Ruiz's research group from Instituto Madrileño de Estudios Avanzados en Nanociencia (IMDEA Nanociencia), following a published protocol[115]. Briefly, the peptide chains (Table 3-2) were assembled via solid phase peptide synthesis (SPPS) using fluorenylmethyloxycarbonyl (Fmoc) as N-terminal protecting group. The peptides were subsequently labelled with the organic dye cyanine 5 (Cy5) via a maleimide-thiol reaction between the N-terminal cysteine residues of the peptides and the commercially available Cy5-maleimide. The final peptides were purified via reverse phase HPLC, dissolved in DMSO to a final 2.5 mM concentration and stored in small aliquots at −20 °C.

Table 3-2. Peptide sequences employed in the synthesis of kinesin and dynein tracking probes

Name	Sequence (N terminal – C terminal)
Kinesin-binding peptide (**KBP**)	CGGLEWDDSTLSYR$_8$
Dynein-binding peptide (**DBP**)	CGGHPAEPGSTVTTQNTASQTMSR$_8$

3.3.5 Time-lapse intracellular tracking assays with Cy5-KBP and Cy5-DBP probes

SH-SY5Y cells were seeded into µ-Slide 8-wells ibiTreat plates (ibidi®, flat polymer coverslip-bottom, tissue culture treated) at a concentration of $3.5 \cdot 10^4$ cells/well and incubated for 48h at 37°C and 5% CO_2. Solutions of the tested compounds at the desired concentrations (1 µM for paclitaxel and flutax-2, 2.5 µM for **1a** and **1b**) with and without 2.5 µM Cy5-KBP or Cy5-DBP were prepared in Gibco™ DMEM without phenol red, previously supplemented with 10% v/v fetal calf serum, 2 mM L-glutamine, 1 mM sodium pyruvate, 40 µg/mL gentamycin, 100 IU/mL penicillin and 100 µg/mL streptomycin. The spent medium was removed from each well and rapidly substituted with 200 µL of the drug-supplemented medium without Cy5 peptide, followed by 20 min incubation at 37°C and 5% CO_2. After this time, the culture medium was replaced again by 200 µL of the drug working solution containing either Cy5-KBP or Cy5-DBP, and the plate was incubated for an additional 15 min at 37°C and 5% CO_2. Then, the culture medium was replaced one last time with drug working solution without labelled peptide and the cells were imaged using a confocal laser scanning microscope Leica TCS SP8 with a 63x oil immersion objective that included a humidified incubation chamber, a CO_2 controller and a heating unit. Cy5 dye was excited at 635 nm and the fluorescence emission was collected at 645-690 nm. Images were recorded every 1.793 s for 3 min as 2-layer-z-stacks. For each condition, two to three different fields were imaged in two separate experiments.

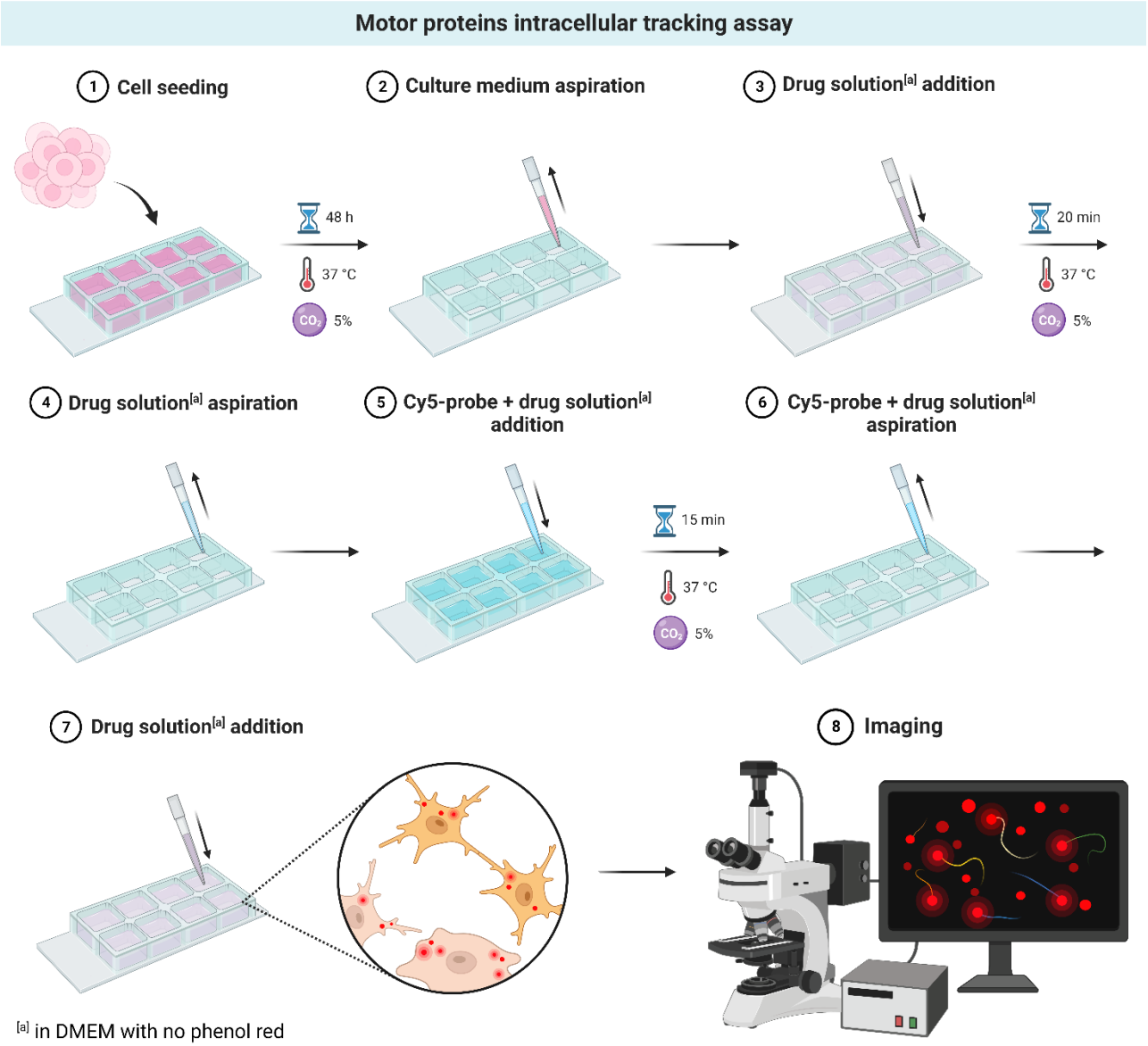

Figure 3-10. Schematic illustration of the workflow of a motor protein intracellular tracking assay. Adherent neuroblastoma cells are seeded in an 8-wells chamber slide with coverslip bottom [**1**]. The cells are left growing for 48h in a cell culture incubator, after which the spent culture medium is removed [**2**]. A drug solution prepared in transparent culture medium is gently added to each well [**3**]. After 20 min incubation, the drug solution is aspirated [**4**] and substituted with an equivalent solution containing the fluorescent Cy5-probe of interest [**5**]. After a 15 min incubation to allow the tracking peptides to enter the cells, the Cy5-porbe containing solution is removed [**6**] and the cells are washed with the original drug solution [**7**]. Finally, the intracellular movement of the fluorescent probes can be monitored in a confocal microscope [**8**].

3.3.6 Time-lapse motility assays data analysis

Single-particle trajectories were analyzed with the TrackMate plugin from the Fiji® package software. Fluorescent particles, or *spots*, with an estimated blob diameter of 1-1.5 µm were identified in each frame of the movie using the LoG detector, which applies a Laplacian of Gaussian filter for edge detection before finding the local intensity maxima. Then, *tracks* were created by linking spots in different frames through the Kalman tracker. This tracker is well suited for particles that exhibit a nearly constant velocity vector, as expected in transported motion. The search radius, which determines how far from a predicted position the

tracker should look for candidate sports, was set equal to the estimated blob diameter, with a maximum frame gap of 2. An additional filter was included to discard trajectories with less than 6 spots. Track mean displacement and track mean velocity were calculated and normalized to control cells in each experiment. Mean Square Displacement (MSD) analysis was performed with MATLAB® software using the toolbox @msdanalyzer previously described by Tarantino at al. in 2014[138,139] for the determination of the mode of displacement of peptides over time. More specifically, the MSD function was calculated for each individual particle as:

$$r_i^2(t,\tau) = \big(r_i(t+\tau) - r_i(t)\big)^2 \qquad [27]$$

where $r_i(t)$ is the position of particle i at time t, and τ is the delay. The function $r_i^2(t,\tau)$ was then averaged over all possible t for a given delay τ to yield the MSD function related to the trajectory $MSD_i(\tau)$. For a freely diffusing particle the following relationship holds:

$$MSD_i(\tau) = 2dD\tau \qquad [28]$$

where d is the dimensionality of the problem (d = 2 for 2D, etc...) and D is the diffusion coefficient. Hence, the log-log representation of [28] must be a linear function of slope 1:

$$\log\big(MSD_i(\tau)\big) = 1 \cdot \log(\tau) + C \qquad [29]$$

Therefore, by fitting the log-log plot to a linear equation, it is possible to verify if the particle is moving of Brownian motion or with a different displacement mode.

The MSD log-log plots of all trajectories were fitted to a linear function. MSD curves for which the quality of the fitting was poor (R^2 coefficient < 0.8) were discarded, and the remaining curves were classified according to the slope α value. According to the modelling study by Quian. et al. (1991)[140], α = 1 indicates free diffusive movement (Brownian Motion, BM), α < 1 indicates constrained movement (CM), and 1 < α < 2 indicates transported movement (TM). The ratio TM/CM was calculated and normalized to control cells in each experiment. Statistically significant differences in the normalized track mean displacement, track mean speed and TM/CM ratio were evaluated by unpaired t-test with Welsh correlation using GraphPad Prism® 8 software (**** P < 0.0001, *** P < 0.001, ** P < 0.01, * P < 0.05).

4 Results

4.1 Molecular modeling of new C7-modified paclitaxel derivatives

The starting point of this thesis work was the design of novel paclitaxel derivatives that could imitate the binding mode of flutax-2 to tubulin, ultimately aiming to evaluate their potential for producing similar structural effects on microtubules. To achieve this objective, I selected a combination of five distinct spacers and 10 different bulky aromatic substituents, including six amines and four alcohols, choosing from the available materials in our laboratory (Figure 4-1).

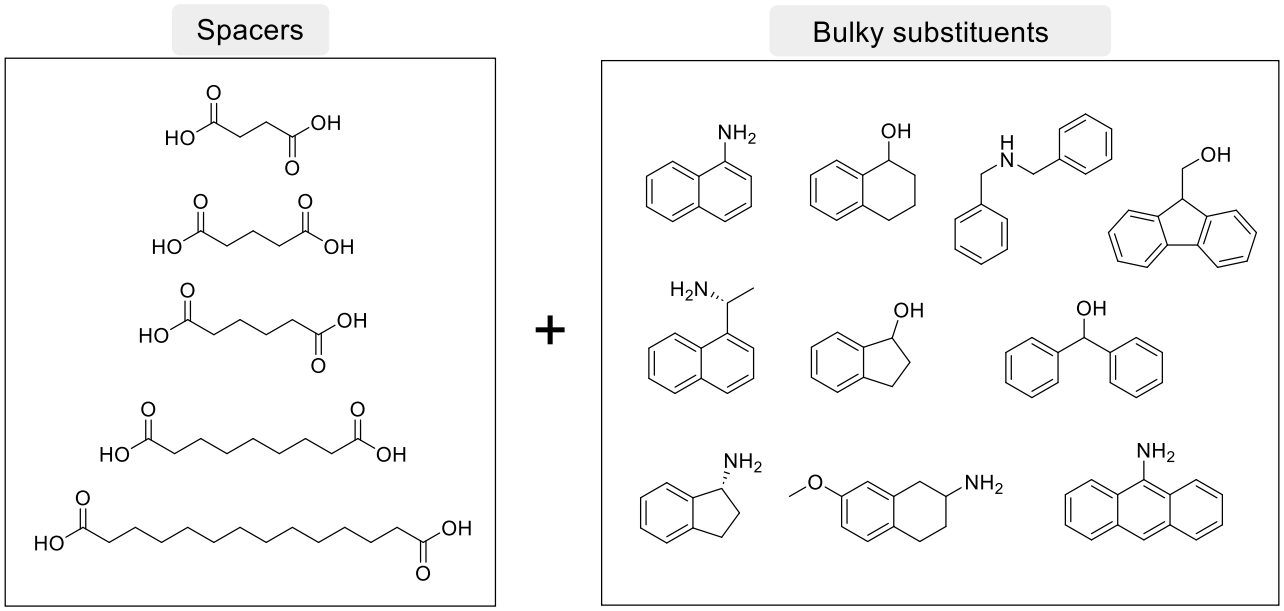

Figure 4-1. Chemical structure of the spacers (left) and bulky substituents (right) combined for the generation of 50 decorations.

The *in-silico* combination of these molecular frameworks led to the generation of 50 possible decorations to be attached at the C7 position of paclitaxel, resulting in an equivalent number of potential new derivatives. To screen the generated molecules, I established a collaboration within the TubInTrain consortium with the computational group at Università degli Studi di Milano leaded by Prof. Pieraccini. The molecular modeling studies were conducted by Helena Pérez Peña and are briefly described below. It is crucial to emphasize that these studies aimed not to discover a high-affinity binder but rather a paclitaxel derivative exhibiting a binding pose similar to flutax-2 when bound to tubulin, based on the rationale that the binding mode and conformation of the molecule in the tubulin binding pocket should be key factors determining its impact on microtubule structure and stabilization.

Due to the lack of an experimentally solved high-resolution structure of flutax-2 in complex with tubulin, the first step involved the study the binding mode of flutax-2 at the taxane site of tubulin using S4MPLE, a molecular docking tool (Figure 4-2). The C7-decoration appears to be exposed to the solvent, rather than

being buried within the protein. The docking result revealed a hydrogen bond interaction between flutax-2 and βArg278. However, an exposed hydrogen bond in a solvent is not considered significant. Taken together, these two considerations support the hypothesis that the C7-modification exerts its effect through a steric mechanism, rather than specific non-covalent interactions.

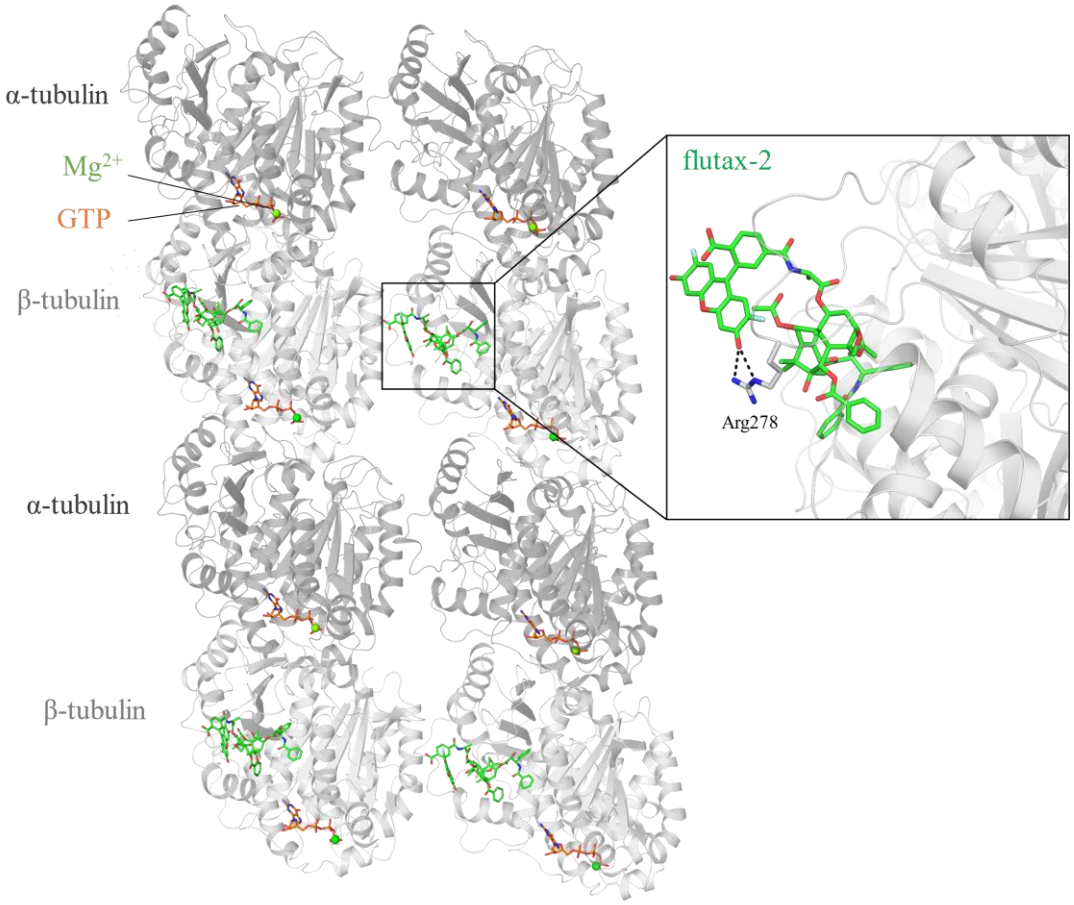

Figure 4-2. Section of two adjacent protofilaments containing two tetramers of α,β-tubulin. The docking conformer of flutax-2 (green) is highlighted in a black square and its interactions with the binding site residue βArg278 are displayed as dashed black lines. The interacting residues and ligands are represented as sticks. Oxygen atoms are in red, nitrogen atoms in navy blue, and fluorine atoms in cyan. The α-tubulin and β-tubulin are represented in dark gray and light gray ribbons, respectively.

The binding mode predicted for the best conformer of each of the 50 proposed paclitaxel derivatives was then compared to that predicted for flutax-2 as illustrated in Figure 4-3. Using docking fingerprints were used to monitor the nearest ligand atoms placed in the vicinity of selected protein atoms. In this way, contact fingerprints were useful for identifying molecules with similar spatial arrangements. Some of the decorations (made up of a certain spacer and bulky substituent) were predicted to bind very differently to flutax-2 based on docking fingerprints (for instance, molecule **1c**), while four were found to bind to the same site as the flutax-2 decoration by establishing hydrophobic interactions, with molecules **1a** and **1b** being the closest to the reference molecule. Therefore, molecules **1a** and **1b** were selected for subsequent synthesis.

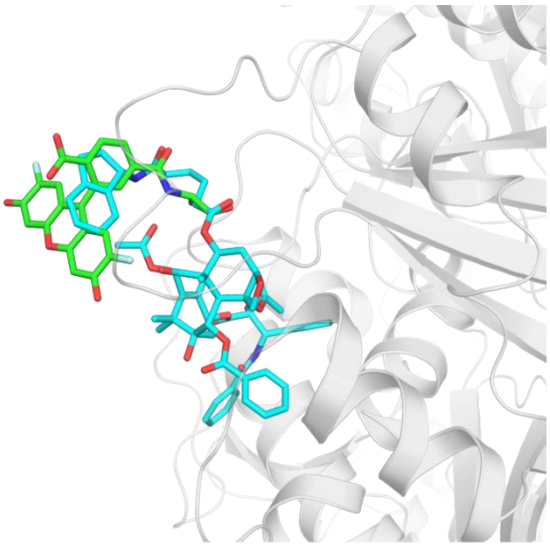

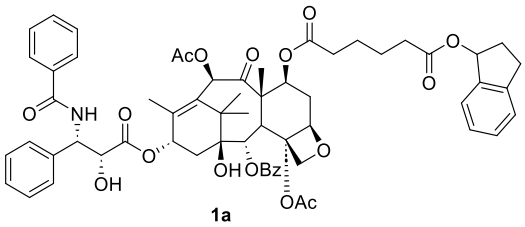

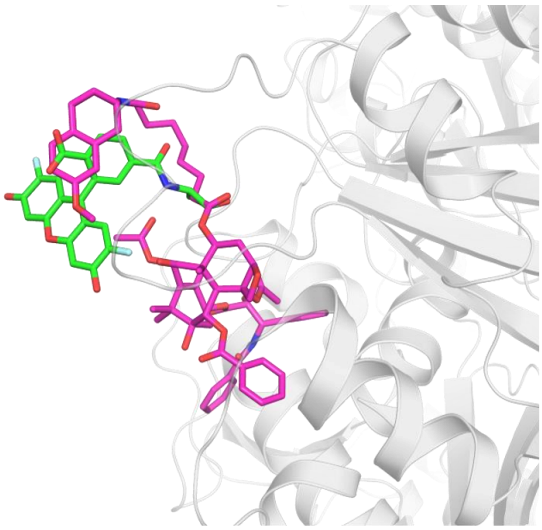

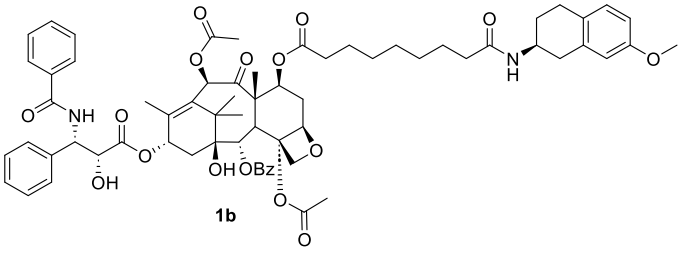

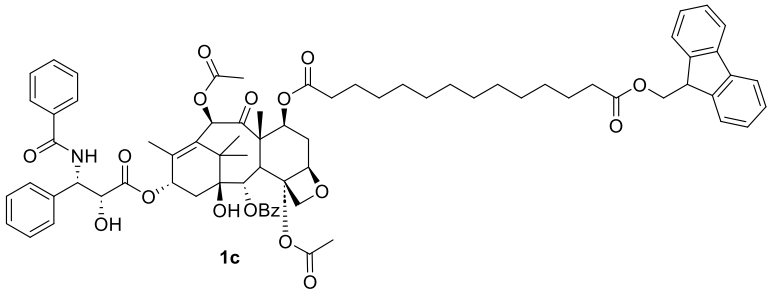

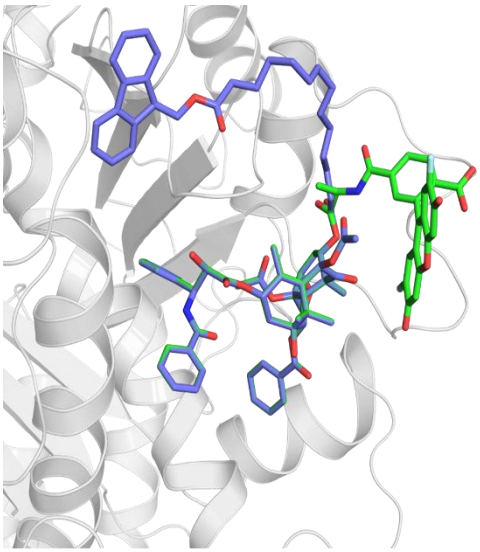

Figure 4-3. Superimposition of the selected hits from the virtual library of new paclitaxel derivatives with the docking conformer of flutax-2 (green). The interacting residues and ligands are represented as sticks. Oxygen atoms are in red, nitrogen atoms in navy blue, and fluorine atoms in cyan. β-tubulin is represented by a light gray ribbon.

4.2 Synthesis and characterization of C7-modified taxanes 1a and 1b

4.2.1 Retrosynthetic analysis

I envisioned two possible retrosynthetic strategies for the selective conjugation of bulky substituents at the desired C7 position of paclitaxel employing a dicarboxylic linker of suitable length (Scheme 4-1, A and B).

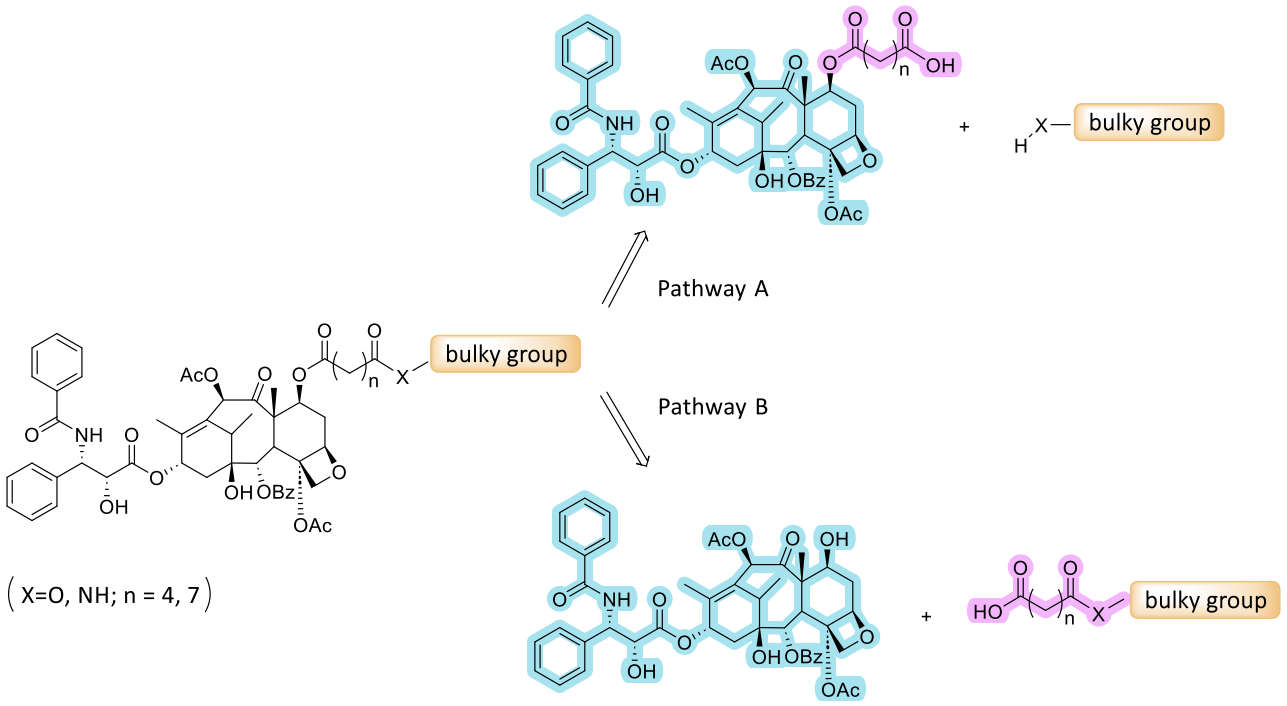

Scheme 4-1. Retrosynthetic pathways A and B; paclitaxel in light blue, dicarboxylic linker in purple.

Strategy A involved the initial coupling of the mono-protected dicarboxylic linker to the taxane core, followed by the condensation of the sterically hindered amine or alcohol. In contrast, strategy B required coupling the mono-protected dicarboxylic acid moiety with the bulky group first, and the subsequent reaction with the taxane to achieve the desired C7-decorated paclitaxel derivative. Upon evaluating both synthetic routes, which require the same number of reaction steps, I chose pathway A because of its inherent versatility, as it provides access to a paclitaxel-linker intermediate that can be easily conjugated with a variety of diverse bulky substituents in the subsequent stages of the project. However, the synthesis encountered difficulties that made the initially planned route impracticable (evidence shown below), eventually pointing toward pathway B as a better option to fulfill the synthesis of the target compounds.

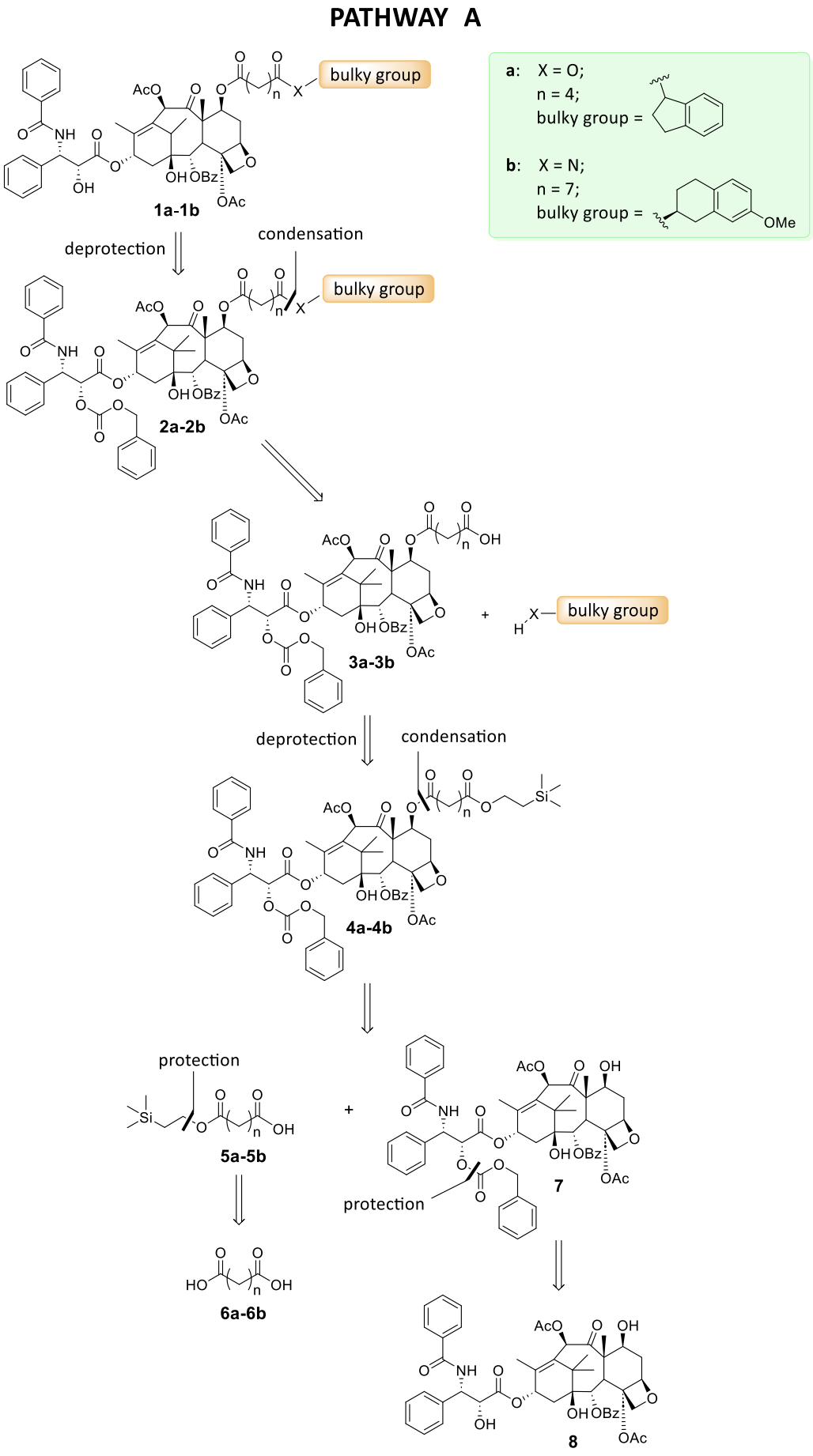

Scheme 4-2. Retrosynthetic pathway A.

Scheme 4-2 outlines a detailed version of retrosynthetic approach A for preparing compounds **1a** and **1b**. According to the planned route, the target molecules can be achieved by deprotecting the corresponding 2'-carboxybenzoyl derivatives of paclitaxel **2a**-**2b**, which in turn can be synthesized from the conjugation of compounds **3a**-**3b** with the desired bulky amine or alcohol via Steglich esterification or amine acylation. These paclitaxel-linker adducts are obtained from molecules **4a**-**4b** by freeing the carboxyl moiety from the protective 2-(trimethylsilyl)ethyl group (TSE). In turn, **4a** and **4b** are derived from the condensation of the corresponding (trimethylsilyl)ethyl monoesters **5a**-**5b** with 2'-carboxybenzoylpaclitaxel **7**. Paclitaxel derivative **7** is obtained from the parent drug by protecting the hydroxyl group in position 2' as a carbonate ester. Indeed, the protection of this position with a benzyloxycarbonyl (Cbz) functionality, which can then be removed by hydrogenolysis, has been reported in the literature[141–143]. Finally, compounds **5a**-**5b** are obtained from the mono-protection of the corresponding di-carboxylic acids **6a**-**6b** as 2-substituted ethyl esters.

The second possible retrosynthetic strategy B is outlined in Scheme 4-3. Similar to the previous approach, final compounds **1a**-**1b** are obtained by deprotecting the corresponding 2'-carboxybenzoyl derivatives of paclitaxel **2a**-**2b** through a hydrogenolysis reaction. However, in this second route **2a** and **2b** are synthesized by directly coupling the decorated linkers **9a**-**9b** with 2'-O-Cbz-paclitaxel **7**, with the latter being produced as in pathway A via carboxybenzoylation reaction from paclitaxel **8**. Compounds **9a** and **9b** are obtained by freeing the carboxyl moiety of the corresponding TSE-protected esters **10a**-**10b**. In turn, **10a** and **10b** are the products of direct conjugation of the desired bulky amine or alcohol to the (trimethylsilyl)ethyl monoesters **5a** and **5b**. The last retrosynthetic step is common with pathway A, with **5a** and **5b** being obtained from the mono-esterification of the commercially available di-carboxylic acids **6a**-**6b**.

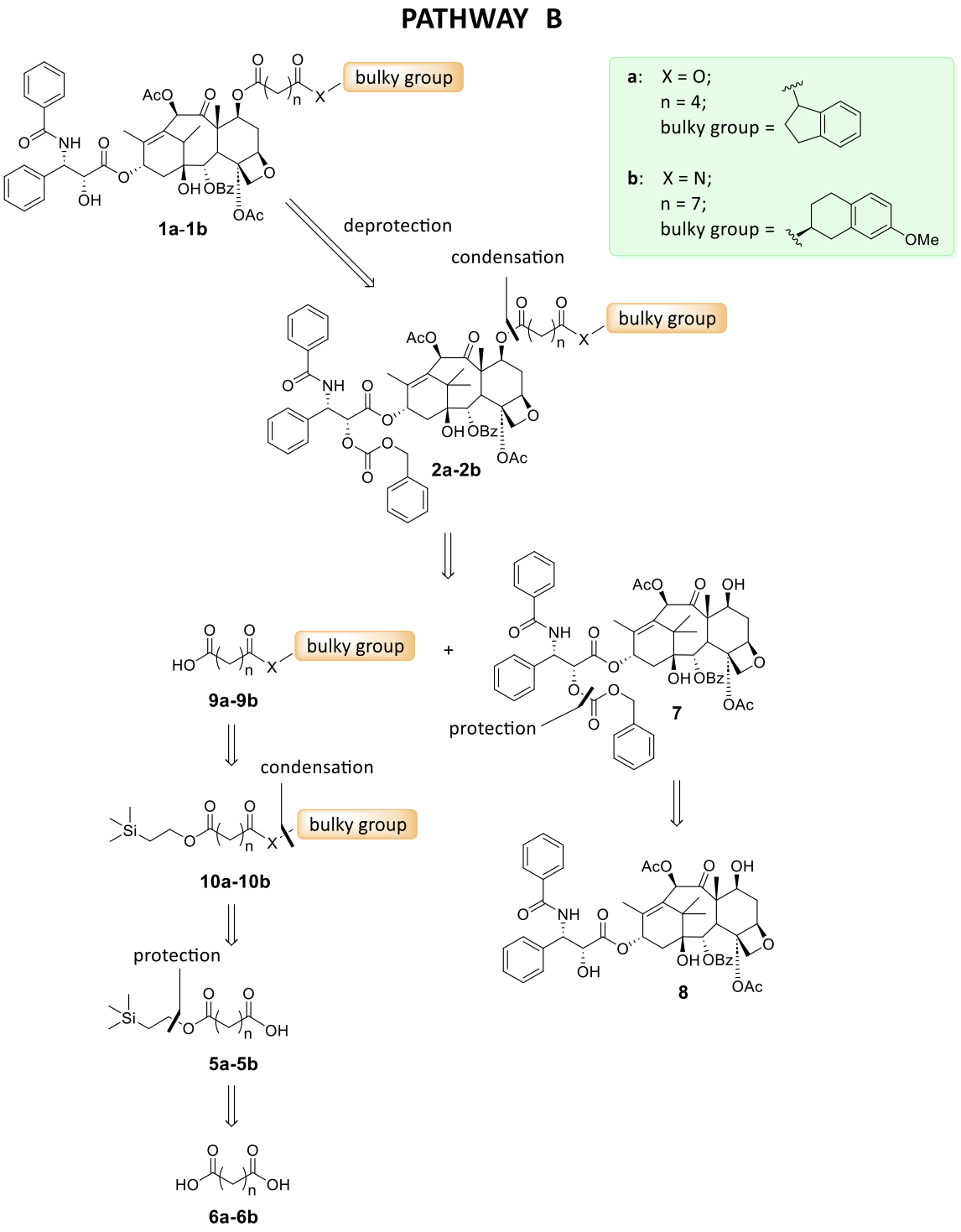

Scheme 4-3. Retrosynthetic pathway B.

4.2.2 Synthesis of molecules common to both pathways

4.2.2.1 Synthesis of 2'-*O*-Cbz-paclitaxel 7

The first step of the synthesis entailed the protection of the 2'-hydroxy functionality of paclitaxel **8**. This reaction constituted an essential prerequisite for the successful execution of the synthetic strategy, as the 2'-hydroxy group is known to exhibit superior reactivity compared to the target 7'-hydroxy group[144]. To this end, I selected the benzyloxy carbonyl group as protecting group due to its reported effectiveness in this particular reaction[141–143].

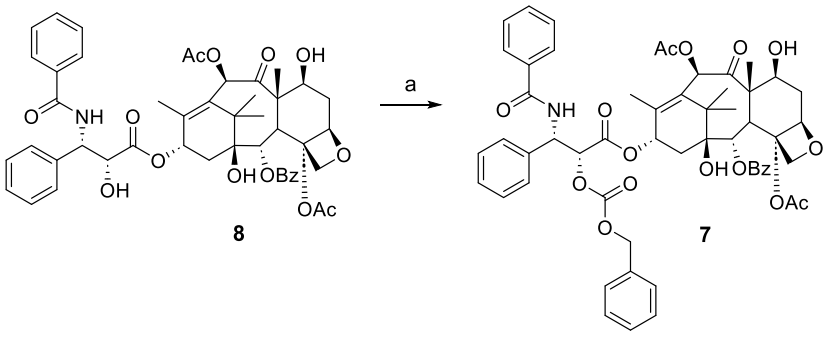

Scheme 4-4. Reaction conditions: a) CbzCl, Py, CH_2Cl_2, RT, 24h, 70% (**7**).

Therefore, I performed a carboxybenzoylation reaction (Scheme 4-4) on paclitaxel **8** employing benzyl chloroformate (CbzCl) and pyridine in dichloromethane as solvent. Pyridine (Py) is essential to neutralize the hydrochloric acid generated during the reaction. Upon complete consumption of the starting material, confirmed by TLC monitoring, I quenched the excess benzyl chloroformate with saturated ammonium chloride and obtained the desired compound **7** in 70% yield after aqueous work-up and chromatographic purification. I confirmed the structure of **7** by proton nuclear magnetic resonance (^{1}H-NMR) of the molecule. The ^{1}H-NMR spectrum revealed a new signal centered at 5.19 ppm characteristic of the methylene of the benzyloxycarbonyl group, as well as five additional hydrogens in the integration of the aromatic multiplet at 7.49 – 7.34 ppm. Moreover, the shift downfield of the H-2' doublet from 4.79 to 5.48 ppm was symptomatic of the de-shielding effect of the neighboring carbonate group, further confirming the reaction's success.

4.2.2.2 Synthesis of *mono*(trimethylsilyl)ethyl esters 5a-5b

The next step of the planned synthetic pathway was the selective protection of one of the two carboxylic functionalities of the commercially available hexanedioic acid **6a** and nonanedioic acid **6b**. This reaction was needed because dicarboxylic acids form dimeric side products under condensation conditions, which would result in the loss of precious quantities of 2'-carboxybenzoylpaclitaxel while complicating the purification of the target products. I performed the reaction using 2-(trimethylsilyl)ethanol (2-TMSE) as esterifying agent –

protective group in a Steglich-like esterification, using 1-ethyl-3-(3-dimethylaminopropyl)carbodiimide (EDC) and 4-dimethylaminopyridine (DMAP) as coupling agents and a 1:10 mixture of pyridine and dichloromethane as solvent (Scheme 4-5)[145].

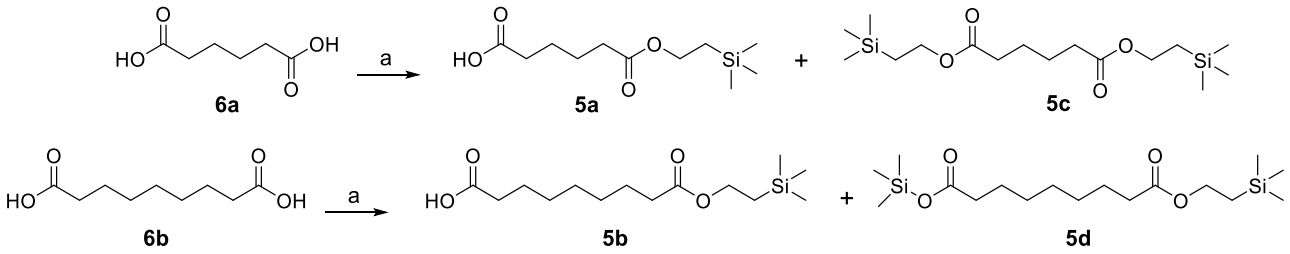

Scheme 4-5. Reaction conditions: a) 2-TMSE, EDC·HCl, DMAP, Py, CH_2Cl_2, RT, 24h, 66% (**5a**), 70% (**5b**).

To reduce the amount of diester byproducts produced in the course of the reaction, I used sub-stoichiometric amounts of the esterifying agents. Even so, small amounts of diesters **5c** and **5d** were formed alongside the desired monoesters **5a** and **5b**, which were obtained as major products in 66% and 70% yield, respectively, after flash chromatography purification. I confirmed the formation of the desired products through the analysis of their ^{1}H-NMR spectra, where the characteristic ester signals appeared. In both spectra, I could identify a 9H-multiplet around 0 ppm, typical of silicon-bound methyl groups, as well as the 2H-multiplets around 4 ppm and 0.8 ppm that can be attributed to the two remaining carbon atoms of the 2-(trimethylsilyl)ethyl moiety. The integration of these signals indicated the presence of a single TSE moiety per molecule, allowing the differentiation of the major products **5a** and **5b** from the byproducts **5c** and **5d**.

4.2.3 Synthesis of molecules specific to pathway A

At this point of the synthesis, rather than proceeding in parallel with each set of reactions toward final compounds **1a** and **1b**, I chose to focus on the pursuit of the first final taxane derivative **1a**. This approach allowed me to assess the feasibility of the reactions while minimizing the potential waste of 2-*O*-Cbz-paclitaxel **7** in case any difficulties arose during the synthesis.

4.2.3.1 Synthesis of hexanedioic acid TSE monoester – 2'-*O*-Cbz-paclitaxel conjugate 4a

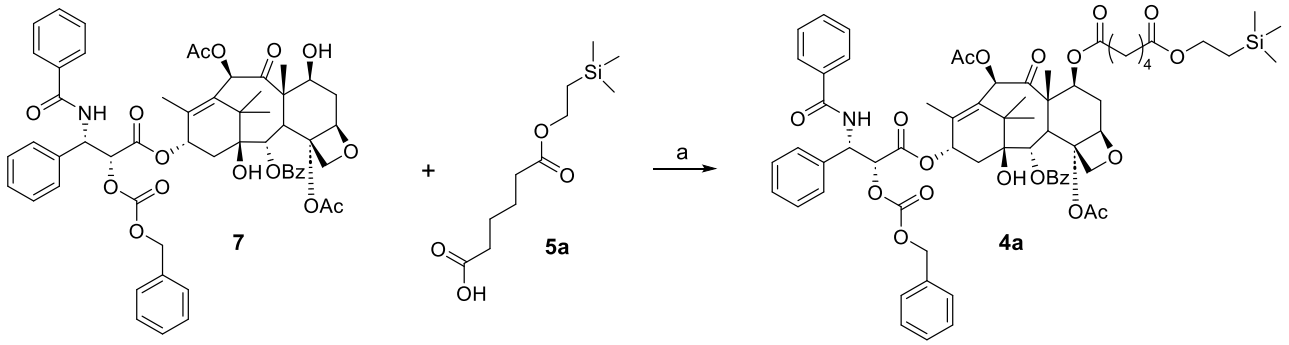

Scheme 4-6. Reaction conditions: a) DCC, DMAP, CH_2Cl_2, RT, 18h, 90% (**4a**).

The third step of the synthesis when approaching compound **1a** through pathway A consisted in the condensation of 2'-*O*-Cbz-paclitaxel **7** with TSE monoester **5a** to form conjugate **4a**. I carried out this reaction at room temperature, employing *N*,*N*'-dicyclohexylcarbodiimide (DCC) and DMAP in dichloromethane (Scheme 4-6), finally obtaining target compound **4a** in high yield (90%) after chromatographic purification. The product characterization by ^{1}H-NMR revealed a signal shift of the hydrogen in position 7 of the paclitaxel scaffold from 4.47 to 5.45 ppm. The shift indicates the influence of an electron-withdrawing group on the H-7 signal, hence confirming the esterification of the 7-hydroxy group.

4.2.3.2 Synthesis of hexanedioic acid – 2'-*O*-Cbz-paclitaxel conjugate 3a

The subsequent synthetic step entailed the formation of compound **3a** via a fluoride-mediated β-elimination reaction, which lead to the deprotection of the TSE moiety of conjugate **4a**. This reaction takes advantage of the high Si-F affinity to weaken the Si-C bond, and one of the standard methods to perform it employs tetrabutylammonium fluoride (TBAF) as fluoride source[146].

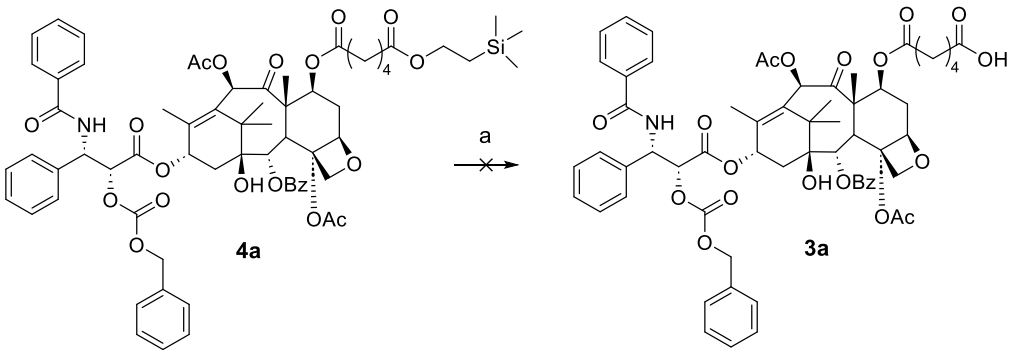

Scheme 4-7. Reaction conditions: a) TBAF, THF, -20°C to RT, 20h.

I conducted an initial trial with TBAF in tetrahydrofuran (THF) at -20°C, but no evidence of product formation was observed by TLC monitoring after 6h. To increase the reaction rate, I gradually raised the temperature

to 0°C first (for 4h) and then to room temperature (for 10h). After these additional 14h, the starting material had been entirely consumed (Scheme 4-7), but the appearance of multiple spots on the TLC indicated the formation of several products. Upon chromatographic separation of the mixture, I was able to isolate three main pure products, but none of them was the targeted compound **3a**, as confirmed by NMR characterization. All the products exhibited modifications in the paclitaxel core, such as the removal of aromatic substituents and 2-debenzoylation. Two of them had lost the 2'-*O*-Cbz protecting group, and only one had the linker freed by the TSE protecting group. Based on these findings, I speculated that the structural modifications to the paclitaxel core occur before the TSE deprotection, making this route unsuitable for my objectives.

4.2.4 Synthesis of molecules specific to pathway B

After ruling out the fluoride-promoted β-elimination route, I evaluated alternative methods for TSE deprotection. Another methodology reported in literature[146] is the use of sodium hydride (NaH) in dimethylformamide. However, the treatment of paclitaxel with NaH is known to lead to 7-OH epimerization[147]. Thus, rather than further optimizing strategy A, I decided to pursue the second retrosynthetic pathway B, hoping to achieve better results.

4.2.4.1 Synthesis hexanedioic acid asymmetric diester 10a

According to the new synthetic strategy, the next step upon getting the hexanedioic acid TSE-monoester **5a** (see section 4.2.2.2 for synthesis) was the formation of the 1-indanol – linker moiety through a condensation reaction between **5a** and 1-indanol **11** (Scheme 4-8).

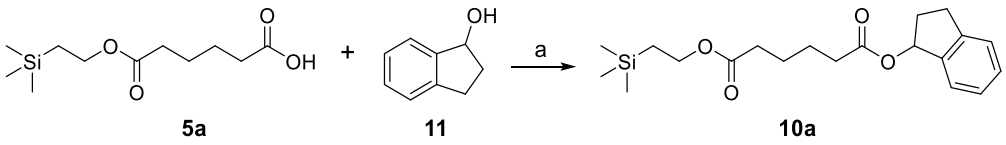

Scheme 4-8. Reaction conditions: a) EDC·HCl, DMAP, CH_2Cl_2/Py, RT, 6h, 61% (**10a**).

To this aim, I performed a traditional Steglich esterification reaction by employing DCC and DMAP as coupling agents and a 1:10 mixture of pyridine and dichloromethane as solvent. I stirred the mixture at room temperature for 6h, after which the reaction appeared to have reached completion according to TLC monitoring. I obtained the desired asymmetric diester **10a** after an acidic workup and Biotage® silicagel chromatography purification, with 63% yield. I confirmed the structure of the final product via ^{1}H-NMR analysis, observing the desymmetrization of the signals of the central hexanedioic chain and the signal shift of indanol H-1, which falls at 5.24 ppm and 6.21 ppm in compounds **11** and **10a**, respectively. This variation

can be explained by the effect of an electron-withdrawing moiety and therefore, confirms the esterification of indanol's hydroxyl group.

4.2.4.2 Synthesis of hexanedioic acid 1-indanyl ester 9a

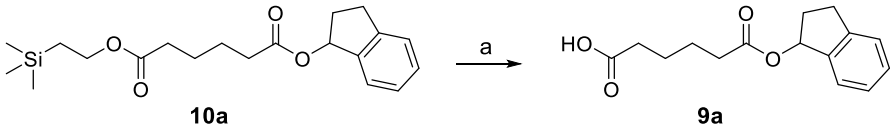

Scheme 4-9. Reaction conditions: a) TBAF, THF, -5°C to RT, 4h, 63% (**9a**).

The subsequent step of synthetic pathway B entailed the removal of the 2-(trimethylsilyl)ethyl protecting moiety from compound **10a** to obtain the target monoester **9a**. Again, I employed TBAF to carry out a fluoride-promoted β-elimination, in which the fluoride anion attacks the silicon atom and expels the carboxylate in addition to one equivalent of ethylene. The reaction, performed in THF by gradually rising the temperature from -5°C to RT, afforded compound **9a** in moderate yield after flash chromatographic purification (63%, Scheme 4-9). I confirmed the product's structure by the disappearance, in the ^{1}H-NMR spectrum, of the TSE group signals (in particular of the singlet at 0.04 ppm, typical of silicon-bound methyl groups).

4.2.4.3 Synthesis of hexanedioic acid 1-indanyl ester – 2'-O-Cbz-paclitaxel conjugate 2a

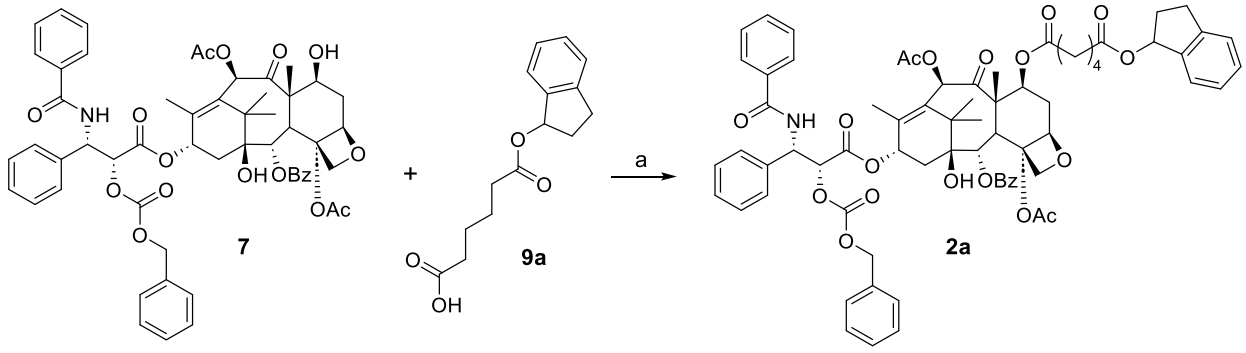

Scheme 4-10. Reaction conditions: a) DCC, DMAP, CH_2Cl_2, RT, 29h, 70% (**2a**).

The key synthetic step of strategy B entailed the coupling of the decorated linker **9a** with the previously synthetized 2'-*O*-Cbz-paclitaxel **7** (Scheme 4-10). I carried out the conjugation reaction in dry dichloromethane in Steglich conditions. However, TLC monitoring evidenced the persistence of 2'-*O*-Cbz-paclitaxel in the reaction mixture, prompting me to double the initial amount of DCC and DMAP in order to consume all the unreacted starting material. After work-up and flash chromatography purification, I obtained target compound **2a** in 70% yield. I verified the esterification of paclitaxel's 7-hydroxyl group by the signal shift of the H-7 from 4.47 to 5.57 ppm in the ^{1}H-NMR spectrum.

4.2.4.4 Synthesis of hexanedioic acid 1-indanyl ester – paclitaxel conjugate 1a

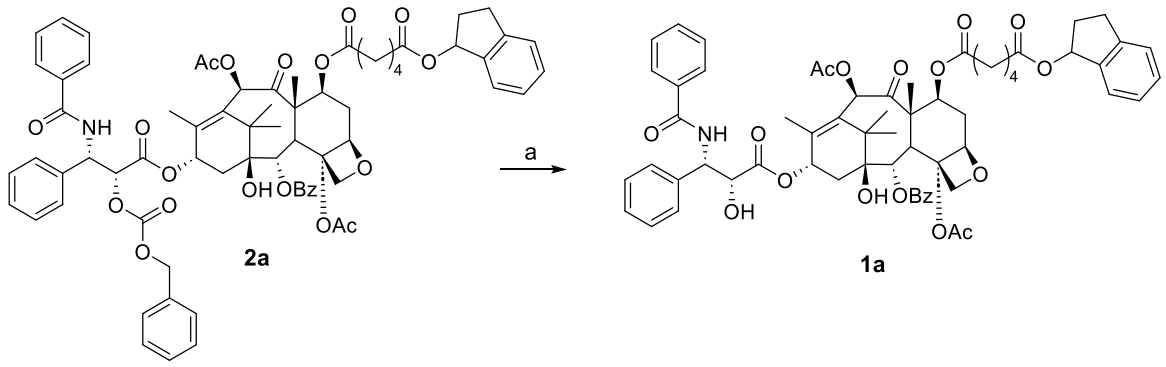

Scheme 4-11. Reaction conditions: a) H_2, 10%$_w$ Pd/C, MeOH, RT, 5h, 98% (**1a**).

The final synthetic step involved the cleavage of the 2'-benzyloxycabronyl group on compound **2a**, which I accomplished through catalytic hydrogenolysis, using hydrogen gas and palladium on carbon (Pd/C) in dry methanol (Scheme 4-11). The reaction was highly efficient, affording the C7-modified paclitaxel analog **1a** in nearly quantitative yield (98%) after a simple filtration on celite to remove the catalyst. Mass spectrometry and ^{1}H-NMR confirmed the formation of the expected product, the latter through the disappearance of the arylic signals in the range 7.54-7.44 ppm and of the methylene signal centered at 5.15 ppm, characteristic of the Cbz group. Another indicator of the reaction's success was the shift of the H-2' doublet from 5.46 to 4.82 ppm, similarly to what is observed in the spectrum of the parental drug, paclitaxel.

The overall yield of the multi-step synthesis to achieve target C7-modified taxane **1a** was 48% over three steps, starting from paclitaxel.

4.2.4.5 Synthesis of nonanedioic acid asymmetric ester amide 10b

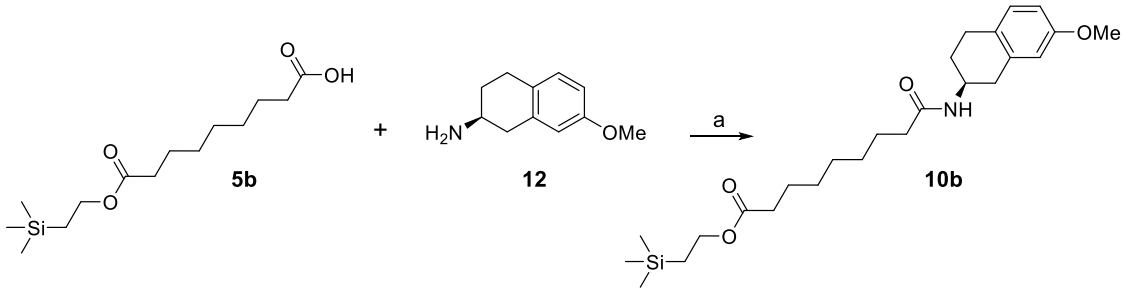

Scheme 4-12. Reaction conditions: a) EDC·HCl, DMAP, CH_2Cl_2/Py, RT, 4h, 98% (**10b**).

Similar to the previous approach, the first reaction towards the synthesis of our second target **1b** was the condensation reaction of nonanedioic acid monoester **5b** with (*S*)-7-methoxy-2-aminotetralin **12** (Scheme 4-12). The same conditions previously used for the formation of hexanedioic acid monoester **5a** performed remarkably well, with the complete consumption of the initial carboxylic acid occurring in only 4h and the recovery of compound **10b** in almost quantitative yield (98%) after flash chromatography purification. The

confirmation of amide bond formation came from the ^{1}H-NMR spectrum, where the signal of the hydrogen in position 2 of (*S*)-7-methoxy-2-aminotetralin shifted from 3.33 ppm toward 4.21 ppm in compounds **12** and **10b**, respectively.

4.2.4.6 Synthesis of nonanedioic acid amide derivative 9b

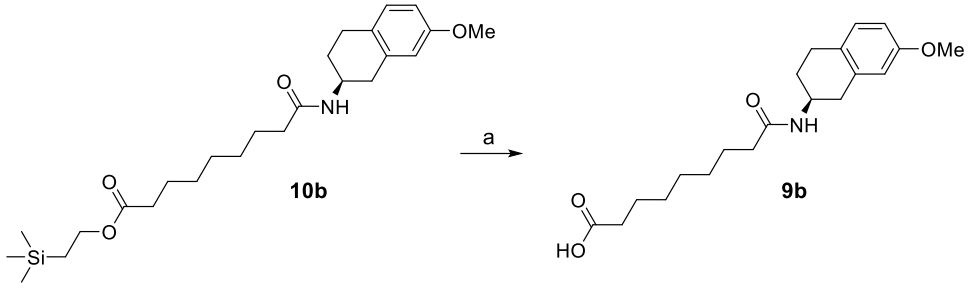

Scheme 4-13. Reaction conditions: a) TBAF, THF, -5°C to RT, 4h, 87% (**9b**).

Subsequently, I employed a treatment with TBAF to free the carboxyl moiety of compound **10b** and obtain nonanedioic acid amidic derivative **9b** (Scheme 4-13). Flash chromatography purification afforded **9b** in 87% yield, and ^{1}H-NMR analysis confirmed the occurred deprotection as the TSE signals disappeared.

4.2.4.7 Synthesis of nonanedioic acid amide derivative – 2'-O-Cbz-paclitaxel conjugate 2b

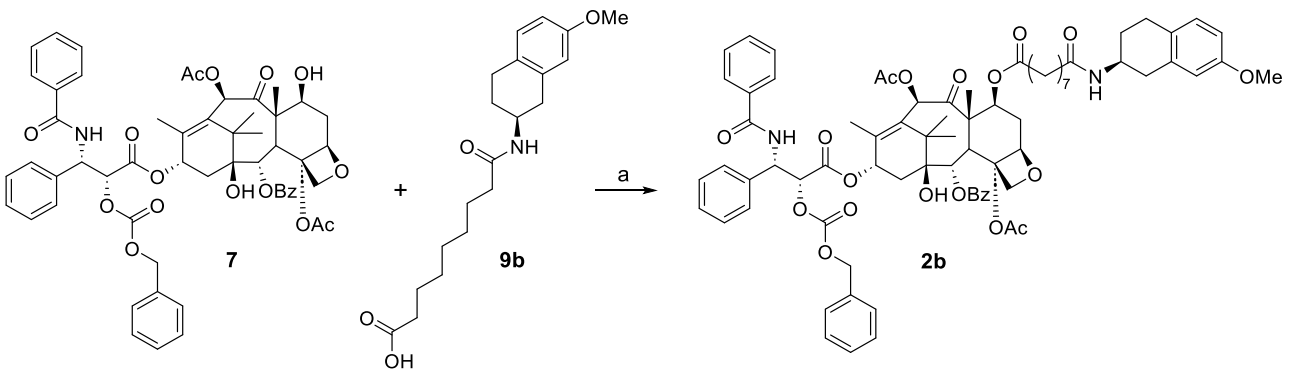

Scheme 4-14. Reaction conditions: a) DCC, DMAP, CH_2Cl_2, RT, 26h, 87% (**2b**).

The next step in the synthetic route was paclitaxel's decoration at the desired position 7. I carried out the conjugation of the decorated linker **9b** with 2'-*O*-Cbz-paclitaxel **7** employing the same protocol used for the synthesis of conjugate **2a**, i.e., DCC and DMAP in dichloromethane. Subsequent purification using Biotage® direct phase flash chromatography afforded compound **2b** in 87% yield. I was able to confirm the success of the esterification by the observed upfield shift of the signal of paclitaxel's H-7 in the ^{1}H NMR spectrum.

4.2.4.8 Synthesis of nonanedioic acid amide derivative – paclitaxel 1b

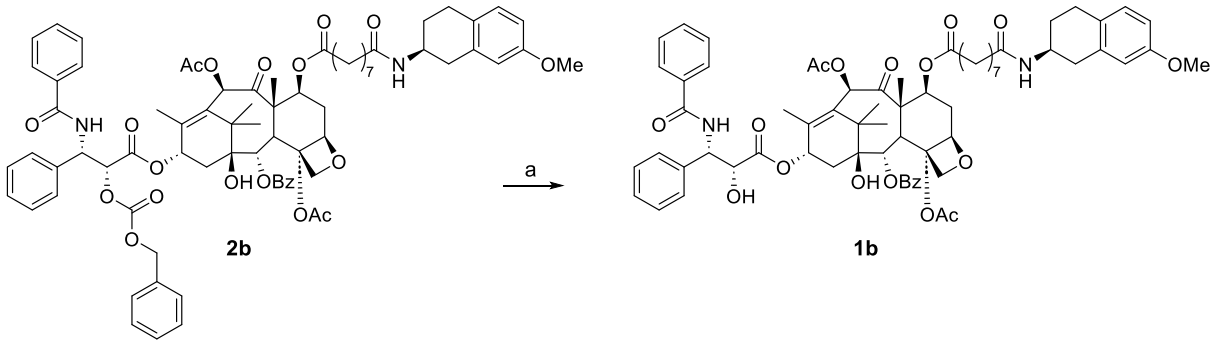

Scheme 4-15. Reaction conditions: a) H_2, 10%$_w$ Pd/C, MeOH, RT, 4h, 45% (**1a**).

The final reaction to achieve the target molecule **1b** was the palladium-catalyzed hydrogenolysis of **2b** that allows the deprotection of the hydroxyl group in position 2' (Scheme 4-15). Although the reaction was successful, the crude mixture contained several compounds with similar retention factors that were difficult to separate by direct flash chromatography. Therefore, I decided to employ the Biotage® automated chromatography system for purification, as it would allow me to follow in real-time the elution of the compounds via UV detection. After numerous attempts to optimize the elution conditions by varying the solvent ratio and gradient, I identified a slow isocratic elution strategy employing a 7:3 mixture of n-hexane and ethyl acetate as the most effective approach for the isolation of the target compound. With this method, I was able to successfully isolate pure compound **1b** in a moderate 45% yield. The overall yield of the multi-step synthesis to achieve the second C7-modified taxane **1b** from paclitaxel (three steps) was 38%.

4.2.5 Characterization of final compounds 1a and 1b

Organic compounds are typically good chromophores due to their structures' ability to absorb electromagnetic radiation. The molar extinction coefficient (ε) expresses the intensity of the radiation absorption at a given wavelength and hence, allows for the determination of the wavelength for which the absorbance is highest and thus more sensitive to the ligand concentration. It is often calculated from a known compound concentration using the Beer-Lambert law ($A = \varepsilon \cdot c \cdot l$) provided that the conditions of validity of the law are met. In fact, the linearity of the absorbance vs. concentration plot is valid only for low-concentration solutions of the analyte (usually < 0.01 M) when intermolecular processes are virtually absent, chemical reactions are excluded, and contribution of the instrumental errors tends to zero[148].

The recorded absorbance spectra of compounds **1a** and **1b** at a fixed concentration of 20 µM in spectroscopy-grade ethanol are reported in Figure 4-4. Compound **1b** has a clear local maximum of absorption at 278 nm, with a molar extinction coefficient of 3432 M^{-1} cm^{-1}. On the other hand, compound **1a** has a less pronounced local maximum at 271 nm, with a molar extinction coefficient of 3081 M^{-1} cm^{-1}.

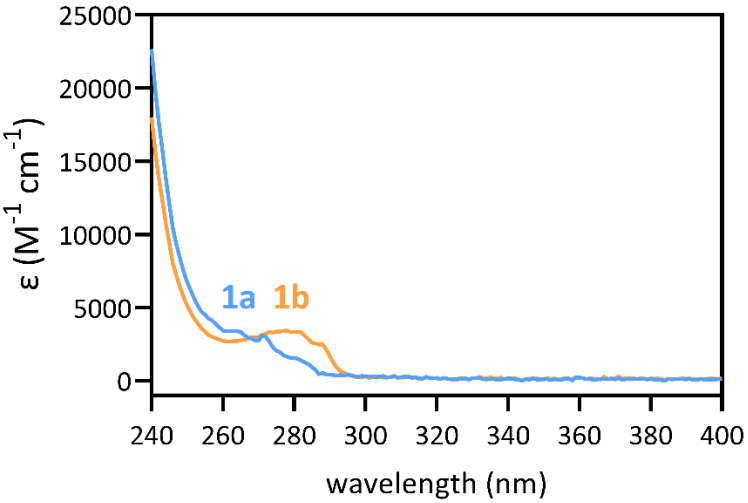

Figure 4-4. UV-Vis spectra of 20 µM solutions of compounds **1a** (steel blue) and **1b** (orange) in ethanol.

Paclitaxel and the other members of the taxane class are characterized by a diterpenoid centered around a bulky, complex and fused taxane ring decorated by several hydrophobic substituents, making them highly lipophilic compounds with poor aqueous solubility. Paclitaxel itself exhibits a solubility below 10 µg/L in aqueous medium[149], with estimations around 6.5 µM (from HMDB)[150]. In order to compare the solubility of the newly synthetized molecules **1a** and **1b** with that of their parental compound, I conducted some preliminary solubility tests in aqueous solution. Briefly, I dissolved the compounds at room temperature in aqueous phosphate buffer and compared to the UV-Vis spectra of the two solutions before and after ultracentrifugation at 100000 *x g* to remove precipitated compound. I repeated the trials at different concentrations ranging from 5 to 50 µM. Compound **1a** was completely soluble at the tested concentrations of 5 and 10 µM, whereas compound **1b** was only marginally soluble even at the lowest concentration tested, as indicated by a marked decrease in the intensity of the signal in the spectrum (not shown). The solubility issues of the taxane family of compounds must always be considered when interpreting experimental results, as the actual concentrations of the compounds in solution may be lower than the reported ones. However, it is also true that the high-affinity binding interaction with tubulin and microtubules subtracts free ligand from the solution, inducing an apparent increase in the compounds' solubility. This mechanism is also likely linked to increased drug concentrations in cellular assays. Indeed, several studies observed that paclitaxel accumulates to a different extent in different cell lines, with reports of treatments with low nanomolar concentrations resulting in clinically relevant intracellular concentrations of 1-9 µM[97,151].

4.3 Biochemical characterization of the interaction of C7-modified taxanes 1a and 1b with tubulin and microtubules

4.3.1 Effect of compounds 1a and 1b on tubulin assembly

Tubulin assembly dynamics can be monitored *in vitro* through time course turbidity measurements, as the increase in optical density of the solution is indicative of the formation of microtubules or other aggregates. As detailed in the Introduction section 1.3.2, the typical tubulin assembly curve exhibits a sigmoidal profile, consisting of a latent phase (tubulin nucleation), an exponential phase (increasing mass of microtubules appearing in solution) and a saturation phase (equilibrium of growing and shrinking microtubules governed by dynamic instability). Complete depolymerization occurs if the system runs out of GTP or the temperature falls dramatically, causing the absorbance to recover basal values. However, in the presence of MSAs such as paclitaxel the lag phase during which nucleation occurs is not observed due to the fast induction of tubulin assembly. Similarly, the equilibrium between growing and shrinking microtubules is never achieved due to the action of the compound that blocks microtubule dynamics. Instead, the absorbance signal reaches the maximum level corresponding to the total mass of microtubules that can be assembled at the concentration of tubulin used in the experiment.

In aqueous phosphate buffer at pH 6.7, in the presence of 1 mM GTP and 6 mM $MgCl_2$, tubulin is not prone to polymerize but will do so upon a temperature increase to 37°C in the presence of MSAs or unspecific assembly promoters such as glycerol and DMSO. Therefore, by monitoring tubulin assembly under non-polymerizing conditions in the presence of a ligand of interest, it is possible to determine whether that ligand behaves as a tubulin polymerization enhancer. To evaluate the effect of the newly synthesized compounds **1a** and **1b** on tubulin assembly, I performed turbidimetric assays under saturating conditions of the tested compounds (10% stoichiometry excess relative to tubulin), as described in section 3.2.7 of Materials and Methods. I compared their activity to that of paclitaxel and its fluorescent derivative, flutax-2, which served as reference compounds. The resulting polymerization curves are presented in Figure 4-5. While both paclitaxel (Figure 4-5, green) and flutax-2 (Figure 4-5, brown) induced microtubule assembly, the former was able to do so with higher potency. Regarding the newly synthesized compounds, the C7-modified taxane **1a** appears to be a good enhancer of microtubule assembly (Figure 4-5, light blue), with an activity comparable to that of paclitaxel. Instead, taxane **1b** is a much less potent polymerization promoter (Figure 4-5, orange), with an effect slightly above the poor assembly achieved by tubulin under these buffer conditions (Figure

4-5, grey) and below that of the fluorescence derivative flutax-2. These results show that while compound **1a** can be described as an MSA, compound **1b** cannot be considered as a good tubulin stabilizer.

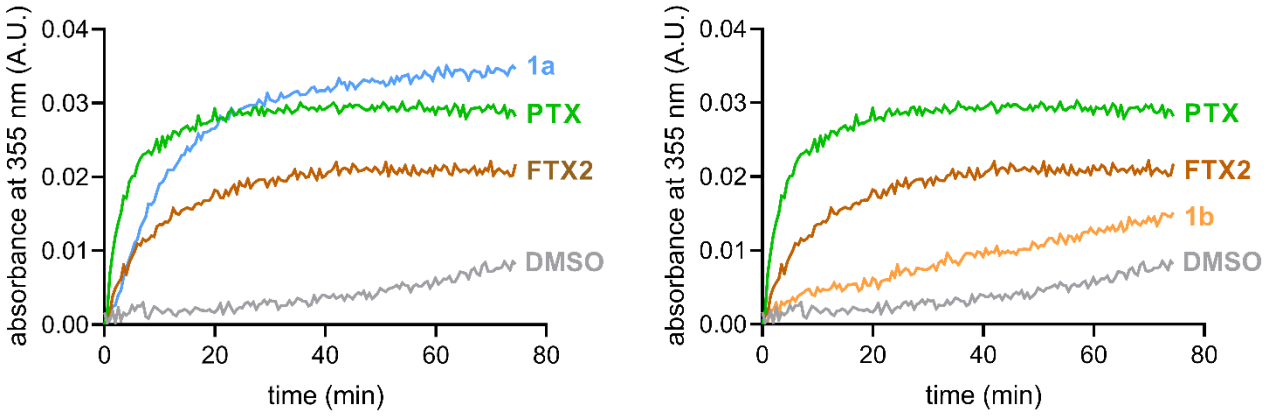

Figure 4-5. Effect of compounds **1a** and **1b** on tubulin assembly. Time courses polymerization of 25 µM tubulin in PEDTA buffer in the presence of vehicle (DMSO; gray line) or 27.5 µM of: paclitaxel (green line), flutax-2 (brown line), compound**1a** (light blue line, left panel), or **1b** (orange line, right panel).

4.3.2 Binding constant of compounds 1a and 1b to tubulin

In parallel, I also investigated the taxane site binding affinities of the newly synthetized compounds **1a** and **1b** via a competition assay with the fluorescent probe flutax-2. This is an established method[8] that tests the compounds' ability to displace flutax-2 from microtubules stabilized through a mild glutaraldehyde-crosslinking[132]. This method addresses two primary issues associated with the binding constant determination of taxane compounds. As this class of molecules typically exhibits high binding affinities, the first requirement is the use of a high-affinity fluorescent probe to observe the competition. Flutax-2 is ideally suited for this purpose, as its binding constant is in the order of 10^{-7} M^{-1} (see Table 3-1). The second requirement concerns the concentration of binding sites, which has to be comparable to the concentration of fluorescent probe employed (in the nanomolar or even picomolar range). This is crucial because an excess of free taxane binding sites would result in both compounds being fully bound to the microtubule, preventing any meaningful competition. However, such a low concentration would not support microtubule assembly, as it would be far below the critical concentration. The unspecific chemical stabilization produced by glutaraldehyde mild cross-linking solves this issue by stabilizing microtubules against dilution (as well as cold and MDAs) while maintaining the properties of the taxane binding site. In this way, it is possible to decrease the total amount of tubulin (i.e., binding sites) to be used in the experiment.

I conducted the competition assay by preparing samples at constant concentrations of both flutax-2 and binding sites while gradually increasing the concentrations of the competitor ligand. After a period of thermal equilibration, I quantified the displacement of flutax-2 by monitoring the change of fluorescence polarization between its bound and free form, a process detailed in section 3.2.10. Upon dissociation, the polarization of

the emitted light decreases as a freely moving molecule scrambles the emitted light by radiating it in different directions. Conversely, when bound to a larger molecule such as tubulin, the fluorescent probe tumbles more slowly, reducing the scrambling effect and increasing the fluorescence polarization value. I measured the displacement isotherms of each ligand at three different temperatures (26°C, 35°C, and 42°C), employing docetaxel, a commercially available taxane with known binding constant to microtubules, as a control to verify the results obtained.

Table 4-1 reports the final equilibrium binding constants (K_b) and dissociation constants (K_d) obtained. The calculated K_b values of docetaxel were comparable to the ones reported in literature[152] ($1.3 \cdot 10^7$ vs. $6.9 \cdot 10^7$ M^{-1} at 26°C, $1.0 \cdot 10^7$ vs. $3.9 \cdot 10^7$ M^{-1} at 35°C, $8.0 \cdot 10^6$ vs. $2.4 \cdot 10^7$ M^{-1} at 42°C) and similar to other measurements carried out in our laboratory. Concerning the investigated C7-modified taxanes, both compounds showed lower potency compared to docetaxel and the parental compound paclitaxel (K_b = $2.64 \cdot 10^7$ M^{-1} at 26°C, $1.43 \cdot 10^7$ M^{-1} at 35°C, $9.4 \cdot 10^6$ M^{-1} at 42°C)[152], with **1a** being the best of the two. In accordance with the polymerization assay results, compound **1a** showed a higher binding affinity (of one order of magnitude) for the taxane site than compound **1b** at 35°C and 42°C, though it was similar at the lowest temperature studied. These results suggest that the C7-decoration has a non-negligible effect on the interaction of the taxane core with tubulin.

Table 4-1. Calculated equilibrium binding constants and equilibrium dissociation constants of selected taxanes at different temperatures.

		Docetaxel	**1a**	**1b**
26°C	K_b [M^{-1}]	$(1.305 \pm 0.004) \cdot 10^7$	$(3.7 \pm 0.2) \cdot 10^5$	$(1.3 \pm 0.1) \cdot 10^5$
	K_d [M]	$(7.66 \pm 0.02) \cdot 10^{-8}$	$(2.7 \pm 0.2) \cdot 10^{-6}$	$(7.9 \pm 0.6) \cdot 10^{-6}$
35°C	K_b [M^{-1}]	$(1.0 \pm 0.1) \cdot 10^7$	$(2.56 \pm 0.07) \cdot 10^5$	$(7.8 \pm 0.8) \cdot 10^4$
	K_d [M]	$(1.1 \pm 0.2) \cdot 10^{-7}$	$(3.92 \pm 0.9) \cdot 10^{-6}$	$(1.3 \pm 0.1) \cdot 10^{-5}$
42°C	K_b [M^{-1}]	$(8 \pm 1) \cdot 10^6$	$(2.3 \pm 0.1) \cdot 10^5$	$(6.5 \pm 0.9) \cdot 10^4$
	K_d [M]	$(1.3 \pm 0.3) \cdot 10^{-7}$	$(4.4 \pm 0.3) \cdot 10^{-6}$	$(1.7 \pm 0.2) \cdot 10^{-5}$

Data are the mean ± SEM values of three independent experiments with duplicates in each one.

The observed negative correlation between the equilibrium binding constant and the temperature provides evidence that the association reaction of compounds **1a** and **1b** to the paclitaxel-binding site is enthalpy-

driven, as opposed to an entropy-driven reaction which becomes more probable with increasing temperature. By measuring the binding affinities at three different temperatures, I was able to estimate the enthalpic and entropic contributions to the standard Gibbs free energy for the association reaction (reported in Table 4-2). Figure 4-6 shows the Van't Hoff scatter plots (natural logarithm of the equilibrium binding constant vs. the reciprocal of the absolute temperature) relative to compounds **1a** and **1b**. Since taxanes don't exhibit any change in heat capacity upon binding[153], I applied a linear regression for data analysis and determined ΔH^0_{app}, which is related to the slope. Like other members of the taxane family, the association reaction of compounds **1a** and **1b** is exothermic, with ΔH^0_{app} values of -24 and -35 kJ mol^{-1}, respectively.

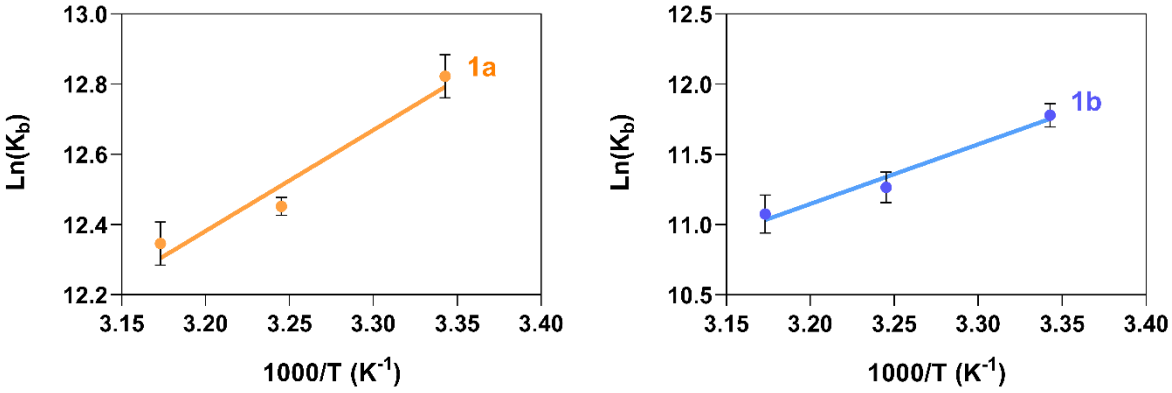

Figure 4-6. Van't Hoff plots of the equilibrium binding constants of compounds 1a and 1b at the assayed temperatures.

Table 4-2. Apparent thermodynamic parameters related to the binding of selected taxanes to the paclitaxel-binding site at different temperatures.

	Docetaxel	**1a**	**1b**
ΔG^0_{app} [kJ mol^{-1}] at 35°C	-41.3 ± 0.4	-31.90 ± 0.07	-28.9 ± 0.3
ΔH^0_{app} [kJ mol^{-1}]	-21 ± 8	-24 ± 4	-35 ± 7
ΔS^0_{app} [J mol^{-1} K^{-1}]	-66 ± 2	-27 ± 5	+20 ± 5

Standard free energies are reported as the mean ± SEM values of three independent experiments with duplicates in each one. Standard enthalpies and entropies are reported as calculated value ± SD.

4.4 Structural characterization of the interaction of 1a and 1b with microtubules

Although microtubules in cells are typically composed of 13 protofilaments, they can incorporate a variable number of protofilaments when assembled in solution. This variability can be influenced by the nucleotide used for inducing tubulin polymerization, as well as the presence of different partner proteins or MSAs. X-ray fiber diffraction is a powerful structural technique that provides accurate information on the average diameter, inter-protofilament distances, and axial interdimeric spacing of an *in vitro* microtubule population. It also provides information on the distribution of subpopulations according to their protofilament number. Compared to other structural techniques, X-ray fiber diffraction yields diffraction signals alone instead of three-dimensional structural information in real space, but it presents several advantages. The technique requires minimal sample preparation, and it allows the study of microtubules in their natural state in solution at 37°C, without the requirement of growing them from seeds which could affect the regularity of the lattice. Moreover, the technique yields ensemble-averaged results from millions of individual microtubules, resulting in high signal-to-noise ratios, while ensuring a precision in the measurements that is better than one-tenth of the employed X-ray wavelength[46,135]. Hence, this technique is ideally suited to study the structural effects of MSAs on the microtubule lattice, such are paclitaxel, flutax-2, and the C7-decorated taxanes **1a** and **1b**. The application of X-ray fiber diffraction to the study of microtubules and other biological filaments requires a uniform orientation of the fibers in solution to obtain diffraction patterns rather than scatter signals. Traditional alignment techniques, such as sedimentation induced by low-gravity centrifugations or generation of biased Brownian motion under strong magnetic fields, are time-consuming and can take several hours to weeks to achieve alignment. The issue was solved in 2009, when the research group of S. Kamimura reported a method to perform quick shear-flow alignment by adding 1% methylcellulose to the biological sample and inserting it into a rotating device[154]. In the experiments detailed below, I employed an optimized version of the shear-flow alignment technique that our research group has implemented at ALBA synchrotron (beamline NCD-SWEET) with the collaboration of the main developer S. Kamimura, as described in section 3.2.12 of Materials and Methods.

First, I studied microtubules polymerized from 50 µM tubulin in the presence of either 1 mM GTP (GDP microtubules, due to GTPase activity) or 0.25 mM GMPCPP (GMPCPP microtubules) to analyze two known lattice conformations: compacted and expanded[46]. GMPCPP is a non-hydrolysable GTP analog that binds the nucleotide E-site, producing fast tubulin polymerization and microtubule stabilization; its stabilizing effect has been related to the induction of an axial lattice expansion[36,37]. These experiments are routinely conducted at the beginning to fit the experimental set-up and ensure the high quality of the final images. For instance, one important parameter to optimize is the sample chamber volume (see section 3.2.12 of Materials and

Methods), which is adjustable by changing the number and thickness of the spacing ring slips. A bigger sample volume guarantees a better quality of the diffraction signals, but at the cost of a worse microtubule alignment. In the following experiments, I employed a chamber gap of 0.72 mm, improving the resolution of the images with respect to previous measurements performed with a gap of 0.36 mm.

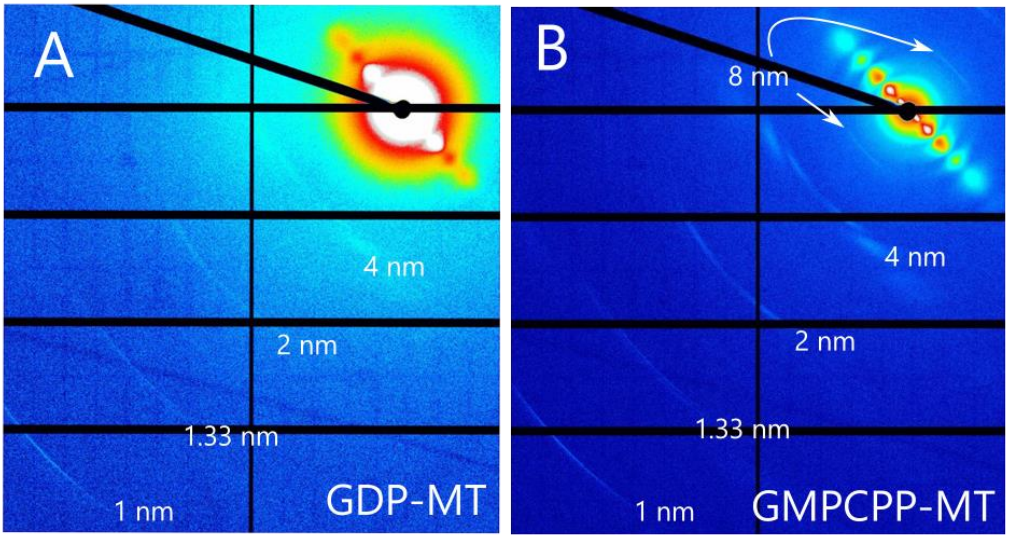

Figure 4-7. Logarithmic average fiber diffraction images of GDP microtubules (GDP-MTs, panel **A**) and GMPCPP microtubules (GMPCPPP-MTs, panel **B**). In both images, the 4 nm layer line (q = 1.57 nm^{-1}) and its harmonics at 2, 1.33 and 1 nm (q = 3.14, 4.72 and 6.22 nm^{-1}, respectively) are visible. In GMPCPP microtubules, the 8 nm layer line (q = 0.79 nm^{-1}), corresponding to the periodicity of the αβ-tubulin heterodimer, is also visible.

Figure 4-7 displays the typical fiber diffraction images obtained from GDP and GMPCPP microtubules in solution. In both images, the meridional profile showed the 4 nm layer line and the second, third and fourth harmonics at 2, 1.33 and 1 nm. The images displayed high signal-to-noise ratios, resulting in well-defined intensity profiles (reported in Figure 4-9 and Figure 4-10, gray lines in panels D and E).

As expected, the meridional intensity profile of GDP and GMPCPP microtubules exhibited variations in the 1 nm layer line peak positions (panels G of Figure 4-9 and Figure 4-10, gray lines) indicating differences in their respective monomer axial rises. The peaks, falling respectively at scattering vector values of 6.20 nm^{-1} and 6.02 nm^{-1}, allowed the calculation of the average axial spacings, which were consistent with those reported in published cryo-EM structures[155]: 4.05 nm vs. 4.075 nm for GDP microtubules and 4.18 nm vs. 4.16 nm for GMPCPP microtubules (Table 4-1). A distinctive feature of GMPCPP microtubules diffraction images was the appearance of an additional weaker set of layer lines at an approximate 8 nm axial spacing (q = 0.75 nm^{-1}), arising from the helical periodicity of the αβ-tubulin heterodimer. A previously reported hypothesis to explain its appearance links it to the increased differences in axial spacing between α- and β-tubulin, due to an asymmetrical dimer expansion[46]. This hypothesis agrees with previous models of GMPCPP microtubules, in which α-tubulin increases its axial spacing while β-tubulin remains unaltered[155].

Concerning the equatorial diffraction, the analysis involved the iterative fitting of the experimental intensities to a sum of Bessel functions of order J_0 + J_N (see section 3.2.13 of Materials and Methods). Specifically, I

limited the fitting to the third (J_{03}) and fourth (J_{04}+J_{N1}) peaks of the equatorial profile as their signal is less perturbated by the central X-ray beam. By deconvoluting the signal according to the proportion of microtubules with different protofilament numbers, I could determine the protofilament number distribution in a microtubule population. The results for GDP- and GMPCPP-MTs are reported in panels F of Figure 4-9 and Figure 4-10 (gray bars); GDP microtubules showed a more equilibrated Gaussian distribution from protofilament numbers 10 to 15, while GMPCPP microtubules displayed a preference for 13-, 14- and 15-protofilaments. This trend is summarized by the difference in their average protofilament number (12.9 vs. 13.6, Table 4-3); the calculated average radius varies accordingly to these results (11.4 vs. 11.7 nm, Table 4-3).

4.4.1 Effects of paclitaxel and flutax-2 on the microtubule lattice in different nucleotide binding states

Secondly, I analyzed the structure of the lattice of GDP and GMPCPP microtubules polymerized in the presence of paclitaxel and flutax-2 to compare the structural parameters of these reference compounds with the values of the investigated taxanes. As X-ray fiber diffraction offers a structural description averaged across the entire sample population, it is essential that all microtubules' taxane binding sites are occupied by the investigated compounds. To ensure this, I prepared the samples under saturating conditions, employing 50 µM tubulin and 100 µM compound. The addition of paclitaxel to both GTP-tubulin and GMPCPP-tubulin resulted in the appearance of the 8 nm layer line, while the analysis of the meridional profile estimated an average monomer length of 4.18 nm, confirming the expansion of the axial lattice. In contrast, the analysis of the meridional profile of GDP- and GMPCPP-MTs in the presence of flutax-2 displayed an average axial rise of 4.06 nm, indicating a compacted lattice in both experimental conditions.

Notably, the 8 nm layer line reflection (at q = 0.78 nm^{-1}) was also evident in these images. In this context, its presence likely resulted from the drug binding to the taxane site of each heterodimer, thereby originating an additional helical structure with 8 nm periodicity. Remarkably, due to the high image resolution, the third, fifth and seventh harmonics of the 8 nm layer line were also faintly visible. They fell at scattering vector values of 2.33, 3.89 and 5.44 nm^{-1}, respectively, that correspond to real axial distances of 2.7, 1.6 and 1.15 nm. The appearance of these higher-order reflections can be attributed to a superior signal-to-noise ratio stemming from better microtubule alignment in solution. This could be linked to a decreased microtubule flexibility induced by flutax-2 with respect to paclitaxel. Indeed, paclitaxel is known to enhance microtubule flexibility[156], and it is plausible that the distinct structural effects, both axially and longitudinally (as discussed below), induced by C7-modified taxanes might exert diverse influences on the overall rigidity of the microtubule. Another alternative hypothesis, still without experimental proof, is that C7-modified taxanes somehow induce the formation of shorter microtubules, which are more easily aligned by shearing.

Regarding the equatorial microtubule intensity profile, flutax-2 appeared to induce the formation of wider GDP and GMPCPP microtubules, with a prevalence of 13, 14 and 15-protofilaments microtubules in solution (panels F of Figure 4-9 and Figure 4-10, brown and ochre, respectively). Accordingly, the average radii are greater compared to the corresponding microtubules without drug: 11.8 nm vs. 11.4 nm for GDP microtubules, 12.4 vs. 11.7 nm for GMPCPP microtubules (Table 4-3). Conversely, samples polymerized in the presence of paclitaxel showed the opposite tendency, with lower mean protofilament numbers (12.4 vs. 12.9 for GDP microtubules, 12.5 vs. 13.6 for GMPCPP microtubules, Table 4-3) and radii (11.0 nm vs. 11.4 nm for GDP microtubules, 11.1 vs. 11.7 nm for GMPCPP microtubules, Table 4-3). Additionally, the estimated average inter-protofilament distances were similar under all these experimental conditions, and the lateral metrics of the reference compounds agreed with published SAXS measurements[92].

Table 4-3. Fiber diffraction analysis of microtubules in various nucleotide-bound states[a].

NT-bound state	GDP	GDP	GDP	GMPCPP	GMPCPP	GMPCPP
Compound	-	**paclitaxel**	**flutax-2**	-	**paclitaxel**	**flutax-2**
radius (nm)	11.4 ± 0.3	11.0 ± 0.2	11.8 ± 0.8	11.7 ± 0.4	11.1 ± 0.6	12.4 ± 0.3
avg. PF number	12.9 ± 0.5	12.4 ± 0.5	13.2 ± 0.7	13.6 ± 0.3	12.5 ± 0.6	13.9 ± 0.4
inter-PF dist. (nm)	5.5 ± 0.3	5.5 ± 0.3	5.6 ± 0.5	5.4 ± 0.2	5.5 ± 0.4	5.5 ± 0.2
avg. axial rise (nm)	4.05 ± 0.01	4.18 ± 0.01	4.06 ± 0.01	4.18 ± 0.01	4.18 ± 0.01	4.06 ± 0.01
1 nm band peak position (nm^{-1})	6.20 ± 0.01	6.02 ± 0.01	6.19 ± 0.01	6.02 ± 0.01	6.02 ± 0.01	6.19 ± 0.01

[a] Data are Mean ± StdErr

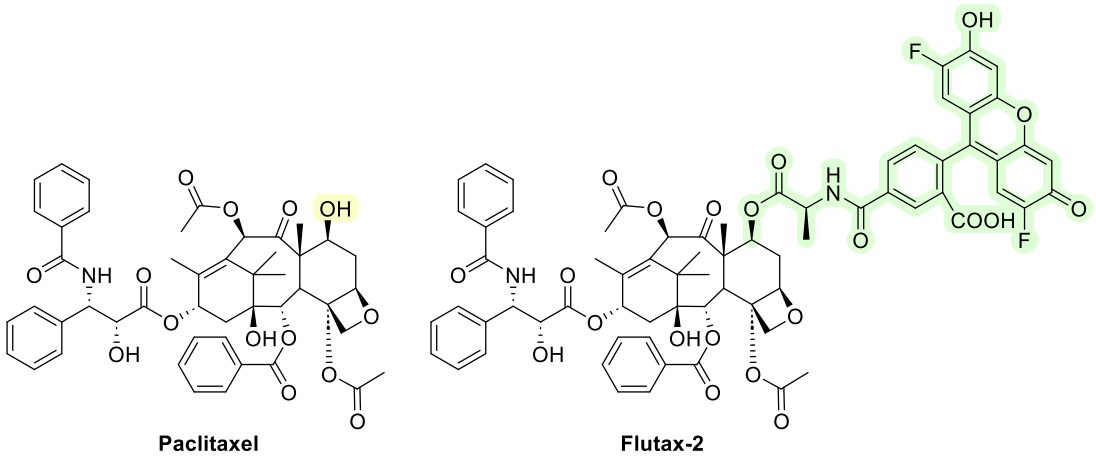

Figure 4-8. Chemical structures of paclitaxel and flutax-2.

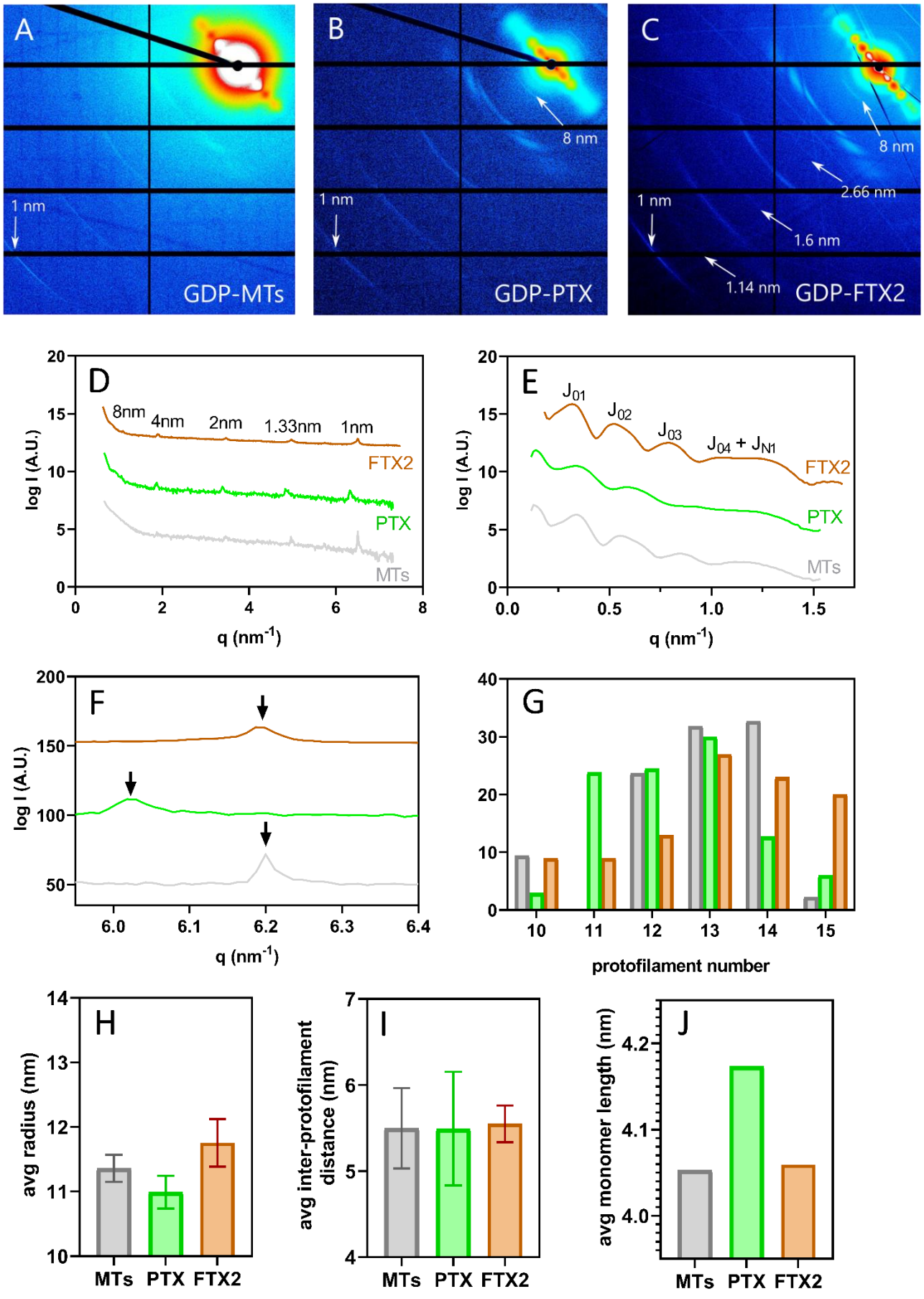
A
1 nm
GDP-MTs
B
8 nm
1 nm
GDP-PTX
C
8 nm
2.66 nm
1 nm
1.6 nm
1.14 nm
GDP-FTX2
D
8nm
4nm
2nm
1.33nm
1nm
FTX2
PTX
MTs
log I (A.U.)
q (nm-1)
E
J01
J02
J03
J04 + JN1
FTX2
PTX
MTs
log I (A.U.)
q (nm-1)
F
log I (A.U.)
q (nm-1)
G
protofilament number
H
avg radius (nm)
MTs PTX FTX2
I
avg inter-protofilament distance (nm)
MTs PTX FTX2
J
avg monomer length (nm)
MTs PTX FTX2

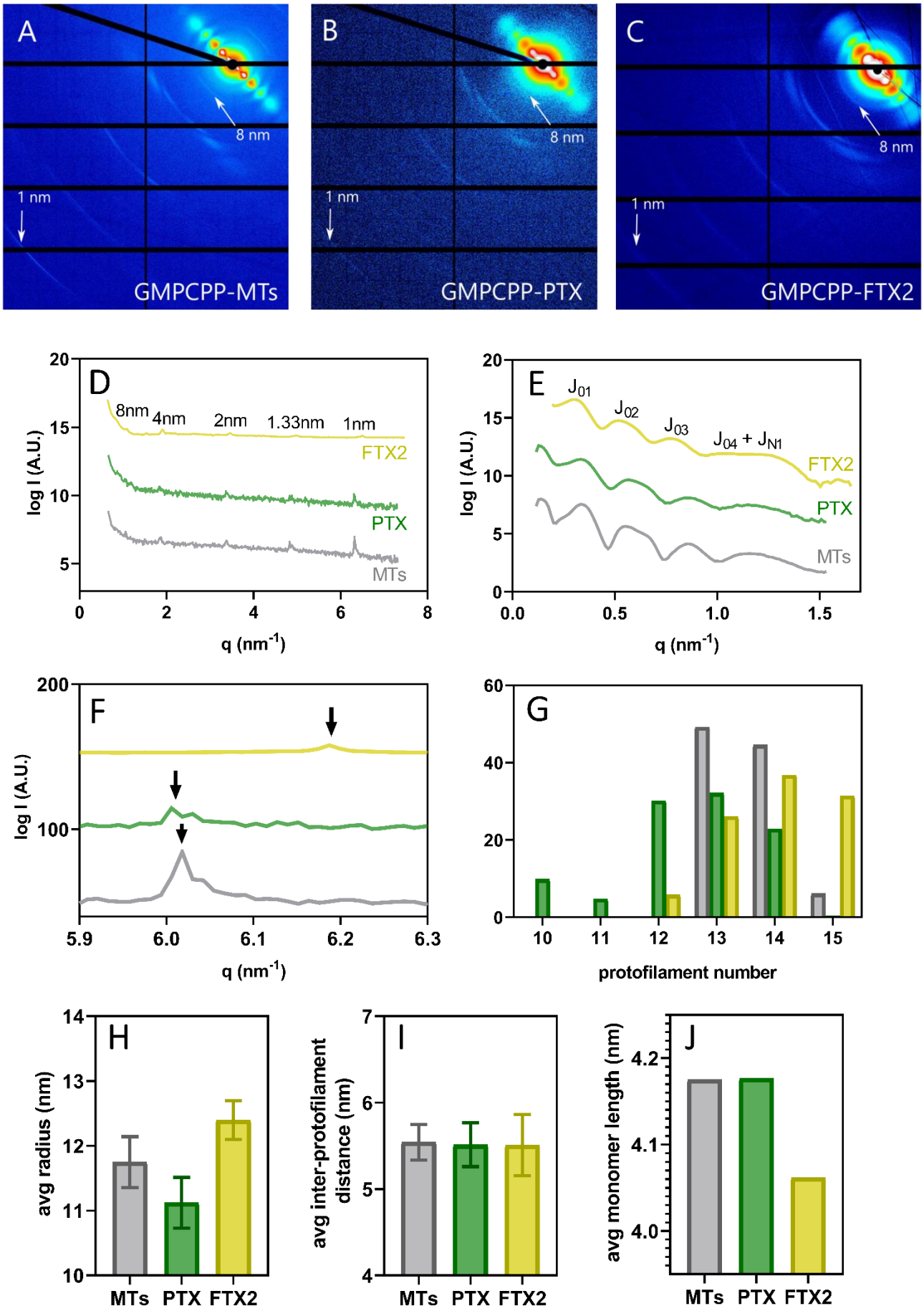
A
8 nm
1 nm
GMPCPP-MTs
B
8 nm
1 nm
GMPCPP-PTX
C
8 nm
1 nm
GMPCPP-FTX2
D
8nm 4nm 2nm 1.33nm 1nm
FTX2
PTX
MTs
log I (A.U.)
q (nm-1)
E
J01
J02
J03
J04 + JN1
FTX2
PTX
MTs
log I (A.U.)
q (nm-1)
F
log I (A.U.)
q (nm-1)
G
protofilament number
H
avg radius (nm)
MTs PTX FTX2
I
avg inter-protofilament distance (nm)
MTs PTX FTX2
J
avg monomer length (nm)
MTs PTX FTX2

Figure 4-9. Effect of paclitaxel (PTX, light green) and flutax-2 (FTX2, brown) on the GDP-microtubule lattice, compared to reference GDP microtubules (MTs, gray). Panels **A**, **B** and **C**: logarithmic average fiber diffraction images of GDP microtubules, indicating the presence of the 1 nm layer line (fourth harmonic of the reflection arising from the tubulin monomer periodicity). Remarkably, in panels **C**, the third, fifth, and seventh harmonics of the 8 nm layer line (arising from the heterodimer periodicity) are also visible, falling at q = 2.33 nm^{-1}, 3.89 nm^{-1}, 5.44 nm^{-1}, respectively. Panel **D**: experimental meridional intensity profiles, describing the position of the 4 nm layer lines and their harmonics. Panel **E**: experimental equatorial intensity profiles, describing the position of the Bessel functions maxima. Panel **F**: enlargement of the equatorial intensity profile between q = 5.8 and q = 6.3 nm^{-1}. The 1 nm layer line peak position is indicated by a black arrow. Panel **G**: estimated frequency distribution of protofilament numbers for each experimental condition. Panel **H**: calculated microtubule radii for each experimental condition. Data are presented as mean ± SEM. Panel **I**: calculated microtubules inter-protofilament distances for each experimental condition. Data are presented as mean ± SEM. Panel **J**: calculated microtubules axial monomer length for each experimental condition. Data are presented as mean ± SEM.

Figure 4-10. Effect of paclitaxel (PTX, green) and flutax-2 (FTX2, ochre) on the GMPCPP-microtubule lattice, compared to reference GMPCPP microtubules (MTs, dark gray). Panels **A**, **B** and **C**: logarithmic average fiber diffraction images of GMPCPP microtubules, indicating the presence of the 1 nm layer line and the 8 nm layer line. Panel **D**: experimental meridional intensity profiles, describing the position of the 4 nm layer lines and their harmonics. Panel **E**: experimental equatorial intensity profiles, describing the position of the Bessel functions maxima. Panel **F**: enlargement of the equatorial intensity profile between q = 5.8 and q = 6.3 nm^{-1}. The 1 nm layer line peak position is indicated by a black arrow. Panel **G**: estimated frequency distribution of protofilament numbers for each experimental condition. Panel **H**: calculated microtubule radii for each experimental condition. Data are presented as mean ± SEM. Panel **I**: calculated microtubules inter-protofilament distances for each experimental condition. Data are presented as mean ± SEM. Panel **J**: calculated microtubules axial monomer length for each experimental condition. Data are presented as mean ± SEM.

4.4.2 Effects of 1a and 1b on the microtubule lattice in different nucleotide binding states

I then proceeded to the acquisition and analysis of fiber diffraction images of GDP and GMPCPP microtubules polymerized in the presence of compounds **1a** and **1b** (Figure 4-12 and Figure 4-13 panels A and B). I also included in the pool of investigated compounds an additional fluorescent taxane already present in our laboratory[157], referred to as hexaflutax. The structure of this compound, reported in Figure 4-11, differs from flutax-2 for the substitution of the di-fluoro-fluorescein moiety with a simpler fluorescein moiety and for the longer aliphatic linker connecting it to the taxane core, which was originally introduced to allow the binding of a fluorescein-targeting monoclonal antibody.

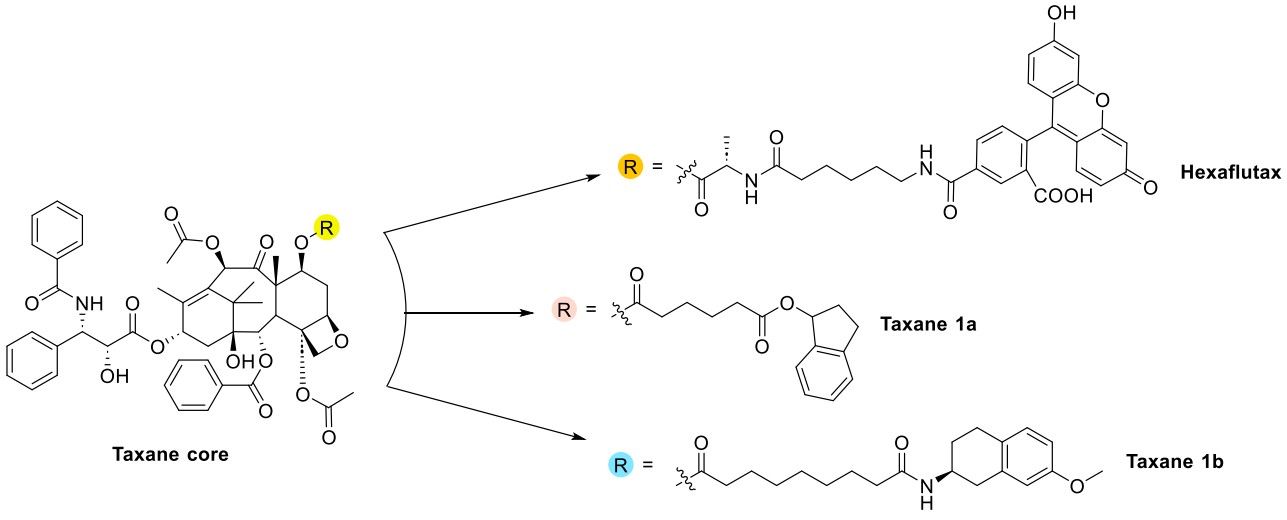

Figure 4-11. Chemical structure of hexaflutax, C7-modified taxane **1a** and **1b**.

The calculated metrics of the microtubules, along with their corresponding standard errors, are reported in Table 4-4. The analysis of the meridional profiles of GDP-microtubule images revealed a 1 nm band peak position of 6.20 nm^{-1} for all the investigated compounds, corresponding to a real space monomer length of 4.05 nm, indicating a compacted axial lattice. Instead, for microtubules polymerized in presence of GMPCPP and either compound **1a**, **1b** or hexaflutax the intensity maximum of the 1 nm layer line fell at q = 6.02 nm^{-1}, which corresponds to an average monomer length of 4.18 nm, suggesting an expanded axial lattice. Therefore, all the analyzed compounds exhibited a more "structurally neutral" behavior compared to flutax-2 and paclitaxel, as none of them induced axial structural changes in either GDP- or GMPCPP-microtubules lattices.

The equatorial intensity profiles of GDP microtubules treated with the compounds in pre-assembly revealed the formation of wider microtubules – with average protofilament numbers of 13.9 (**1a**), 13.3 (**1b**), and 13.5 (hexaflutax) – compared to the non-stabilized ones (12.9, Table 4-3) and those stabilized in the presence of paclitaxel (12.4, Table 4-3), thus denoting a similar effect to that observed in the presence of flutax-2. As expected, the average radius followed a similar trend, with GDP-**1a** microtubules being the largest at 24.2 nm diameter, while inter-protofilament distances remained close to those of reference microtubules. For GMPCPP microtubules polymerized in the presence of compounds **1a** and **1b** the average protofilament number and mean radius (13.4 and 13.6; 12 nm and 11.8 nm) were similar to the reference values (13.6; 11.7 nm; Table 4-3). However, a slightly larger radius was observed in the presence of hexaflutax, which was attributed to a greater inter-protofilament distance (5.7 nm) rather than an increased mean protofilament number.

Table 4-4. Fiber diffraction analysis of microtubules in various nucleotide-bound states[a].

NT-bound state	GDP	GDP	GDP	GMPCPP	GMPCPP	GMPCPP
compound	**1a**	**1b**	**hexaflutax**	**1a**	**1b**	**hexaflutax**
radius (nm)	12.2 ± 0.5	11.6 ± 0.3	12.0 ± 0.3	12.0 ± 0.3	11.8 ± 0.3	12.2 ± 0.3
avg. PF number	13.9 ± 0.5	13.3 ± 0.4	13.5 ± 0.6	13.4 ± 0.5	13.6 ± 0.5	13.2 ± 0.4
inter-PF dist. (nm)	5.5 ± 0.3	5.4 ± 0.2	5.5 ± 0.3	5.6 ± 0.3	5.4 ± 0.2	5.7 ± 0.3
avg. axial rise (nm)	4.05 ± 0.01	4.05 ± 0.01	4.05 ± 0.01	4.17 ± 0.01	4.17 ± 0.01	4.17 ± 0.01
1 nm band peak position (nm^{-1})	6.20 ± 0.01	6.20 ± 0.01	6.20 ± 0.01	6.02 ± 0.01	6.02 ± 0.01	6.02 ± 0.01

[a] Data are Mean ± StdErr

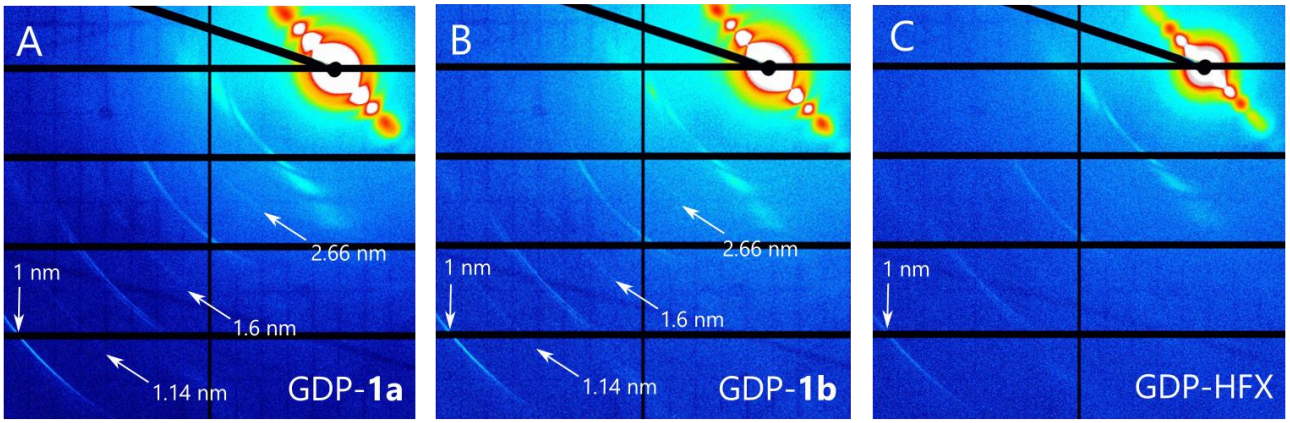
A
2.66 nm
1 nm
1.6 nm
1.14 nm
GDP-1a
B
2.66 nm
1 nm
1.6 nm
1.14 nm
GDP-1b
C
1 nm
GDP-HFX

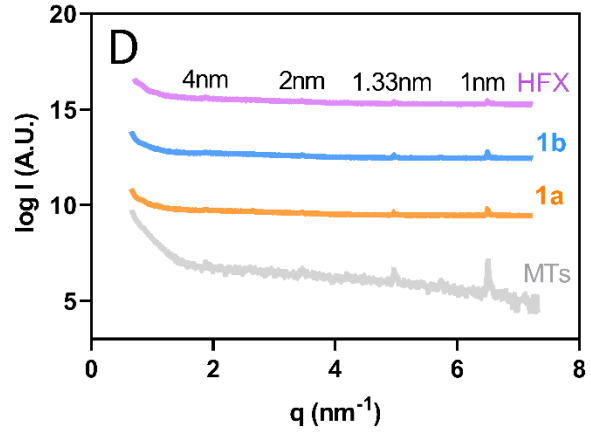
D
4nm
2nm
1.33nm
1nm
HFX
1b
1a
MTs
log I (A.U.)
q (nm-1)

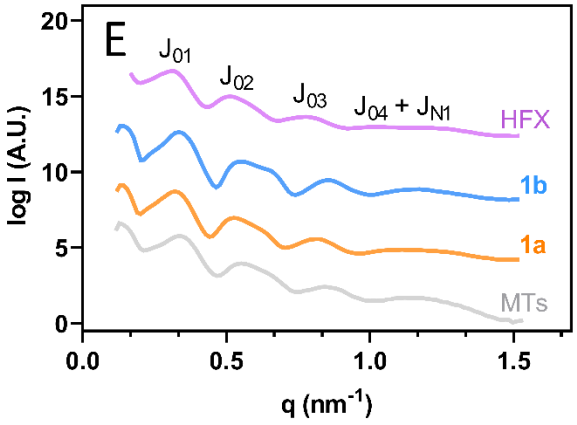
E
J01
J02
J03
J04 + JN1
HFX
1b
1a
MTs
log I (A.U.)
q (nm-1)

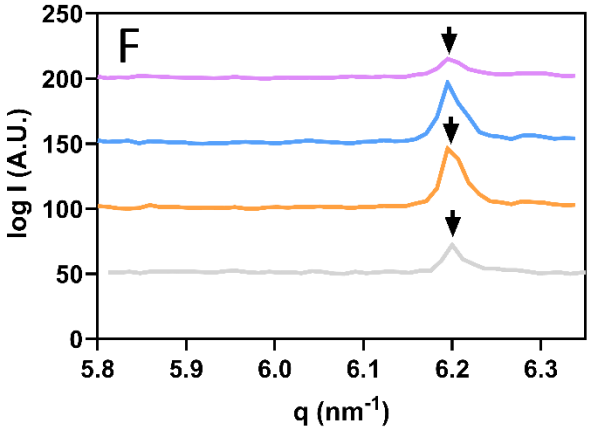
F
log I (A.U.)
q (nm-1)

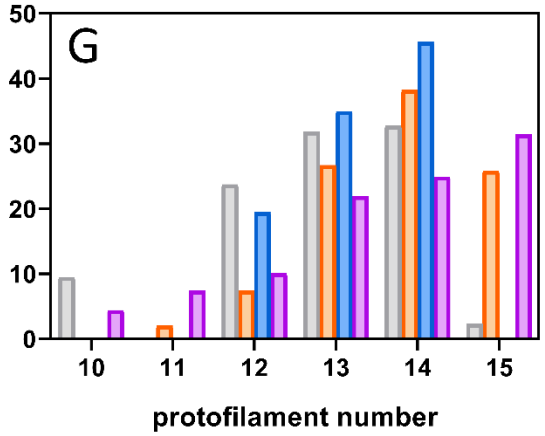
G
protofilament number

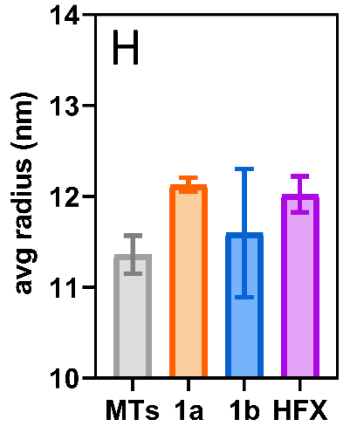
H
avg radius (nm)
MTs 1a 1b HFX

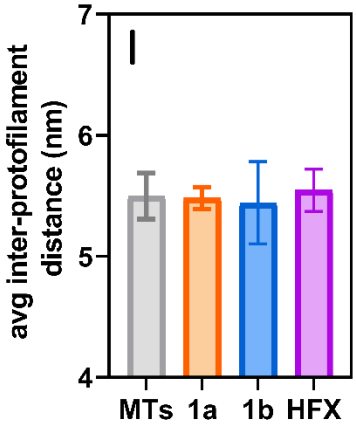
I
avg inter-protofilament distance (nm)
MTs 1a 1b HFX

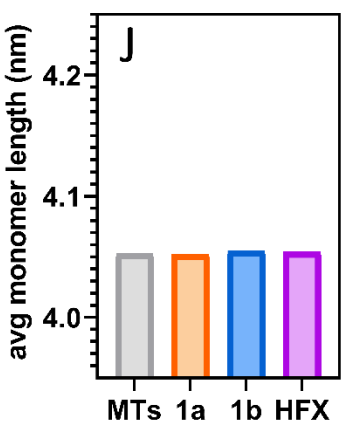
J
avg monomer length (nm)
MTs 1a 1b HFX

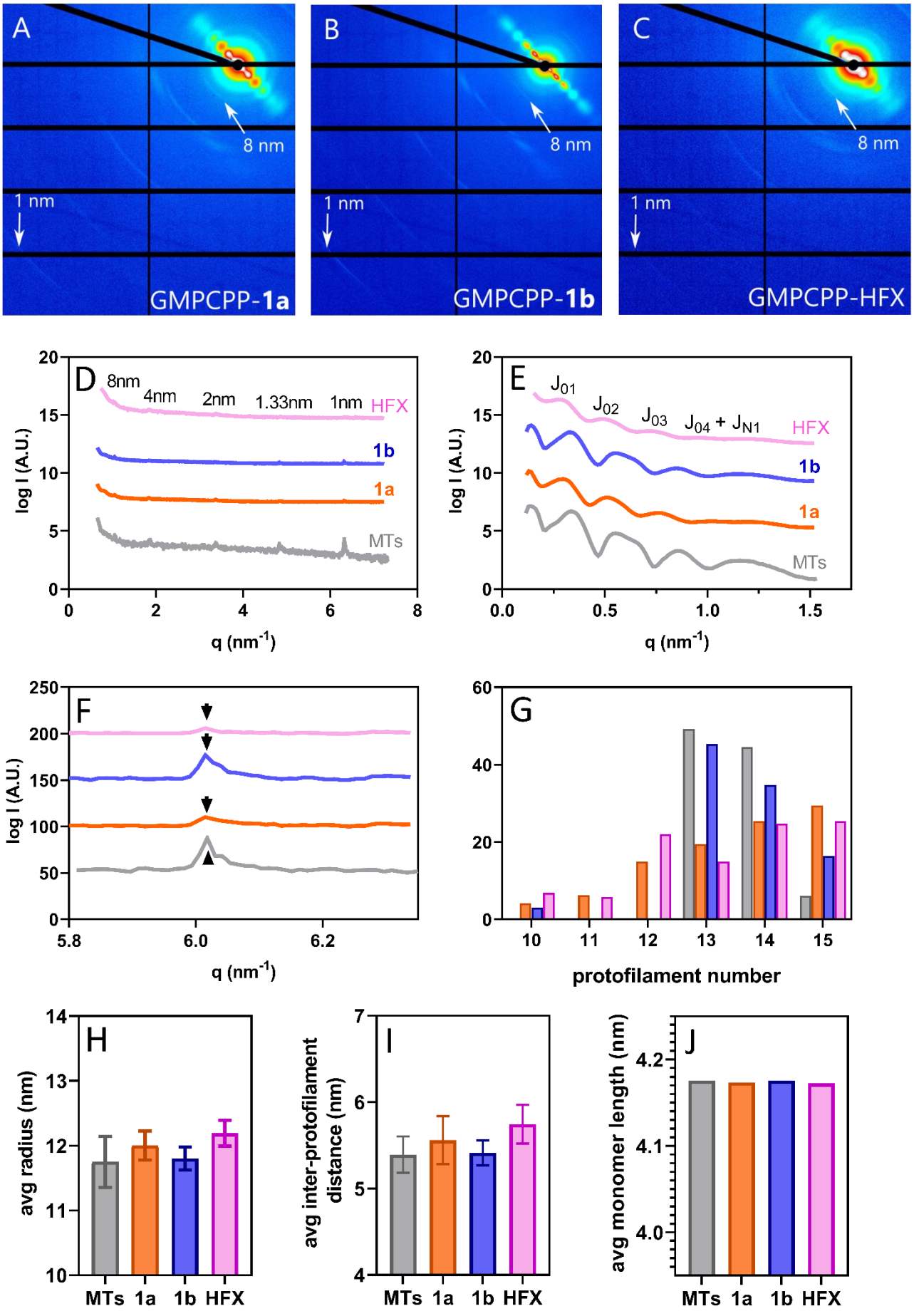
A
8 nm
1 nm
GMPCPP-1a
B
8 nm
1 nm
GMPCPP-1b
C
8 nm
1 nm
GMPCPP-HFX
D
8nm
4nm
2nm
1.33nm
1nm
HFX
1b
1a
MTs
log I (A.U.)
q (nm-1)
E
J01
J02
J03
J04 + JN1
HFX
1b
1a
MTs
log I (A.U.)
q (nm-1)
F
log I (A.U.)
q (nm-1)
G
protofilament number
H
avg radius (nm)
MTs 1a 1b HFX
I
avg inter-protofilament distance (nm)
MTs 1a 1b HFX
J
avg monomer length (nm)
MTs 1a 1b HFX

Figure 4-12. Effect of compound **1a** (orange), **1b** (light blue) and hexaflutax (HFX, lavender) on the GDP-microtubule lattice, compared to reference GDP microtubules (MTs, gray). Panels **A**, **B** and **C**: logarithmic average fiber diffraction images of GDP microtubules, a white arrow indicates the position of the 1 nm layer line (fourth harmonic of the reflection arising from the tubulin monomer periodicity). Remarkably, in panels **A** and **B**, the third, fifth, and seventh harmonics of the 8 nm layer line (arising from the heterodimer periodicity) are also visible, falling at q = 2.33 nm^{-1}, 3.89 nm^{-1}, 5.44 nm^{-1}, respectively. Their positions are marked by white arrows. Panel **D**: experimental meridional intensity profiles, describing the position of the 4 nm layer lines and their harmonics. Panel **E**: experimental equatorial intensity profiles, describing the position of the Bessel functions maxima. Panel **F**: enlargement of the equatorial intensity profile between q = 5.8 and q = 6.3 nm^{-1}. The 1 nm layer line peak position is indicated by a black arrow. Panel **G**: estimated frequency distribution of protofilament numbers for each experimental condition. Panel **H**: calculated microtubule radii for each experimental condition. Data are presented as mean ± SEM. Panel **I**: calculated microtubules inter-protofilament distances for each experimental condition. Data are presented as mean ± SEM. Panel **J**: calculated microtubules axial monomer length for each experimental condition. Data are presented as mean ± SEM.

Figure 4-13. Effect of compound **1a** (orange-red), **1b** (blue) and hexaflutax (HFX, pink) on the GMPCPP-microtubule lattice, compared to reference GMPCPP microtubules (MTs, dark gray). Panels **A**, **B** and **C**: logarithmic average fiber diffraction images of GMPCPP microtubules, indicating the presence of the 1 nm layer line (fourth harmonic of the reflection arising from the tubulin monomer periodicity), and of the 8 nm layer line (first harmonic arising from the heterodimer periodicity). Panel **D**: experimental meridional intensity profiles, describing the position of the 4 nm layer lines and their harmonics. Panel **E**: experimental equatorial intensity profiles, describing the position of the Bessel functions maxima. Panel **F**: enlargement of the equatorial intensity profile between q = 5.8 and q = 6.3 nm^{-1}. The 1 nm layer line peak position is indicated by a black arrow. Panel **G**: estimated frequency distribution of protofilament numbers for each experimental condition. Panel **H**: calculated microtubules radii for each experimental condition. Data are presented as mean ± SEM. Panel **I**: calculated microtubules inter-protofilament distances for each experimental condition. Data are presented as mean ± SEM. Panel **J**: calculated microtubules axial monomer length for each experimental condition. Data are presented as mean ± SEM.

4.5 Cellular effects of C7-modified taxanes 1a and 1b

4.5.1 Effect of compounds 1a and 1b on cell viability

I investigated the impact of compounds **1a** and **1b** on cell's viability across several different cell lines, comparing it to the parental and clinically used drug paclitaxel. I employed the colorimetric MTT (3-(4,5-dimethylthiazol-2-yl)-2,5-diphenyltetrazolium bromide) cell viability assay, originally described by T. Mosmann in 1983[158], to quantify the number of viable cells post-drug treatment. This assay measures the enzymatic reduction of a yellow tetrazolium salt (MTT) into purple formazan crystals by metabolically active cells, due to the activity of NADH and NAPH-dependent oxidoreductases. It is important to note that the assay does not provide a direct result in terms of cellular death, as cells that are still alive but not metabolizing are not counted. Instead, it measures the number of cells with an active mitochondrial respiratory chain, providing a reliable indication of the cells' ability to proliferate after the incubation with the tested compounds. By analyzing the data obtained at different drug concentrations, I determined the concentration of drug at which half of the cellular population in no longer viable (IC_{50}). This parameter is commonly used to determine the potency of a drug effect in a specific cell line, allowing for comparisons between different drugs or across cell lines. I investigated viability post-drug treatment across a panel of five different cell lines: a male epithelial lung carcinoma cell line (A549) and four female epithelial cervical cancer cell lines (HeLa, HeLaβIII, and HeLa-derived Kb-3.1 and Kb-V1). HeLaβIII and Kb-V1[159,160] are resistant subclones of the reference lines HeLa and Kb-3.1. They model the two most common mechanisms of chemoresistance observed in paclitaxel-treated cancer cells: altered expression of β-tubulin isotypes and increased drug efflux,

respectively. The former refers to the positive correlation observed by several studies between the cellular upregulation of certain β-tubulin isotypes (specifically, β-III and β-IVa) and paclitaxel-resistance[161,162]. The latter refers to the decreased drug accumulation in tumoral cells linked to the overexpression of P-gp, of which paclitaxel is a known substrate[102].

Table 4-5 presents the measured IC_{50} values for the parental drug paclitaxel and for the C7-modified taxanes **1a** and **1b**. These results indicate that paclitaxel is significantly more potent than compounds **1a** and **1b** across all five cell lines, but still, the new derivatives retain an effect in the sub-micromolar range. Specifically, compound **1b** performed slightly better than analog **1a** in four out of five cell lines (A549, HeLa, Kb-3.1 and Kb-V1), with IC_{50} values approximately half that of **1a**. Only in HeLaβIII cells did compound **1a** display a lower IC_{50} than **1b**, which may suggest that mutations in the taxane binding site of β-III tubulin were affecting the binding of the latter molecule more significantly.

The resistance/sensitivity ratio (R/S) allows for comparison of a drug's effect on a mutated resistant cell line (R) versus the parental sensitive one (S). An R/S ratio of approximately 1.0 indicates no discernible difference in the IC_{50} values of the compound between the two cell lines, suggesting the compound's ability to override the resistance mechanism. Conversely, a value greater than one indicates resistance of the mutant cell line to the compound. None of the compounds studied were able to override the resistance mechanisms involving PgP or β-III tubulin overexpression. However, it is interesting to note that both compounds **1a** and **1b** exhibited lower R/S ratios than paclitaxel, particularly in the mechanism involving the overexpression of tubulin β-III isotype.

Table 4-5. IC_{50} of investigated taxanes in A549, HeLa, HeLaβIII, Kb-3.1 and Kb-V1 cell lines. [a]

Cmpd	IC_{50} A549 [nM]	IC_{50} HeLa [nM]	IC_{50} HeLaβIII [nM]	R/S HeLa: HeLaβIII	IC_{50} Kb-3.1 [nM]	IC_{50} Kb-V1 [nM]	R/S Kb-3.1: Kb-V1
paclitaxel	3.1 ± 0.7	1.2 ± 0.4	28.7 ± 0.7	24	2.4 ± 0.2	2700 ± 600	1125
1a	510 ± 40	180 ± 20	510 ± 80	3	280 ± 30	>40000	>142
1b	220 ± 20	100 ± 20	720 ± 80	7	150 ± 20	19000 ± 1000	127

[a] Data are the mean ± SEM values of three independent experiments with duplicates in each one.

4.5.2 Effect of compounds 1a and 1b on cellular microtubular network during the cell cycle

Aiming to evaluate the impact of C7-modified taxanes **1a** and **1b** on the intracellular microtubule network, mitotic spindle, and general cellular morphology, I employed indirect immunofluorescence staining to visualize the microtubule cytoskeleton and DNA contents and distribution in A549 cells incubated with various concentrations of the investigated compounds. Due to their voluminous cytoplasm and flat morphology, A549 cells are particularly well-suited for cytoskeleton visualization with this technique, which allows for the imaging of multiple components of pre-treated cells through the use of specific antibodies tagged with fluorophores.

The pre-treatment of the cells involves several passages, including cells' permeabilization, fixation, and a step to block antibodies non-specific binding [163]. The permeabilization step is essential to visualize intracellular epitopes for which antibodies require access to the inside of the cell. Common methods include the use of organic solvents or detergents to weaken the phospholipidic membrane. In my experiments, I achieved permeabilization by briefly incubating the cells with 0.05% Triton X-100, a non-ionic surfactant. The subsequent fixation step involves immobilizing the cells to their support, in order to prevent autolysis and preserve cell morphology for extended periods of time. The ideal fixation method should immobilize targeted cellular components while maintaining maximum antigenicity and minimizing disturbance to the overall cellular architecture. To this aim, I incubated the cells with 3.7% paraformaldehyde, a cross-linking agent that reacts with cellular components via nucleophilic addition, thus forming intra and intermolecular methylene bridges. However, the fixation and permeabilization processes can lead to cell shrinkage and distortion of cellular structures. To minimize these effects, I performed a preliminary incubation of the cells with a buffer containing 4% polyethylene glycol 8000 (PEG 8000), a long chain polyether that acts as a supporting matrix, hence helping to maintain the structural integrity of the cells throughout the immunofluorescence protocol. The final preparatory step is a blocking procedure aimed at preventing antibodies from binding to non-target epitopes. Blocking reagents should ideally have no affinity for the target epitopes, high binding rates to non-target reactive sites, and stabilize cellular morphology. As antibodies are forced to compete with the blocking protein for non-target epitopes, unspecific binding can be reduced. In my experiments, I employed a 3% solution of bovine serum albumin (BSA) for this purpose.

Following these preliminary steps, antibodies can be applied using either a direct or indirect immunofluorescence method. In the direct method, the fluorophore label is conjugated directly to the primary antibody that reacts with the target epitope. The indirect method involves a two-step incubation process: first, a primary antibody binds to the target epitope, then a fluorophore-tagged secondary antibody recognizes and binds to the primary antibody. I used an indirect method employing a combination of a primary anti-alpha-tubulin antibody from mice and a fluorescent secondary anti-mouse antibody to mark the

microtubule network. Additionally, I used a fluorescent intercalating DNA-agent, 4',6-diamidino-2-phenylindole (DAPI), to stain chromatin and further observe changes in nuclear morphology. Finally, I visualized the stained cells in an epifluorescence microscope, acquiring images in different phases of the cell cycle. Figure 4-14 and Figure 4-15 compare the immunofluorescence images acquired from A549 cells treated with DMSO, paclitaxel and the C7-modified taxanes **1a** or **1b** at interphase and mitosis.

During interphase, control cells (treated with vehicle) exhibit a radial distribution of microtubules, that are more concentrated in the perinuclear region and less dense towards the periphery (panel A1, Figure 4-14 and Figure 4-15), and a single and well-defined nucleus (panel A2, Figure 4-14 and Figure 4-15). During mitosis, the cells' dimensions significantly decrease as they adopt a typically rounded shape and constrict of the volume to enable efficient chromosome capture[164]. Microtubules reorganize into a bipolar mitotic spindle (panel A4, Figure 4-14 and Figure 4-15) and, after the disappearance of the nucleolus and the condensation of chromatin in chromosomes, these start to align on the *metaphase* or *equatorial plate* (panel A5, Figure 4-14 and Figure 4-15), an imaginary line equidistant from the centrosome poles along which the centromeres of the chromosomes align before being separated into each of the two daughter cells.

Upon treatment with 100 nM paclitaxel, the interphase microtubule array of A549 cells shows evident alterations, in particular the appearance of cytoplasmic microtubule bundles with a non-radial distribution (panel B1, Figure 4-14 and Figure 4-15) accompanied by a clearing of the central region of the cytosol. Another effect of paclitaxel treatment is the presence of an aberrant nuclear morphology (panel B2, Figure 4-14 and Figure 4-15). This is the result of a highly stable microtubule network unable to promote dynamic instability during segregation, thus leading to the formation of multinucleated cells from clusters of mis-segregated uncondensed chromosomes. The causes of mitotic arrest must be researched in the formation of an abnormal mitotic spindle (panel B4, Figure 4-14 and Figure 4-15) that typically exhibits multiple poles and a characteristic star-like shape. This abnormal morphology leads to the appearance of several metaphase plate-like structures (panel B5, Figure 4-14 and Figure 4-15). All these features can be regarded as hallmarks of taxane treatment, as they have been described in several previous studies[96,165,166].

The treatment with compound **1a** at a concentration comparable with the IC_{50} value (600 nM) induces several features typical of the taxane phenotype. During interphase, A549 cells feature a more densely packed microtubule array (panel C1 of Figure 4-14) and multi-nucleation (panel C2 of Figure 4-14), while during mitosis they exhibit multicentered mitotic spindles and the impairment of chromosome alignment on the equatorial plate (panels C4 and C5 of Figure 4-14). Increasing the concentration of the compound to 2 µM (approximately four times the IC_{50} value) and 8 µM (~12 times the IC_{50}), the cellular landscape is more closely related to that observed in the presence of paclitaxel, with the typical formation of microtubule bundles in

the interphase cytoplasm and a clearing of microtubules in the central perinuclear region. Mitosis is similarly affected no matter the concentration of the compound used (panel C6, D6 and E6 of Figure 4-14).

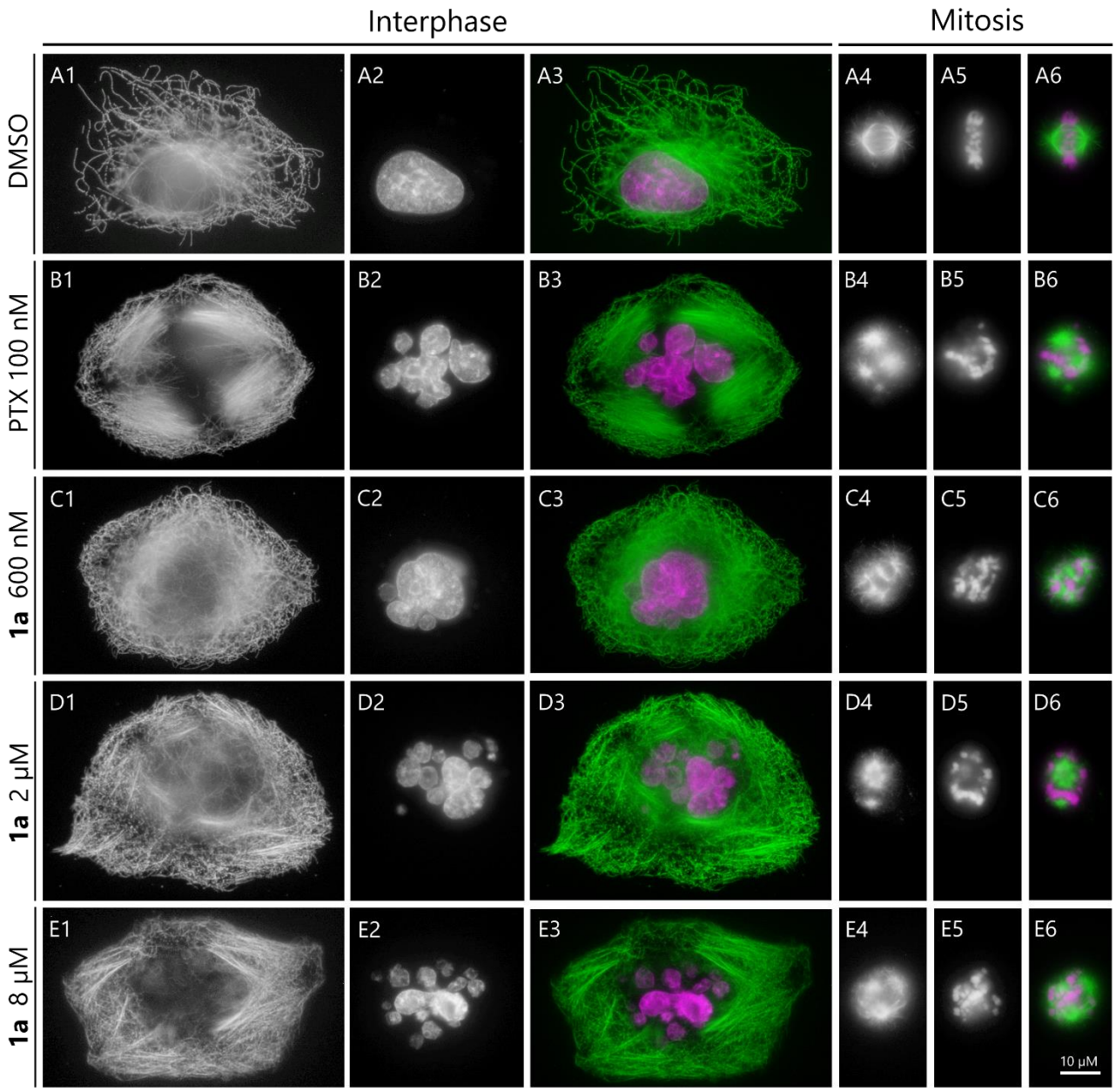

Figure 4-14. Immunofluorescence images of A549 cells with secondary staining of α-tubulin (green) and DAPI staining of chromatin (pink). The images compare representative morphologies of cells treated with DMSO (control, row **A**: maximum volume employed in the other experiments), paclitaxel (PTX, row **B**: 100 nM), and increasing concentration of compound **1a** (row **C**: 600 nM; row **D**: 2 µM, row **E**: 8 µM). For each condition, columns **1**, **2** and **3** show the cytoskeletal and nuclear morphology of a cell during interphase; columns **4**, **5** and **6** show the cytoskeletal and nuclear morphology of a cell during mitosis. All images presented have the same magnification. The bar in panel E6 represents 10 µm.

Similar morphologies characterize cells treated with the second C7-modified taxane analog **1b**. The higher potency of this compound in A549 cells compared to compound **1a** is evident in the appearance of the taxane-associated phenotype at lower concentrations. At near-IC_{50} concentration (300 nM), the density of the interphase microtubule array is already noticeably increased, with the presence of small bundles and a central clearing in the perinuclear region (panel C1, Figure 4-14). At 1 µM concentration, larger microtubule bundles that closely resemble the ones induced by paclitaxel appear (panel D1, Figure 4-14). At both concentrations, the formation of star-shaped, multipolar spindles (panels C4 and D4, Figure 4-14) leads to the formation of several micronuclei (panels C2 and D3, Figure 4-14).

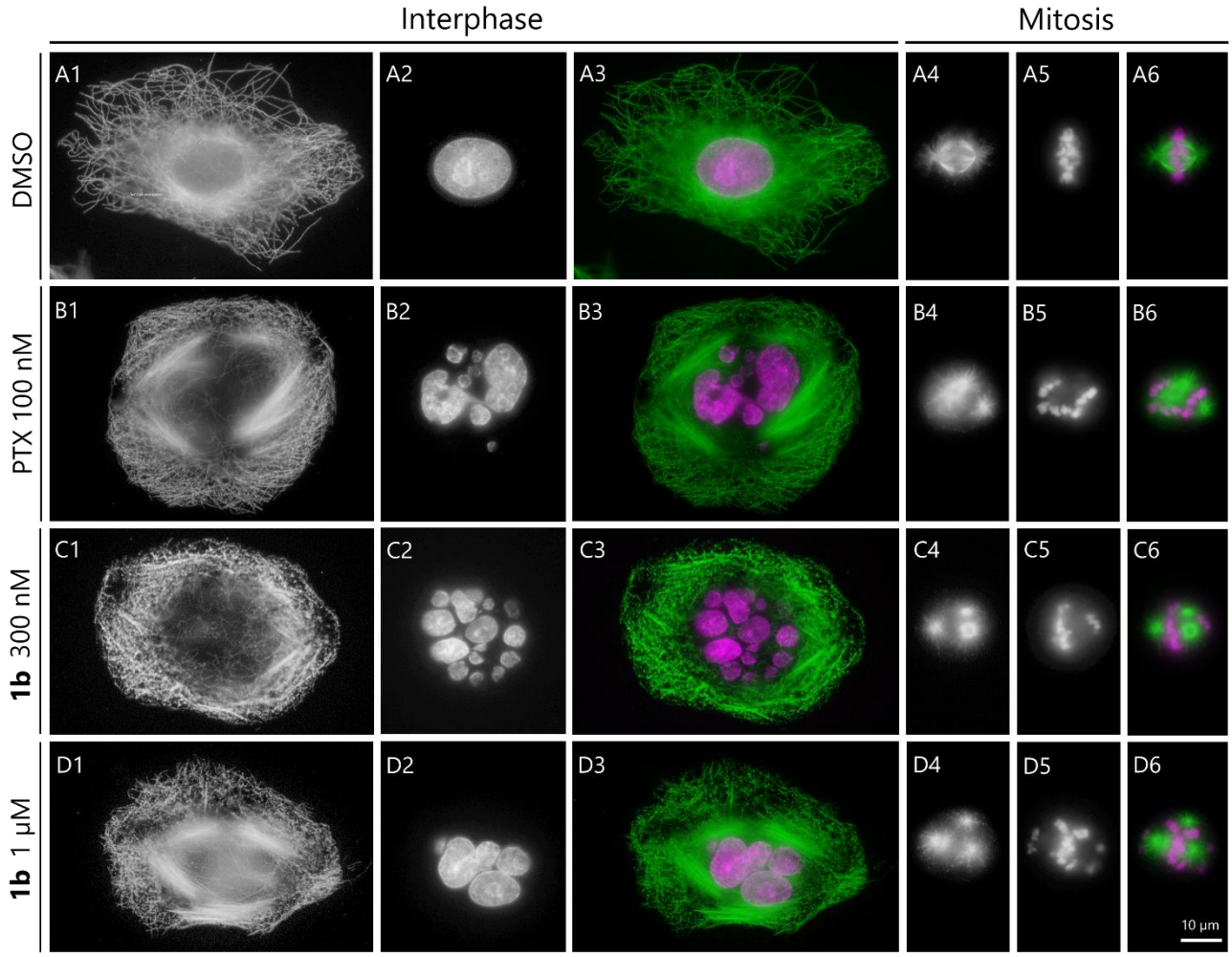

Figure 4-15. Immunofluorescence images of A549 cells with secondary staining of α-tubulin (green) and DAPI staining of chromatin (pink). The images compare representative morphologies of cells treated with DMSO (control, row **A**: maximum volume employed in the other experiments), paclitaxel (PTX, row **B**: 100 nM), and increasing concentration of compound **1b** (row **C**: 300 nM; row **D**: 1 µM). For each condition, columns **1**, **2** and **3** show the cytoskeletal and nuclear morphology of a cell during interphase; columns **4**, **5** and **6** show the cytoskeletal and nuclear morphology of a cell during mitosis. All images presented have the same magnification. The bar in panel D6 represents 10 µm.

4.5.3 Effect of compounds 1a and 1b on microtubule-mediated intracellular transport

As previously described in section 1.4.2, microtubule-mediated intracellular transport is essential for proper cell functioning, as it ensures the efficient movement of molecules and organelles within the cell. By acting as distribution system of nutrients, proteins, and energy-carrying molecules like ATP, while removing waste products, it helps maintain cellular homeostasis, support metabolic processes, and regulate cell signaling pathway. Neurons are particularly reliant on efficient intracellular transport due to their branched and elongated morphologies, which make active transport essential for cargo movement from the cell body to the synaptic termini (kinesin-mediated anterograde transport) and *vice versa* (dynein-mediated retrograde transport). This explains why neurons are particularly susceptible to deficits in this process which may arise from the impairment of microtubule's dynamic instability caused by MTAs. Indeed, patients undergoing MTA-based treatments frequently encounter peripheral neurotoxicity and neutropenia, which stand out as the most prevalent and clinically significant dose-limiting side effects.

Therefore, studying intracellular transport in the presence of MTAs is crucial for finding an effective solution to the ongoing challenge of mitigating MTA-induced neurotoxicity. Traditional methods for tracking and visualizing intracellular trafficking involved the labeling of the transported biomolecules[167]. In early research, newly synthesized biomolecules were labeled with radioactive precursors, and incorporated radioactivity was subsequently assessed using autoradiography coupled to electron microscopy or cellular fractionation[168]. Later, the development of protein-based tools[169,170] like horseradish peroxidase (HRP) simplified labeling. After the discovery and subsequent engineering of green fluorescent protein (GFP) and red fluorescent protein (DsRed), a great variety of fluorescent proteins with different excitation and emission wavelengths, photophysical properties and ion sensitivities become available. However, fluorescent proteins are limited by their large size, which can affect the targeted probes, and their weak photoluminescence. This stimulated the evolution of new, highly fluorescent small molecules from early carbocyanine dyes, leading to the development of the current range of commercially-available mitochondria-specific Mitotrackers and acidic organelle-specific lysotracker dyes. The expansion in protein- and dye-based probes has been accompanied by significant advancements in microscopy techniques, from Nomarski differential interference contrast (DIC) and video-enhanced contrast DIC (AVEC-DIC) microscopy to widefield, confocal, two-photon, super-resolution, and magnetic resonance imaging methods[171].

However, the indirect assessment of intracellular tracking obtained by labelling transported cargos presents an important drawback: alterations found using indirect methods could be related to failures in the intracellular transport machinery but also consequence of an alteration in the transported cargo, which complicates the understanding of the system. For this reason, recent research in the field of intracellular

transport has switched the focus to the direct labelling of motor proteins. This topic is addressed in a recently published research paper[115] (2022), product of a collaboration between our laboratory and Dr. María del Valle Palomo Ruiz's research group from Instituto Madrileño de Estudios Avanzados en Nanociencia (IMDEA Nanociencia). The paper reports the development of new fluorescently-labeled peptide probes to monitor the movement of kinesin and dynein molecular motors along microtubules in live cells. Specifically, the tracking peptides consist of three moieties with distinct functionalities: (1) a cell penetrating domain located in the C-terminus, containing eight arginines (R_8) to facilitate the peptides cellular uptake; (2) a kinesin or dynein-binding domain; (3) a fluorophore binding region, designed to enable conjugation with a Cyanine5 far red-fluorescent dye via a maleimide-thiol reaction. Figure 4-16 depicts the complete structures of the Cyanine5 – kinesin and dynein binding peptides (Cy5-KBP and Cy5-DBP). The kinesin binding motif, composed of 10 amino acids, was selected from a previously published peptide sequence extracted from the membrane protein alcadein, which is known to bind the tetratricopeptide repeat (TDR) domain of kinesin[172]. On the other hand, the 19-amino acid dynein binding motive was chosen from a set of published viral peptide sequences that are reported to bind to dynein motor proteins. These viruses strategically co-opt the host cell's intracellular transport machinery to promote their replication and dissemination. Specifically, the selected sequence derives from the African swine fever virus[173].

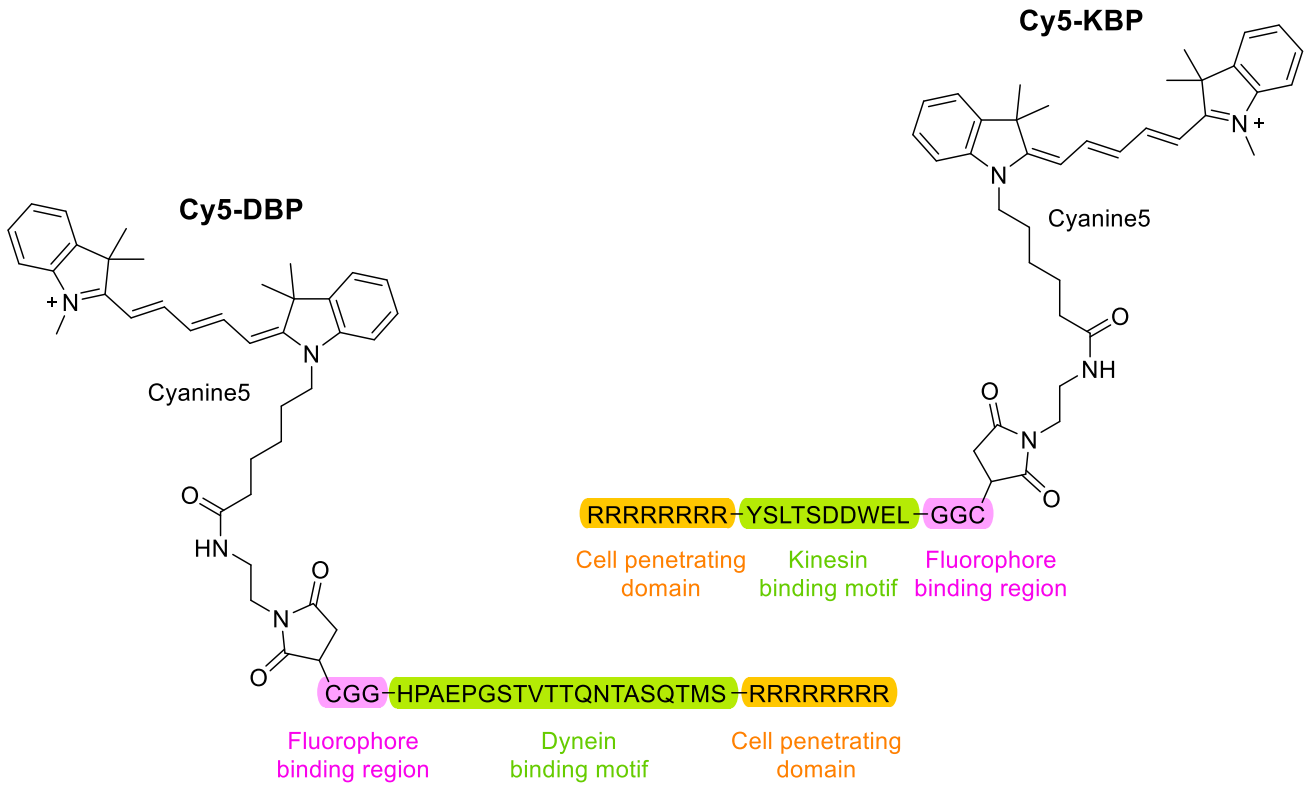

Figure 4-16. Structures of Cy5-KBP and Cy5-DBP. The three different functional moieties are highlighted in different colors: the fluorophore binding region in pink, the motor binding motive in green and the cell penetrating domain in orange.

In order to evaluate the effect on axonal transport of compounds **1a** and **1b**, as well as that of the reference compounds paclitaxel and flutax-2, I carried out time-lapse motility experiments of kinesin and dynein motors in neuroblastoma SHSY5Y cells employing the aforementioned fluorescent tracking peptides. To study the effects of taxane compounds on intracellular transport without causing mitotic arrest and compromising cell viability, I treated the cells with high drug concentrations (1 µM paclitaxel or flutax-2, 2.5 µM **1a** or **1b**) for a relatively brief incubation time, ranging from 1 to 2.5 hours (including imaging time). Due to their lower potency compared to the reference compounds, I increased the concentration of compounds **1a** and **1b** to a level where the characteristic microtubule bundles became visible in immunofluorescence images. I monitored the movement of the fluorescent probes within the treated cells using a confocal microscope, capturing 3-min movies of frames taken every 1.739 s as 2-layer-z-stacks. Finally, I analyzed the particle behavior considering three parameters: mean track displacement, mean track velocity, and the ratio of transported over constrained motion (TM/CM), which indicates changes in the displacement mode of the peptides over time. I used the TrackMate plug-in in Fiji® software for mean track displacement and velocity analysis, and MATLAB software for the TM/CM ratio calculation. The latter was determined by performing a mean square displacement analysis, which allowed me to classify the observed particle movement into three categories: Brownian or diffusive motion, constrained motion (CM), and transported motion (TM). Constrained motion refers to sub-diffusive motion, and typically indicates hindrance to free diffusion by steric obstacles or by friction resulting from motion through a (continuum) viscoelastic medium. On the contrary, transport induced by molecular motors and other active processes result in super diffusion. It is important to note that in all the experiments, a constant “non-mobile” fraction of particles (about 25% of the total) can be observed, which is categorized as Brownian motion.

Table 4-6 presents the normalized particle movement parameters relative to compounds **1a** and **1b**, as well as the reference compounds paclitaxel and flutax-2 (see Figure 4-17 for a comparison with untreated cells). Overall, the results obtained with paclitaxel treatment are consistent with published data referring to transport motion in epithelia A549 cells[115]. Specifically, the proportion of Cy5-KBP-tagged particles and the mean displacement were respectively reduced by 16% and 20% compared to the control (while in A549 cells were 17% and 16%). However, while in A549 cells there was no significant change in the Cy5-KBP mean velocity, the mean speed measured in these experiments showed a reduction of 14%. The impact of paclitaxel on dynein-mediated transport appeared equally evident, with a decrease in the proportion of transported motion of 21% compared to the control (27% in A549 cells). Similarly, the distance covered by Cy5-DBP diminished by 19%, whereas the mean speed remained unaltered.

Interestingly, flutax-2 treatment had different consequences on the movement of Cy5-KBP and Cy5-DBP. All the parameters associated with kinesin-mediated transport were slightly reduced, with a decrease of the TM/CM ratio, track mean distance and speed of 12%, 9% and 15%, respectively. However, the fraction of

DBP-transported particles as well as the track mean distance of the dynein motor remained unchanged. Even more surprisingly, the mean speed of the retrograde transport appeared to increase by 20% compared to the control. These results underscore significant differences in motor tracking behavior along microtubules depending on the stabilization agent employed, indicating that drug-induced structural alterations of the microtubule lattice may have notable implications for cellular trafficking.

Overall, the impact on intracellular transport of the two newly synthetized taxanes **1a** and **1b** was more subtle, with **1a** exhibiting the closest-to-neutral effect on motor proteins of the entire taxane series analyzed. Treatment of the cells with 2.5 µM of compound **1a** did not result in any statistically significant variation in the ratio of kinesin-mediated transport motion or in the observed velocity and displacement of Cy5-KBP probes. Conversely, treatment with compound **1b** appeared to be slightly more disruptive. Although the mean TM/CM ratio remained unaltered, both the track mean displacement and the mean speed of KBP molecules were reduced by 15% and 13%, respectively, which is closely similar to the effect of paclitaxel and flutax-2. Concerning the motion analysis of the retrograde trafficking, both compounds exhibited similar behavior: the TM/CM ratio was slightly reduced (15%), but the velocity and distance covered by Cy5-DBP remained unaltered compared to the control.

Table 4-6. Particle movement parameters normalized to control measured in SHSY5Y cells with Cy5-tracking peptides. [a]

	TM/CM **Cy5-KBP**	Track mean distance **Cy5-KBP**	Track mean speed **Cy5-KBP**	TM/CM **Cy5-DBP**	Track mean distance **Cy5-DBP**	Track mean speed **Cy5-DBP**
1a	1.05 ± 0.02	0.922 ± 0.009	0.95 ± 0.01	0.85 ± 0.02	0.92 ± 0.01	0.98 ± 0.02
1b	0.978 ± 0.007	0.852 ± 0.005	0.874 ± 0.007	0.85 ± 0.02	0.921 ± 0.008	1.07 ± 0.01
paclitaxel	0.84 ± 0.02	0.80 ± 0.02	0.86 ± 0.02	0.79 ± 0.03	0.81 ± 0.02	0.96 ± 0.03
flutax-2	0.88 ± 0.01	0.906 ± 0.003	0.853 ± 0.007	1.03 ± 0.03	1.06 ± 0.02	1.21 ± 0.02

[a] Data are the mean ± SEM values of two independent experiments with two to three different fields analyzed.

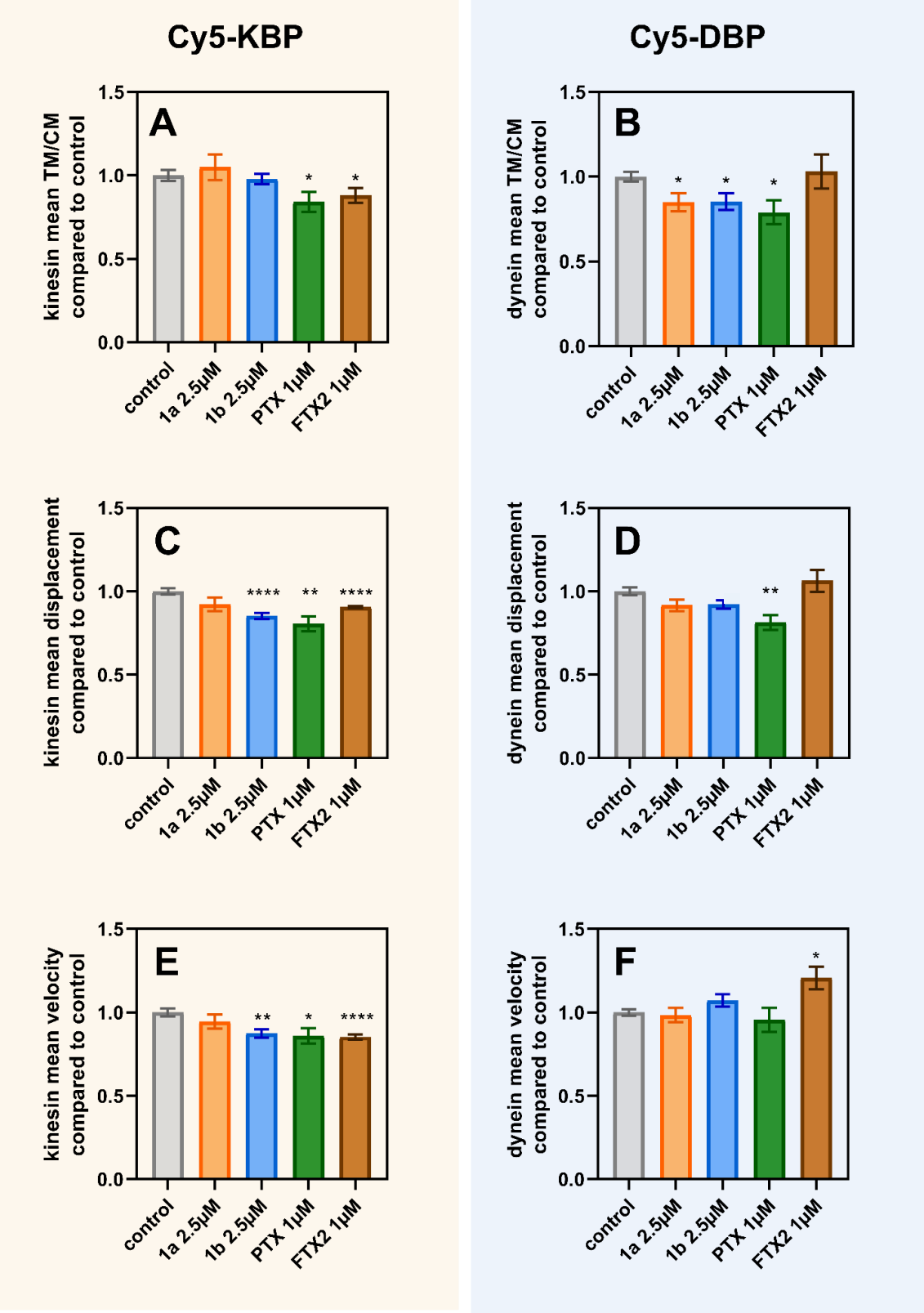

Figure 4-17. Effect on SHSY5Y intracellular transport of compound **1a** (2.5 µM, orange), **1b** (2.5 µM, orange, light blue), paclitaxel (PTX, 1 µM, green), and flutax-2 (FTX2, 1 µM, brown) compared to control (untreated cells, gray). Panels **A** and **B**: track displacement normalized to control of Cy5-KBP (**A**) and Cy5-DBP (**B**). Panels **C** and **D**: track mean velocity normalized to control of Cy5-KBP (**C**) and Cy5-DBP (**D**). Panels **E** and **F**: mean TM/CM ratio normalized to control of Cy5-KBP (**E**) and Cy5-DBP (**F**). Data are the mean ± SEM values of two independent experiments with two to three different fields analyzed. Unpaired t-test with Welsh correlation using GraphPad Prism 8 software was performed to determine significance (**** $P < 0.0001$, *** $P < 0.001$, ** $P < 0.01$, * $P < 0.05$).

5 Discussion

For the past three decades, molecules from the taxane family have been extensively used in clinics, starting with the approval of paclitaxel for cancer chemotherapy in 1992. Currently, three active principles (paclitaxel, docetaxel, and cabazitaxel) in various formulations are used to treat solid tumors, including breast cancer, ovarian carcinoma, pancreatic adenocarcinoma, non-small lung cancer, and prostate cancer. However, the use of taxanes in anti-cancer treatment is hindered by peripheral nerve toxicity, which severely affects up to 30% of patients and frequently results in therapy discontinuation.

As described in section 1.4.2, microtubule-mediated intracellular transport is indispensable for proper cell functioning, particularly in neuronal cells. Neurons rely on intracellular active transport for cargo movement along the axon, making them especially susceptible to deficits in this process, which may arise from the impairment of microtubule's dynamic instability caused by MTAs. While the impairment of intracellular transport can be justified for MDAs in light of their destabilizing effect on microtubules, the causes behind MSA-induced neurotoxicity are more challenging to explain. A recent hypothesis suggests a link between axonal transport impairment and alterations of microtubule signaling caused by taxane-induced lattice distortion. In particular, the expanded intermediate state normally represents a spatially defined structural signal in proximity to the microtubule tip[46], but taxane binding to the microtubule causes this minority structural signal to spread along the whole fiber. Since structural signals are the basis of MAP-microtubule recognition, changes in the microtubule lattice signaling could seriously affect the binding of regulatory MAPs. Therefore, paclitaxel could act as a disruptor not only of the microtubule dynamics but also of natural recognition patterns affecting dynamics regulators (like tau or EBs) and motor proteins (dyneins and kinesins). Interestingly, unpublished results from our laboratory show that flutax-2, a C7-modified fluorescent taxane, does not induce microtubule lattice expansion.

In this thesis work, I designed and synthesized new C7-decorated taxanes aiming to provide new insights on microtubule's chemical-structural signaling with motor proteins. The ultimate goal was to explore (1) the relationship between the effect of C7 modifications of the taxane core and alterations of the microtubule lattice, and (2) the existence of a correlation between structural signal modifications and impairment of intracellular transport.

5.1 Synthetic insights into the preparation of C7-modified taxanes

The first synthetic strategy A, planned to introduce the C7-decoration on paclitaxel, involved the initial coupling of the mono-protected dicarboxylic linker to the taxane core, followed by the condensation of the bulky group, as described in chapter 4.2.1. This strategy, which would afford a versatile paclitaxel-linker intermediate, required the introduction of two orthogonal protecting groups for the 2'-hydroxyl group and for one carboxylic group of the diacid linker. These were masked as a benzyloxy carbonyl carbonate and a

(trimethylsilyl)ethyl ester, respectively, following published protection protocols[141–143,145]. Since the former is hydrogenation-labile and the latter fluoride-labile, this selection provided orthogonal deprotection conditions. However this approach proved to be impracticable due to the instability of the paclitaxel core in the presence of TBAF. As a result, the switch to pathway B became necessary in order to re-use the intermediates already synthetized. Nonetheless, alternative scenarios can be envisioned to potentially make strategy A successful. One such alternative involves protecting the 2'-OH group as a silyl ether – a method well-documented in literature, with examples of transformation in *tert*-butyldimethylsilyl (TBS)[174,175] or triethylsilyl (TES)[176] ethers. Ether formation can be achieved in high yields (89 – 95%) by treatment of paclitaxel with the desired silyl chloride (TBSCl, TESCl) in basic conditions (DMAP or imidazole) at room temperature and in common organic solvents, such as dichloromethane. The protecting groups can be removed in mild acidic conditions, with hydrochloric or hydrofluoric acid diluted in an organic solvent, affording the deprotected product in 70 – 95% yield. To successfully implement this alternative approach, a non-acid labile masking group would be required for the protection of the carboxylic acid linker. For instance, this could be transformed into a hydrogenation-labile benzyl ester, via reaction with low-cost benzoyl bromide in basic conditions (e.g., triethylamine, potassium hydroxide) in a 2:1 reaction stoichiometry[177,178].

5.2 Impact of taxanes C7-decoration on their binding interaction with tubulin

Paclitaxel structure-activity relationships have demonstrated that modification at C7 is generally tolerated, as the substitution of the 7-hydroxyl group with small substituents does not significantly affect the activity[179]. As a result, the C7 position has traditionally been considered suitable for developing new derivatives and prodrugs. However, the tolerance for modifications at this position tends to decrease as the substituent introduced becomes larger and bulkier. This appears evident when considering three previously published C7-modified fluorescent taxanes: flutax-1, flutax-2, and hexaflutax, whose structures are reported in Figure 5-1. Of the three compounds, flutax-1 and -2 displayed a binding constant[92] of the same order of magnitude as paclitaxel (~10^7 M^{-1}), while hexaflutax showed a lower affinity[96] (of the order of 10^6 M^{-1}). Nonetheless, the cellular activity of all three analogs was negatively affected, as demonstrated by cell viability assays against A2780 ovarian carcinoma cells. In these studies, hexaflutax exhibited the lowest activity (IC_{50} = 2300 nM) compared to flutax-1 and -2 (IC50 values of 260 nM and 800 nM, respectively), but all fluorescent derivatives were significantly less active than paclitaxel (1.1 nM)[96]. This data aligns with the observation that Flutax-2, in particular, falls short of paclitaxel in its ability to induce tubulin assembly *in vitro* under non-polymerizing conditions (see section 4.3.1).

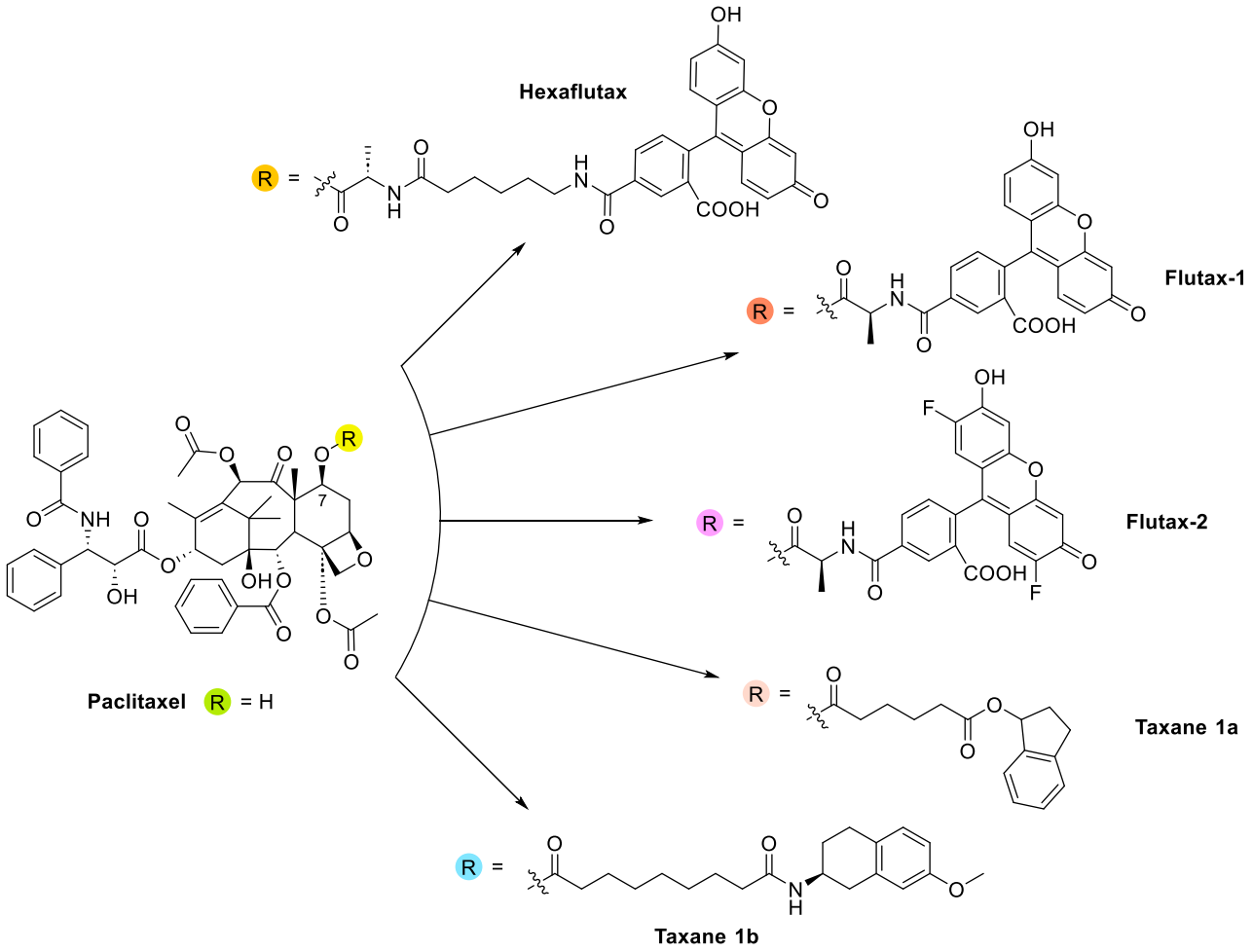

Figure 5-1. Chemical structures of C7-modified taxanes of interest.

Similarly, the newly synthetized C7-modified analogs **1a** and **1b** (Figure 5-1) displayed lower binding affinities (~10^5 M^{-1} at RT) and cytotoxicity values, as well as reduced capacity to promote tubulin assembly under non-polymerizing conditions *in vitro*. Assessing the affinities of various ligands for their binding sites is a traditional method to examine the specificity of a protein-ligand interaction, and it allows to estimate the incremental binding energy contributed by each group[180]. The incremental binding free energy variation related to the modification of ligand A into ligand B is defined as:

$$\Delta\Delta G^0_{app}(A \rightarrow B) = \Delta G^0_{app}(B) - \Delta G^0_{app}(A) \qquad [30]$$

A similar procedure can be performed for incremental enthalpy and entropy variations; however, the analysis of these individual contributions is complicated by the enthalpy-entropy compensation effect. In aqueous solution, enthalpy alterations caused by the formation of new electrostatic interactions can transform into entropy changes as a result of water molecule rearrangement, potentially leading to uncertainty in the interpretation of incremental enthalpy and entropy factors.

Thus, the differential binding energy changes $\Delta\Delta G_{35°C}$ (paclitaxel → **1a**) and $\Delta\Delta G_{35°C}$ (paclitaxel → **1b**) can be used to evaluate the effect of their specific structural modifications on the taxane core. Considering ΔG^0_{app}(paclitaxel) equal to -41.7 kJ mol^{-1} at 35°C[181] and the free Gibbs energies at 35°C reported in Table 4-2 for compounds **1a** and **1b**, the calculated values of $\Delta\Delta G_{35°C}$ are +9.8 kJ mol^{-1} and +12.8 kJ mol^{-1}, respectively, which suggest that the C7-decorations introduced are quite unfavorable. When comparing these results to previously published data[96], it is possible to notice a similar effect caused by hexaflutax, with a ΔG^0_{app}(35°C) equal to -34.8 kJ mol^{-1}, resulting in a $\Delta\Delta G_{35°C}$ (paclitaxel → hexaflutax) of +6.9 kJ mol^{-1}. However, in the case of flutax-1 and -2, the ΔG^0_{app} values at 35°C are much closer to paclitaxel (-43.3 and -41.4 kJ mol^{-1}, respectively)[92], leading to a sightly favorable affinity change in the first case ($\Delta\Delta G_{35°C}$ = -1.6 kJ mol^{-1}) and a neutral affinity shift in the second ($\Delta\Delta G_{35°C}$ = +0.3 kJ mol^{-1}). Therefore, not all bulky substituents in position C7 are disadvantageous: bulky, negatively charged groups (such as the fluorescein moieties, which exist as mono-anions or di-anions in solution) seem to be more advantageous than the smaller organic groups found in compounds **1a** and **1b**.

The $\Delta\Delta G_{35°C}$ discrepancy between hexaflutax and flutax-1, both containing the same bulky fluorescent group, seems to imply that a significant portion of the unfavorable interaction originates from the nature of the linker connecting the fluorophore to the taxane core (alanine-aliphatic chain vs. single alanine). Similarly, the Gibbs free energy difference between compounds **1a** and **1b** seems to suggest that a shorter aliphatic chain is desirable. In conclusion, increasing the number of polar substituents and reducing the linker length for C7-substitued taxanes appears to yield higher binding affinities for the taxane site.

In accordance with the measured binding affinities, the IC_{50} data related to the reduction of cell viability upon treatment with compounds **1a** and **1b** revealed that both compounds are less potent than paclitaxel. However, it is noteworthy that in most of the tested cell lines compound **1b** performed better than its analog **1a**, despite having a lower capacity to enhance tubulin polymerization *in vitro* and a weaker binding affinity. Two theories can be proposed to explain this unexpected result. The first one suggests that compound **1b** may induce a certain degree of off-target cytotoxicity, possibly due to its 7-methoxy-2-aminotetralin moiety. However, immunofluorescence imaging of cells treated with the drug revealed evidence of a taxane-induced phenotype already at the IC_{50} value, with microtubule stabilization and bundle formation. The second theory posits that compound **1b** might exhibit increased cellular uptake compared to analog **1a**. In particular, the compound is more lipophilic, as denoted by the value of the computationally calculated *n*-octanol/water partition coefficient (clogP = 8.97 (**1b**) vs. 8.08 (**1a**) calculated using Molinspiration® software, Molinspiration Chemoinformatics). While the increased lipophilicity should enhance membrane permeability, a decreased interaction with the P-gp pump might contribute to decreased efflux (see next section). The combination of these factors might potentially result in increased intracellular concentrations, compensating at the same time for the compound's low solubility.

5.3 Impact of C7-decoration on taxanes' ability to avoid the main mechanisms of resistance

It has been postulated that alterations in the C7 region of paclitaxel could lead to a reduction in its specific binding to P-gp, resulting in decreased drug efflux. This is exemplified by BMS-184476[176], a paclitaxel analog bearing a methylthiomethyl ester group at C7, which showed enhanced cytotoxicity compared to paclitaxel in MDR cell lines and was tested against non-small lung carcinoma in Phase II clinical trials[182]. However, compounds **1a** and **1b** were unable to overcome P-gp mediated resistance, as the measured IC_{50} values indicated lower potency in Kb-V1 cell line compared to the reference Kb3.1 line (see section 4.5.1). Nevertheless, the lower R/S ratio of **1b** compared to paclitaxel suggests that the C7 decoration at least partially disrupts the interaction with P-gp. These findings are consistent with evidence that the attachment of a photo-affinity label to the C7- hydroxyl group of paclitaxel successfully labels P-gp[183], further indicating that the C7- region of paclitaxel may play a crucial role in interactions with the P-gp binding site.

Additionally, compounds **1a** and **1b** also displayed significantly lower R/S ratio compared to paclitaxel in cell lines modeling β-III overexpression related resistance (HeLaβ-III/HeLa, see section 4.5.1). A less efficient binding of paclitaxel to β-III compared to β-I isotype could partially explain the emergence of the drug-resistant phenotype, as several studies demonstrated that HeLa-tubulin is composed predominantly of β-I (up to 80%) and β-IV (around 20%)[184,185]. The comparison of the sequences of these two isotypes (retrieved from the UniProt database, codes: TBB1_HUMAN, Q9H4B7 and TBB3_HUMAN, Q13509) reveals a single mutation in the taxane binding site, precisely within the M-loop. Here, Gln276 of β-I tubulin is replaced by an arginine residue in β-III.

In 2006, Magnani and colleagues conducted an *in-silico* analysis of the binding modes of paclitaxel to these two tubulin isotypes, aiming to gain a deeper understanding of their distinct molecular interactions[186]. Despite their original intention to compare β-I and β-III tubulin isotypes, an error in the protein sequence stored in the SwissProt database at the time led them to conduct a comparative analysis of β-II vs. β-III instead. Nonetheless, their findings provide some useful insights for this discussion.

Their study revealed that in β-II isotype, the carbonyl group of Ser275 is directed towards the C7 position of the paclitaxel ring, establishing a hydrogen ring with its hydroxyl group. However, this interaction becomes unfeasible in the β-III isotype due to the replacement of Ser275 with an arginine residue. In the case of C7 modified taxanes, the interaction of 7-OH with Ser275 is inherently impossible, and thus, the difference in binding affinity between the two isotypes should be smaller. Moreover, the C7 decoration might compensate for the lost free energy of binding by establishing new favorable interactions with the binding site.

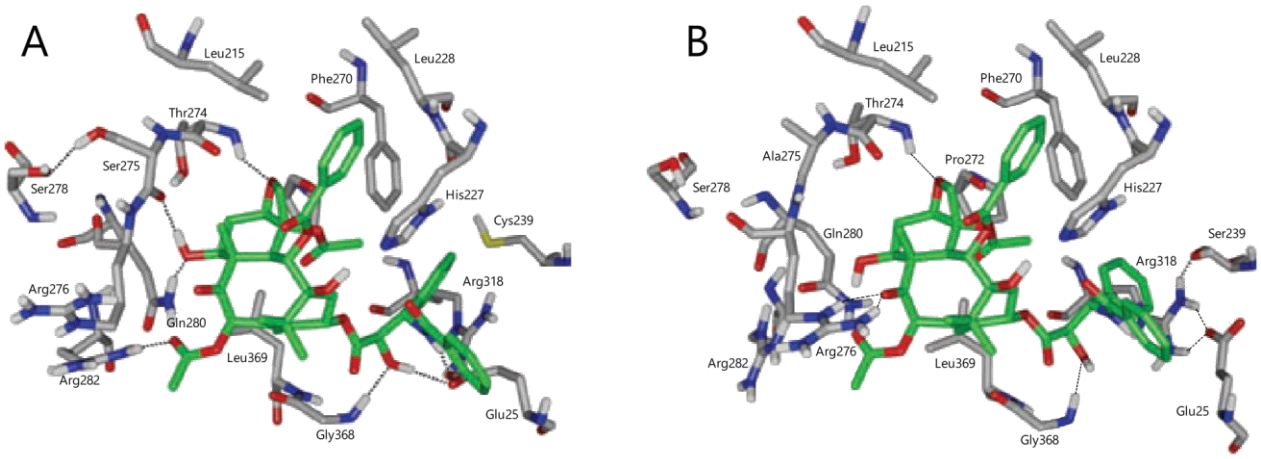

Figure 5-2. Paclitaxel (green chain) in complex with βII-tubulin (panel A, gray chain), and βIII-tubulin (panel B, gray chain). Nonpolar hydrogen atoms are omitted, and hydrogen bond interactions are represented by black dashed lines. Image adapted from [186].

A similar mechanism can be envisioned for the differential interaction of β-I and β-III, where, given its spatial proximity, the glutamine residue in position 276 of β-I could potentially establish a non-covalent interaction with the C7-hydroxyl group of paclitaxel.

When comparing compounds **1a** and **1b**, the former exhibits both the lowest R/S ratio and the lowest IC_{50} value, which is significant considering that the tendency is inverted in the parental HeLa line. Taking into account the considerations above, there are two possible explanations: (1) the C7-decoration of **1a** can establish new favorable interactions with the binding site or (2) the interaction pattern of **1a** is less impacted by the Gln276-Arg276 mutation compared to **1b**. To gain an insight into the distinct structural effects of MTAs with different tubulin isotypes, our laboratory is currently teaming up with Dr. Ivan Plaza's research group at Centro Nacional de Investigaciones Oncológicas (CNIO) for the purification of different human β-tubulin isotypes expressed in insect cells, aiming for its use in binding affinities and structural studies.

5.4 Interplay between microtubule structural alterations and intracellular transport impairment

Kinesin and dynein motor proteins perform complementary functions on microtubules, being responsible for (+)-end and (-)-end-directed motion, respectively. Despite their similar role as intracellular cargo transporters, they exhibit distinct structural features and mechanism of action. Kinesin-1 typically moves along a single protofilament track on the microtubule and almost exclusively steps forward[68]. In contrast, dynein exhibits a large diffusional component in its stepping behavior, resulting in frequent sideways and backward steps. This can be attributed to the positioning of dynein monomers on adjacent protofilaments and the lack of strict coordination in their stepping, allowing either motor to step while the other remains tethered to the microtubule[187]. The movement of these molecular motors on microtubules is influenced by various factors, such as opposing motor traffic, lattice defects, and microtubule crowding (caused, for

instance, by the presence of MAPs, organelles, protein aggregates, and cross-linked cytoskeletal filaments)[188].

Although the exact method by which motor proteins navigate within the cell amid these obstacles is not fully understood, there is a general consensus that kinesin-mediated movement is more affected than dynein-mediated transport by both structural defects/alterations, including those that may arise from MSA treatment, and microtubule crowding[188]. When encountering an obstacle or a lattice defect, kinesin-1 tends to stall or detach from the microtubule, with the preferred behavior possibly depending on the number of motors simultaneously transporting the cellular cargo. This is supported by the observation that multiple motors carry cargo with increased processivity (i.e., the number of consecutive steps) compared to single motors[128]. Conversely, dynein can bypass obstacles and lattice defects more easily, as expected due to its ability to take side steps.

My working hypothesis proposed that a distinct type of microtubule lattice alteration, axial expansion, could be responsible for motor protein dysfunction in cells treated with MSAs from the taxane family. According to this hypothesis, anterograde transport could be especially affected as kinesin moves along microtubules with a fixed stepping size, corresponding to the axial rise of one heterodimer (8 nm)[63]. Lattice expansion resulting by taxane treatment under saturating conditions necessarily modifies the step size, potentially leading to the early detachment of the motors. In non-saturating conditions, axial expansion is localized within the dimers that bind the drug, introducing lattice defects that motor proteins must navigate around, and that might equally result in premature detachment and/or stalling.

To test this theory, I identified C7-modified taxanes capable of generating distinct structural modifications in the microtubule's lattice. As mentioned in chapter 1.6, the molecular mechanism considered responsible for the taxane-induced expansion of the microtubule lattice involves the displacement of the βS9-βS10 loop upon drug binding. This loop essentially functions as a lid, covering and fixing the bound compounds in their final position[89]. Therefore, the capacity of C7-bulky decorations to modulate taxanes' expansion behavior is likely related to their ability to induce a subtle adjustment in the orientation of the taxane core within the binding pocket, which in turn prevents the displacement of the aforementioned loop. In this context, a compelling direction for future research could involve the design and synthesis of a panel of C7-modified compounds bearing increasingly smaller decorations in order to elucidate if there is a minimal steric requirement that prevents the lattice expansion, or rather this effect is directly related to the masking of the C7-hydroxyl group.

More specifically, the four taxanes identified had differential effects on both the axial and lateral metrics of the microtubule (as per X-ray fiber diffraction measurements reported in chapter 4.4):

- Paclitaxel, which induces axial expansion and promotes the *in vitro* formation of microtubules of smaller diameters (i.e., decreased number of protofilaments).
- Flutax-2, which does not expand the microtubule lattice and even demonstrates the ability to compact intrinsically expanded lattices (such as those of GMPCPP-microtubules). Moreover, it forms *in vitro* microtubules of slightly wider diameter (i.e., increased protofilament number).
- The newly synthesized taxane **1a,** which does not expand GDP-microtubule lattice nor is able to override the lattice expansion induced by GMPCPP, and forms microtubules with wider diameter *in vitro*.
- The newly synthesized taxane **1b**, that behaves as **1a** on the microtubule axial arrangement, and it has an almost neutral effect on the lateral parameters.

In accordance with the premise, tracking experiments of fluorescently tagged motors in cells treated with paclitaxel, flutax-2, and the C-7 modified taxanes **1a** and **1b** (section 4.5.3) revealed that microtubule structural alterations induced by taxanes do affect intracellular transport. Specifically, kinesin-mediated transport was negatively impacted under nearly all tested conditions. However, both the fraction of kinesin-transported motion and the mean speed of the moving particles were similarly reduced in cells treated with paclitaxel and flutax-2. The only distinction between the two treatments was the mean distance travelled by the moving particles – a 20% reduction in the case of paclitaxel and a 9% reduction with flutax-2 – possibly suggesting a greater tendency to detachment vs. stalling in the first case. Interestingly, the two C7-modified taxanes **1a** and **1b** had lesser impact on anterograde transport, since neither compound altered the fraction of kinesin-transported particles in the cell. Compound **1b** resulted in a reduced average speed and displacement of the transported particles, while no significant changes were observed in cells treated with analog **1a**.

In summary, these findings suggest that lattice expansion alone cannot account for the altered kinesin transport within taxanes-treated cells, as modifications of the motor behavior are observed even with drugs that preserve an axially compacted lattice. Nonetheless, taxane treatment can introduce other forms of lattice alterations in the microtubule structure, such as missing tubulin heterodimers[189] and sites where the microtubule gains or loses one or more protofilaments[190] (dislocations), thus inducing the microtubule to adopt a skew angle. Hence, alterations in intracellular transport might arise from a combination of these factors. Specifically, we anticipate that taxanes introduce dislocations during microtubule growth in cells in accordance with the lateral effects they exert on microtubules *in vitro*. In this context, the observation that paclitaxel produces a more significant reduction in both the fraction of kinesin-based transport motion and mean distance compared to the other taxanes might indicate that kinesin is more affected by a reduction of the number of protofilaments rather than an increase. Notably, compound **1a**, which induces the formation of larger microtubules *in vitro* with respect to both flutax-2 and analog **1b**, does not affect kinesin-mediated

transport at all. This promising result highlights the potential of C7-modification for generating taxanes with a more neutral effect on kinesin-mediated transport.

Interpreting the results from dynein tracking experiments is more complex, especially considering the higher mobility of this motor across the microtubule lattice. In the experiments performed, the fraction of particles moving via transported motion in cells treated with paclitaxel significantly decreased (-21%), as did the mean displacement (-19%); however, the average velocity remained unalerted compared to the control. Conversely, flutax-2 treatment resulted in the opposite effect on dynein transport, with the TM/CM ratio and mean distance remaining unchanged compared to the control and a surprising 20% increase in the mean speed of moving particles. Lastly, for cells treated with compounds **1a** and **1b**, the fraction of transported motion decreased (-15%), while the mean speed and displacement remained constant.

These results indicate that dyneins are more susceptible to stalling and/or early detachment in cells treated with paclitaxel compared to other taxanes, which might be caused by either the expanded lattice state or dislocations resulting in a lower protofilament number. In contrast to kinesin-mediated transport, dynein seems to be also affected by dislocations leading to an increased number of protofilaments, as both compounds **1a** and **1b** are associated with a reduction in the fraction of dynein-transported motion. Indeed, these two compounds induce larger microtubules *in vitro,* while Flutax-2, whose associated lateral metrics are closer to the wild type, does not disturb the interaction.
Concerning the increase in the velocity of the dynein motors observed in cells treated with Flutax-2, this result agrees with recent evidence indicating that dynein and the microtubule have electrostatically complementary binding interfaces. A study from 2016 by Li and co-workers demonstrated via multi-scale modeling that the electrostatic component of the binding free energy of the microtubule-binding domain of dynein to the microtubule is linearly correlated with the motor's velocity[191]. Normally, the surface of the microtubule is negatively charged[192], and Flutax-2, being a di-anion at physiological pH, could contribute to the increase of the net charge and cause the observed effect.

Providing an explanation for the taxanes different behaviors on intracellular transport is particularly challenging due to the lack of an important piece of information about these compounds: the experimental network of molecular interactions established with the binding site and the position of the C7-decoration. It is possible that the C7-decorations could induce an allosteric conformational change in tubulin's MAP-binding region, thereby modulating the interaction with the cytoskeletal motors. To further investigate this possibility, attempts were made to acquire the X-ray crystallographic structures of these compounds in complex with tubulin. Regrettably, these efforts encountered a familiar obstacle frequently observed with taxanes: a compatibility issue between the drug binding and the curved conformation assumed by tubulin in crystallographic complexes. However, recent advancements have yielded high-resolution tubulin

crystallographic structures in complex with C13-modified taxanes[89], as elaborated in section 1.6 of the Introduction. This development opens up a promising alternative approach: the incorporation of the C7-decorations discussed in this thesis onto the C13-modified paclitaxel derivatives could be pursued in order to increase the chance for a successful crystallographic analysis.

However, X-ray crystallography is not the only way to obtain structural information. As part of our ongoing efforts, we established a collaboration within the TubInTrain consortium with Dr. Andrea Prota's research group at the Paul Scherrer Institut (Villigen, Switzerland), and dispatched paclitaxel, flutax-2, and compounds **1a** and **1b** to in order to perform cryo-EM studies on GDP- and GMPCPP-microtubules. These studies hold the promise of providing the missing structural information crucial for (1) unraveling the molecular mechanisms behind the distinct axial expansion behaviors exhibited by C7-modified taxanes, and (2) providing insight on potential allosteric alterations on the MAP-binding region of tubulin.

Moreover, I have been working to establish a single particle *in vitro* assay to visualize via total internal reflection fluorescence microscopy the movement of overexpressed kinesin's heavy chains, labeled with quantum dots, along fluorescent microtubules. This approach is complementary to intracellular tracking and offers some unique advantages. Firstly, it will allow for the direct visualization of the paths traveled by the motors, enabling the specific analysis of transported motion. Secondly, it will facilitate the study of the impact of microtubules' structural alterations on kinesin transport by enabling the use of MSAs in a 1:1 stoichiometry relative to tubulin. In fact, under saturating conditions of the tested MSAs their effect on the microtubule will be amplified and it will be possible to better appreciate the differences between different compounds.

6 Conclusions

For the first general objective proposed, the conclusions obtained in this thesis are:

1.1. Out of the initial fifty C7-modified taxanes computationally designed, docking analysis identified four as promising candidates for mimicking the binding mode of flutax-2 to tubulin. The synthesis of the two of these compounds, labeled **1a** and **1b**, was successfully completed other three steps starting from paclitaxel, with overall yields of 48% and 38%, respectively.

1.2. The effect of the C7 decorations of **1a** and **1b** on the binding interaction with tubulin was unfavorable, resulting in lower binding affinities and a lower capacity to enhance tubulin polymerization *in vitro*. When comparing these results with other C7-modified taxanes, it appears that the presence of negatively charged moieties, an increase in the polarity of the linker and a reduction of the linker length lead to higher binding affinities for the taxane site.

1.3. X-ray fiber diffraction experiments highlighted that compounds **1a**, **1b**, flutax-2 and paclitaxel exhibited differential structural effects on the axial and lateral parameters of the microtubule. Therefore, modification in position C7 of the taxane core can effectively modulate microtubule lattice expansion.

From the second general objective proposed, the conclusions obtained in this thesis are:

2.1. Cellular studies revealed that C7-modified taxanes **1a** and **1b** are less cytotoxic than paclitaxel, but C7 decoration showed the potential to overcome the main mechanisms of resistance of taxanes.

2.2. Studies on intracellular transport concluded that axial expansion is not directly correlated to impairment of kinesin-mediated intracellular transport, but a correlation might exist for dynein-related transport. The results obtained with analog **1a** highlighted the potential of C7-modification for reducing the impact of taxanes on kinesin-mediated transport.

7 Bibliography

1. Conklin, E. G. Effects of centrifugal force on the structure and development of the eggs of Crepidula. *Journal of Experimental Zoology* **22**, 311–419 (1917).

2. Wintrebert, P. La rotation immediate de l'oeuf pondu et la rotation d'activation chez Discoglossus pictus Otth. *C R Seances Soc Biol Fil* **106**, 439–442 (1931).

3. Straub, F. & Szent-Gyorgyi, A. *Studies from the Institute of Medicinal Chemistry University Szeged, Volume II*. (Town Printer and Book Publisher KFT of Szeged, 1942).

4. Straub, F. & Szent-Györgyi, A. *Studies from the Institute of Medicinal Chemistry University Szeged, Volume III*. (Town Printer and Book Publisher KFT of Szeged, 1943).

5. Huxley, A. F. Muscle Structure and Theories of Contraction. *Prog Biophys Biophys Chem* **7**, 255–318 (1957).

6. Manton, I. & Clarke, B. An Electron Microscope Study of the Spermatozoid of Sphagnum. *J Exp Bot* **3**, 265–275 (1952).

7. Fawcett, D. W. & Porter, K. R. A study of the fine structure of ciliated epithelia. *J Morphol* **94**, 221–281 (1954).

8. Ishikawa, H., Bischoff, R. & Holtzer, H. Mitosis and intermediate-sized filaments in developing skeletal muscle. *J Cell Biol* **38**, 538–55 (1968).

9. Zampieri, F., Coen, M. & Gabbiani, G. The prehistory of the cytoskeleton concept. *Cytoskeleton* **71**, 464–471 (2014).

10. Frixione, E. Recurring views on the structure and function of the cytoskeleton: A 300-year epic. *Cell Motil Cytoskeleton* **46**, 73–94 (2000).

11. Pollard, T. D. & Goldman, R. D. Overview of the Cytoskeleton from an Evolutionary Perspective. *Cold Spring Harb Perspect Biol* **10**, (2018).

12. Jung, M., Kim, D. & Mun, J. Y. Direct Visualization of Actin Filaments and Actin-Binding Proteins in Neuronal Cells. *Front Cell Dev Biol* **8**, 1368 (2020).

13. Bruce Alberts *et al. Molecular Biology of the Cell*. (W. W. Norton & Company, 2022).

14. Amos, L. A. & Hirose, K. Studying the structure of microtubules by electron microscopy. *Methods Mol Med* **137**, 65–91 (2007).

15. Bryan, J. & Wilson, L. Are Cytoplasmic Microtubules Heteropolymers? *Proceedings of the National Academy of Sciences* **68**, 1762–1766 (1971).

16. Oakley, C. E. & Oakley, B. R. Identification of gamma-tubulin, a new member of the tubulin superfamily encoded by mipA gene of Aspergillus nidulans. *Nature* **338**, 662–664 (1989).

17. Chang, P. & Stearns, T. Delta-tubulin and epsilon-tubulin: two new human centrosomal tubulins reveal new aspects of centrosome structure and function. *Nat Cell Biol* **2**, 30–35 (2000).

18. Ruiz, F. *et al.* The SM19 gene, required for duplication of basal bodies in Paramecium, encodes a novel tubulin, η-tubulin. *Current Biology* **10**, 1451–1454 (2000).

19. Vaughan, S. *et al.* New tubulins in protozoal parasites. *Current Biology* **10**, R258–R259 (2000).

20. Gard, D. L. & Kirschner, M. W. Microtubule assembly in cytoplasmic extracts of Xenopus oocytes and eggs. *J Cell Biol* **105**, 2191–2201 (1987).

21. Verdier-Pinard, P. *et al.* Direct Analysis of Tubulin Expression in Cancer Cell Lines by Electrospray Ionization Mass Spectrometry. *Biochemistry* **42**, 12019–12027 (2003).

22. Nogales, E., Wolf, S. G. & Downing, K. H. Structure of the αβ tubulin dimer by electron crystallography. *Nature 1998 391:6663* **391**, 199–203 (1998).

23. Löwe, J., Li, H., Downing, K. H. & Nogales, E. Refined structure of αβ-tubulin at 3.5 Å resolution. *J Mol Biol* **313**, 1045–1057 (2001).

24. Menéndez, M., Rivas, G., Díaz, J. F. & Andreu, J. M. Control of the Structural Stability of the Tubulin Dimer by One High Affinity Bound Magnesium Ion at Nucleotide N-site*. *J Biol Chem* **273**, 167–176 (1998).

25. Nogales, E., Downing, K. H., Amos, L. A. & Löwe, J. Tubulin and FtsZ form a distinct family of GTPases. *Nat Struct Biol* **5**, 451–458 (1998).

26. Gao, Y., Vainberg, I. E., Chow, R. L. & Cowan, N. J. Two cofactors and cytoplasmic chaperonin are required for the folding of alpha- and beta-tubulin. *Mol Cell Biol* **13**, 2478–2485 (1993).

27. Melki, R., Rommelaere, H., Leguy, R., Vandekerckhove, J. & Ampe, C. Cofactor A Is a Molecular Chaperone Required for β-Tubulin Folding: Functional and Structural Characterization. *Biochemistry* **35**, 10422–10435 (1996).

28. Martín, L., Fanarraga, M. L., Aloria, K. & Zabala, J. C. Tubulin folding cofactor D is a microtubule destabilizing protein. *FEBS Lett* **470**, 93–95 (2000).

29. Detrich, H. W. & Williams, R. C. Reversible dissociation of the αβ dimer of tubulin from bovine brain. *Biochemistry* **17**, 3900–3907 (1978).

30. Shearwin, K. E., Perez-Ramirez, B. & Timashef, S. N. Linkages between the Dissociation of αβ Tubulin into Subunits and Ligand Binding: The Ground State of Tubulin Is the GDP Conformation. *Biochemistry* **33**, 885–893 (1994).

31. Shearwin, K. E. & Timasheff, S. N. Effect of Colchicine Analogues on the Dissociation of αβ Tubulin into Subunits: The Locus of Colchicine Binding. *Biochemistry* **33**, 894–901 (1994).

32. Caplow, M. & Fee, L. Dissociation of the Tubulin Dimer Is Extremely Slow, Thermodynamically Very Unfavorable, and Reversible in the Absence of an Energy Source. *Mol Biol Cell* **13**, 2120–2131 (2002).

33. Montecinos-Franjola, F., Schuck, P. & Sackett, D. L. Tubulin Dimer Reversible Dissociation. *Journal of Biological Chemistry* **291**, 9281–9294 (2016).

34. Fineberg, A., Surrey, T. & Kukura, P. Quantifying the Monomer–Dimer Equilibrium of Tubulin with Mass Photometry. *J Mol Biol* **432**, 6168–6172 (2020).

35. Tilney, L. G. *et al.* Microtubules: evidence for 13 protofilaments. *J Cell Biol* **59**, 267–75 (1973).

36. Alushin, G. M. *et al.* High-Resolution Microtubule Structures Reveal the Structural Transitions in αβ-Tubulin upon GTP Hydrolysis. *Cell* **157**, 1117–1129 (2014).

37. Zhang, R., Alushin, G. M., Brown, A. & Nogales, E. Mechanistic Origin of Microtubule Dynamic Instability and Its Modulation by EB Proteins. *Cell* **162**, 849–859 (2015).

38. Zhang, R., LaFrance, B. & Nogales, E. Separating the effects of nucleotide and EB binding on microtubule structure. *Proceedings of the National Academy of Sciences* **115**, E6191–E6200 (2018).

39. Nogales, E., Whittaker, M., Milligan, R. A. & Downing, K. H. High-Resolution Model of the Microtubule. *Cell* **96**, 79–88 (1999).

40. Mandelkow, E. M., Schultheiss, R., Rapp, R., Müller, M. & Mandelkow, E. On the surface lattice of microtubules: helix starts, protofilament number, seam, and handedness. *Journal of Cell Biology* **102**, 1067–1073 (1986).

41. Pierson, G. B., Burton, P. R. & Himes, R. H. Alterations in number of protofilaments in microtubules assembled in vitro. *J Cell Biol* **76**, 223 (1978).

42. Guyomar, C. *et al.* Changes in seam number and location induce holes within microtubules assembled from porcine brain tubulin and in Xenopus egg cytoplasmic extracts. *Elife* **11**, e83021 (2022).

43. Chaaban, S. & Brouhard, G. J. A microtubule bestiary: structural diversity in tubulin polymers. *Mol Biol Cell* **28**, 2924–2931 (2017).

44. Kollman, J. M., Polka, J. K., Zelter, A., Davis, T. N. & Agard, D. A. Microtubule nucleating γ-TuSC assembles structures with 13-fold microtubule-like symmetry. *Nature* **466**, 879–882 (2010).

45. Chrétien, D. & Wade, R. H. New data on the microtubule surface lattice. *Biol Cell* **71**, 161–174 (1991).

46. Estévez-Gallego, J. *et al.* Structural model for differential cap maturation at growing microtubule ends. *Elife* **9**, 1–26 (2020).

47. Chrétien, D. & Fuller, S. D. Microtubules switch occasionally into unfavorable configurations during elongation. *J Mol Biol* **298**, 663–676 (2000).

48. Weisenberg, R. C. Microtubule Formation in vitro in Solutions Containing Low Calcium Concentrations. *Science (1979)* **177**, 1104–1105 (1972).

49. Gaskin, F., Cantor, C. R. & Shelanski, M. L. Turbidimetric studies of the in vitro assembly and disassembly of porcine neurotubules. *J Mol Biol* **89**, 737–55 (1974).

50. Mitchison, T. & Kirschner, M. Dynamic instability of microtubule growth. *Nature* **312**, 237–242 (1984).

51. Horio, T. & Hotani, H. Visualization of the dynamic instability of individual microtubules by dark-field microscopy. *Nature* **321**, 605–607 (1986).

52. Walker, R. A. *et al.* Dynamic instability of individual microtubules analyzed by video light microscopy: rate constants and transition frequencies. *Journal of Cell Biology* **107**, 1437–1448 (1988).

53. Melki, R., Carlier, M. F., Pantaloni, D. & Timasheff, S. N. Cold depolymerization of microtubules to double rings: geometric stabilization of assemblies. *Biochemistry* **28**, 9143–9152 (1989).

54. Walker, R. A., Pryer, N. K. & Salmon, E. D. Dilution of individual microtubules observed in real time in vitro: evidence that cap size is small and independent of elongation rate. *J Cell Biol* **114**, 73–81 (1991).

55. Brouhard, G. J. & Rice, L. M. Microtubule dynamics: An interplay of biochemistry and mechanics. *Nat Rev Mol Cell Biol* **19**, 451–463 (2018).

56. McIntosh, J. R. *et al.* Microtubules grow by the addition of bent guanosine triphosphate tubulin to the tips of curved protofilaments. *Journal of Cell Biology* **217**, 2691–2708 (2018).

57. Pegoraro, A. F., Janmey, P. & Weitz, D. A. Mechanical properties of the cytoskeleton and cells. *Cold Spring Harb Perspect Biol* **9**, (2017).

58. Seetharaman, S. & Etienne-Manneville, S. Microtubules at focal adhesions – a double-edged sword. *J Cell Sci* **132**, (2019).

59. De Vos, K. J. & Hafezparast, M. Neurobiology of axonal transport defects in motor neuron diseases: Opportunities for translational research? *Neurobiol Dis* **105**, 283–299 (2017).

60. Hirokawa, N. & Takemura, R. Molecular motors and mechanisms of directional transport in neurons. *Nat Rev Neurosci* **6**, 201–214 (2005).

61. Hirokawa, N., Noda, Y., Tanaka, Y. & Niwa, S. Kinesin superfamily motor proteins and intracellular transport. *Nat Rev Mol Cell Biol* **10**, 682–696 (2009).

62. Hirokawa, N. *et al.* Submolecular domains of bovine brain kinesin identified by electron microscopy and monoclonal antibody decoration. *Cell* **56**, 867–878 (1989).

63. Svoboda, K., Schmidt, C. F., Schnapp, B. J. & Block, S. M. Direct observation of kinesin stepping by optical trapping interferometry. *Nature* **365**, 721–727 (1993).

64. Cross, R. A. Review: Mechanochemistry of the kinesin-1 ATPase. *Biopolymers* **105**, 476–482 (2016).

65. Rice, S. *et al.* A structural change in the kinesin motor protein that drives motility. *Nature* **402**, 778–784 (1999).

66. Diamant, A. G. & Carter, A. P. Dynein Family Classification. in *Encyclopedia of Biophysics* 552–558 (Springer Berlin Heidelberg, 2013).

67. Reck-Peterson, S. L., Redwine, W. B., Vale, R. D. & Carter, A. P. The cytoplasmic dynein transport machinery and its many cargoes. *Nat Rev Mol Cell Biol* **19**, 382–398 (2018).

68. Ray, S., Meyhöfer, E., Milligan, R. A. & Howard, J. Kinesin follows the microtubule's protofilament axis. *J Cell Biol* **121**, 1083–1093 (1993).

69. Canty, J. T., Tan, R., Kusakci, E., Fernandes, J. & Yildiz, A. Structure and Mechanics of Dynein Motors. *Annu Rev Biophys* **50**, 549–574 (2021).

70. Kollman, J. M., Merdes, A., Mourey, L. & Agard, D. A. Microtubule nucleation by γ-tubulin complexes. *Nat Rev Mol Cell Biol* **12**, 709–721 (2011).

71. Richard Mcintosh, J. Mitosis. *Cold Spring Harb Perspect Biol* **8**, (2016).

72. Viswanadha, R., Sale, W. S. & Porter, M. E. Ciliary motility: Regulation of axonemal dynein motors. *Cold Spring Harb Perspect Biol* **9**, (2017).

73. Etienne-Manneville, S. Microtubules in Cell Migration. *Annu Rev Cell Dev Biol* **29**, 471–499 (2013).

74. Janke, C. & Magiera, M. M. The tubulin code and its role in controlling microtubule properties and functions. *Nat Rev Mol Cell Biol* **21**, 307–326 (2020).

75. Nsamba, E. T. & Gupta, M. L. Tubulin isotypes – functional insights from model organisms. *J Cell Sci* **135**, (2022).

76. Akhmanova, A. & Steinmetz, M. O. Control of microtubule organization and dynamics: two ends in the limelight. *Nat Rev Mol Cell Biol* **16**, 711–726 (2015).

77. Steinmetz, M. O. & Prota, A. E. Microtubule-Targeting Agents: Strategies To Hijack the Cytoskeleton. *Trends Cell Biol* **28**, 776–792 (2018).

78. Dumontet, C. & Jordan, M. A. Microtubule-binding agents: a dynamic field of cancer therapeutics. *Nat Rev Drug Discov* **9**, 790–803 (2010).

79. Amoroso, E. C. Colchicine and Tumour Growth. *Nature* **135**, 266–267 (1935).

80. Mühlethaler, T. *et al.* Rational Design of a Novel Tubulin Inhibitor with a Unique Mechanism of Action. *Angewandte Chemie International Edition* **61**, (2022).

81. Mühlethaler, T. *et al.* Comprehensive Analysis of Binding Sites in Tubulin. *Angewandte Chemie International Edition* **60**, 13331–13342 (2021).

82. Wani, M. C., Taylor, H. L., Wall, M. E., Coggon, P. & McPhail, A. T. Plant antitumor agents. VI. Isolation and structure of taxol, a novel antileukemic and antitumor agent from Taxus brevifolia. *J Am Chem Soc* **93**, 2325–2327 (1971).

83. Gallego-Jara, J., Lozano-Terol, G., Sola-Martínez, R. A., Cánovas-Díaz, M. & de Diego Puente, T. A Compressive Review about Taxol®: History and Future Challenges. *Molecules* **25**, 5986 (2020).

84. Denis, J. Noel. *et al.* Highly efficient, practical approach to natural taxol. *J Am Chem Soc* **110**, 5917–5919 (1988).

85. Nicolaou, K. C. *et al.* Total synthesis of taxol. *Nature* **367**, 630–634 (1994).

86. Kingston, D. G. I. The shape of things to come: Structural and synthetic studies of taxol and related compounds. *Phytochemistry* **68**, 1844–1854 (2007).

87. Fang, W.-S. & Wang, S.-R. Structural studies of taxol analogues for drug discovery. *Expert Opin Drug Discov* **3**, 1109–1122 (2008).

88. *Taxus, the genus Taxus*. (Taylor & Francis, 2003).

89. Prota, A. E. *et al.* Structural insight into the stabilization of microtubules by taxanes. *Elife* **12**, (2023).

90. Prota, A. E. *et al.* Molecular Mechanism of Action of Microtubule-Stabilizing Anticancer Agents. *Science (1979)* **339**, 587–590 (2013).

91. Prota, A. E. *et al.* Structural Basis of Microtubule Stabilization by Discodermolide. *ChemBioChem* **18**, 905–909 (2017).

92. Díaz, J. F., Strobe, R., Engelborghs, Y., Souto, A. A. & Andreu, J. M. Molecular Recognition of Taxol by Microtubules. *Journal of Biological Chemistry* **275**, 26265–26276 (2000).

93. Díaz, J. F., Barasoain, I. & Andreu, J. M. Fast Kinetics of Taxol Binding to Microtubules. *Journal of Biological Chemistry* **278**, 8407–8419 (2003).

94. Buey, R. M. *et al.* Cyclostreptin binds covalently to microtubule pores and lumenal taxoid binding sites. *Nat Chem Biol* **3**, 117–125 (2007).

95. Magnani, M., Maccari, G., Andreu, J. M., Díaz, J. F. & Botta, M. Possible binding site for paclitaxel at microtubule pores. *FEBS Journal* **276**, 2701–2712 (2009).

96. Barasoain, I. *et al.* Probing the Pore Drug Binding Site of Microtubules with Fluorescent Taxanes: Evidence of Two Binding Poses. *Chem Biol* **17**, 243–253 (2010).

97. Weaver, B. A. How Taxol/paclitaxel kills cancer cells. *Mol Biol Cell* **25**, 2677–2681 (2014).

98. Mitchison, T. J. The proliferation rate paradox in antimitotic chemotherapy. *Mol Biol Cell* **23**, 1–6 (2012).

99. Komlodi-Pasztor, E., Sackett, D., Wilkerson, J. & Fojo, T. Mitosis is not a key target of microtubule agents in patient tumors. *Nat Rev Clin Oncol* **8**, 244–250 (2011).

100. Mitchison, T. J., Pineda, J., Shi, J. & Florian, S. Is inflammatory micronucleation the key to a successful anti-mitotic cancer drug? *Open Biol* **7**, 170182 (2017).

101. Zasadil, L. M. *et al.* Cytotoxicity of Paclitaxel in Breast Cancer Is due to Chromosome Missegregation on Multipolar Spindles. *Sci Transl Med* **6**, (2014).

102. Lim, P. T., Goh, B. H. & Lee, W.-L. Taxol: Mechanisms of action against cancer, an update with current research. in *Paclitaxel* 47–71 (Elsevier, 2022).

103. Lafanechère, L. The microtubule cytoskeleton: An old validated target for novel therapeutic drugs. *Front Pharmacol* **13**, (2022).

104. Chatterji, B. P., Jindal, B., Srivastava, S. & Panda, D. Microtubules as antifungal and antiparasitic drug targets. *Expert Opin Ther Pat* **21**, 167–186 (2011).

105. Messaritakis, J. *et al.* High mebendazole doses in pulmonary and hepatic hydatid disease Familial growth hormone releasing factor deficiency in pseudopseudohypoparathyroidism. **22**, 532–533 (1991).

106. Katiyar, S. K., Gordon, V. R., McLaughlin, G. L. & Edlind, T. D. Antiprotozoal activities of benzimidazoles and correlations with beta-tubulin sequence. *Antimicrob Agents Chemother* **38**, 2086–2090 (1994).

107. Panda, D., Rathinasamy, K., Santra, M. K. & Wilson, L. Kinetic suppression of microtubule dynamic instability by griseofulvin: Implications for its possible use in the treatment of cancer. *Proceedings of the National Academy of Sciences* **102**, 9878–9883 (2005).

108. Gaillard, N. *et al.* Inhibiting parasite proliferation using a rationally designed anti-tubulin agent. *EMBO Mol Med* **13**, 1–12 (2021).

109. Boiarska, Z. & Passarella, D. Microtubule-targeting agents and neurodegeneration. *Drug Discov Today* **26**, 604–615 (2021).

110. Soliman, A., Bakota, L. & Brandt, R. Microtubule-modulating Agents in the Fight Against Neurodegeneration: Will it ever Work? *Curr Neuropharmacol* **20**, 782–798 (2021).

111. Golovyashkina, N. *et al.* Region-specific dendritic simplification induced by Aβ, mediated by tau via dysregulation of microtubule dynamics: a mechanistic distinct event from other neurodegenerative processes. *Mol Neurodegener* **10**, 60 (2015).

112. Döhner, K., Nagel, C.-H. & Sodeik, B. Viral stop-and-go along microtubules: taking a ride with dynein and kinesins. *Trends Microbiol* **13**, 320–327 (2005).

113. Wang, I.-H., Burckhardt, C., Yakimovich, A. & Greber, U. Imaging, Tracking and Computational Analyses of Virus Entry and Egress with the Cytoskeleton. *Viruses* **10**, 166 (2018).

114. Portilho, D. M., Persson, R. & Arhel, N. Role of non-motile microtubule-associated proteins in virus trafficking. *Biomol Concepts* **7**, 283–292 (2016).

115. Oliva, M. Á. *et al.* Effect of Clinically Used Microtubule Targeting Drugs on Viral Infection and Transport Function. 1–22 (2022).

116. Was, H. *et al.* Mechanisms of Chemotherapy-Induced Neurotoxicity. *Front Pharmacol* **13**, (2022).

117. LaPointe, N. E. *et al.* Effects of eribulin, vincristine, paclitaxel and ixabepilone on fast axonal transport and kinesin-1 driven microtubule gliding: Implications for chemotherapy-induced peripheral neuropathy. *Neurotoxicology* **37**, 231–239 (2013).

118. Rivera, E. & Cianfrocca, M. Overview of neuropathy associated with taxanes for the treatment of metastatic breast cancer. *Cancer Chemother Pharmacol* **75**, 659–670 (2015).

119. Brady, S. T., Tytell, M. & Lasek, R. J. Axonal tubulin and axonal microtubules: biochemical evidence for cold stability. *J Cell Biol* **99**, 1716–1724 (1984).

120. Baas, P. W. & Black, M. M. Individual microtubules in the axon consist of domains that differ in both composition and stability. *J Cell Biol* **111**, 495–509 (1990).

121. Song, Y. *et al.* Transglutaminase and Polyamination of Tubulin: Posttranslational Modification for Stabilizing Axonal Microtubules. *Neuron* **78**, 109–123 (2013).

122. Theiss, C. & Meller, K. Taxol impairs anterograde axonal transport of microinjected horseradish peroxidase in dorsal root ganglia neurons in vitro. *Cell Tissue Res* **299**, 213–224 (2000).

123. Shemesh, O. A. & Spira, M. E. Paclitaxel induces axonal microtubules polar reconfiguration and impaired organelle transport: implications for the pathogenesis of paclitaxel-induced polyneuropathy. *Acta Neuropathol* **119**, 235–248 (2010).

124. Carbonaro, M., Escuin, D., O'Brate, A., Thadani-Mulero, M. & Giannakakou, P. Microtubules Regulate Hypoxia-inducible Factor-1α Protein Trafficking and Activity. *Journal of Biological Chemistry* **287**, 11859–11869 (2012).

125. Nakata, T. & Yorifuji, H. Morphological evidence of the inhibitory effect of taxol on the fast axonal transport. *Neurosci Res* **35**, 113–122 (1999).

126. Hammond, J. W. *et al.* Posttranslational Modifications of Tubulin and the Polarized Transport of Kinesin-1 in Neurons. *Mol Biol Cell* **21**, 572–583 (2010).

127. Théry, M. & Blanchoin, L. Microtubule self-repair. *Curr Opin Cell Biol* **68**, 144–154 (2021).

128. Liang, W. H. *et al.* Microtubule Defects Influence Kinesin-Based Transport in Vitro. *Biophys J* **110**, 2229–2240 (2016).

129. Estévez Gallego, J. PhD thesis: Implications of the microtubule cap structure in the molecular mechanism of paclitaxel. (2020).

130. Andreu, J. M. Large Scale Purification of Brain Tubulin With the Modified Weisenberg Procedure. in *Microtubule Protocols* (ed. Zhou, J.) 17–28 (Humana Press, 2007).

131. Andreu, J. M. & Timasheff, S. N. Conformational states of tubulin liganded to colchicine, tropolone methyl ether, and podophyllotoxin. *Biochemistry* **21**, 6465–6476 (1982).

132. Walt, D. R. & Agayn, V. I. The chemistry of enzyme and protein immobilization with glutaraldehyde. *TrAC Trends in Analytical Chemistry* **13**, 425–430 (1994).

133. DÍaz José Fernando and Buey, R. M. Characterizing Ligand-Microtubule Binding by Competition Methods. in *Microtubule Protocols* (ed. Zhou, J.) 245–260 (Humana Press, 2007).

134. Lakowicz, J. R. *Principles of Fluorescence Spectroscopy*. (Springer US, 2006).

135. Kamimura, S., Fujita, Y., Wada, Y., Yagi, T. & Iwamoto, H. X-ray fiber diffraction analysis shows dynamic changes in axial tubulin repeats in native microtubules depending on paclitaxel content, temperature and GTP-hydrolysis. *Cytoskeleton* **73**, 131–144 (2016).

136. Blanton, T. N., Barnes, C. L. & Lelental, M. Applied Crystallography Preparation of silver behenate coatings to provide low-to mid-angle diffraction calibration. *J. Appl. Cryst* **33**, (2000).

137. Klug, A., Crick, F. H. C. & Wyckoff, H. W. Diffraction by helical structures. *Acta Crystallogr* **11**, 199–213 (1958).

138. Tinevez, J.-Y. & Herbert, S. The NEMO Dots Assembly: Single-Particle Tracking and Analysis. in 67–96 (2020). doi:10.1007/978-3-030-22386-1_4.

139. Tarantino, N. *et al.* Tnf and il-1 exhibit distinct ubiquitin requirements for inducing NEMO-IKK supramolecular structures. *Journal of Cell Biology* **204**, 231–245 (2014).

140. Qian, H., Sheetz, M. P. & Elson, E. L. Single particle tracking. Analysis of diffusion and flow in two-dimensional systems. *Biophys J* **60**, 910–921 (1991).

141. Guy, R. K., Scott, Z. A., Sloboda, R. D. & Nicolaou, K. C. Fluorescent taxoids. *Chem Biol* **3**, 1021–1031 (1996).

142. Efthimiadou, E. K. *et al.* Synthesis and characterization of novel natural product-Gd(III) MRI contrast agent conjugates. *Bioorg Med Chem Lett* **18**, 6058–6061 (2008).

143. Lis, L. G., Smart, M. A., Luchniak, A., Gupta, M. L. & Gurvich, V. J. Synthesis and biological evaluation of a biotinylated paclitaxel with an extra-long chain spacer arm. *ACS Med Chem Lett* **3**, 745–748 (2012).

144. Kingston, D. G. I. The chemistry of taxol. *Pharmacol Ther* **52**, 1–34 (1991).

145. Colombo, E. *et al.* New Class of Betulinic Acid-Based Nanoassemblies of Cabazitaxel, Podophyllotoxin, and Thiocolchicine. *ACS Med Chem Lett* **11**, 895–898 (2020).

146. Wuts, P. G. M. & Greene, T. W. *Greene's Protective Groups in Organic Synthesis*. (Wiley, 2014).

147. Chaudhary, A. G., Rimoldi, J. M. & Kingston, D. G. I. Modified taxols. 10. Preparation of 7-deoxytaxol, a highly bioactive taxol derivative, and interconversion of taxol and 7-epi-taxol. *J Org Chem* **58**, 3798–3799 (1993).

148. Skoog, D. A., West, D. M., Holler, F. J. & Crouch, S. R. *Fundamentals of Analytical Chemistry*. (Cengage, 2021).

149. Straubinger, R. M. Biopharmaceutics of Paclitaxel (Taxol): Formulation, Activity, and Pharmacokinetics. in *TAXOL®* 237–258 (CRC Press, 2021).

150. Wishart, D. S. *et al.* HMDB 5.0: the Human Metabolome Database for 2022. *Nucleic Acids Res* **50**, D622–D631 (2022).

151. Yvon, A.-M. C., Wadsworth, P. & Jordan, M. A. *Taxol Suppresses Dynamics of Individual Microtubules in Living Human Tumor Cells*. *Molecular Biology of the Cell* vol. 10 (1999).

152. Buey, R. M. *et al.* Interaction of Epothilone Analogs with the Paclitaxel Binding Site. *Chem Biol* **11**, 225–236 (2004).

153. Diaz, J. F., Menendez, M. & Andreu, J. M. Thermodynamics of ligand-induced assembly of tubulin. *Biochemistry* **32**, 10067–10077 (1993).

154. Sugiyama, T. *et al.* Quick shear-flow alignment of biological filaments for X-ray fiber diffraction facilitated by methylcellulose. *Biophys J* **97**, 3132–3138 (2009).

155. Kellogg, E. H. *et al.* Insights into the Distinct Mechanisms of Action of Taxane and Non-Taxane Microtubule Stabilizers from Cryo-EM Structures. *J Mol Biol* **429**, 633–646 (2017).

156. Mitra, A. & Sept, D. Taxol allosterically alters the dynamics of the tubulin dimer and increases the flexibility of microtubules. *Biophys J* **95**, 3252–3258 (2008).

157. Díaz, J. F., Barasoain, I., Souto, A. A., Amat-Guerri, F. & Andreu, J. M. Macromolecular accessibility of fluorescent taxoids bound at a paclitaxel binding site in the microtubule surface. *Journal of Biological Chemistry* **280**, 3928–3937 (2005).

158. Mosmann, T. Rapid colorimetric assay for cellular growth and survival: Application to proliferation and cytotoxicity assays. *J Immunol Methods* **65**, 55–63 (1983).

159. Shen, D. W. *et al.* Multiple drug-resistant human KB carcinoma cells independently selected for high-level resistance to colchicine, adriamycin, or vinblastine show changes in expression of specific proteins. *Journal of Biological Chemistry* **261**, 7762–7770 (1986).

160. Cornwell, M. M., Gottesman, M. M. & Pastan, I. H. Increased vinblastine binding to membrane vesicles from multidrug-resistant KB cells. *Journal of Biological Chemistry* **261**, 7921–7928 (1986).

161. Kanakkanthara, A. & Miller, J. H. βIII-tubulin overexpression in cancer: Causes, consequences, and potential therapies. *Biochimica et Biophysica Acta (BBA) - Reviews on Cancer* **1876**, 188607 (2021).

162. Stengel, C. *et al.* Class III B-tubulin expression and in vitro resistance to microtubule targeting agents. *Br J Cancer* **102**, 316–324 (2010).

163. Im, K., Mareninov, S., Diaz, M. F. P. & Yong, W. H. An introduction to performing immunofluorescence staining. in *Methods in Molecular Biology* vol. 1897 299–311 (Humana Press Inc., 2019).

164. Cadart, C., Zlotek-Zlotkiewicz, E., Le Berre, M., Piel, M. & Matthews, H. K. Exploring the Function of Cell Shape and Size during Mitosis. *Dev Cell* **29**, 159–169 (2014).

165. Leung, J. C. & Cassimeris, L. Reorganization of paclitaxel-stabilized microtubule arrays at mitotic entry: roles of depolymerizing kinesins and severing proteins. *Cancer Biol Ther* **20**, 1337–1347 (2019).

166. Khing, T. M. *et al.* The effect of paclitaxel on apoptosis, autophagy and mitotic catastrophe in AGS cells. *Sci Rep* **11**, (2021).

167. Surana, S. *et al.* The evolution of the axonal transport toolkit. *Traffic* **21**, 13–33 (2020).

168. Kidwai, A. M. & Ochs, S. Components of fast and slow phases of axoplasmic flow. *J Neurochem* **16**, 1105–12 (1969).

169. Zhang, J., Campbell, R. E., Ting, A. Y. & Tsien, R. Y. Creating new fluorescent probes for cell biology. *Nat Rev Mol Cell Biol* **3**, 906–918 (2002).

170. Takihara, Y. *et al.* In vivo imaging of axonal transport of mitochondria in the diseased and aged mammalian CNS. *Proceedings of the National Academy of Sciences* **112**, 10515–10520 (2015).

171. Swedlow, J. R. Innovation in biological microscopy: Current status and future directions. *BioEssays* **34**, 333–340 (2012).

172. Kawano, T. *et al.* A Small Peptide Sequence is Sufficient for Initiating Kinesin-1 Activation Through Part of TPR Region of KLC1. *Traffic* **13**, 834–848 (2012).

173. Dalmau-Mena, I. *et al.* Nanoparticles engineered to bind cellular motors for efficient delivery. *J Nanobiotechnology* **16**, (2018).

174. Bhat, L., Liu, Y., Victory, S. F., Himes, R. H. & Georg, G. I. Synthesis and evaluation of paclitaxel C7 derivatives: Solution phase synthesis of combinatorial libraries. *Bioorg Med Chem Lett* **8**, 3181–3186 (1998).

175. Georg, G. I., Liu, Y., Boge, T. C. & Himes, R. H. 7-O-acylpaclitaxel analogues: potential probes to map the paclitaxel binding site. *Bioorg Med Chem Lett* **7**, 1829–1832 (1997).

176. Altstadt, T. J. *et al.* Synthesis and antitumor activity of novel C-7 paclitaxel ethers: Discovery of BMS-184476. *J Med Chem* **44**, 4577–4583 (2001).

177. Thetiot-Laurent, S., Nadal, B. & Le Gall, T. Synthesis of Bis(tetronic acid)s via Double Dieckmann Condensation. *Synthesis (Stuttg)* **2010**, 1697–1701 (2010).

178. Curvey, N., Luderer, S., Walker, J. & Gokel, G. Improved Syntheses of Benzyl Hydraphile Synthetic Cation-Conducting Channels. *Synthesis (Stuttg)* **46**, 2771–2779 (2014).

179. Xiao, X. *et al.* Effects of C7 substitutions in a high affinity microtubule-binding taxane on antitumor activity and drug transport. *Bioorg Med Chem Lett* **21**, 4852–4856 (2011).

180. Fersht, A. *Structure and Mechanism in Protein Science*. vol. 9 (WORLD SCIENTIFIC, 2017).

181. Buey, R. M. *et al.* Microtubule interactions with chemically diverse stabilizing agents: Thermodynamics of binding to the paclitaxel site predicts cytotoxicity. *Chem Biol* **12**, 1269–1279 (2005).

182. Camps, C. *et al.* Phase II trial of the novel taxane BMS-184476 as second-line in non-small-cell lung cancer. *Annals of Oncology* **16**, 597–601 (2005).

183. Maryanoff, B. E. & Reitz, A. B. *Advances in medicinal chemistry. Volume 4.* (Elsevier Science, 1999).

184. Newton, C. N. *et al.* Intrinsically Slow Dynamic Instability of HeLa Cell Microtubules in Vitro. *Journal of Biological Chemistry* **277**, 42456–42462 (2002).

185. Fourest-Lieuvin, A. Purification of tubulin from limited volumes of cultured cells. *Protein Expr Purif* **45**, 183–190 (2006).

186. Magnani, M. *et al.* The βI/βIII-tubulin isoforms and their complexes with antimitotic agents: Docking and molecular dynamics studies. *FEBS Journal* **273**, 3301–3310 (2006).

187. DeWitt, M. A., Chang, A. Y., Combs, P. A. & Yildiz, A. Cytoplasmic Dynein Moves Through Uncoordinated Stepping of the AAA+ Ring Domains. *Science (1979)* **335**, 221–225 (2012).

188. Ferro, L. S., Can, S., Turner, M. A., ElShenawy, M. M. & Yildiz, A. Kinesin and dynein use distinct mechanisms to bypass obstacles. *Elife* **8**, (2019).

189. Schaedel, L. *et al.* Microtubules self-repair in response to mechanical stress. *Nat Mater* **14**, 1156–1163 (2015).

190. Rai, A. *et al.* Lattice defects induced by microtubule-stabilizing agents exert a long-range effect on microtubule growth by promoting catastrophes. *Proceedings of the National Academy of Sciences* **118**, (2021).

191. Kalra, A. P. *et al.* Investigation of the Electrical Properties of Microtubule Ensembles under Cell-Like Conditions. *Nanomaterials* **10**, 265 (2020).

192. Li, L., Alper, J. & Alexov, E. Cytoplasmic dynein binding, run length, and velocity are guided by long-range electrostatic interactions. *Sci Rep* **6**, 31523 (2016).